Master's thesis

NTNU
Norwegian University of Science and Technology
Faculty of Natural Sciences
Department of Physics

Marthe Linnerud

Building a framework for domain characterisation of $K_3Nb_3B_2O_{12}$ by electron diffraction and transmission electron microscopy

Master's thesis in Nanotechnology
Supervisor: Antonius T.J. van Helvoort
Co-supervisor: Dennis Meier and Ivan Ushakov
June 2022

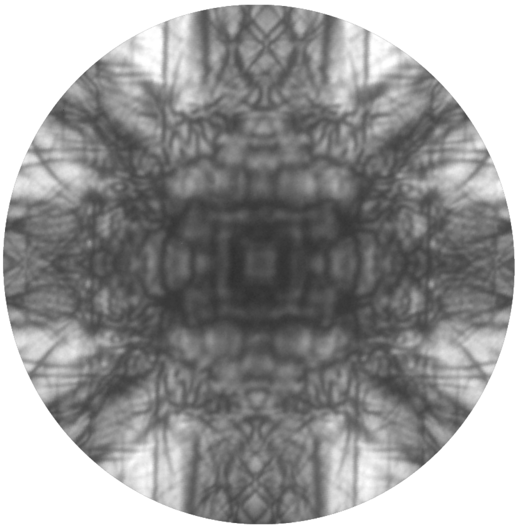

NTNU
Norwegian University of
Science and Technology

Marthe Linnerud

Building a framework for domain characterisation of $K_3Nb_3B_2O_{12}$ by electron diffraction and transmission electron microscopy

Master's thesis in Nanotechnology
Supervisor: Antonius T.J. van Helvoort
Co-supervisor: Dennis Meier and Ivan Ushakov
June 2022

Norwegian University of Science and Technology
Faculty of Natural Sciences
Department of Physics

NTNU
Norwegian University of
Science and Technology

Abstract

The orthorhombic ferroelastic oxide $K_3Nb_3B_2O_{12}$ (KNBO) has been suggested as a candidate material for domain wall engineering because of its proposed (anti)ferroelectric properties. Previous work on KNBO has reported conflicting results regarding its true ferroic properties and crystal structure. The only two previous studies that have inspected this material with transmission electron microscopy (TEM) have underlined the difficulties with localising structural changes in KNBO in areas containing ferroic domain walls. They both proposed that standard procedures for domain inspections in TEM are complicated by the pseudo-hexagonal crystal structure of KNBO, and that there is a need for determining the zones at which the electron diffraction of KNBO changes sufficiently at a domain wall to detect it.

This thesis proposes a framework for domain characterisation of KNBO using several electron diffraction techniques, conventional TEM, and high-angle annular-dark field (HAADF) scanning TEM (STEM) for detecting domain walls in KNBO. A correlated microscopy study is included, with the aim of investigating the relation between the crystal structure and ferroic properties of KNBO. This was conducted by combining TEM, polarised-light microscopy (PLM), and piezo-response force microscopy (PFM), with a special focus on structural characterisation in the TEM.

High-quality TEM specimens with the *c*-axis in-plane and *c*-axis out-of-plane were prepared by mechanical tripod polishing. Structural characterisation and domain localisation were successfully performed, although KNBO is prone to charging and beam damage. By comparing the experimental diffraction patterns to dynamical Bloch wave and multislice simulations, the crystal structure of thin film KNBO was determined to deviate from that of bulk KNBO. Electron diffraction patterns were successfully mapped for eleven zones, whereof nine from a tilt-series, in addition to more than 60 zones with Bloch wave simulations. The dynamical diffraction simulations of KNBO need further optimalisation with respect to the crystal potential model. Furthermore, an implementation that reduces the computational memory requirements for simulating diffraction patterns of KNBO is desired.

Structural 120° twin domains were for the first time characterised down to lattice resolution and confirmed that the twinning axis of KNBO is the *c*-axis. The domains were most efficiently localised with HAADF STEM by the observation of distinct extended twin boundaries, several hundred nanometres wide, when the specimen was oriented between two zones with the *c*-axis in-plane. In addition, extended low-angle grain boundaries with a 0.6° rotation of the crystal structure were for the first time identified. They are proposed to either separate two antiferroelectric domains or two sub-grains. The correlated microscopy study indicates that KNBO loses its ferroelastic properties below a threshold thickness when thinned from a facet with the *c*-axis in-plane. Further work for assessing the altered crystal structure of thin film KNBO, the disappearance of polar domains in TEM specimens with the *c*-axis in-plane, and the origin of the low-angle grain boundaries are proposed for future studies on KNBO.

Sammendrag

Det ortorombiske, ferroelastiske oksidet $K_3Nb_3B_2O_{12}$ (KNBO) har blitt foreslått som et kandidatmateriale for domeneveggbasert teknologi på grunn av dets foreslåtte (anti)ferroelektriske egenskaper. Tidligere har det blitt rapportert motstridende resultater angående de ferroiske egenskapene til KNBO og dets krystallstruktur. De to eneste tidligere transmisjonselektronmikroskopi (TEM) studiene på dette materialet har understreket at det er utfordrende å lokalisere strukturelle endringer ved ferroiske domenevegger i KNBO. Begge studiene foreslo at standardprosedyrer for domeneinspeksjoner i TEM kompliseres av den pseudoheksagonale krystallstrukturen, og at det er et behov for å bestemme de sone-aksene hvor diffrakjsonsmønsteret endres tilstrekkelig ved en domenevegg til å oppdage den.

Denne oppgaven foreslår et rammeverk for domenekarakterisering av KNBO ved bruk av flere elektrondiffraksjonsteknikker, konvensjonell TEM og høyvinkel annulær-mørkefelt (HAADF) sveipe TEM (STEM) for å detektere domenevegger i KNBO. Et korrelert mikroskopistudie ble også utført for å undersøke sammenhengen mellom krystallstrukturen og de ferroiske egenskapene til dette materialet ved å kombinere TEM, polarisert lysmikroskopi (PLM) og piezo-responskraftmikroskopi (PFM), med et spesielt fokus på strukturell karakterisering i TEM.

TEM-prøver av høy kvalitet med c-aksen i-planet og c-aksen ut-av-planet ble forberedt ved mekanisk stativpolering. Strukturell karakterisering og domenelokalisering ble vellykket utført, selv om KNBO var mottakelig for oppladning og stråleskade. Ved å sammenligne de eksperimentelle diffraksjonsmønstrene med dynamiske Bloch-bølge og "multislice"-simuleringer har det blitt funnet at krystallstrukturen til tynnfilm KNBO avviker fra krystallstrukturen til bulk KNBO. Elektrondiffraksjonsmønstrene til elleve soner ble kartlagt, hvorav ni fra en helningsserie, i tillegg til mer enn 60 soner fra Bloch-bølgesimuleringer. De dynamiske diffraksjonssimuleringene av KNBO trenger ytterligere optimalisering med hensyn til krystallpotensialmodellen. Videre ønskes en implementering som reduserer kravene til beregningsminnet under dynamiske diffraksjonssimuleringer av dette materialet.

120°-tvillingdomener ble for første gang karakterisert ned til gitteroppløsning, og det ble bekreftet at c-aksen er tvillingaksen til KNBO. Domenene ble mest effektivt lokalisert med HAADF STEM på grunn av den enkle observasjonen av tydelige utvidede tvillinggrenser, med en bredde på flere hundre nanometer, når prøven var orientert mellom to soner med c-aksen i-planet. I tillegg ble det for første gang identifisert utvidede lav-vinkel korngrenser med en 0.6° rotasjon av krystallstrukturen. Det foreslås at disse korngrensene enten skiller to antiferroelektriske domener eller at de skiller to sub-korn. Det korrelerte mikroskopistudiet indikerer at KNBO mister sine ferroelastiske egenskaper under en viss tykkelse når den fortynnes fra en fasett med c-aksen i-planet. Videre arbeid for å vurdere den endrede krystallstrukturen til tynnfilm KNBO, forsvinningen av polare domener i TEM-prøver med c-aksen i-planet, og opprinnelsen til lav-vinkel korngrensene blir foreslått.

Preface

This master's thesis concludes my M.Sc. degree in Nanotechnology with a specialization in Nanotechnology for materials, energy, and the environment at the Faculty of Natural Sciences at the Norwegian University of Science and Technology (NTNU).

The work presented in this thesis was conducted during the spring semester of 2022 at the TEM Gemini Centre in the NORTEM infrastructure at the Department of Physics. This is a continuation of the project written in the autumn of 2021 [1]. Therefore, parts of this thesis are based on or reproduced from the project, most noticeably the theory in Chapter 2, and the specimen preparation in Chapter 3. All of the experimental work and results presented in this study were acquired in the spring of 2022, with the exception of the specimen preparation of a specimen with the *c*-axis out-of-plane that was prepared for the project thesis. Henceforth, polarised light microscopy images acquired prior to the specimen preparation were also obtained in the autumn of 2021. These results are therefore re-used since the specimen was further investigated in this work. Both studies were supervised by Prof. Antonius T.J. van Helvoort at the Department of Physics, including co-supervision by Prof. Dennis Meier and Ph.D. candidate Ivan Ushakov at the Department of Materials Science and Engineering. All work in this project has been performed by me, except for the piezo-response force microscopy measurements on the TEM specimens, which were performed by my co-supervisor, Ivan, with me present.

Crystal structures presented in this thesis were visualised with Vesta [2]. Dynamical diffraction simulations were conducted with the software JEMS [3] and the Python package py_multislice [4]. The diffraction patterns were analysed and indexed with the software ReciPro [5]. TEM data analysis was conducted using Fiji [6] and Digital Micrograph [7]. PFM micrographs were analysed with Gwyddion [8]. Figures have been designed with Adobe Illustrator [9] and Inkscape [10].

Marthe Linnerud

Marthe Linnerud
Trondheim
20th June 2022

Acknowledgements

Throughout the course of writing this master's thesis, several individuals deserve to be acknowledged for their support. The work was initialised from the key findings from the project work preceding this thesis, where it was evident that $K_3Nb_3B_2O_{12}$ displayed several unexpected diffraction properties that complicated the characterisation and localisation of ferroic domains in $K_3Nb_3B_2O_{12}$. Because of this, the application of several additional electron diffraction techniques for structural characterisation were needed, including advanced simulations. I would like to thank Postdoctoral Fellow Ding Peng for LACBED training and insight on simulation procedures. I would also like to thank Senior Engineer Emil Frang Christiansen for granting me access to the IDUN cluster, and Postdoctoral Fellow Jonas Frafjord for helping me set up the simulations on the IDUN cluster.

Further, I would like to extend my gratitude to Senior Engineer Bjørn Gunnar Solheim and Emil Frang Christiansen for training on the TEMs and specimen preparation. Their help was much appreciated in many of the countless hours in the lab. I would also like to thank my co-supervisor Ivan Ushakov at the Department of Materials Science and Engineering for carrying out the PFM measurements, and co-supervisor Prof. Dennis Meier for fruitful discussions and valuable insight on ferroic materials.

Most importantly, I would like to thank my supervisor, Prof. Antonius T.J. van Helvoort. I am grateful for his excellent guidance and feedback the past year. In most of the hours I have spent in the lab, I have returned from the sessions with several unexpected results. Although this work has at times been somewhat frustrating, it was ever more satisfying when possible solutions and explanations for the observed behaviour of the material were found. Thanks for granting me such an interesting and motivating project.

Furthermore, I would like to thank my fellow students in the Nanotechnology study programme for the long lunch breaks, late-night discussions, laughter, and our collective poor sense of humour. Especially thanks to Julie, Ida, and Charlotte for always being available when I have been stressed and needed a big hug, but also in times of joy. Finally, a special thanks to my family for remotely supporting me at my highs and lows this semester.

In addition, two key infrastructures need to be acknowledged:

- The Research Council of Norway is acknowledged through the Norwegian Center for Transmission Electron Microscopy, NORTEM (197405/F50).
- The computing resources available via the IDUN cluster at NTNU are acknowledged.

Abbreviations

BF Bright-field

BK Bird and King model

CBED Convergent-beam electron diffraction

CIF Crystallographic information file

DF Dark-field

DLF Diamond lapping film

DT Doyle-Turner model

EJK Earl J. Kirkland model

FIB Focused ion beam

FOLZ First-order Laue zone

GM Gjønnes-Moodie

HAADF High-angle annular dark-field

HOLZ Higher-order Laue zone

HRTEM High-resolution transmission electron microscopy

ITA International tables of crystallograpahy

KNBO $K_3Nb_3B_2O_{12}$

LACBED Large-angle convergent-beam electron diffraction

PFM Piezo-response force microscopy

PLM Polarised light microscopy

PRDW Peng-Ren-Dudarev-Whelan model

SAED Selected-area electron diffraction

SOLZ Second-order Laue zone

SPED Scanning-precession electron diffraction

STEM Scanning transmission electron microscopy

TEM Transmission electron microscopy

VLM Visible light microscopy

WK Weickenmeier-Kohl model

ZOLZ Zeroth-order Laue zone

Contents

1 Introduction

At the time of writing, there is a continuing search for new technologies that can increase the computing power and develop the computers of tomorrow. New technologies are needed to continue improving the efficiency of electronics [11–13]. Domain wall engineering in ferroic materials is a new, innovative technology that searches to push Moore's law by forming electronic components on the atomic scale using ferroic domain walls [14–17].

Ferroic materials are divided into three categories: ferroelectric, ferroelastic, and ferromagnetic materials. These materials display a spontaneous order which can be switched by an external field. In ferroelectric, ferroelastic, and ferromagnetic materials the switchable order parameter is the electronic polarisation, strain field and magnetisation respectively, and these order parameters can correspondingly be switched by an external electric, mechanical and magnetic field. Ferroic materials divide into domains to minimise their total potential energy. The boundaries between domains are typically only a few nanometres wide and are called domain walls. The domain walls may display extraordinary properties other than those usually observed in the separate domains, including the ability to move them, their thermal conductivity, unusual electric conductivity, superconductivity, and superionic conductivity. In domain wall engineering, these boundaries are utilised to make electrical components at the atomic scale for nanocircuitry in solid-state electronic devices, memory devices and neuromorphic computing [15, 18–25].

By manipulating the structural order of the domains, the domain walls can be engineered to display new functionality for the desired applications [21]. Hence, an understanding of the crystal structure of candidate materials is important for possible applications [26, 27]. Transmission electron microscopy (TEM) allows for performing a series of high-resolution imaging and electron diffraction techniques [28, 29], and is therefore an important tool for characterising domain wall structures at the atomic scale [23, 27, 30]. Several materials have been proposed as candidate materials for domain wall engineering, such as $BiFeO_3$, $CaTiO_3$, $ErMnO_3$, $SrMnO_3$ and many more [17, 31–33]. Multiferroic materials have especially been explored, such as those displaying an interplay of ferroelastic and ferroelectric order [17, 33, 34].

A new candidate material for domain wall engineering is the multiferroic anhydrous potassium niobate borate; $K_3Nb_3B_2O_{12}$ (KNBO). KNBO is ferroelastic, and from optical inspections KNBO has been observed to order in 120° twin domains with the *c*-axis as the twin axis [35]. Some studies have suggested that KNBO is ferroelectric with the *a*-axis as the polar axis, while others have suggested that it is antiferroelectric with the *c*-axis as the antiferroelectric axis [36, 37]. This has raised a number of questions about the true ferroic nature of KNBO. The majority of earlier work has been based on methods that cannot correlate the measured physical properties to KNBO's crystal structure [35–44]. Moreover, there has been a lack of research on the domain structure of KNBO at the atomic scale, or even in medium resolution TEM.

Previously, only two studies have been conducted with the aim of characterising the domain structure of KNBO at the atomic scale; the work by Oskar Ryggetangen [45], and the project on which this master's thesis is an extension [1]. Ryggetangen developed a method for investigating domain wall structures in KNBO by a correlated microscopy approach, combining polarised light microscopy (PLM), TEM and piezo-response force microscopy (PFM) to investigate the connection between KNBO's crystal structure and functional properties. Both studies attempted to characterise the domain structure in the [0 0 1], or *c*-plane, of the crystal. However, they underlined the difficulty of assigning the crystal orientation, and hence also characterising the domain structure of KNBO at the atomic scale in the *c*-plane. Overall, the correlated studies needed adjustments to construct an absolute approach for crystal structure determination of ferroic domains in KNBO using TEM.

Henceforth, the aim of this master's thesis has been to build a framework for domain characterisation of KNBO. To do this, four sub-goals were set: 1) To map the electron diffraction patterns of KNBO at several zones to gain a better understanding of its diffraction properties and crystal structure, 2) to identify the diffraction and imaging techniques that are most optimal for assessing ferroic domains, 3) to identify the zones which display a sufficient change in the diffraction pattern at a domain wall to obtain domain contrast, and 4) to conduct correlated microscopy studies of KNBO by combining measurements of the piezo-response and crystal structure of several domains in KNBO at one of the zones identified in sub-goal 3. The combined knowledge gained by reaching these subgoals would allow for a better understanding of the ferroic properties of KNBO, and the structural origin of these properties.

To map the electron diffraction of several zones, a TEM specimen had to be prepared that allowed for such a study. It was also highly desirable to prepare a specimen which could be used for assessing the polar axis and domains. It was hypothesised that the [0 1 0] zone would be an efficient zone, as it would allow for the assessment of both the polar *a*-direction and the proposed antiferroelectric *c*-direction. Additionally, any twin would allow for inspecting the zones 120° to the [0 1 0] zone. Henceforth, the framework suggested in this thesis will include a methodology for preparing TEM specimens with a high probability of containing a domain with the [0 1 0] direction perpendicular to the specimen surface. The structural characterisation was performed using selected area electron diffraction (SAED), convergent-beam electron diffraction (CBED) and large-angle CBED (LACBED). Experimental results and simulations were performed in an iterative process to find the optimal zones for assessing polarity, and for gaining a better understanding of the diffraction properties of KNBO. Combining experimental and simulated CBED patterns is a well-known technique to assess polarity [46, 47], which is why this thesis has put extra emphasis on such an approach. Both Bloch wave and multislice simualtions were performed. Finally, domain imaging was conducted using correlated microscopy, which included 1) PLM before specimen preparation, 2) high-angle annular dark-field scanning TEM (HAADF STEM), bright-field (BF) and dark-field (DF) TEM before structural domain characterisation, and 3) PFM to measure the piezo-response of the specimens.

This thesis consists of seven chapters, including this introduction. The second chapter introduces the main theory that forms the foundations of this thesis, including the basics of crystallography, ferroic materials, electron diffraction, the transmission electron microscope, and a short literature review of KNBO. The third chapter outlines the experimental procedures. After this, the results are presented and discussed in the fourth and fifth chapter. Lastly, conclusions are made and suggestions for future work are proposed.

2 Theory

This chapter presents the theoretical background related to the results and discussions obtained in this work. First, a general introduction to crystallography will be presented, followed by an outline of crystal defects and boundaries. Further, a short, qualitative introduction to ferroic materials is given. After this, kinematic and dynamic electron diffraction theory is outlined, followed by an introduction to the TEM. This includes the TEM techniques utilised in this thesis, and how they can be used for structural analysis of a crystal. Finally, the recent work on KNBO will be summarised. Parts or complete sections are based on, or re-prints, from the theory chapter from the project written prior to this thesis [1]. Some important additions are included.

2.1 Crystallography

Crystallography is the study of crystal structures and how to describe them. The most important terms in the field of crystallography will be presented in this section, but it is assumed that the reader has some knowledge of the general laws of group theory and crystallography. This section is based on Dauter and Jaskolski [48], Hammond [49] and the International Table of Crystallography [50].

2.1.1 Crystal systems

A crystal is a regular structure with long-range order. It can be described by a repeating unit that is translated to other crystal sites by the lattice translation vector, $\mathbf{R}$, defined by the vectors $\mathbf{a}$, $\mathbf{b}$, $\mathbf{c}$ and scalars u, v, and w.

$$\mathbf{R} = u\mathbf{a} + v\mathbf{b} + w\mathbf{c} \tag{2.1}$$

The lattice translation vectors $\mathbf{a}$, $\mathbf{b}$, and $\mathbf{c}$ has a length a, b and c respectively, and they are separated by an angle α between $\mathbf{c}$ and $\mathbf{b}$, an angle β between $\mathbf{a}$ and $\mathbf{c}$, and an angle γ between $\mathbf{a}$ and $\mathbf{b}$. This makes up the axis system in a crystal with crystallographic axes a, b and c.

A 3D crystal belongs to one of seven crystal systems. These are illustrated in figure 2.1. The seven crystal systems are the triclinic, monoclinic, orthorhombic, tetragonal, hexagonal, rhombohedral and cubic systems. Each point in the illustration represents a primary unit cell. The primitive unit cell is the least repeating unit in the crystal, and can be composed of several atomic units. There are in total 14 ways that these primary unit cells can be repeated, described by the 14 Bravais lattices. Each of these Bravais lattices belong to one of the seven crystal systems, but are additionally described by being either primitive (P), base-centered ($S = A/B/C$), face-centered

(F), body-centered (I) or primitive rhombohedral (R). There are in total 1 triclinic (P), 2 monoclinic (P, S), 4 orthorhombic (P, S, I, F), 2 tetragonal (P, I), 1 hexagonal (P), 1 rhombohedral (R) and 3 cubic (P, I, F) Bravais lattices. The four orthorhombic Bravais lattices are illustrated in figure 2.2. Hence, a crystal can be uniquely defined by its primary unit cell, and translation vector.

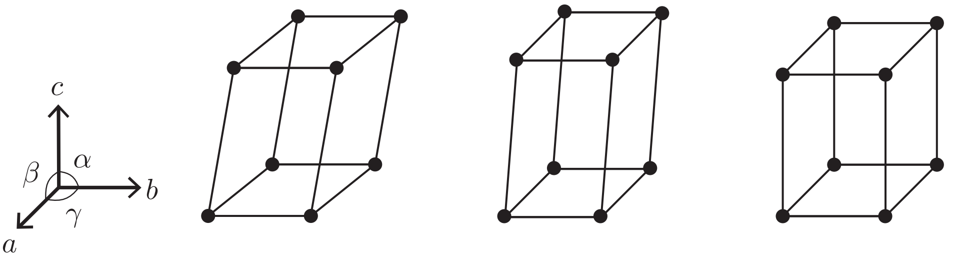

Triclinic
$a \neq b \neq c$
$\alpha \neq \beta \neq \gamma \neq 90°$

Monoclinic
$a \neq b \neq c$
$\alpha = \gamma = 90°, \beta \neq 90°$

Orthorhombic
$a \neq b \neq c$
$\alpha = \beta = \gamma = 90°$

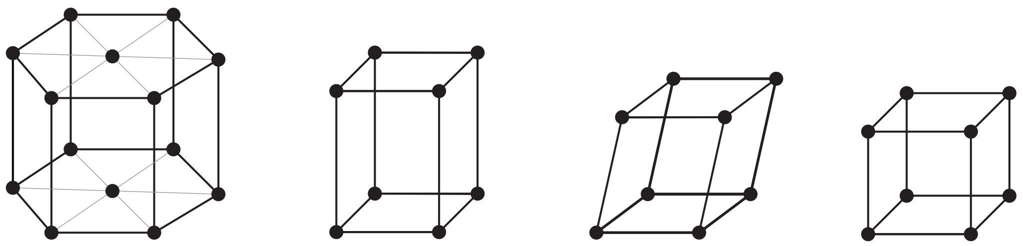

Hexagonal
$a = b \neq c$
$\alpha = \beta = 90°, \gamma = 120°$

Tetragonal
$a = b \neq c$
$\alpha = \beta = \gamma = 90°$

Rhombohedral
$a = b = c$
$\alpha = \beta = \gamma \neq 90°$

Cubic
$a = b = c$
$\alpha = \beta = \gamma = 90°$

Figure 2.1: Illustration of the seven crystal systems. Each of them may be described by three lattice constants a, b and c, and the angle between them, α, β, γ.

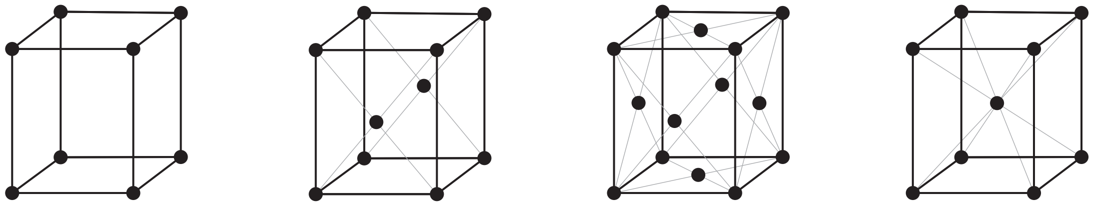

Primitive
(P)

Base-centered
(A/B/C)

Face-centered
(F)

Body-centered
(I)

Figure 2.2: The four orthorhombic Bravais lattices: Primitive (P), base-centered (A/B/C), face-centered (F), and body-centered (I).

2.1.2 Symmetry in crystals

Because of the regularity of crystals, they can be classified by the symmetry elements which they display. In crystallography, every point can be described by either mirror planes, rotational axes or rotoinversion axes. n-fold rotation means for instance that the unit cell can be rotated $360/n°$, and still appear equivalent. A rotoinversion is the combination of a rotation and an inversion of the symmetry through an inversion center. Such symmetries are present in crystals. For example, a cubic crystal has four 3-fold axes along its body-diagonals, and an orthorhombic crystal has three orthogonal 2-fold axes perpendicular to the a- b- and c-planes. Additionally, the crystal structures can be described by translational symmetry in space that are represented by glide planes or screw axes. A glide plane is a lattice translation parallel to the plane combined with a mirror reflection about that plane, while a screw axis is a lattice translation along an axis combined with a rotation about that axis. If a crystal lacks an inversion center, it is defined as non-centrosymmetric. If the crystal also lacks mirror symmetry, it is said to be chiral, describing that the crystal can be left-handed or right-handed.

The symmetry elements that can describe a crystal lattice are given in table 2.1. There are two styles for describing crystal symmetry. The Schöneflies and the Hermann-Mauguin notations. For crystallography, Hermann-Mauguin, also referred to as *the international notation*, is most commonly used. Therefore, this style will be used when describing crystallographic point and space groups.

Table 2.1: Point symmetries and translational symmetries that may be present in a crystal lattice.

Point symmetry			Translational symmetry	
Rotation	Rotoinversion	Mirror plane	Glide planes	Screw axes
1	$\bar{1}$	$\bar{2} = m$	a	2_1
2	$\bar{3}$		b	3_1
3	$\bar{4}$		c	3_2
4	$\bar{6}$		d	4_1
6			n	4_3
			e	6_1

The crystals are grouped in point groups according to the unique symmetry operations which can be imposed on them. This results in 32 point groups. 21 of these point groups are non-centrosymmetric. By combining the 32 space groups with the 14 Bravais lattices, taking into account the translational symmetry that describe the periodicity of the unit cell in space, one arrives at 230 possible space groups in 3D. The space group is in other words the point group convoluted with the crystal lattice. These are the total 230 possible ways a primitive unit cell can be oriented to make up a crystal. Every crystal can therefore be described by one of the 230 space groups. Thus, it is not only possible to uniquely define crystals by their lattice translation vectors, but also by the symmetry elements they contain.

2.1.3 Nomenclature

In order to effectively describe crystal structures, crystal directions, and crystal planes, there exist a set of nomenclature rules. These will be presented in this section. As will become clear in Section 2.6, KNBO has been suggested to be orthorhombic. Therefore, any further crystallographic considerations will mostly be explained in terms of orthorhombic crystals. Some examples may be given for cubic crystals for simplicity, or other crystal systems to illustrate important aspects of the given nomencalture.

Crystal planes and directions can be described by Miller indices [51]. A crystal plane is labelled $(h\,k\,l)$, where h, k and l represent the reciprocal of the fractional distance along the $\mathbf{a}$, $\mathbf{b}$, and $\mathbf{c}$ vectors. The corresponding crystal direction, $[h\,k\,l]$, is allways perpendicular to the crystal plane for cubic systems, but may not necesarily be perpendicular to the crystal plane for non-cubic systems depending on the length and angles between the lattice vectors. This is illustrated in figure 2.3 for a $(2\,1\,0)$ plane, and its corresponding $[2\,1\,0]$ direction for a cubic crystal. Crystal planes and crystal directions that display equivalent symmetry compose a family of crystal directions and planes. These are labelled $\langle h\,k\,l\rangle$ and $\{h\,k\,l\}$ respectively. A bar above any of the indices indicate that it is a negative value. Note especially that the $[1\,0\,0]$ direction correspond to the a-direction, the $[0\,1\,0]$ direction to the b-direction, and $[0\,0\,1]$ direction to the c-direction in a crystal.

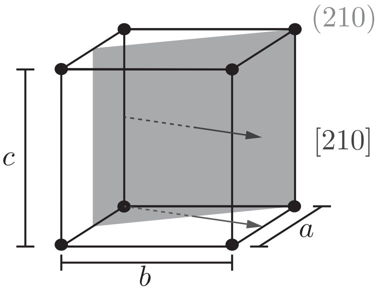

Figure 2.3: Basic principles of Miller indices. The $(2\,1\,0)$ plane and the $[2\,1\,0]$ direction for a cubic crystal are presented.

Sometimes, an orthorhombic crystal can be close to hexagonal, as is the case for KNBO. In these cases, it can be described by a pseudo-hexagonal axis system with an alternative a and b axis given by a_{hex} and b_{hex}. This is illustrated in figure 2.4.

There are several settings for describing point and space groups which depend on the crystal system. Which setting is normally used, depend on the unique axis. For orthorhombic space groups, there are six possible settings: $\mathbf{abc}$, $\mathbf{ba\bar{c}}$, $\mathbf{cab}$, $\mathbf{\bar{c}ba}$, $\mathbf{bca}$, $\mathbf{a\bar{c}b}$. These settings can be thought of as describing the choice of axis system. The **abc**-setting is the standard setting which is used in the International Tables of Crystallography, but it is easy to transform symmetry considerations from this setting, to any of the other settings. Transforming between space group settings, can simply be thought of as transforming from axis system (a, b, c) to (a', b', c'). This is written out in appendix A.

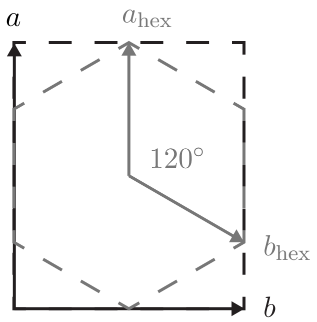

Figure 2.4: Pseudo-hexagonal axes, a_{hex} and b_{hex}, for an orthorhombic crystal with axes, a and b.

The point group and space group nomenclature depend on the crystal structure. An orthorhombic crystal can either be secribed by the 222, mmm or $2mm$ point groups (**cab**-setting), where the first, second and third letters described the symmetry along the a-, b- and c-axes respectively. For example, a crystal with point group $2mm$ will display a 2-fold rotation axis along the a-direction, and two mirror planes along the b- and c-planes.

As described in Section 2.1.2, the crystal space group combines the point group symmetry with the lattice type, in other words the translational symmetry. The space group in an orthorhombic crystal is written on the form $Xpqr$, where X describes the Bravais lattice as given in figure 2.2, and pqr describe the symmetry along the crystallographic axes a, b and c or their perpendicular planes. For example, space group 26 in the **cab**-setting is $P2_1ma$, where the c-axis has been defined as the unique axis. This describes that the crystal is primitive, with a 2_1 screw axis along the a-axis, a mirror plane along the b-plane and an a-glide plane with a reflection about the c-plane.

Note that other crystal systems have other conventions for describing characteristic symmetry. For example, in hexagonal space groups, the first letter after the Bravais symbol refers to the symmetry along the unique c-axis, the second to the a- or b-axis, and the third describes the symmetry along the diagonal between the a- and b-axis.

Henceforth, the space group notation is an effective notation for expressing the crystal structure of crystalline materials, but symmetry notation must be interpreted with care. Further, the crystal directions and planes are most effectively described by Miller indices.

2.2 Defects

The previous theory considered perfect crystals. Real crystals are not perfect and may contain stacking faults, point defects, line defects and planar defects. Such defects are also present at crystal interfaces. The presence of a defect results in a strain field which alters the properties of the crystal at that specific site. Point defects have a tendency of accumulating at crystal boundaries and ferroic domain walls. This section presents the main defects that may be present in a crystal. Unless otherwise stated, this theory is based on West [52] and Tilley [53].

2.2.1 Point defects

The two most common point defects are interstitials and vacancies, and are illustrated in figure 2.5. A vacancy is the absence of an atom at an atomic lattice site, while an interstitial is the presence of an atom in a non-crystallographic site.

Typical point defects are anion vacancies and metal-cation interstitials. Point defects can therefore be assigned a charge. Anion vacancies are positively charged point defects, because the anion is missing at an atomic site, while cation interstitials are positively charged point defects because an additional positive charge is added to an unoccupied lattice point. Similarly, anion interstitials and cation vacancies are point defects that can be assigned a negative charge. Defects must form such that charge neutrality is conserved. Thus, the presence of a cation vacancy is typically accompanied by either an anion vacancy or a cation interstitial. These properties of interstitials and vacancies may alter the conductivity of the crystal at an interface or a boundary.

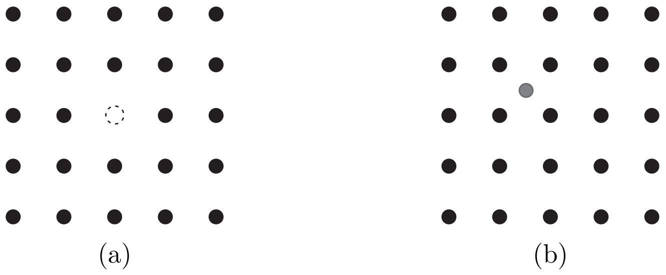
(a) (b)

Figure 2.5: (a) A vacancy (dashed) is the absence of an atom at an atomic lattice site. (b) An interstitial (grey) is the presence of an atom in a non-atomic lattice site.

2.2.2 Line and planar defects

A line defect is the presence of a series of crystal irregularities along a line, also called dislocations. Examples of line defects are edge dislocations, where an extra half-plane of atoms is introduced to the lattice, and screw dislocations, where the dislocation shifts like a spiral staircase. The crystal lattice may be shifted, compressed or strained along line defects, and they may or may not occur along specific crystallographic planes. Similarly, a planar defect is a disruption in the periodicity of the crystal along a 2D plane. Such planar defects are typically observed along crystal boundaries.

2.2.3 Special grain boundaries

A crystal may contain several boundaries including its surface, phase boundaries, grain boundaries and other homo-interfaces. If two different single crystals grow together, grain boundaries are formed and the crystal is termed polycrystalline. A phase boundary is the interface of crystals with different composition. Neither random grain boundaries, surface boundaries, or phase boundaries will be considered in this thesis, but rather specific low-energy boundaries. Low-energy boundaries arise as a result of other phenomena than two crystals growing together. One example is twin boundaries, where two domains of different crystal directions meet.

A twin boundary is an interface where the crystal structure on either side of the boundary mirrors or *twins* each other, forming two twin domains. If the domains on either side of the twin boundary do not mirror each other directly, but are for example related by a rotation, the correct term to use is a composition plane. However, these terms are often used interchangeably. Figure 2.6a illustrates a 120° twin boundary for a 2D rectangular lattice. The two domains in figure 2.6a represent the same crystal, but rotated 120° with respect to each other. Three 120° domain walls may also strike each other at a single vortex, as illustrated in 2.6b. At the boundary, there will be a complex defect structure with an accumulation of point defects due to lattice mismatch. This results in broad boundary of several nanometers. Hence, twin domains should be easily recognised by high-resolution microscopy techniques.

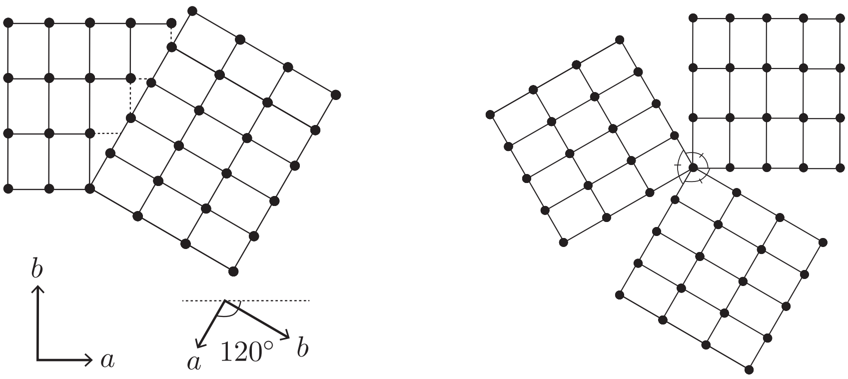

(a) (b)

Figure 2.6: Twin boundary between 120° twin domains. (a) Two twin domains meeting at a 120° twin boundary. (b) Three 120° twin domains meeting at a single vortex.

Another low-energy boundary is an antiphase boundary. An antiphase boundary is a homo-interface where two domains of the same crystal meets with a relative lateral displacement. For example, if the crystal can be described by an ABABAB stacking, the stacking of the crystal at the antiphase boundary will be AA or BB resulting in an ABABAABABA stacking. This is illustrated in figure 2.7. Antiphase boundaries are often observed in ferroelectric and antiferroelectric materials.

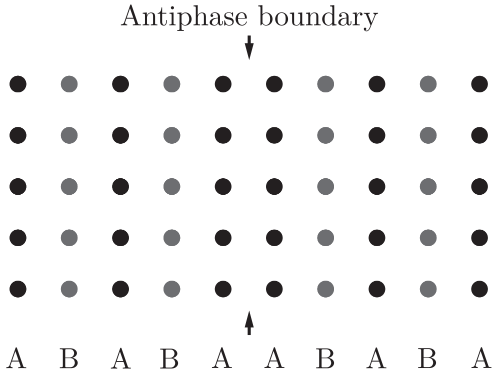

Figure 2.7: Schematic of an antiphase boundary.

2.3 Ferroics

$K_3Nb_3B_2O_{12}$ is said to be multiferroic with ferroelastic and ferroelectric or antiferroelectric domains. This section will describe the main theory about ferroic materials, the crystallographic prerequisites of such materials, and defect structures in ferroic domain walls. Lastly, techniques that directly measure ferroicity will be presented.

2.3.1 Ferroic materials and crystallography

The symmetry of the physical properties of a crystal is at least as high as the crystallographic symmetry of the host material. This is known as Neumann's principle, and is one of the most basic principles of solid state physics and functional materials [50]. This principle is especially important for materials which display ferroic properties. A ferroic material exhibits the property of having a spontaneous switchable order-parameter. Examples of such order-parameters are polarisation, elasticity and magnetisation[1].

Materials that exhibit a spontaneous switchable polarisation are classified as ferroelectric, while materials that show spontaneous switchable elasticity are ferroelastic, and materials which display a spontaneous switchable magnetisation are ferromagnetic [52]. These materials are readily recognised by their hysteresis curves which show the response of the order parameter to the application of an external electric, mechanical and magnetic field respectively. Ferroelastic and ferroelectric switching is illustrated in figure 2.8a and 2.8b. A special case of ferroelectric order is antiferroelectricity, where the polarisation of the individual electric dipoles in the material preferably order antiparallelly resulting in a net-polarisation of zero when no external electric field is applied to the material. The dipoles can, however, be reversibly switched to a net polarisation by the application of an external electric field. Antiferroelectric switching is illustrated in figure 2.8c.

---

[1] Note that ferromagnetic materials will not be considered in this report, but are included in this section for completeness.

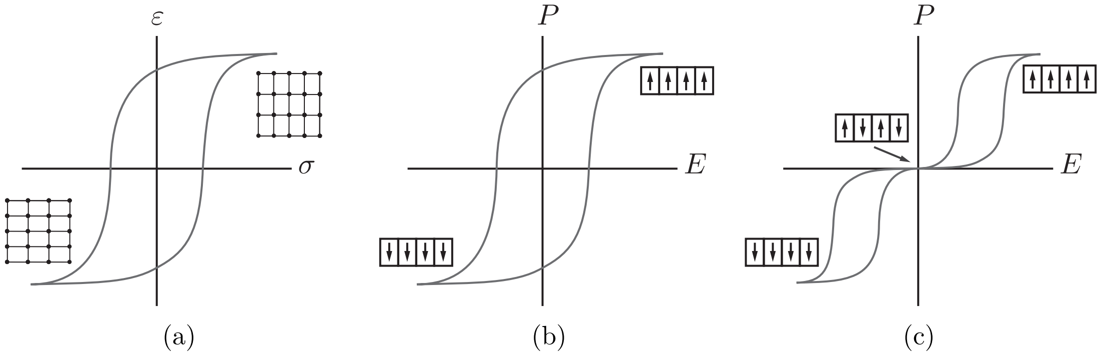

(a) (b) (c)

Figure 2.8: Ferroic switching and hysteresis. (a) Ferroelastic hysteresis where a given strain state is switched by an external strain field. ε is the strain and σ is the stress. (b) Ferroelectric hysteresis, where the spontaneous polarisation is switched by an external electric field. (c) Antiferroelectric hysteresis, where the material has a net polarisation of zero, but may obtain a switchable net-polarisation by the application of an electric field. The arrows in (b) and (c) indicate the polarisation of electric dipoles.

Ferroic materials that display coupled ferroic properties are said to be multiferroic. For example in coupled ferroelectric and ferroelastic multiferroics, the application of an external stress may result in a reversible change in the electric dipole of the material. Or equally, the application of an electric field will change the polarisation of the material, but simultaneously result in a mechanical switching of the elastic strain state.

All ferroelectric and ferroelastic materials are also piezoelectric, where a mechanical force exerted along the polar axis of the material will generate an electric field in the material. A polar axis is symmetrically in-equivalent in its opposite directions. Consequently, only rotation axes or screw axes can be polar [50]. For a material to be piezoelectric, it must be described by one of the 21 non-centrosymmetric point groups [50]. Piezoelectric materials are dielectric, and are therefore electrically insulating. Note that although all ferroelectric and ferroelastic materials are piezoelectric, not all piezoelectric materials are ferroelectric or ferroelastic.

2.3.2 Ferroelastics

Ferroelastic materials are materials which exhibit a spontaneous deformation to an applied stress. In other words, it exhibits a mechanical switching of at least two energetically stable oriental states by an external mechanical stress [54]. Such behaviour can be identified in the stress-strain curve of the material by the presence of hysteresis, as illustrated in figure 2.8a. The two stable oriental states can be two low-energy crystal structures, or two twin domains. If two separate ferroelastic domains are twin domains, the ferroelastic domain wall is the twin boundary.

Ferroelastic domains can be recognised as parallel, needle-shaped domains [54]. The domains form these shapes to minimise the local strain, where the crystallographic orientations that construct low strain fields will extend, while the strained crystallographic orientations will be narrow. Ferroelastic domains may therefore be easily recognised by their characteristic shape.

2.3.3 Ferroelectrics

Ferroelectric materials are characterised by having a permanent electric dipole that can be reversibly switched by the application of an electric field [50]. The order parameter which describes ferroelectricity is the polarisation of the dipoles. One typical example of ferroelectric materials are perovskites, where the polarisation depends on the position of the cation in the central octahedra. Ferroelectricity is also present in other crystal structures, but a common denominator is that they are perovskite-like. Ferroelectric switching is illustrated in figure 2.9 in a schematic perovskite for simplicity.

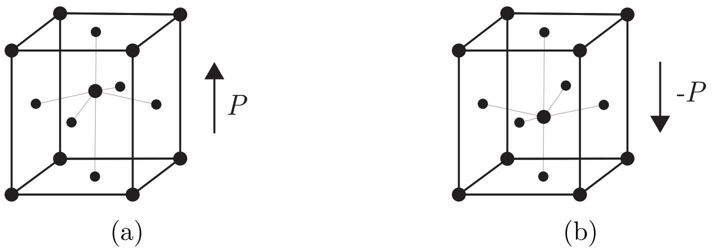

(a) (b)

Figure 2.9: Ferroelectric switching in perovskite structures from a state of polarisation P (a) to $-P$ (b). The position of the cation in the octahedra can reversibly shift when an external electric field is applied.

It is common to distinguish between proper and improper ferroelectrics [17]. Proper ferroelectrics have the polarisation as the primary order parameter that breaks the point symmetry of the crystal. Contrarily, improper ferroelectrics have another ferroic property as the primary order parameter, while the ferroelectric polarisation arises as a secondary effect. Thus, in improper ferroelectrics the polarisation is a symmetry-enforced result of a structural (ferroelastic) or magnetic (ferromagnetic) phase transition, and are henceforth multiferroic. In an improper ferroelectric where the primary order parameter is elasticity, there will be twice as many types of ferroelectric domains as ferroelastic domains. For example, if the material has three ferroelastic domains, it will have six ferroelectric domains.

2.3.4 Domain walls

Ferroic materials order in domains separated by domain walls. The size and number of domains and domain walls are determined by the competition between the energy cost of forming domain walls, and the energy gain of forming domains [31]. In ferroelectric materials, it is energetically favourable to form domains because this will lead to a net polarisation of zero for the bulk. However, the formation of domain walls is energetically unfavourable because there will be uncompensated charges and point defects in the domain walls. The same principles can be applied to ferroelastic domains and minimizing the net strain in the material. The size of a domain wall can range from a few unit cells, to several nanometers.

There are several types of ferroelectric domain walls, depending on the orientation of the polarisation in each of the domains. The extremes are head-to-head, tail-to-tail, and neutral domain walls. This is illustrated in figure 2.10. Because of the polarisation, the head-to-head domain walls will be positively charged, the tail-to-tail domain walls will be negatively charged, and the up and down configuration will result in neutral domain walls. There may also be some intermediates of these, such as 120° domain walls. The orientation of the polarisation and thus also the characteristics of the domain walls are restricted to, and determined by, the crystallographic properties the material.

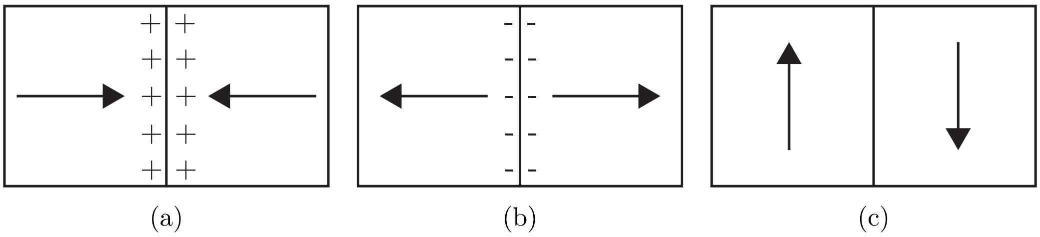

(a) (b) (c)

Figure 2.10: (a) Positively charged head-to-head domain walls. (b) Negatively charged tail-to-tail domain walls. (c) Neutral domain walls. The arrows indicate the net-polarisation of the domains.

Ferroelectric and ferroelastic domains are insulating, while the domain walls may be conductive. This is because a charge may arise at the domain wall from the polarisation, leading to locally diverging electrostatic potentials that require screening by redistributing the charges along the boundaries. Thus, there may be a high charge carrier concentration at the domain boundaries. This enhanced conductance is a result of either extrinsic or intrinsic effects. Intrinsic effects are changes in the electronic band structure, while extrinsic effects are the occurrence of point defects at the domain wall. For example, oxygen vacancies will accumulate at negatively charged domain walls, while they will be depleted at positively charged domain walls.

To summarise, ferroelectric and ferroelastic materials both order in domains separated by a domain wall. The main difference between ferroelectric and ferroelastic domains is the switchable order parameter that characterises the domain. Ferroelastic domains are characterised by a net spontaneous polarisation, while ferroelastic domains are characterised by displaying a net polar strain field caused by for example twinning. These domains are separated by domain walls that can be recognised by the accumulation of point defect. Hence, domain walls may be recognised by high-resolution microscopy techniques such as TEM. Further, some domain walls may be charged, such that there is a measurable electric field across the domain walls. Such an electric field may be measured directly by electric field sensitive instruments.

2.3.5 Imaging of polar domains

There are several instruments that can measure or identify ferroic properties, domains and domain walls. Two important microscopy techniques used to lacalise ferroelectric and ferroelastic domains are polarised light microscopy (PLM) and piezo-response force microscopy (PFM).

2.3.5.1 PLM

Ferroelastic domains can be observed in a polarised light microscope by a property called birefringence [55]. This is an optical property where the refractive index of the material depends on the polarisation of the light. The refracted wave at one structural domain of an anisotropic material will have a different polarisation than at another structural domain [56]. This technique is often used to image ferroelectric domains, but this is only possible if the ferroelectric domains also are ferroelastic. There is no difference in the birefringence of 180° domains [57]. Thus, such domains will appear identical in PLM. In other words, it is not possible to image ferroelectric, non-ferroelastic domains by PLM. Domain contrast is one type of birefringence contrast, and appear as an intensity and colour difference between domains. However, birefringence contrast may also arise due to other strain fields. Thus, lattice defects may also be the cause of birefringence contrast.

2.3.5.2 PFM

With PFM, the piezo-response of polar domains can be quantitatively measured with by the converse piezo-electric effect. An alternating current is applied to the material, and the deformation of the material is measured by the deflection of an atomically sharp conductive tip that is scanned across a polar specimen. Thus, different domains will be imaged depending on the strength of the piezo-response of the domains. Hence the contrast observed in PFM micrographs is directly dependent on the strength and direction of the polarisation of the domains [58]. Since PFM can distinguish $+P$ and $-P$ polarisations, it may be used to identify 180° ferroelectric domains.

2.4 Electron diffraction

Electron diffraction is the process where electrons scatter on the inner Coulomb potential of the atoms in a material. The scattered waves will interact constructively and destructively to create a diffraction pattern. The diffraction pattern will therefore contain information about the size and geometry of the crystal structure of the specimen. In diffraction theory, it is common to distinguish between kinematical diffraction and dynamical diffraction. The former is defined as a single scattering event. Kinematic diffraction theory is valid when the crystal specimen is sufficiently thin, typically below 100 nm or even below 10 nm for elements of higher atomic mass. If the specimen is thick, dynamical diffraction theory must be applied. This section will therefore present the basics of kinematic and dynamical electron diffraction in order to explain how a TEM is used to form diffraction patterns and display diffraction contrast. Most theory in this section is based on Fultz and Howe [28] unless otherwise is specified.

2.4.1 Kinematic diffraction theory

Kinematic diffraction theory is based on coherent elastic scattering of electrons. Scattering from crystal planes can be described in terms of Bragg's law, as in figure 2.11. In real space, Bragg's law is given by equation 2.2,

$$2d \sin\theta = n\lambda \tag{2.2}$$

where d is the interplanar spacing, λ is the wavelength of the wave, θ is the angle between the incoming and diffracted wave, and n is an integer representing the order of the diffraction spot. The wavelength of an electron is given by the de-Broglie relation in equation 2.3[2], where h is Planck's constant, p_e is the momentum of the electron, m_e is the electron mass, e is the charge of an electron, c is the speed of light, and V_a is the acceleration voltage of the electrons [29].

$$\lambda = \frac{h}{p_e} = \frac{h}{\sqrt{2m_e eV_a\left(1+\frac{eV_a}{2m_e c^2}\right)}}, \tag{2.3}$$

---

[2] A relativistic correction must be included when the electrons are accelerated over 100 kV.

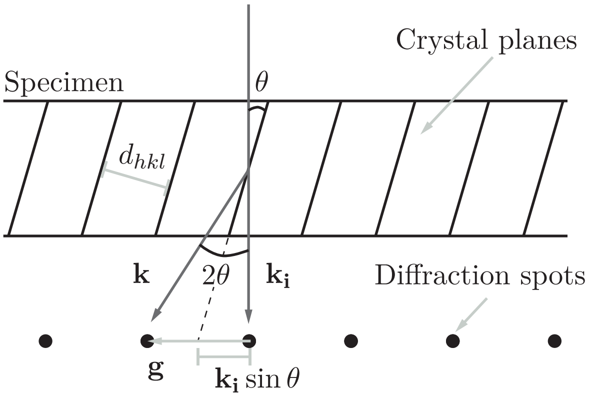

Figure 2.11: Schematic illustration of Bragg's law. An incident beam enters the crystal. The two waves scatter from crystal planes separated by a distance, d_{hlk}. $\mathbf{k_i}$ is the forward scattered beam and $\mathbf{k}$ is the diffracted beam. Both waves scatter at an angle, θ, such that the two waves interfere constructively only if the path difference between them is $2d_{hkl}\sin\theta$, where $g = \frac{1}{d_{hkl}}$.

For 200 keV electrons the wavelength would be 0.0251 Å. This distance is approximately equal to, or below, the interatomic spacings in a crystal. In the orthorhombic system, d is given by the distance between $(h\,k\,l)$ planes d_{hkl}, as given in equation 2.4.

$$\frac{1}{d} = \frac{1}{d_{hkl}} = \sqrt{\frac{h^2}{a^2} + \frac{k^2}{b^2} + \frac{l^2}{c^2}} \tag{2.4}$$

One can index a diffraction pattern by combining Bragg's law and the known interplanar distance in the crystal system. That is, the intensity maxima of the diffraction pattern can be labelled according to the $(h\,k\,l)$ plane spacing they represent. Hence, the diffraction pattern can give a direct relation to the crystal structure and its relative orientation with respect to the electron beam. The diffraction pattern is a representation of the so-called reciprocal crystal lattice of a material, and exists in the reciprocal space. Since diffraction occurs at crystal planes in real space, each point in the reciprocal lattice will correspond to $(h\,k\,l)$ planes of the real lattice. For a crystal with lattice parameters described by the vectors $\mathbf{a}$, $\mathbf{b}$ and $\mathbf{c}$, the reciprocal lattice will have reciprocal lattice vectors described by the vectors $\mathbf{a}^*$, $\mathbf{b}^*$ and $\mathbf{c}^*$.

$$\begin{aligned} \mathbf{a}^* &= 2\pi\frac{\mathbf{b}\times c}{\mathbf{a}\cdot\mathbf{b}\times\mathbf{c}} \\ \mathbf{b}^* &= 2\pi\frac{c\times\mathbf{a}}{\mathbf{b}\cdot\mathbf{c}\times\mathbf{a}} \\ \mathbf{c}^* &= 2\pi\frac{\mathbf{a}\times\mathbf{b}}{\mathbf{c}\cdot\mathbf{a}\times\mathbf{b}} \end{aligned} \tag{2.5}$$

Given the reciprocal lattice parameters, the reciprocal lattice vector is defined as $\mathbf{g} = h\mathbf{a}^* + k\mathbf{b}^* + l\mathbf{c}^*$ with a length $g \equiv \frac{1}{d}$. In reciprocal space, it is useful to define the wave vector of the electron, **k**. The magnitude of the wave vector is the reciprocal of the de-Broglie wavelength of the electron $k = \frac{1}{\lambda}$, and its direction is equal to the velocity of the electron. Diffraction occur if the change in the wave vector of the incoming and scattered electron coincides with the reciprocal lattice.

$$\Delta\mathbf{k} = \mathbf{g} \tag{2.6}$$

This is the Laue condition, which describes Bragg's law in reciprocal space. The Laue condition can be applied to enumerate diffraction spots. However, it gives no information about specific reflections from the basis, in other words individual atoms in the unit cell. Under certain conditions, diffraction from the basis can provide specific extinction rules that cannot be explained by Bragg's law. For example, the presence of screw axes and glide planes will lead to systematic absences in diffraction patterns of certain planes. Hence, a more detailed set of rules must be applied, the so-called structure factor rules. Firstly, consider the diffracted electron wave:

$$\psi_s = \sum_{\mathbf{r}_i}^{\text{lattice}} e^{-i2\pi\mathbf{\Delta k}\cdot\mathbf{r}_i} \sum_{\mathbf{r}_j}^{\text{basis}} f_{\text{at}}\left(\mathbf{r}_j\right) e^{-i2\pi\mathbf{\Delta k}\cdot\mathbf{r}_j} = \mathcal{S}\left(\mathbf{\Delta k}\right)\mathcal{F}\left(\mathbf{\Delta k}\right) \tag{2.7}$$

In equation 2.7, $\mathbf{r}_j = x_j\mathbf{a} + y_j\mathbf{b} + z_j\mathbf{c}$ is the position vector of the jth atom in the basis, $\mathbf{r}_i = x_i\mathbf{a} + y_i\mathbf{b} + z_i\mathbf{c}$ is the position vector of the ith lattice point in the crystal, f_{at} is the atomic form factor of the crystal, $\mathcal{F}$ is the structure factor, and $\mathcal{S}$ the shape factor. The atomic form factor is a function that describes the decrease of the scattered wave amplitude at angles away from the forward, non-diffracted direction. This factor depends on the mass of the atom, the Coulomb potential of the atom, and the change in the wave vector of the incoming and scattered electron.

$$f_{\text{el}}(\mathbf{\Delta k}) \equiv -\frac{m}{2\pi\hbar^2}\int V_{\text{at}}(\mathbf{r})e^{-i\mathbf{\Delta k}\cdot\mathbf{r}}\mathrm{d}^3\mathbf{r} \tag{2.8}$$

Further, the structure factor $\mathcal{F}$ describes the intensity contributions from the atoms in the basis, and the shape factor $\mathcal{S}$ describes the sum of the contributions from the crystal lattice.

$$\mathcal{S} \equiv \sum_{\mathbf{r}_i}^{\text{lattice}} e^{-i2\pi\mathbf{\Delta k}\cdot\mathbf{r}_i} \tag{2.9}$$

$$\mathcal{F} \equiv \sum_{\mathbf{r}_j}^{\text{basis}} f_{\text{at}}\left(\mathbf{r}_j\right) e^{-i2\pi\mathbf{\Delta k}\cdot\mathbf{r}_j} \tag{2.10}$$

From this, the structure factor rules can be derived by applying the Laue conditions.

$$\mathbf{\Delta k} \cdot \mathbf{r}_j = \mathbf{g} \cdot \mathbf{r}_j = hx_j + ky_j + lz_j \tag{2.11}$$

This results in a structure factor that depend on the $(h\,k\,l)$ planes from which the electrons scatter, the elements in the basis, and the position of the elements in the basis.

$$\mathcal{F} \equiv \sum_{\mathbf{r}_j}^{\text{basis}} f_{\text{at}} e^{-i2\pi(hx_j + ky_j + lz_j)} \tag{2.12}$$

By substituting the positions of the atoms in the basis of a crystal in equation 2.12, it is possible to derive the extinction rules for a given crystal. The structure factor rules can therefore be used to index diffraction patterns, as only the allowed reflections are present.[3] For crystals with few atoms in the basis, one may calculate the extinction rules and index the diffraction patterns by hand. However, when the basis consists of many atoms, the interference between different scattered waves is more complicated. In such cases, it is more common to simulate the diffraction pattern by providing the atomic positions of the crystal to a software, and use the simulations to index the diffraction pattern. KNBO, with 24 atoms in its basis, is one such crystal where it is useful to give a crystallographic information file (CIF) with the atomic positions to a software, simulating the diffraction pattern. Nevertheless, these softwares are based on the structure factor as described here, and the intensity of the coherently scattered wave function.

$$I \propto |\mathcal{F}|^2 \tag{2.13}$$

Hence, the intensity of a given reflection is proportional to the absolute square of the structure factor. From equation 2.13, one of the characteristics of kinematical diffraction can be derived; Friedel's law. Friedel's law states that the intensity of reflection $(h\,k\,l)$ is equal to the intensity of reflection $(\overline{h}\,\overline{k}\,\overline{l})$ [29]. Thus, kinematic diffraction patterns will always appear centrosymmetric, even when the crystal is non-centrosymmetric.

2.4.2 The Ewald sphere

The Ewald sphere is a visual representation of the Laue conditions given in equation 2.6. Consider the wave vector of the incident wave of an electron $\mathbf{k_i}$, and the wave vector of all scattered waves $\mathbf{k}$ in reciprocal space. These form a sphere of radius $\mathbf{k}$. This is the Ewald sphere. Since diffraction only occurs if the Laue condition is satisfied, all points in the reciprocal lattice which intersects the circumference of this sphere will satisfy the Laue condition and appear as bright diffraction spots in reciprocal space. This is illustrated in figure 2.12a.

---

[3] For coherent scattering, the intensity in reciprocal space is $I(\Delta\mathbf{k}) = \mathcal{F}\mathcal{F}^*$. For the description given in this thesis, it is sufficient to analyse $\mathcal{F}$

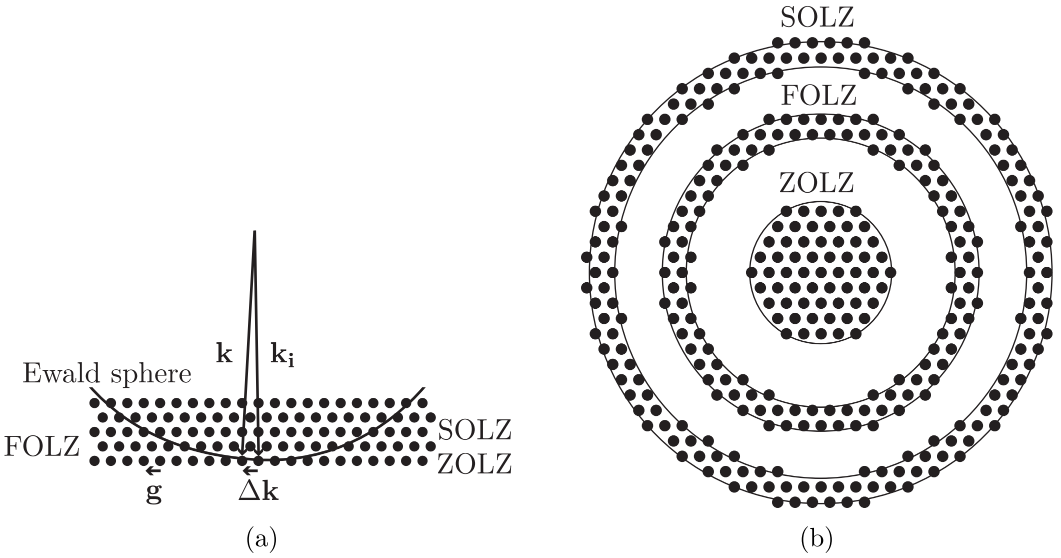

Figure 2.12: Illustrations of the Ewald sphere and HOLZ. (a) The Ewald sphere has a radius **k**, where only points in reciprocal space with $\mathbf{\Delta k} = \mathbf{g}$ will appear as bright diffraction spots. Because of the curvature of the Ewald sphere, points further out in reciprocal space will also satisfy the Laue conditions. These are the HOLZ. The ZOLZ, FOLZ, and the SOLZ are illustrated. (b) An illustration of the diffraction pattern that is generated.

For high energy electrons, the wavelength will be short. The Ewald sphere will therefore have a large radius and appear flat on the reciprocal lattice. If the specimen is sufficiently thin, as is the case for TEM specimens, the reciprocal lattice will be confined to a finite volume. This will result in shape effects modulated by the shape factor, which broaden the reciprocal lattice points into rel-rods along the direction where the specimen is thin. Hence, the shape effect loosens the Laue conditions, allowing for several points near the Ewald sphere to be visible in the diffraction pattern. This allows for the presence of diffraction spots even when the Laue conditions are not exactly met. The diffracted wave can then be modulated by the excitation error, $\mathbf{s_g}$, which descibes a small deviation from the Laue conditon[4].

$$\mathbf{\Delta k} = \mathbf{g} - \mathbf{s} \tag{2.14}$$

The curvature of the Ewald sphere over the reciprocal lattice results in diffraction from higher-order Laue zones (HOLZ). This is illustrated in figure 2.12b. When the incoming wave is perpendicular to a crystallographic plane, the crystal is said to be on-zone. The zero-order Laue zone (ZOLZ) is the origin of the diffraction pattern in reciprocal space. Around the ZOLZ, there is a dark area where no diffraction conditions are met, before a bright ring of diffraction spots appears again in the first-order Laue zone (FOLZ). Further out in reciprocal space, several such rings of HOLZ are visible, such as the second-order Laue zone (SOLZ). The symmetry in the HOLZ give detailed information about small features and symmetry in the unit cell of the crystal. These symmetries are important for crystal structure analysis, as will be explained in Section 2.5.8.

---

[4] The excitation error is sometimes referred to as the deviation paramter.

2.4.3 Dynamic diffraction theory

The kinematical diffraction theory assumes single-scattering of electrons. However, as the electron-matter interaction is strong, kinematical diffraction theory is not sufficient for explaining diffraction phenomena exceeding conventional electron diffraction with a parallel beam, such as different convergent beam electron diffraction techniques and contrast mechanisms in bright-field and dark-field imaging.[5] Dynamical theory distinguishes itself from kinematic diffraction theory by including the crystal's periodic potential energy and how it affects the wave function of the forward-scattered and diffracted electrons. Conceptually, the periodic potential causes the amplitude of the electrons to be transferred back and forth between the forward-scattered and diffracted electrons. This leads to a redistribution of the intensity over the non-diffracted and diffracted beam which depends on for instance the specimen thickness. Quantitatively, dynamical theory can be explained both in terms of the beam and a Bloch wave representation.

Dynamical diffraction theory is important for explaining diffraction phenomena which are utilised for crystal structure determination of non-centrosymmetric, polar materials, and hence also for dynamical diffraction simulations. This section is based on Marc de Graef [59] and Kirkland [60]. Only the most important equations describing dynamical diffraction theory will be presented. Extensive derivation of these equations can be found in the abovementioned books.[6] Following, the most important equations for describing multislice and Bloch wave electron diffraction simulations will be introduced.[7]

2.4.3.1 Basics of dynamical diffraction

Dynamical diffraction theory aims to describe the electron wavefunction at the exit surface of a crystalline specimen. The crystalline specimen can be described by a complex crystal potential V given in equation 2.15.

$$V = V_0 + \frac{h^2}{2me}\left(U(\mathbf{r}) + iU'(\mathbf{r})\right) \tag{2.15}$$

---

[5] These techniques and phenomena will be presented in Sections 2.5.

[6] There are several conventions for describing dynamical electron diffraction theory. The book by Fultz and Howe [28] also considered dynamical diffraction theory. However, they derive dynamical diffraction theory under the assumption of centrosymmetric crystals, which is an invalid assumption for KNBO. Please note that Fultz and Howe uses another definition of the Fourier transform where the exponential does not include the term 2π, while Marc de Graef and Kirkland use the definition where this term is included in the exponential. Hence, some expressions given in this section will differ slightly from its kinematic equivalent.

[7] Please note that the theory outlined in this section does not include the appearance of kinematically forbidden reflections, although they are important for determining some space groups and crystal systems. However, it was considered to be out of the scope of this thesis.

$U(\mathbf{r})$ and $U'(\mathbf{r})$ describe the real and imaginary part of the electrostatic lattice potential and can be expanded as,

$$U + iU' = \sum_{\mathbf{q}} \left(U_{\mathbf{q}} + iU_{\mathbf{q}}\right) e^{2\pi i \mathbf{q}\cdot\mathbf{r}} \tag{2.16}$$

where $\mathbf{q}$ is a reciprocal lattice vector.

The electron wave function at the exit surface will be on the form,

$$\Phi(\mathbf{r}) = \phi_{\mathbf{g}} \sum_{\mathbf{g}} e^{2\pi i (\mathbf{k_0}+\mathbf{g})\cdot\mathbf{r}} \tag{2.17}$$

where ϕ can be found by solving the Schrödinger equation for dynamic electron scattering. It can be shown that the solution is

$$\frac{\mathrm{d}\phi_{\mathbf{g}}}{\mathrm{d}z} = 2\pi i s_{\mathbf{g}} \phi_{\mathbf{g}} + i\pi \sum_{g'} \frac{U_{\mathbf{g}-\mathbf{g}'} + iU'_{\mathbf{g}-\mathbf{g}'}}{|\mathbf{k_0} + \mathbf{g}'| \cos\alpha} \phi_{\mathbf{g}'} \tag{2.18}$$

where $s_{\mathbf{g}}$ is the excitation error as defined in equation 2.14 for a 2-beam approximation where the direct beam is denoted $\mathbf{0}$, and the diffracted beam is denoted $\mathbf{g}$.

$$s_{\mathbf{g}} = \frac{k_0^2 - (\mathbf{k_0} + \mathbf{g})^2}{2|\mathbf{k_0} + \mathbf{g}| \cos\alpha} \tag{2.19}$$

Equation 2.18 is known as the Howie-Whelan-Darwin equation (HWD) and is the backbone of dynamical electron diffraction theory. Two important parameters in electron diffraction can be derived from the HWD equation; the extinction length ξ and absorption distance ξ'.

$$\frac{1}{\xi_{\mathbf{g}}} = \frac{|U_{\mathbf{g}}|}{|\mathbf{k_0} + \mathbf{g}| \cos\alpha} \tag{2.20}$$

$$\frac{1}{\xi'_{\mathbf{g}}} = \frac{|U'_{\mathbf{g}}|}{|\mathbf{k_0} + \mathbf{g}| \cos\alpha} \tag{2.21}$$

In equations 2.20 and 2.21, α is the angle between the unit vector in the z-direction[8], $\mathbf{e}_z$, and $\mathbf{k_0} + \mathbf{g}$, and the crystal potential has been expanded to a Fourier series with Fourier components $|U_{\mathbf{g}}|$ and $|U'_{\mathbf{g}}|$, and phase factors $\theta_{\mathbf{g}}$ and $\theta'_{\mathbf{g}}$.

$$U_{\mathbf{g}} = |U_{\mathbf{g}}| e^{i\theta_{\mathbf{g}}} \tag{2.22}$$

$$U'_{\mathbf{g}} = |U'_{\mathbf{g}}| e^{i\theta'_{\mathbf{g}}} \tag{2.23}$$

---

[8] The z-direction is the direction along the thickness of the specimen.

These parameters can be used to simplify the HWD equation,

$$\frac{\mathrm{d}\phi_{\mathbf{g}}}{\mathrm{d}z} = i\pi \sum_{g'} \left[2s_{\mathbf{g}}\delta_{\mathbf{g}-\mathbf{g}'} + \frac{e^{i\theta_{\mathbf{g}-\mathbf{g}'}}}{q_{\mathbf{g}-\mathbf{g}'}} \right] \phi_{\mathbf{g}'} \tag{2.24}$$

where δ is the Dirac delta-function, and

$$\frac{1}{q_{\mathbf{g}-\mathbf{g}'}} = \frac{1}{\xi_{\mathbf{g}-\mathbf{g}'}} + i\frac{e^{i(\theta'_{\mathbf{g}-\mathbf{g}'} - \theta_{\mathbf{g}-\mathbf{g}'})}}{\xi'_{\mathbf{g}-\mathbf{g}'}}. \tag{2.25}$$

In order to solve the HWD equations, it can be useful to further simplify them. By introducing the substitution,

$$\phi_n = S_n e^{i\theta_n} e^{\frac{-\pi z}{\xi'_{\mathbf{0}}}} \tag{2.26}$$

the HWD equation can be simplified to,

$$\frac{\mathrm{d}\mathbf{S}}{\mathrm{d}z} = i\mathcal{A}\mathbf{S} \tag{2.27}$$

where S_n is the scattering amplitudes constituting the vector $\mathbf{S}$, and $\mathcal{A}$ is the crystal transfer matrix.

$$\begin{aligned} \mathcal{A}_{nn} &= 2\pi s_n \\ \mathcal{A}_{nn'} &= \frac{\pi}{q_{n-n'}}, \; n \neq n' \end{aligned} \tag{2.28}$$

The solution to the HWD equation can then be written on the form,

$$\mathbf{S}(z_0) = e^{i\mathcal{A}z_0}\mathbf{S}(0) = \mathcal{S}\mathbf{S}(0) \tag{2.29}$$

where z_0 is the crystal thickness and $\mathcal{S}$ is the scattering matrix. [9] From this, the intensity of the nth scattered beam is given by,

$$I_n = |\phi_n|^2 = e^{\frac{-2\pi z}{\xi'_{\mathbf{0}}}} |S_n|^2. \tag{2.30}$$

---

[9] Please note that the scattering matrix is not the same as the shape factor in kinematical theory, although the same notation is used.

The crystal potential, extinction length, crystal thickness and especially the Bragg angle are important parameters determining the intensity of a diffracted beam. The intensity variations with the thickness and reflections **g** are important for polarity determinations using convergent-beam electron diffraction. Combining experimental data with simulations is therefore an important tool to aid in polarity characterisation, considering that dynamic diffraction is likely to affect the intensity distributions at reflections that fulfill Bragg's law. There are essentially two methods for solving the electron wavefunction at the exit surface. One is to solve for the scattering amplitude, S_n, using the multislice method, while the other is to solve for the electron wave function using the Bloch wave method. Both of these methodologies include solving the scattering matrix. This scattering matrix contains the extinction length and absorption distance, which again are dependent on the complex crystal potential. There are several ways to model U and U', as will be further discussed in Section 2.4.3.4.

2.4.3.2 Multislice

Multislice simulations are performed by solving the HWD equation on thin slices of the specimen. This is illustrated in figure 2.13.

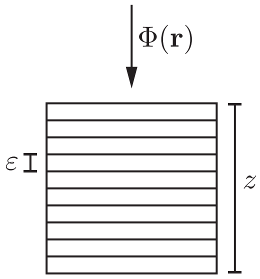

Figure 2.13: Multislice simulations. ε is the slice thickness, z is the specimen thickness, and $\Phi(\mathbf{r})$ is the electron wave function.

The scattering amplitude can be expressed by the scattering matrix of n slices of thickness ε and the scatting amplitude of the incident electron beam, $\mathbf{S}(0)$:

$$\mathbf{S}(z_0) = [\mathcal{S}(\varepsilon)]^n \mathbf{S}(0) \tag{2.31}$$

The solution can be found by convoluting the projected crystal potential with the diffracted beam. Performing this convolution at consecutive slices is the essence of multislice simulations. There exist several versions of the multislice algorithm, and specifics of the recursive steps can be found in [28, 29, 60]. The common denominator is that there are three important functions that must be calculated; the projected potential at a slice, the transmission function, and the propagator. From this, the diffracted wave at the exit plane will be in the form,

$$\phi(x, y, z_0) = e^{\bar{\Delta}\varepsilon} e^{i\sigma V_p^n} \cdots e^{\bar{\Delta}\varepsilon} e^{i\sigma V_p^2} e^{\bar{\Delta}\varepsilon} e^{i\sigma V_p^1} \tag{2.32}$$

where the projected potential V_p, the transmission function t_n and the propagator p are given by,

$$V_p = \int_0^{z_0} V(x, y, z)\mathrm{d}z \tag{2.33}$$

$$t_n = e^{i\sigma V_p^n} \tag{2.34}$$

$$p = e^{\bar{\Delta}\varepsilon} \tag{2.35}$$

and $\bar{\Delta} = \frac{i\lambda}{4\pi}\Delta_{xy}$ is a complex differential operator described by the Laplacian operator, Δ_{xy}. After this, the electron wave function must be modulated by the characteristics of the microscope. In other words, the wavefunction must be calculated at the back focal plane and at the image plane of the simulated microscope by including interactions with the objective lens and characteristic abberations. Hence, the multislice algorithm can simulate diffraction patterns with intensity distributions as a function of specimen thickness for a given crystallographic plane.

2.4.3.3 Bloch wave formulism

Instead of suggesting a solution of the electron wave function at the exit surface as a set of differential equations, as was done for the multislice algroritm, the final intensity distribution can be described by a set of Bloch waves,

$$\Psi(\mathbf{r}) = \sum_{\mathbf{g}} \psi_{\mathbf{g}}(z) e^{2\pi i(\mathbf{k_0}+\mathbf{g})\cdot\mathbf{r}} \tag{2.36}$$

where $\psi_{\mathbf{g}}$ is described by the Fourier coefficients $C_{\mathbf{g}}^{(j)}$ and Bloch wave excitation coefficients $\alpha^{(j)}$.

$$\psi_{\mathbf{g}}(z) = \sum_{j} \alpha^{(j)} C_{\mathbf{g}}^{(j)} e^{2\pi i\Gamma^{(j)} z} \tag{2.37}$$

Here, $\Gamma^{(j)}$ are eigenvalues for the wavefunction inside the crystal, and can be directly related to the wave vector of the diffracted beam,

$$\mathbf{k}^{(j)} = \mathbf{k_0} = \mathbf{k_0} + \Gamma^{(j)}\mathbf{n} \tag{2.38}$$

where $\mathbf{n}$ is the unit vector normal to the specimen surface.

For an N-beam problem, ψ can be rewritten on matrix form such that,

$$\begin{pmatrix} \psi_{\mathbf{0}}(z) \\ \psi_{\mathbf{g}}(z) \\ \vdots \\ \psi_{\mathbf{h}}(z) \end{pmatrix} = \mathcal{C} \times \begin{pmatrix} e^{2\pi i \Gamma^{(1)} z} & 0 & \dots & 0 \\ 0 & e^{2\pi i \Gamma^{(2)} z} & \dots & 0 \\ \vdots & \vdots & \ddots & \\ 0 & 0 & \dots & e^{2\pi i \Gamma^{(N)} z} \end{pmatrix} \begin{pmatrix} \alpha^1 \\ \alpha^2 \\ \vdots \\ \alpha^n \end{pmatrix} \tag{2.39}$$

where $\mathbf{h}$ is a reciprocal lattice vector and $\mathcal{C}$ is a matrix of Fourier coefficients,

$$\mathcal{C} = \begin{pmatrix} C_{\mathbf{0}}^{(1)} & C_{\mathbf{0}}^{(2)} & \dots & C_{\mathbf{0}}^{(N)} \\ C_{\mathbf{g}}^{(1)} & C_{\mathbf{g}}^{(2)} & \dots & C_{\mathbf{g}}^{(N)} \\ \vdots & \vdots & \ddots & \\ C_{\mathbf{h}}^{(1)} & C_{\mathbf{h}}^{(2)} & \dots & C_{\mathbf{h}}^{(N)} \end{pmatrix}. \tag{2.40}$$

Bloch wave simulations are based on solving for the eigenvalues Γ and excitation coefficients, α. α can be found by solving the eigenvalue problem at the entrance plane of the crystal,

$$\begin{pmatrix} \psi_{\mathbf{0}}(0) \\ \psi_{\mathbf{g}}(0) \\ \vdots \\ \psi_{\mathbf{h}}(0) \end{pmatrix} = \begin{pmatrix} C_{\mathbf{0}}^{(1)} & C_{\mathbf{0}}^{(2)} & \dots & C_{\mathbf{0}}^{(N)} \\ C_{\mathbf{g}}^{(1)} & C_{\mathbf{g}}^{(2)} & \dots & C_{\mathbf{g}}^{(N)} \\ \vdots & \vdots & \ddots & \\ C_{\mathbf{h}}^{(1)} & C_{\mathbf{h}}^{(2)} & \dots & C_{\mathbf{h}}^{(N)} \end{pmatrix} \begin{pmatrix} \alpha^1 \\ \alpha^2 \\ \vdots \\ \alpha^n \end{pmatrix} = \begin{pmatrix} 1 \\ 0 \\ \vdots \\ 0 \end{pmatrix}. \tag{2.41}$$

The eigenvalues can be found by solving the eigenvalue problem at the exit plane,

$$\begin{pmatrix} iU'_{\mathbf{0}} & U_{-\mathbf{g}} + iU'_{-\mathbf{g}} & \dots & U_{-\mathbf{h}} + iU'_{-\mathbf{h}} \\ U_{\mathbf{g}} + iU'_{\mathbf{g}} & 2k_0 s_{\mathbf{g}} + iU'_{\mathbf{0}} & \dots & U_{\mathbf{g}-\mathbf{h}} + iU'_{\mathbf{g}-\mathbf{h}} \\ \vdots & \vdots & \ddots & \\ U_{\mathbf{h}} + iU'_{\mathbf{h}} & U_{\mathbf{h}-\mathbf{g}} + iU'_{\mathbf{h}-\mathbf{g}} & \dots & 2k_0 s_{\mathbf{h}} + iU'_{\mathbf{0}} \end{pmatrix} \begin{pmatrix} C_{\mathbf{0}}^{j} \\ C_{\mathbf{g}}^{j} \\ \vdots \\ C_{\mathbf{h}}^{j} \end{pmatrix} = 2k_n \Gamma^j \begin{pmatrix} C_{\mathbf{0}}^{j} \\ C_{\mathbf{g}}^{j} \\ \vdots \\ C_{\mathbf{h}}^{j} \end{pmatrix}. \tag{2.42}$$

Hence, Bloch wave simulations essentially involve four important steps: 1) Determining the Fourier components of the crystal potential, 2) finding the excitation coefficients, 3) solving for the eigenvalues, and 4) calculating the wavefunction at the exit surface. The most important drawback of the Bloch wave formulism for diffraction simulations is that the memory storage requirements scale with N^2. Hence, the simulations quickly become computationally heavy as the number of beams are increased, for example when simulating large crystals.

2.4.3.4 Models for crystal potentials and scattering factors

The complex crystal potential U and U' can be calculated from the atomic scattering factors f_l and absorbtive scattering factor f_l',

$$\begin{aligned} U_g &= \frac{\gamma}{V_c} \sum_l f_l(g) e^{-2\pi i \mathbf{g}\cdot\mathbf{r_l}} e^{-\frac{1}{4}B_l g^2} \\ U_g' &= \frac{\gamma}{V_c} \sum_l f_l'(\mathbf{g}) e^{-2\pi i \mathbf{g}\cdot\mathbf{r_l}} e^{-\frac{1}{4}B_l g^2} \end{aligned} \tag{2.43}$$

where r_l is the atomic position of atom l, $\gamma = \frac{1}{(1-(v/c)^2)^{1/2}}$ is the relativistic correction factor, and $B_l = 8\pi^2 \langle u_l^2 \rangle$, where $\langle u_l^2 \rangle$ is the mean square atomic displacement of the lth atom as a result from thermal vibrations.

There are several models which estimate the atomic scattering factors and absorptive form factors. The specifics of these models will not be outlined in this thesis, but it is important to note that various simulation softwares provide these values based on different models, and that the choice of model may severely affect the geometry of the simulated diffraction pattern.

The models that are most commonly used are the Doyle-Turner (DT) model [61], Earl J. Kirkland (EJK) model [62], Bird and King (BK) model [63], Peng-Ren-Dudarev-Whelan (PRDW) model [64, 65], the Weickenmeier-Kohl (WK and WKc) models [66]. The main differences between these models are the descriptions of diffuse and inelastic scattering processes, and the curve-fitting algorithms used. Generally, it has been shown that the DT, WK, and WKc models result in relatively large errors at high scattering angles because they calculate the electron scattering factors based on the X-ray scattering factors through the Mott-Bethe formula. The most accurate models so far are the BK, EJK and PRDW models, including a newly developed model by Lobato and van Dyck [67].

To summarise, this section has introduced the electron diffraction as phenomena as well as the very basics of dynamic electron diffraction simulations relevant for the present work.

2.5 TEM

Transmission electron microscopy is used for characterizing materials at the micro-, nano- and atomic scale. A TEM can be used in several modes to perform numerous techniques, such as bright-field (BF) TEM, dark-field (DF) TEM, high-resolution TEM (HRTEM), scanning TEM (STEM), selected-area electron diffraction (SAED), convergent-beam electron diffraction (CBED), and large-angle CBED (LACBED). The theory presented in this section is based on Fultz and Howe [28], unless otherwise is stated.

2.5.1 Microscope setup

A TEM consists of an electron gun, accelerators, pumps, a set of magnetic lenses, stigmators, deflectors and apertures. A schematic of a typical TEM column is illustrated in figure 2.14a, and the optics of the objective lens and intermediate lens columns during apertureless imaging of the specimen are illustrated in figure 2.14b. Only the magnetic lenses and apertures are included for simplicity.

The electron gun is at the top of the column. Typical electron sources are thermionic emitters, field emitters and Schottky emitters. Thermionic emitters are electron guns that emit electrons when thermally heated, while field emitters are electron guns that emit electrons when a strong electric field is applied to the electron source. An intermediate of these two are Schottky emitters, where the electron source is heated whilst applying a strong electric field. Schottky emitters are so-called thermal field emitters. The electric field required for electrons to overcome the work function is lowered due to the thermal heating. Note that the electron source in Schottky emitters is not heated as severely as for thermionic emitters. For most TEM experiments, the electrons are accelerated with an acceleration voltage of 200 keV.

Following the electron gun, there are a set of condenser lenses and a condenser lens aperture that are used to change the convergence angle of the electron beam. The condenser lenses, aperture and gun makes up the illumination system. The specimen is inserted below the condenser column in a vacuum chamber with a pressure in the order of 10^{-5} Pa. Below and above the specimen chamber, there are a set of objective lenses and an objective aperture, making up the objective system. In the back focal plane of the objective lens, a diffraction pattern will be formed, and an image of the specimen is formed in the image plane of the objective lens. An objective aperture can be inserted in the back focal plane of the objective lens to create diffraction contrast. It is also possible to limit the electron signal to a selected area of the specimen by inserting a field-limiting aperture in the image plane of the objective lens. Lastly, a set of intermediate lenses and a projector lens is used to focus either the image plane or the back focal plane onto the viewing screen, hence magnifying the image or diffraction pattern. In diffraction mode, the camera length is used as a measure for the indicated magnification of the diffraction pattern. It is defined as the length between the specimen and the viewing screen if the intermediate lens was omitted. The projector lens, intermediate lenses and the field limiting aperture makes up the imaging system.

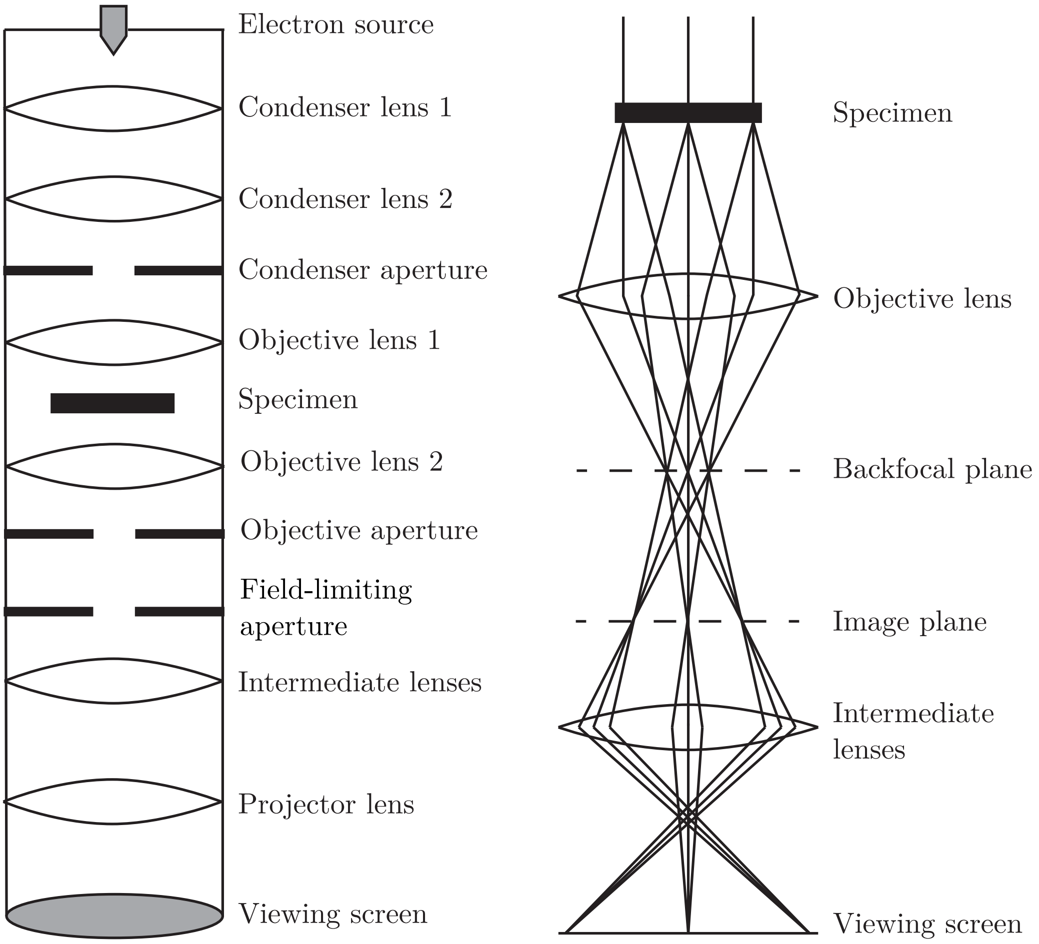

(a) (b)

Figure 2.14: Schematics of the transmission electron microscope. (a) Simplified TEM set-up showing the electron source, magnetic lenses, and apertures. (b) Schematic illustrating the image formation in a TEM. Note that the electron path is only included from the specimen, through the objective and intermediate lens columns. Notice also that the projector lens is omitted for simplicity.

2.5.2 TEM modes

There are several imaging modes in the TEM. The most common ones are the standard imaging and diffraction modes with a broad illumination, where the imaging plane and back focal plane are focused on the viewing screen respectively. However, because of the Lorentz force on the electrons in the magnetic lenses, the image may rotate when the strength of the magnetic lens changes, such as when the magnification is changed. Fortunately, it is possible to correct for this rotation such that the TEM image is directly related to the SAED patterns, although this correction may not allways be set up for all imaging modes in the TEM. Most TEMs can also be operated in STEM mode, where the electron beam is focused to a probe onto the specimen and scanned across it. STEM images can usully not be directly related to the SAED patterns, because the orientation of the specimen in the image is dependent on the scanning direction.

2.5.2.1 STEM setup

The STEM set-up consists of a convergent probe of size $\sim$ 0.1 nm – 1 nm focused onto the specimen, and a STEM detector below the specimen. When the probe is scanned across the specimen, its position is written to a pixelated grid, and the intensity of the electrons are detected by a bright-field (BF) or high-angle annular dark-field (HAADF) detector. The detected intensity is related to the given pixels associated with the probe position. By scanning the probe across the specimen, the intensity variations at each probe position is used to form an image. As the name suggests, the BF STEM detector only detects the forward-scattered electrons, in other words the direct beam. Conversely, only electrons that have scattered to high angles, typically 50 mrad – 150 mrad, are detected by the HAADF detector. The STEM set-up is illustrated in figure 2.15.

HAADF STEM detects incoherent elastcially-scattered electrons, forming mass-contrast images because each atom will behave as individual scatterers. The camera length of the detector can be adjusted to tailor the contrast. A detector at a lower camera length will detect electrons that are scattered at larger angles, thus enhancing the mass-contrast. HAADF STEM is important for directly imaging the crystal lattice, as will be further explained in Section 2.5.7.

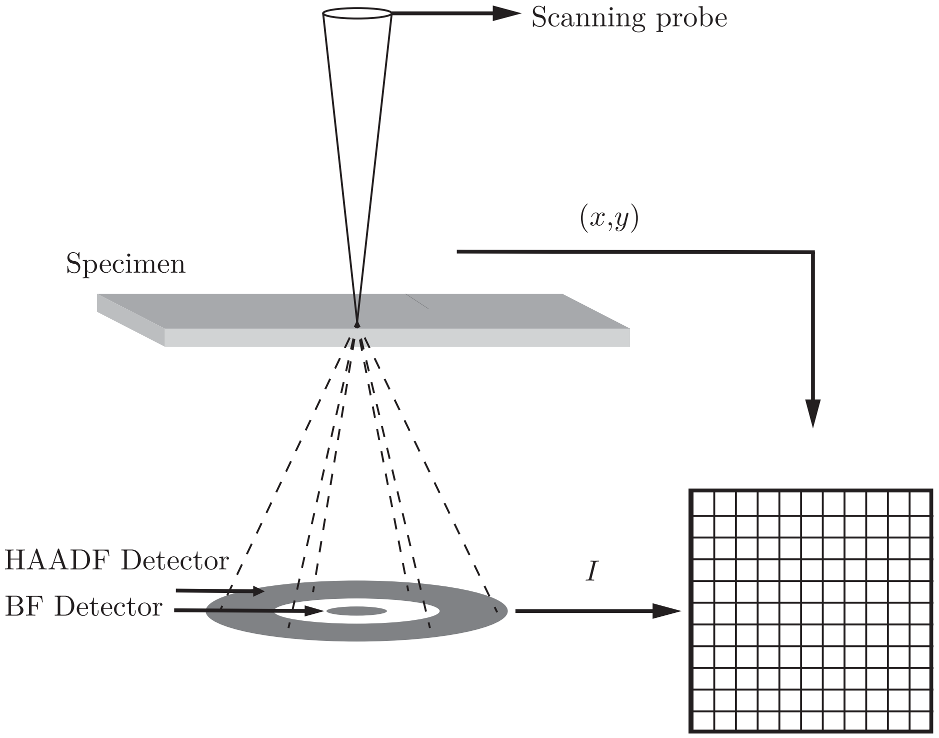

Figure 2.15: BF and HAADF STEM set-up. A focused beam is scanned across the specimen, and a raster image is formed by the intensity I of the electrons detected by the BF or HAADF detector at probe positions (x, y).

2.5.3 Aberrations, astigmatism, and alignment in TEM

The TEM column is typically 1 – 2 m long, and the features that are imaged by the TEM may be sub-nanometers small. Small distortions of the electromagnetic lenses, the electron gun, specimen height in the column and the apertures may therefore significantly affect the quality of the images or diffraction patterns acquired. It is therefore important to align the beam properly. If the beam or column is not properly aligned, it may contain aberrations including astigmatism, that may affect the image which is formed. These will be explained in more detail in this section.

Spherical aberration occur if the electron beam is out of focus, such that the image formed in the image plane appears larger and more blurry. The electron beam may also suffer from chromatic aberration, where electrons of different energies are deflected to different focal points. The main source of chromatic aberration, that is easy to improve, is inelastic scattering. Electrons may scatter inelastically from thicker specimen, hence the outgoing electrons may have different energies. To avoid chromatic aberration, it is good practice to prepare thin TEM specimens.

To focus the specimen on the viewing screen, the strength of the objective lens can be altered. However, it is much more common to adjust the specimen height to align the image plane or back focal plane on the viewing-screen, while adjusting the strength of the lenses for fine adjustments of the focus.

Further, if the strength of a lens varies across the lens, the electron beam suffers from astigmatism. This also leads to a blurry image because the electrons do not focus at the same spot. The stigmatism of condenser lens 1 and the objective lens can be corrected by the condenser lens and objective lens stigmators. Correcting stigmatism and spherical aberration are especially important for HRTEM imaging, as will become clear in Section 2.5.7.

Finally, when operating the TEM in STEM mode, the images are not magnified by lenses, and are therefore not susceptible to any aberration in the imaging system. However, the resolution is dependent on the size and shape of the beam. Hence, it is sensitive to any aberration and astigmatism arising from the illumination and objective lens systems. One of the most important aberrations to correct in STEM is spherical aberration, as the resolution of the STEM image is directly dependent on the size and shape of the probe.[29]

To summarise, there are several beam aberrations, astigmatisms and misalignment that may affect the image or diffraction pattern acquired by the TEM. It is therefore important to perform proper alignment of the beam prior to experiments for acquiring high quality (S)TEM data.

2.5.4 Kikuchi lines, Kikuchi maps and the zone axis

Kikuchi lines and Kikuchi maps arise from dynamical diffraction phenomena, and can be used as tools for performing TEM experiments at a single crystallographic plane. Under specific conditions, Kikuchi lines appear in specimens that are electron transparent but thick enough to allow for diffuse scattering. They provide crystallographic information about the specimen and can be used for oriental mapping to find specific zone axes, $[u\,v\,w]$. The zone axis is the crystallographic direction perpendicular to the crystallographic plane from which the diffraction pattern is acquired. The electron beam is said to be on-zone when the direct beam is parallel to the zone axis.

Kikuchi lines appear as a result of two consecutive scattering events − incoherent scattering followed by coherent elastic scattering. This results in a set of bright and dark, nearly parallel, straight lines. These lines correspond to diffuse scattering from certain $(h\,k\,l)$ planes in the specimen. The distance between the bright and dark Kikuchi lines is the same as the distance from the $(0\,0\,0)$ diffraction spot to $(h\,k\,l)$ spot. Further, the Kikuchi lines will be perpendicular to a line drawn from the $(0\,0\,0)$ spot to the corresponding diffraction spot. Hence, the angle between two separate sets of Kikuchi lines will also be the same as the angle between diffraction spots. Figure 2.16 illustrate a set of Kikuchi lines superimposed on a diffraction pattern for a face-centered cubic crystal in the $[1\,0\,0]$ zone axis.

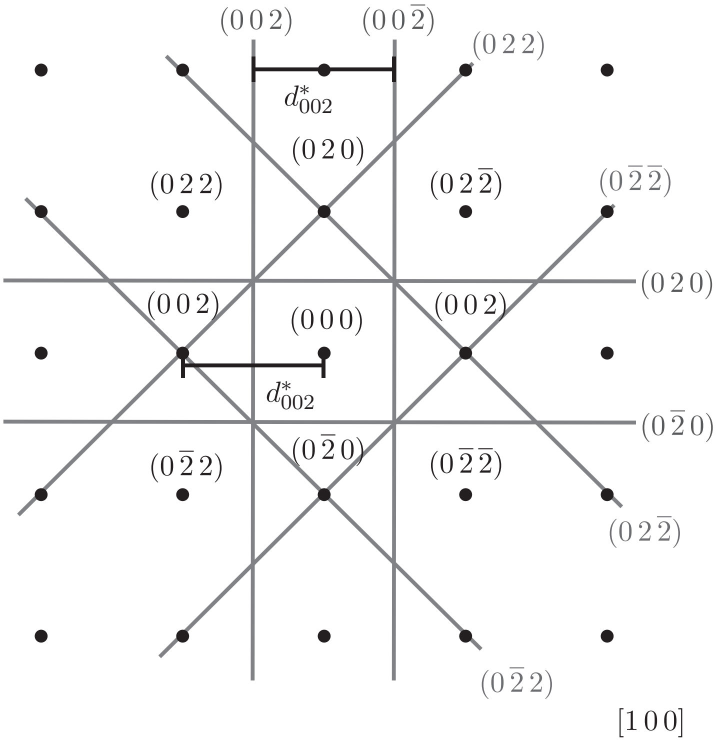

Figure 2.16: Illustration of Kikuchi lines superimposed on a diffraction pattern of a monoatomic face-centered cubic crystal in the $[1\,0\,0]$ zone axis. The Kikuchi lines and indices are shown in grey, while the indices of the diffraction pattern are shown in black. The distance between Kikuchi lines is equal to the distance between the $(0\,0\,0)$ reflection and the corresponding $(h\,k\,l)$ reflection; here d^*_{002}.

If a diffraction spot from a certain $(h\,k\,l)$ plane appears in the diffraction pattern of two separate zones, the Kikuchi lines will extend between these zones. Therefore, the Kikuchi lines form a map that can be used to rotate the specimen to different zone axes. A point where several Kikuchi lines meet correspond to a high symmetry zone axis. This way, the Kikuchi lines can be used to tilt the specimen on-zone, and for oriental mapping. Kikuchi maps are thus a handy tool for TEM experiments.

2.5.5 SAED, CBED and LACBED

Three common techniques used to acquire diffraction patterns are selected-area electron diffraction (SAED), convergent-beam electron diffraction (CBED), and large-angle CBED (LACBED) as presented in figure 2.17a, 2.17b and 2.17c respectively. These diffraction techniques will be explained in this section.

The conventional electron diffraction patterns are acquired by SAED. Figure 2.17a shows the basic principles of how the diffraction pattern is generated in the back focal plane. A parallel beam is focused on the specimen, generating a set of sharp diffraction spots. A field-limiting aperture, also called a selected-area aperture, is inserted in the image plane of the objective lens, such that a diffraction pattern is acquired from this selected area.

CBED is a technique that allows for acquiring nanobeam diffraction from regions that are only a few nanometers in size. A convergent electron beam is focused on a small region of the specimen. The resulting diffraction pattern consists of a set of disks rather than spots as in SAED. A simple procedure for doing CBED is by inserting a small condenser aperture and focusing the electron beam into a small spot. The beam can be focused further by specific settings of the condenser and objective lenses.

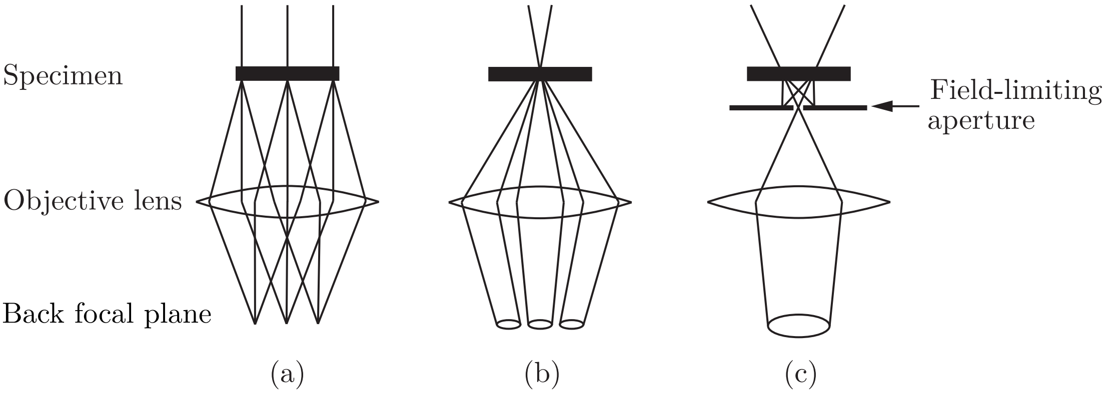

Figure 2.17: Difference between (a) SAED, (b) CBED, and (c) LACBED. (a) A parallel electron beam passes through the specimen, generating a set of diffraction spots in the back focal plane. (b) A convergent electron beam illuminates the specimen, generating a set of diffraction disks in the back focal plane. (c) A convergent beam is underfocused on the specimen, such that a spot pattern is visible in the image plane of the specimen. By inserting a field-limiting aperture around the direct spot, a BF-LACBED pattern will be visible in the back focal plane.

The main difference between SAED and CBED is that one can assume kinematic diffraction during SAED experiments but not during CBED experiments. Hence, Friedel's law applies during SAED experiments, and the diffraction patterns appear centrosymmetric even when the crystal is non-centrosymmetric. Since the electron beam has a convergence angle during CBED, one cannot assume kinematic diffusion. Thus, this technique can reveal the real non-centrosymmetric symmetry of non-centrosymmetric crystals.

The dynamical effects in CBED can be observed as intensity variations inside the diffraction disks, where there may be a presence of deficiency lines from higher-order Laue zones (HOLZ), also known as HOLZ lines. These lines originate from Bragg reflections at HOLZ planes, and will therefore give information about the 3D symmetry of the crystal. Outside the disks, one may also observe HOLZ Kikuchi lines which are line extensions of the HOLZ lines. The main difference between the HOLZ lines and the HOLZ Kikuchi lines, is that the former originate only from the elastic part of the latter. This can give complex and detailed information about the unit cell. CBED is therefore a common technique used for space group determination, as will be discussed further in Section 2.5.8. This is one of the primary advantages of CBED.

LACBED is an alternative to CBED where the diffraction pattern is projected from the image plane rather than the back focal plane, and the diffraction pattern presents HOLZ lines with a very large condenser aperture, or with none inserted at all, resulting in a very large convergence angle. During LACBED, the electron beam is either focused slightly above or below the specimen, such that a diffraction pattern is observed in the image plane. After this, a field-limiting aperture is inserted to enclose either the direct or a diffracted spot. This gives rise to BF- or DF-LACBED. After this, the microscope is set to diffraction mode, and a LACBED pattern is observed. [68]

The LACBED technique may be advantageous over CBED when the unit cell is large, since a small condenser aperture is needed to avoid overlap in normal CBED, and the bright field disk therefore loses information, often appearing too bright. Since only one large CBED disk is visible in LACBED, there are no issues with overlapping disks as may be an issue for CBED. Henceforth, it is possible to image a large angular range with LACBED. Another advantage of LACBED is that the intensity of the electron beam is lower than in CBED, since the beam is defocused. Hence, the intensity of the BF disk is less intense, and it may be easier to observe symmetry lines. A disadvantage of LACBED over CBED is that any symmetry information based on intensity variations inside the CBED disks are lost. [68]

In summary, SAED is a diffraction technique that allows for easy interpretation of diffraction patterns, but may contain symmetry effects that do not display the real symmetry of a crystal. CBED is a diffraction technique that require more detailed analysis but allows for correctly assigning symmetries of the crystal. Lastly, LACBED is advantegeous when the unit cell of the inspected crystal is large, as it allows for inspecting the symmetry in a single, large CBED disk. Hence, all three techniques may be advantageous depending on the crystal structure and the crystallographic plane which is analysed.

2.5.6 BF TEM, DF TEM, and diffraction contrast

Variations in the electron diffraction across a specimen cause diffraction contrast. This can be especially useful for identifying defect structures in materials. By inserting an objective aperture in the back focal plane, one can select certain diffraction conditions to retrieve a BF TEM or DF TEM image. This is illustrated in figure 2.18.

Only areas of the specimen that contribute to a selected diffraction condition will appear bright on the BF or DF image, while areas on the specimen that do not contribute to this specific diffraction condition will appear dark. Since the intensity of the nth scattered wave is dependent on the Bragg angle, the conrast in BF and DF imaging will be a direct result of the scattering angle of the beam. The Bragg angle is affected by point defects, line defects, dislocations, strain fields, crystal grains and boundaries, sudden changes in crystal structure, bending, and changes in the specimen thickness, amongst others. Hence, a variation in any of these parameters will generate contrast in BF and DF imaging. DF TEM is therefore useful for identifying thickness variations, dislocations, line-defects, strain, and crystal interfaces such as antiphase boundaries, twin boundaries and ferroic domain walls.

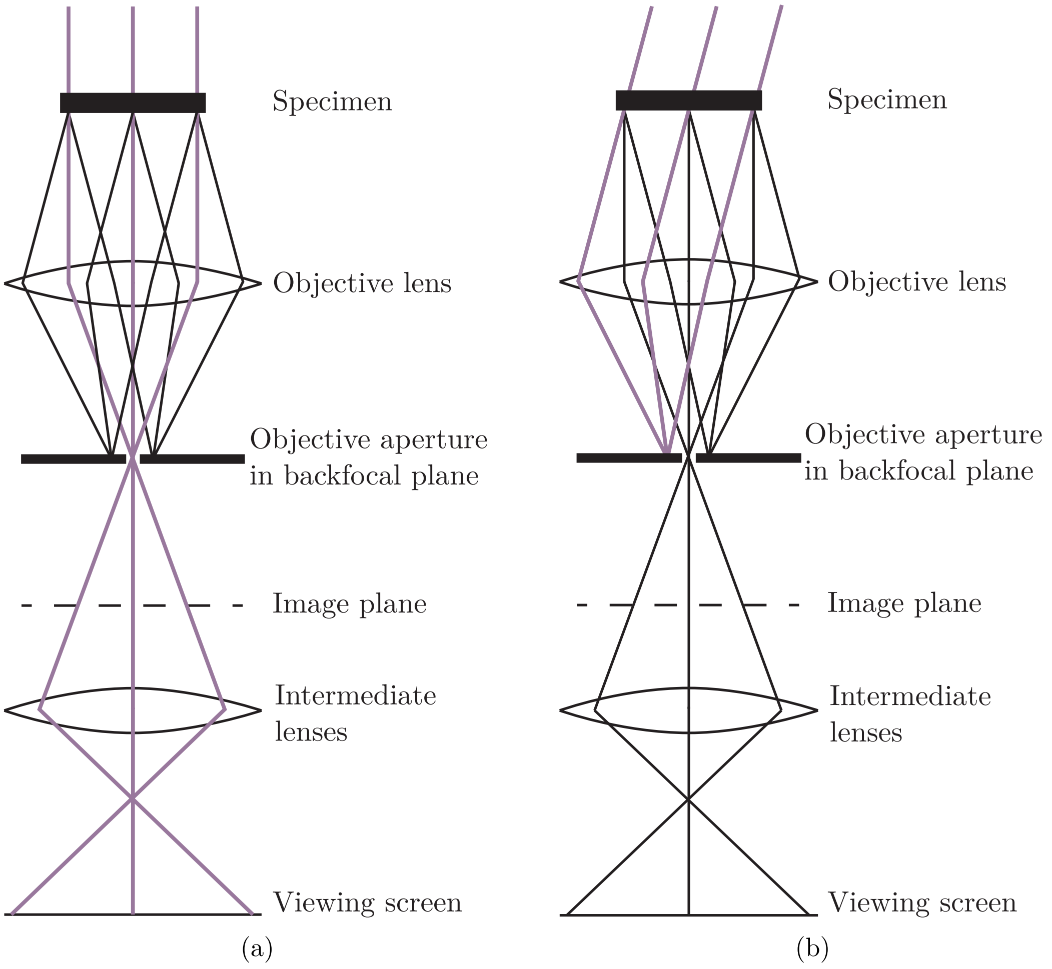

Figure 2.18: Schematic representing (a) BF and (b) DF imaging in TEM. The direct beam is shown in violet.

In BF imaging, the objective aperture is inserted about the central diffraction spot, in other words the direct beam. During DF imaging, the objective aperture is inserted about a diffraction spot. This results in opposing contrast in the BF and DF images, where for example the background appears bright in the BF image, and dark in the DF image. Examples of BF and DF images are shown in figure 2.19 for a KNBO crystal.

Thickness fringes and bend contours are typical contrasts that appear during DF imaging. They occur as a result of interference effects because of thickness gradients or bending of the specimen. Thus, a set of bright and dark fringes are observed. Thickness fringes and bend contours are more visible in thin specimens than in thick specimens. This can be explained by electron absorption when the material is thick. An example of thickness fringes is given in figure 2.19b, where the fringes are observable along the edge of the crystal.

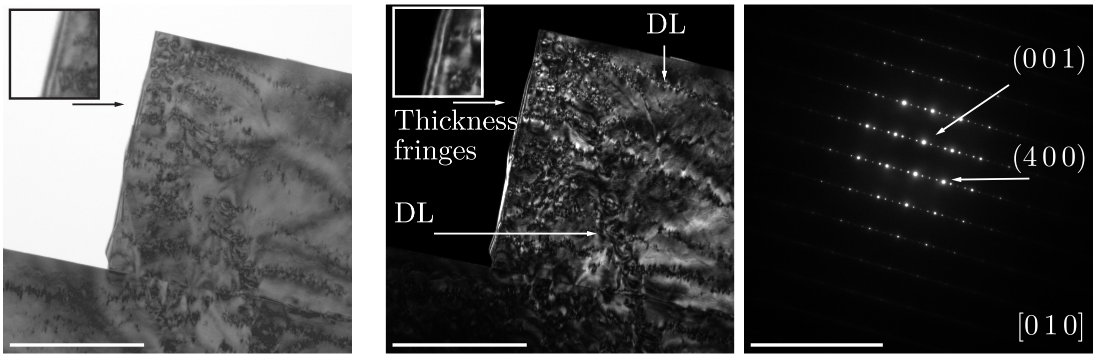

(a) (b) (c)

Figure 2.19: Examples of (a) BF imaging, (b) DF imaging, and (c) the corresponding SAED pattern of a KNBO crystal. The objective aperture is placed about the direct beam for BF imaging, and about a diffracted beam for DF imaging – here, about the (0 0 1) spot. The DF image in (b) show examples of thickness fringes and dislocation loops (DL), but many of the same features are also visible in the BF image. The scale bars are 1 µm in the TEM images, and 10 nm^{-1} in the diffraction pattern.

Strain fields may also generate a specific set of contrasts. For example, strain fields from precipitates and small particles generate a contrast in DF TEM referred to as coffee beans, recognised by their line of no contrast. Further, the coalescence of interstitials or vacancies may appear as dislocation loops, where the coalescence of point defects result in stacking fault contrast inside a well-defined loop [29]. Examples of dislocation loops are indicated in figure 2.19.

Another interference effect that is visible during BF and DF imaging is Moiré fringes. This is a contrast phenomenon that arise when the lattice spacing between two overlapping domains almost coincide. They appear for example when a specimen delaminates, and the two lamella are rotated with respect to one another.

Hence, BF and DF TEM are two techniques that can be used for easy identification of defects, strain fields, thickness variations and bending. It can also be used for identifying changes in the crystal lattice, and can thus also acquire contrast in domains where the crystal structure of the specimen changes.

2.5.7 HRTEM and HRSTEM

High-resolution images can be acquired by TEM and STEM. These two techniques are fundamentally different because the image is formed by different contrast mechanisms. Both techniques and contrast mechanisms will be outlined in this section.

High-resolution TEM is a technique used to investigate the lattice structure of a crystal, and for identifying point defects, line defects, misplacements in atomic stacking and interfaces at the atomic scale. HRTEM images are formed by coherent elastically scattered electrons. The contrast observed in HRTEM is referred to as phase-contrast imaging. A set of interference fringes appear from the phase relationship between a set of diffracted beams. These fringes are referred to as lattice fringes, and reflect the geometry and orientation of the unit cell. HRTEM is typically performed without an objective aperture, because it requires that the image projected includes at least the direct beam and one diffracted beam. Since HRTEM images are interference patterns, they are not directly interpretable. The interference pattern is affected by spherical aberrations, illumination, focus and specimen thickness. Consequently, the atoms may appear as dark spots in some areas of the image, or as bright spots in other areas. Hence, HRTEM images should be analysed with great caution, and interpretations should always be supported by diffraction data. Figure 2.20 shows an example of a HRTEM image of KNBO.

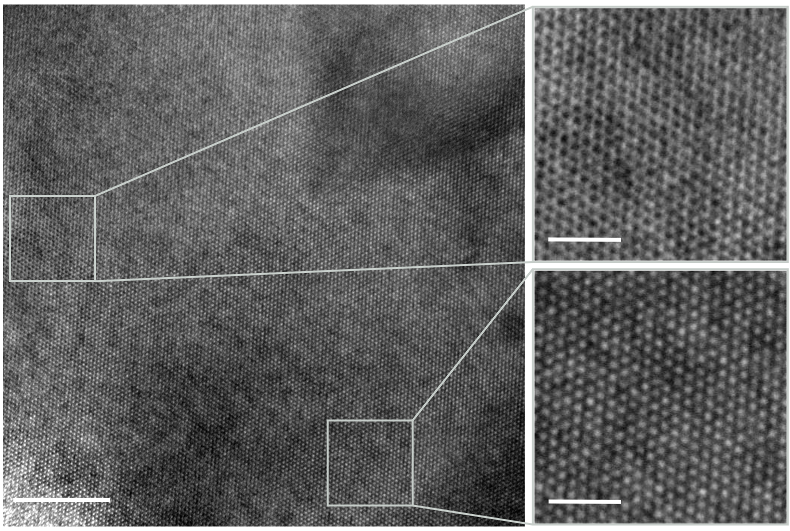

Figure 2.20: High-resolution TEM image of KNBO. The fringes are easily distinguished. Depending on the defocus of the beam, the fringes will appear as bright or dark spots. The scale bar on the left main image is 20 nm, and the scale bar on the right enlarged images are 5 nm.

During HRTEM imaging, it is also important to consider general mass-thickness contrast. The origin of mass contrast is the elastic scattering of single atoms, where electrons scatter more strongly from heavier elements than lighter elements. Thus, regions in the specimen consisting of heavier elements will appear darker on the image. Furthermore, the thickness of the specimen will also create contrast. This is because thicker areas are less electron transparent and can allow for multiple scattering, resulting in a lower electron signal in the image plane. Therefore, thicker regions in the specimen will also appear darker. Mass-thickness contrast is generally present when an objective aperture is not inserted in the back focal plane and is therefore also present during normal TEM imaging when an objective aperture is not inserted.

HAADF STEM can be used to acquire HR-HAADF STEM images. Because the image is formed by coherent elastcially-scattered electrons, every atom can be described as individual scatterers. Thus, the scattered beams from each atom cannot interfere with each other, resulting in an intenisty variation that is not dependent on the relative phases of the scattered electrons. Hence, the contrast mechanism in HR-HAADF STEM originates from mass contrast entirely. Therefore, HR-HAADF STEM images can be more directly interpreted in terms of atomic positions and elemental composition than HRTEM images. A pre-requisite for HRSTEM is that the probe is properly aligned such that the full-width half-maximum of the beam is smaller than the interatomic distance, a prerequisite that is not important for HRTEM. Henceforth, the alignment procedure needed to acquire high-quality HRTEM images is often more straight-forward and less tedeous than the alignment procedures for acquiring high-qualtiy HRSTEM images.

2.5.8 Space group determination by electron diffraction

This subsection will present space group determination by electron diffraction. The basic principles will be explained, but the detailed mathematics will not be presented. For an extensive procedure for determining the space group of any crystal, it is referred to chapter 21 in *Transmission Electron Microscopy* by Williams and Carter from 2009 and 2016 [29, 68].

The space group of a crystal can be experimentally determined by CBED experiments of two to three low-index zone axes. The low-index zones will typically show the highest order of symmetry, which is why these planes are commonly used for space group determination. One the most important steps to determine the space group of a crystal is to identify the diffraction group of the low-index zones.

The diffraction group is a three dimensional pattern symmetry that can be obtained from a CBED pattern. It can be found by inspecting the bright-field symmetry, whole-pattern symmetry and projection-diffraction symmetry of the CBED patterns. The whole-pattern symmetry is acquired by imaging the diffraction pattern at a low camera length to include diffraction effects from HOLZ reflections and Kikuchi lines giving symmetry informations from fine details in the unit cell. The bright-field symmetry is the symmetry of the $(0\,0\,0)$ disk imaged at a large camera length to include detailed HOLZ lines, giving symmetry information from far out in real space. Finally, the projection-diffraction symmetry is the symmetry of the intensity variations in the ZOLZ. This includes only 2D symmetry since the HOLZ lines are not present when examining projection-diffraction symmetry. There exist tables that relate the whole-pattern, bright-field and projection-diffraction symmetries of to the diffraction group of the CBED pattern [69].

In total, there are 31 diffraction groups that are directly related to the 32 point groups. Hence, the point group can be determined by finding the diffraction group of several high-symmetry zone-axes of the crystal, and there exist standard tables that relate the diffraction groups of a crystal to its point group [69]. Hence, by directly evaluating the point symmetries of several diffraction patterns, one can assess the point group symmetry.

An important step for space group determination is to find the lattice centering of the unit cell. One can find the lattice centering by examining the diffraction reflections in the ZOLZ and FOLZ. If the FOLZ can be directly superimposed on the ZOLZ, it is a primitive lattice.

To further assess the correct space group symmetry, one must be able to distinguish rotational symmetry from screw axes, and mirror planes from glide planes. Glide planes, and screw axes can be identified by forbidden reflections in the diffraction pattern and Gjønnes-Moodie (GM) lines in the CBED disks of kinematically forbidden reflections. GM lines appear in the $(0\,0\,0)$ reflection and in the kinematically forbidden CBED disks if the electron beam is either parallel to a glide plane or perpendicular to a 2-fold screw axis. They are a result of double diffraction due to the presence of the screw axes or glide planes. Each double diffraction route has an alternative double diffraction route of the same amplitude but opposite phase. This results in certain extinct lines in the kinematically forbidden CBED disks where the intensity of of the double-diffracted beams cancel. Note that these lines only appear if the beam orientation is at one of the exact symmetry conditions that result in the appearance of GM lines. The GM lines are allways present, regardless of the thickness of the specimen, although the width of the line may change. Hence, GM lines is an importnat tool for assessing the translational symmetry of the unit cell. LACBED can also be used to identify GM lines, but only if the field-limiting aperture is insetred about one of the kinematically forbidden reflections.

It is possible to identify the polarity of a non-centrosymmetric crystal by variations in the intensity of the diffraction disks. The difference between the diffraction patterns of the two polarities are often small, and can be tricky to identify. However, intensity variations in the diffraction pattern may also arise as a consequence of thickness variations in the specimen, surface cracks or bending. Thus, it is not straight-forward to assess polarity. In order to isolate intensity variations due to thickness from polarity effects, it is important to compare experimental CBED patterns in a thickness series to simulated CBED patterns [28, 70–72].

From the above introduction to space group determination, it is clear that space group determination is complex, requiring a set of skills. Several crystallographic planes must be analysed for a set of symmetries, and high-quality data analysis must be performed. Hence, space group determination is a time-consuming process. In return, it allows for acquiring detailed information about the crystal structure of a material.

2.6 Literature review on KNBO

This section presents a literature review of the existing research on $K_3Nb_3B_2O_{12}$. Although KNBO has been studied since 1977, there has only been published a handful of articles discussing this crystal. From that work, it has become clear that KNBO shows interesting ferroic properties. However, there are important, fundamental properties of this crystal that are not fully understood, as there has been produced a set of conflicting results. First, the crystal structure of KNBO will be presented, including important crystallographic considerations about its space group. After this, the reported ferroic properties are outlined, followed by a summary of reported deviations in the current structural model. Finally, the two recent TEM studies will be summarised, and a note will be given on the assumptions made on the characteristsics and properties of KNBO to form a baseline for this thesis.

2.6.1 Crystal structure

The first study of KNBO was conducted by Choisnet *et al.* in 1977, who performed X-ray experiments to determine the crystal structure of KNBO. They determined that KNBO was described as a trigonal phase crystal at room temperature with space group $P31m$ and lattice dimensions $a = b = 4 \times 8.75$Å, $c = 3.7$Å [38]. This crystal structure was however corrected by Becker *et al.* in 1995. They conducted Buerger precession X-ray diffraction experiments and determined that room temperature KNBO can be described by the non-centrosymmetric orthorhombic space group $P2_1ma$ with lattice dimensions $a = 17.506$Å, $b = 15.162$Å, $c = 3.968$Å , where the **cab**-setting was used [36]. This crystal structure is pseudo-hexagonal, as the hexagonal-orthorhombic distortion is only 0.01%. These findings have been reproduced [37, 44]. Therefore, most research conducted in later years assume that KNBO is described by this crystal symmetry. The crystal structure of KNBO is shown in figure 2.21. As will be further explained in Seciton 2.6.2, KNBO has been proposed to display an antiferroelectric arrangement. This antiferroelectric ordering is also indicated by the arrows in figure 2.21b.

The crystal consists of $[NbO_6]$ octahedra, $[BO_3]$ planar triangles, and interstitial potassium. The $[NbO_6]$ groups order as triplets, where the octahedra share two oxygen atoms in the equatorial plane. The O-Nb-O bond angle is between 172.1° and 173°, and the bond length of the Nb-O bond is 1.8 Å - 2.2 Å. In other words, the Nb atoms are strongly distorted. The niobate groups are also linked by planar $[BO_3]$ triangles. The B-O bond lengths are 1.35 Å - 1.67 Å, and the O-O bond lengths are 2.3 Å - 2.4 Å. The linked $[NbO_6]$ and $[BO_3]$ form sheets along the c-plane which are stacked along the c-direction, and the sheets are bonded by the apical oxygen atoms in $[NbO_6]$. The remaining potassium atoms occupy interstitial pentagonal prismatic cavities. The K-B bond lengths are 2.73 Å - 3.15 Å.

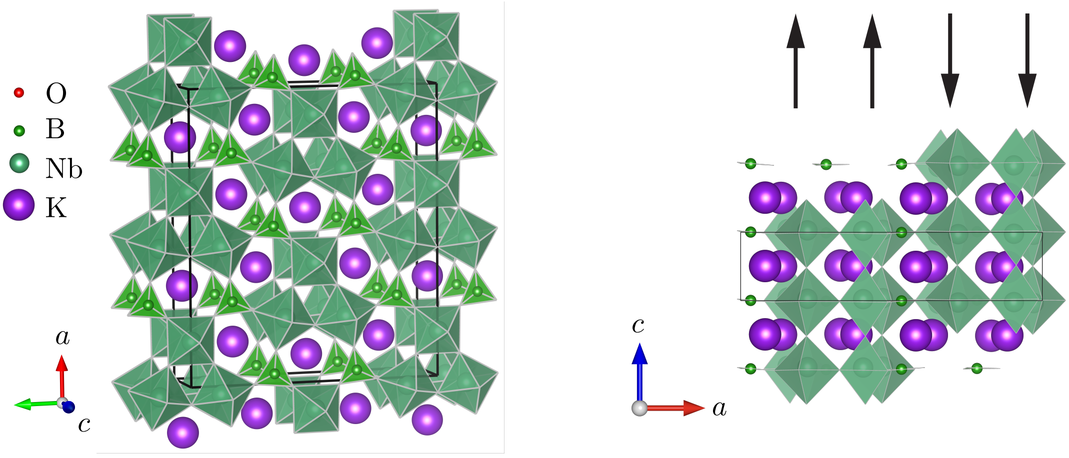

(a) (b)

Figure 2.21: Crystal structure of $K_3Nb_3B_2O_{12}$ in (a) the *c*-plane, and (b) the *b*-plane. The black box illustrates the boundaries of the orthorhombic unit cell. The figures clearly illustrates the sheets in the *c*-plane containing [NbO_6] triplets, [BO_3] units, and K atoms in the pentagonal interstitial sites. Crystal structrures were drawn in VESTA [2], and the oxygen atoms are omitted for simplicity. The proposed antiferroelectric arrangement of KNBO is also illustrated by the arrrows in (b).

Kaminskii *et al.* pointed out the point symmetry of the unique atomic sites [35]. There are four non-equivalent potassium atoms. Two of these have site symmetry m, while the other two show site symmetry 1. Similarly, there are four non-equivalent niobium atoms, where two of them have site symmetry m, and two have site symmetry 1. Lastly, there are two non-equivalent boron atoms, both of which have site symmetry 1. By close inspection, this can also be seen in figure 2.21b.

Since KNBO is described by space group 26, one should be able to identify the *a*-axis as a 2_1-screw axis, the *b*-plane as a mirror plane, and the *c*-plane as an *a*-glide plane. By close inspection of figures 2.21a and 2.21b, it is possible to identify all of these symmetries. The *a*-axis is a screw axis, which can be observed in the *c*- and *b*-planes. The *b*-plane is a mirror plane, which can be observed in the *a*- and *c*-planes. The *c*-plane is an *a*-glide plane, which can be observed in the *b*-plane. An illustrative model is also presented in figure 2.22 to help visualise these complex symmetries. One niobate octahedral unit is presented, since the displacement of the central niobium atom is most easily recognised when assessing these symmetry operations in crystal visualisation softwares.

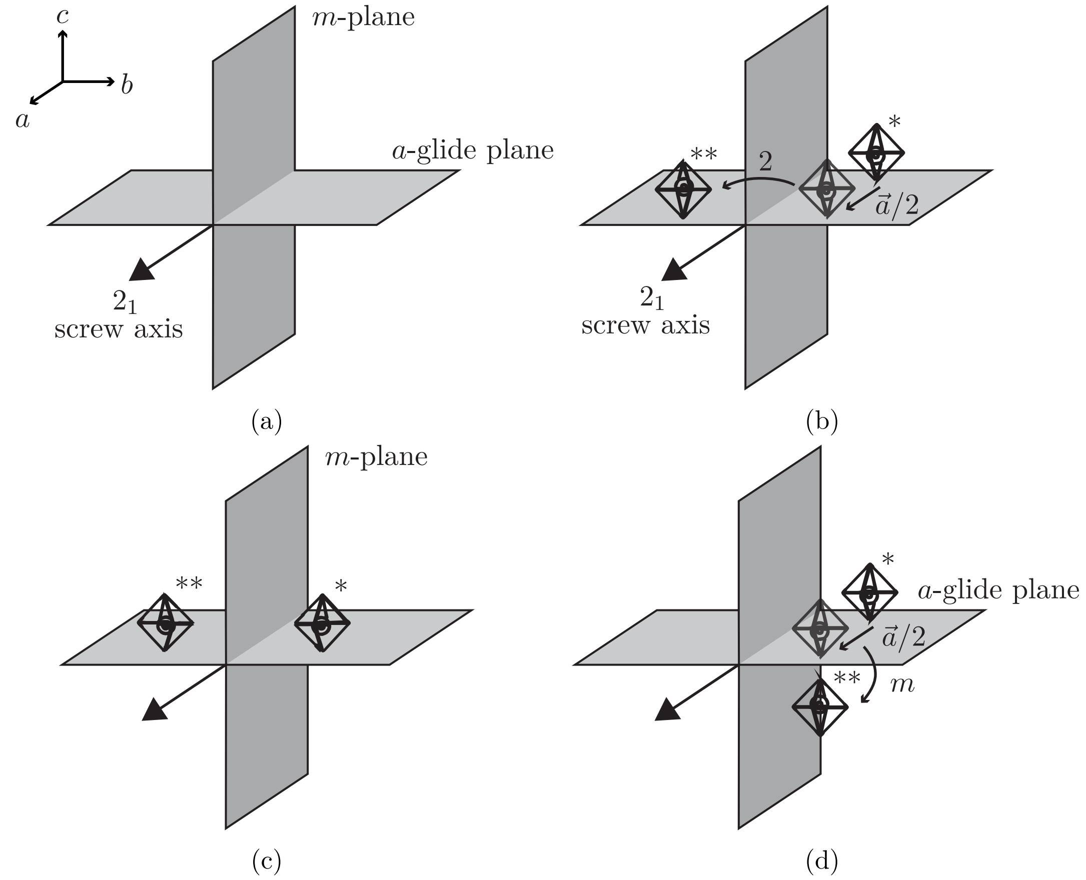

Figure 2.22: Symmetries in space group 26, $P2_1ma$, in the **cab**-setting. (a) The symmetries can be represented as a set of planes and a vector. The a-axis is a 2_1 screw axis, the b-plane is a mirror plane, and the c-plane is an a-glide plane. (b-d) Illustrates the 2_1, m and a symmetry operations with the niobate octahedra. The symmetry operations are carried out from a set of atoms at position $*$ to an equivalent set of atoms at position $**$. Any intermediate steps are illustrated by the opaque set of atoms.

2.6.1.1 Theoretical considerations about space group 26

The International Tables of Crystallography (ITA) contains useful information about every space group that can come in handy for structural characterisation of crystals and for indexing diffraction patterns [50]. It gives information about symmetries of special projections, and about the reflection conditions of crystals described by that specific space group. Information given about the space groups are given in the **abc**-setting, while the information about KNBO has been reported in the **cab** setting in the literature. To relate the information given in ITA about space group 26 to the information given about KNBO in the **cab** setting, the information given in ITA must be transformed to this setting. A summary of the transformations are given in table 2.2. See Appendix A for details on how symmetry information can be transformed from the **abc**-setting to the **cab**-setting.

Table 2.2 presents the space group, point group, projection symmetries, polar axis and reflection conditions as given from ITA. If the information given in ITA are transformed to the **cab**-setting, the space group is $P2_1ma$ with the point group $2mm$ and a polar axis along the [1 0 0]-direction, in other words the a-axis. This is consistent with the information reported in the literature about KNBO. The symmetries of the [1 0 0]-, [0 1 0]-, and [0 0 1]-projections in space group 26 are $pm2m$, $p11g$, and $pm11$ respectively. From ITA, the reflection conditions of space group 26 are given as $(h\,k\,0)$ for all $h = 2n$, and $(h\,0\,0)$ for all $h = 2n$ when transformed to the **cab**-setting. The exact reflection conditions are however expected to differ slightly due to atomic contributions from the basis, resulting in additional reflections or extinction rules for KNBO.

Table 2.2: Symmetry information about space group 26 given in the **abc**- and the **cab**-settings.

	The **abc**-setting	The **cab**-setting
Space group	$Pmc2_1$	$P2_1ma$
Point group	$mm2$	$2mm$
[1 0 0]-projection	$p1g1$	$pm2m$
[0 1 0]-projection	$p11m$	$p11g$
[0 0 1]-projection	$p2mm$	$pm11$
Polar axis	[0 0 1]	[100]
Reflection conditions	$(h\,0\,l)$ for all $l = 2n$, $(0\,0\,l)$ for all $l = 2n$	$(h\,k\,0)$ for all $h = 2n$, $(h\,0\,0)$ for all $h = 2n$
Diffraction groups	[0 0 1]: $2mm$ $\langle 1\,0\,0\rangle$: $m1_R$ $[u\,0\,w]$: m $[u\,v\,0]$: m_R $[u\,v\,w]$: 1	[1 0 0]: $mm2$ $\langle 0\,1\,0\rangle$: 1_Rm $[u\,v\,0]$: m $[0\,v\,w]$: m_R $[u\,v\,w]$: 1

Table 2.2 also list the expected diffraction groups of KNBO based on its point group. The diffraction groups are retrieved from Buxton and are based on group theory [69]. From crystallographic assessment of KNBO, GM lines are also expected to be present in the CBED patterns of the [0 0 1] and [0 1 0] zone axes. This is a direct result of the a-axis being a 2_1 screw axis and the c-plane being an a-glide plane.

Although the real diffraction conditions of KNBO are expected to deviate from the theoretically deduced conditions for space group 26, this information may be useful as a first approach to assess the diffraction data acquired by KNBO, together with the reported diffraction groups of point group $2mm$. The abovementioned transformations are also useful when comparing symmetries in KNBO and its diffraction properties to similar crystals in the literature where the **abc**-setting has been used.

An additional note is given on crystal planes and directions in KNBO. Since KNBO is orthorhombic, crystal directions perpendicular to a plane are not directly related by the corresponsing hkl values. The relationship between some key crystal planes and directions in KNBO that are referred to in this thesis are schematically presented in figure 2.23 on a pseudo-hexagon.

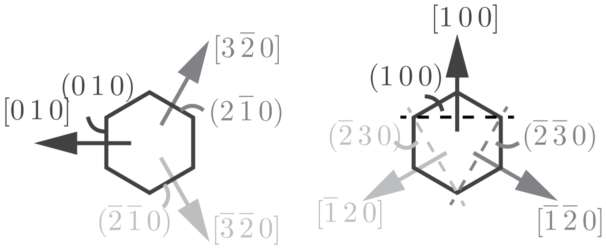

Figure 2.23: Relationship between the crystallographic planes and directions in KNBO indicated on a pseudo-hexagon. These relations were determined by the author with ReciPro [5].

2.6.2 Ferroic properties of KNBO

KNBO has long been considered a ferroelectric and ferroelastic material with the *a*-axis as the polar axis. According to Becker *et al.*, KNBO orders in needle-like ferroelastic domains with lamellar twinning. This is shown in figure 2.24. The twin axis is the *c*-axis, and the angle between the twin domains are 120°, where the boundaries have been reported to be perpendicular to the *a*-axis. The twin boundaries are easily moved by an applied mechanical force, and therefore, KNBO is considered to have three distinct ferroelastic domains. No work have, however, identified exactly how these ferroelastic domains orient on the atomic scale.

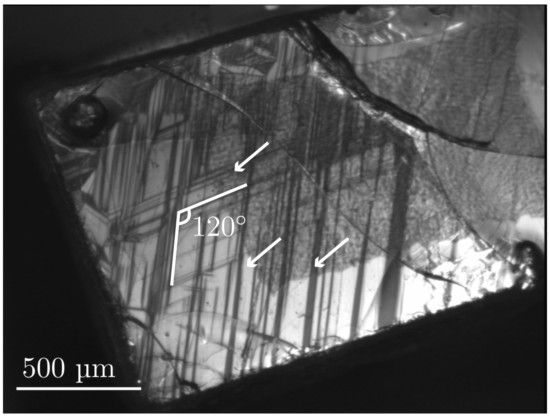

Figure 2.24: Polarised light microscopy image highlighting three separate needle-shaped ferroelastic twin domains in KNBO. The image is reprinted from [1].

Because KNBO is described by the non-centrosymmetric space group, 26, it was early expected to show ferroelectric properties along the polar *a*-axis. Previous research have reported both ferroelectric and antiferroelectric behaviour in KNBO, but no work has previously reported ferroelectric switching along the theoretically polar *a*-axis, as far as the author could verify. KNBO has however been reported to be ferroelectric from dielectric measurements and second harmonic generation [35, 39–41] with the *c*-axis as the polar axis.

Antiferroelectric response in KNBO was first reported by Shan *et al.* [37, 42], by the presence of double P-E hysteresis loops along the *c*-axis. Additionally, local dipole analysis performed by Shan *et al.* showed that the KNBO crystal is divided into two antiparallel sublattices where the dipoles of [NbO_6], [KO_{13}], and [BO_3] are antiparallely aligned along the *c*-direction. Shan *et al.* attribute the antiferroelectric properties mainly to distortions in the potassium and niobium atoms, as the polar distortions of boron are very small. This is also illustrated in figure 2.21b. From this analysis, Shan *et al.* found no ferroelectric behaviour in any directions within the *c*-plane, but they did measure a polar response. They acquired a second harmonic generation response, that was caused by polar displacements of the potassium and niobium atoms along the *a*-axis.

Hence, the true ferroic properties of KNBO is still under debate. In addition to the inconsistent findings on these physical properties, there are several other discrepansies reported in the literature.

2.6.3 Deviations in the current structural model

Although a set of properties have been mapped for KNBO, conflicting results have caused researchers to debate. There are for example discussions on whether $P2_1ma$ is the true space group of KNBO at room temperature. Additionally, there are several reportings of discrepancies in the physical properties of KNBO that are not consistent with the suggested space group, including the abovementioned antiferroelectric ordering of KNBO along the *c*-direction.

Maczka *et al.* reported discrepancies that indicate that room-temperature KNBO is incorrectly described as orthorhombic. Brillouin spectra of KNBO revealed transverse acoustic modes that are forbidden in orthorhombic crystals [43, 44]. This has also lead researchers to believe that the true polar axis of KNBO is the *c*-axis. Additionally, KNBO has been reported to be superionic along the *c*-axis, where the potassium ions can hop between interstitial pentagonal sites [39, 40, 44], further supporting the hypothesis of a polar *c*-axis. Because of the abovementioned discrepancies, both Kharitonova *et al.* and Maczka *et al.* suggested that the true crystal structure of KNBO is monoclinic or triclinic instead of orthorhombic. Despite these suggestions, no research has identified any alternative space group description of KNBO. Contrarily, the reported $P2_1ma$ space group has been reproduced [37, 42].

Another discrepancy between the reported physical properties of KNBO is the absence of a macroscopic piezoelectric response reported by Shan *et al.* [42], which should be present in a ferroelastic material. However, I. Ushakov and D. Meier have locally measured piezo-response in KNBO using PFM, confirming the presence of three polar domains in KNBO [73]. This is given in figure 2.25, as kindly provided by I. Ushakov and D. Meier. They propose that the local piezo-reponse of each ferroelastic domain may macroscpoically cancel out, leaving a net piezo-response of zero for the macroscopic crystal. Further, the reported absence of six polar domains with opposite polarities suggest that KNBO is incorrectly described as ferroelectric.

Hence there are many conflicting results in the literature, that are important to consider when performing experiments on KNBO.

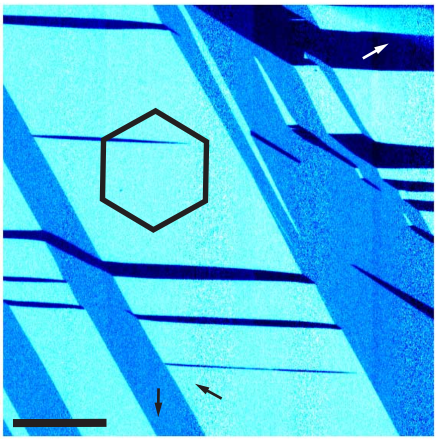

Figure 2.25: PFM micrograph showing the three distinct polar domains in KNBO. The arrows indicate the direction of the strongest piezo-response, and the pseudo-hexagon illustrates the orientation of the KNBO specimen. The Scale bar is 10 µm. Courtesy of I. Ushakov and D. Meier for providing the image [73].

2.6.4 Recent TEM studies on KNBO

There have only been perfomed two previous TEM studies on KNBO, as far as the author could verify. The first TEM study on KNBO was performed by Oskar Ryggetangen [45] with the aim of identifying ferroic domain walls in the *c*-plane of KNBO. Both PLM and PFM identified three distinct polar domains, further verifying the absence of ferroelectric domains, but verifying the presence of the three distinct ferroelstic twin domains. His work also demonstrated that the SAED pattern of KNBO contain $6mm$ symmetry, but that the on-zone CBED pattern displayed a rigid $3m$ symmetry, with three concrete mirror lines along the $[1\,0\,0]$ direction, $[\bar{1}\,2\,0]$ and $[\bar{1}\,\bar{2}\,0]$ directions. Further, off-zone CBED experiments displayed two mirror lines, along the $[1\,0\,0]$ and the $[0\,1\,0]$ directions, hence the *a*- and *b*-direction of the crystal. These results were however not in agreement with simulations performed by Ryggetangen, where the off-zone CBED simulations only revealed a mirror line along the $[1\,0\,0]$-direction. The experiments by Ryggetangen thus showed that the symmetry of the thin KNBO specimen did not coincide with the symmetry considerations of space group 26 in the *c*-plane, but the simulations were consistent with the theoretical considerations. Although correlated microscopy performed by Ryggetangen localised several polar domains by PLM and PFM, none of these were easily recognised by TEM.

The second correlated TEM study on KNBO was the the project work perfomed by the author [1]. In that work, it was attempted to reproduce the results given by Ryggetangen by investigating the domain structure of KNBO in the $[0\,0\,1]$ zone axis. The SAED and on-zone CBED patterns obtained in that project confirmed the diffraction symmetries reported by Ryggetangen, demonstrating a $6mm$ and $3m$ symmetry respectivelty. However not only the on-zone, but also the off-zone CBED patterns reavealed the same $3m$ symmetry with the $[1\,0\,0]$, $[\bar{1}\,2\,0]$ and $[\bar{1}\,\bar{2}\,0]$ directions as mirror lines. Hence, the off-zone experiments carried out by the author were not in direct agreement with those reported by Ryggetangen. Additionally, it was established that standard procedures for domain wall investigations were not sufficient for localizing the domain walls in the $[0\,0\,1]$ zone by TEM, although they had previously been localised by PLM. DF and BF TEM did not yield any domain contrast, and neither did HAADF STEM. The inability to yield structural domain contrast was attributed to the crystal symmetry in the $[0\,0\,1]$ direction, that was strikingly close to $3m$. Hence, any 120° rotation of the crystal lattice at a twin boundary would be difficult to identify because the diffraction pattern would appear identical. Further, it was reported that it is challenging to conclusively assign the crystal orientation and polar axis in the $[0\,0\,1]$ zone, which further complicated the assessment of possible domains. Hence, the previous TEM inspections of KNBO emphasised the need for a better framework for domain inspections in TEM.

2.6.5 Note on assumptions

From the above literature review, it is clear that the existing literature is inconclusive on the true ferroic nature of KNBO, and that there are some discrepancies with regard to its proposed crystal structure. The crystal structure of a material is important for the diffraction characteristics of the material. It also serves as a baseline for designing TEM experiments to identify specific features of the material. Because the existing research have reported inconsistent crystal symmetries and ferroic properties of KNBO, it is important to make a set of assumptions as a baseline for planning the correct TEM experiments.

Although previous TEM inspections have revealed diffraction symmetries of the $[0\,0\,1]$ zone that are not consistent with the theoretical diffraction symmetry of the $2mm$ point group, the previous work have suggested that the $3m$ symmetry is a direct consequence of the pseudo-hexagonal nature of KNBO. Hence it will be assumed that KNBO is correctly described by space group 26, $P2_1ma$. It will also be assumed that KNBO is ferroelastic with the a-axis as the polar axis. The possibility of a polar or antiferroelectric c-axis is however not excluded, and no assumption is made on the true (anti)ferroelectric nature of KNBO. It is rather noted that one of these configurations could be present in KNBO.

3 Experimental

This work will build a framework for domain characterisation of KNBO which can be utilised in later work to relate the structural properties of this crystal to its functional properties. As will become evident in the results and discussion, the physical properties of KNBO complicate both the structural characterisation and domain inspections. Several methods for structural characterisation and domain inspections were therefore required, exceeding techniques that are typically needed for such characterisation. This chapter will present these experimental procedures.

This chapter firstly presents the major considerations with respect to the electron diffraction simulations required for orientational and polarity assessment, including important parameters. After this, details on the material and specimen preparation are given. Specimens were prepared in two different directions – one direction with the *c*-axis out-of-plane, and one with the *c*-axis in-plane. The experimental details on TEM are listed in an own section. The analysis of KNBO is separated into two parts. The first is a structural analysis of KNBO at several zones in order to gain an understanding of the electron diffraction properties of KNBO. The knowledge gained from this structural analysis is required to find the optimal zones for domain inspections, hence leading to the second part of the experimental procedure which is the domain inspections using a correlated approach. The correlated microscopy study included PLM, TEM, STEM and PFM. The correlated TEM studies will be used as a proof-of-concept, and will not be further detailed in this work. However, by identifying the optimal procedure for these inspections, the framework for structural and functional domain inspections of KNBO can be established. The primary focus of the correlated approach is on the TEM characterisation.

3.1 Simulations

Dynamical diffraction simulations were performed using the softwares *JEMS* [3], *ReciPro* [5] and the Python package *py_multislice* [4]. The cif-file used for the crystal input is given in Appendix B.[1] JEMS was used to simulate SAED, CBED and LACBED patterns of KNBO, py_multislice was used to simulate CBED patterns, and ReciPro was used as a tool for zone-determination. The multislice algorithm provided by py_multislice was used as a complimentary tool to JEMS because its Bloch wave algorithm became computationally heavy when simulating CBED patterns that required a large number of beams to be included, such as in the [0 0 1] zone.

---

[1] py_multislice actually requires the file to be in a "P1" format, but Vesta can easily convert a cif-file to a p1 format.

3.1.1 Bloch wave simulations

Bloch wave simulations were performed with JEMS. The JEMS software has implemented all of the models for simulations outlined in Section 2.4.3.4, except from the BK model and the Lobato and van Dyck model. Although Lobato and van Dyck have shown that the EJK model provide slightly lower root-mean-square values than the PRDW [67], initial simulations in JEMS showed that the PRDW model matched the experimental diffraction patterns better. This model was therefore used for simulations of diffraction patterns in JEMS. The simulations were performed using the parameters given in table 3.1[2]. The microscope was specified to the *JEOL JEM - 2100F* with an acceleration voltage of 200 keV, and the dynamical simulations were performed using an all-beam Bloch wave approach.

Table 3.1: Parameters used in the Bloch wave simulations in the software JEMS, simulating diffraction patterns in the $[0\,1\,0]$, $[0\,\bar{1}\,0]$, $[0\,0\,1]$, $[0\,0\,\bar{1}]$, $[\bar{3}\,2\,0]$, $[3\,\bar{2}\,0]$, $[3\,2\,0]$, and $[\bar{3}\,\bar{2}\,0]$ zone axes.

	SAED	CBED	LACBED
Nr of HOLZ	5	5	5
Half convergence angle (mrad)	–	0.5-1.25	40
Crystal potential model	PRDW	PRDW	PRDW
Thickness (nm)	50 - 500	50 - 500	50 - 500
Thickness step size (nm)	15	15	50
Zones	All	All	$[0\,0\,1]$, $[0\,0\,\bar{1}]$ $[0\,1\,0]$, $[0\,\bar{1}\,0]$, $[\bar{3}\,2\,0]$, $[\bar{3}\,\bar{2}\,0]$

ReciPro was used for zone-determination using the tools *spotID v1* and *spotID v2*. In *spotID v1*, the distances between diffracted spots of three experimental SAED patterns were given, including the experimental x- and y-tilts of the specimen holder. In *spotID v2*, experimental SAED patterns were individually uploaded to the software. In both tools, ReciPro compares the experimental data to Bloch wave simulations. ReciPro uses a model for the crystal potential which is based on thermal diffuse scattering, fitting the atomic scattering factors by the superposition of Gaussian functions, and only including the imaginary part of the crystal potential. For all analysis performed in ReciPro, the acceleration voltage was specified to 200 keV, and the camera length and pixel size was specified according to the experimental SAED pattern. An error of up to 5% was allowed in the distances between diffracted spots, and an error of up to 3% in the tilt-angles.

---

[2] The zones suggested by ReciPro for the tilt-series were also simulated in JEMS with similar parameters, but it was considered that listing all of these zones here would be inefficient. See rather table 4.1 in Section 4.1.2 for details on these zones. This will also be further specified in Section 3.5.

3.1.2 Multislice simulations

Multislice CBED simulations were performed in py_multislice as an alternative to the Bloch wave simulations in JEMS. py_multislice is a GPU accelerated script written in Python for running dynamical multislice simulations, and is developed by Hamish G. Brown and Thomas Aarhodt [4]. py_multislice uses crystal potential model by Lobato and van Dyck, and a frozen phonon approach.

Two important parameters in the multislice algorithm are the tiling and grid shape. The tiling describes how the unit cell is repeated in real space, while the grid shape describes the number of sampling points. First, the appropriate grid shape and tiling was chosen by running convergence tests based on a Jupyter Notebook provided on the py_multislice's Github repository [4]. After this, the CBED simulations were perfomed using the premixed routine, *CBED*, in the py_multislice source code. The simulations were run on NTNU's IDUN cluster on a NVIDIA Tesla V100 32GB GPU [74]. The main parameters used in the multislice simulations are given in table 3.2.

Table 3.2: Essential parameters used in the multislice CBED simulations based on the code developed by Hamish G. Brown and Thomas Aarhodt.

	[0 0 1]	[0 1 0]
Convergence angle (mrad)	1.25	1.25
Grid shape	[2048, 2048]	[2048, 2048]
	[3072, 3072]	[3072, 3072]
Tiling	$[8, \lvert 8a/b \rvert]$	$[8, \lvert 8a/c \rvert]$
	$[32, \lvert 32a/b \rvert]$	$[32, \lvert 32a/c \rvert]$
Thickness (nm)	10 - 500	10 - 500
Nr. frozen phonons	25	25

A varying slice thickness was used for slicing the unit cell, and was therefore optimised for each of the zones. The unit cells were sliced according to fractional distances along the thickness of the specimen. For the [0 1 0] simulations, the thickness of the specimen was sliced along the following fractional distances in the b-direction: 0.06, 0.115, 0.15, 0.185, 0.23, 0.28, 0.32, 0.36, 0.39, 0.47, 0.55, 0.615, 0.645, 0.685, 0.735, 0.78, 0.82, 0.855, 0.89, 0.95, 1.0. For the [0 0 1] simulations, the specimen was sliced along the following fractional distances in the c-direction: 0.2, 0.4, 0.6, 0.8, 1.0. This is also illustrated in figure 3.1. Further experimental details can be found in the script given in Appendix C.

py_multislice required the crystal to be cubic, which is why the tiling was scaled according to the lattice parameters. Please note that the convergence tests for [0 1 0] only passed for thicknesses up to approximately 100 nm. In order to make the convergence test pass for thicker specimens, the grid shape and tiling would have to be increased. However, because the lattice parameter along the a-directions is much longer than in the c-direction, this would require more memory storage. At larger tilings and grid shapes than those listed, the 32 GB Nvidia GPU ran out of memory. Hence, any further optimisation of the tiling and grid shape were out of reach. The convergence tests can be found in Appendix C.

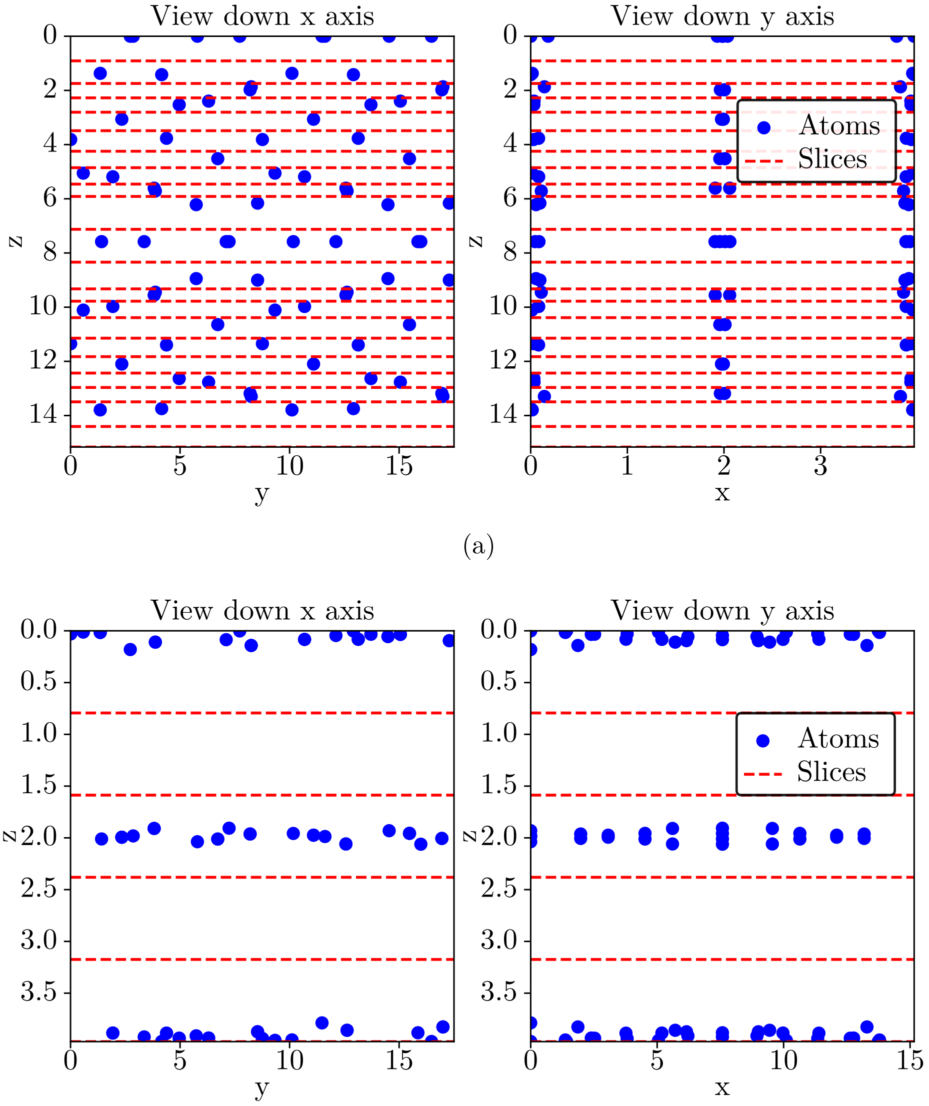

(a)

(b)

Figure 3.1: Figures illustrating the fractional distances at which the crystal was sliced during multislice CBED simulations in the (a) [0 1 0] and (b) [0 0 1] direction. z is along the thickness of the specimen, in other words the crystallographic. In (a) the x, y and z are the crystallographic c-, a-, and b-direction. In (b) the x, y and z are the crystallographic b-, a-, and c-direction respectively.

3.2 Material

The $K_3Nb_3B_2O_{12}$ crystals were grown by *top seeded solution growth* at the University of Cologne [36]. The initial melt temperature was 1210 K, the withdrawal speed of the rod was 0.1 mm/day, and the temperature was lowered by 0.1 K/day. To ensure that the crystal growth was correct, the melt was inspected by X-ray diffraction and electron microprobe analysis continuously. The final shape of the KNBO crystal had a morphology similar to a hexagonal-prism with the c-axis along its height.

3.3 Specimen preparation

TEM specimens were prepared by tripod polishing. Tripod polishing is a standard preparation technique that produces high-quality, wedge-shaped TEM specimens in a single crystal plane. The thin edge usually acquires a thickness on the nanoscale. This is highly desirable because it allows for TEM inspections at both thinner and thicker regions of a known crystallographic plane. The tripod polishing scheme was adapted from Oskar Ryggetangen's work [45], based on Håkon Wiik Ånes polishing scheme [75]. A detailed procedure can be found in Appendix D. The specimen preparation is illustrated in figure 3.3 and figure 3.4 for the c-axis in-plane specimen and the c-axis out-of-plane specimen respectively. A summary of the polishing scheme is given below.

Two TEM specimens were investigated in this thesis; a specimen with the c-axis out-of-plane, and one with the c-axis in-plane. In order to investigate the polar a-axis, it was ensured that the a-axis was in-plane as well. The c-axis out-of-plane specimen automatically had the a-axis in-plane. The c-axis out-of-plane specimen was prepared in a previous project by the same author [1], and a thorough procedure for preparing that specimen can be found there. A summary is given below.

To investigate the polar axis in the c-axis in-plane specimen, the specimen had to be prepared such that the $[0\,1\,0]$ zone could be inspected. From the bulk crystal, there were three facets perpendicular to the c-plane, the $(0\,1\,0)$, $(3\,\bar{2}\,0)$ and $(\bar{3}\,\bar{2}\,0)$ facets, as illustrated in figure 3.2. It was however not straight-forward to distinguish these facets on the bulk KNBO sample. Since KNBO is ferroelastic with 120° domain walls, it was expected that preparing a facet with several ferroelastic domains would increase the probability of inspecting the $[0\,1\,0]$ zone.

Before polishing, the KNBO sample was cut in appropriate dimensions. The c-axis in-plane specimen was prepared from a KNBO single crystal of height approximately 3.3 mm. First, the bulk KNBO sample was imaged by PLM in the c-plane to identify the facet parallel to the c-direction that intersected the most domains. The crystal was cut using a *Testbourne Model 650 Low Speed Diamond WeelSaw* with a *60-20085* diamond metal bonded, low concentration, 150 µm wafering blade. The resulting specimen had a height of approximately 1.5 mm in the polishing direction, and a width and length of approximately 1 mm. This specimen was once more inspected by PLM to confirm the direction of the needle domains, and thereafter mounted on a sample holder for polishing. The specimen holder consisted of a pyrex stub, and the identified facet was glued on the stub using *Loctite* acetone soluble glue. This is illustrated in figure 3.3.

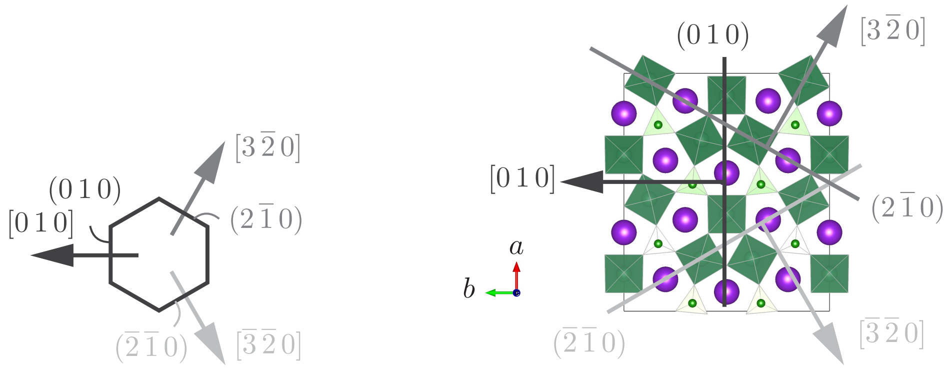

(a) (b)

Figure 3.2: (a) Twin directions and planes to $[010]$ and (010). (b) The 120° twins are illustrated on the unit cell of KNBO with the c-direction out of the screen.

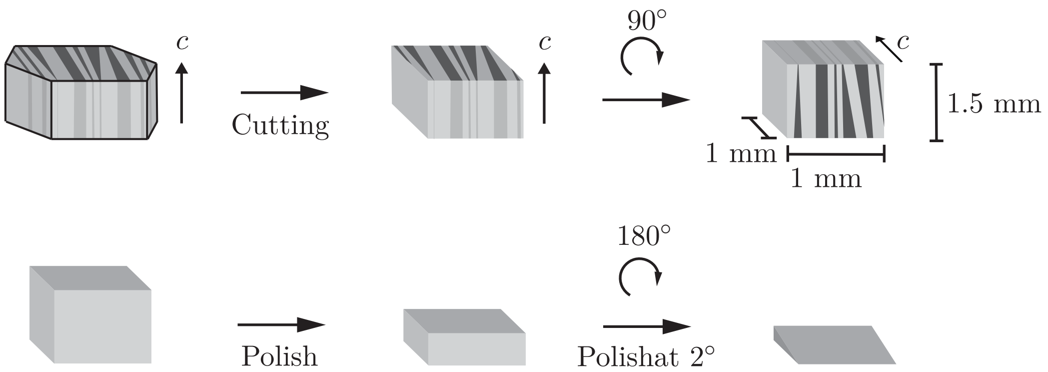

Figure 3.3: Tripod polishing scheme for the c-axis in-plane specimen. The sample was first imaged by PLM in the c-direction. The facet perpendicular to the c-facet intersecting the largest number of ferroelastic domains was identified, and cut in appropriate dimensions. The specimen was thereafter turned 90° such that this facet with the c-axis in-plane could be polished into a wedge-shaped TEM specimen.

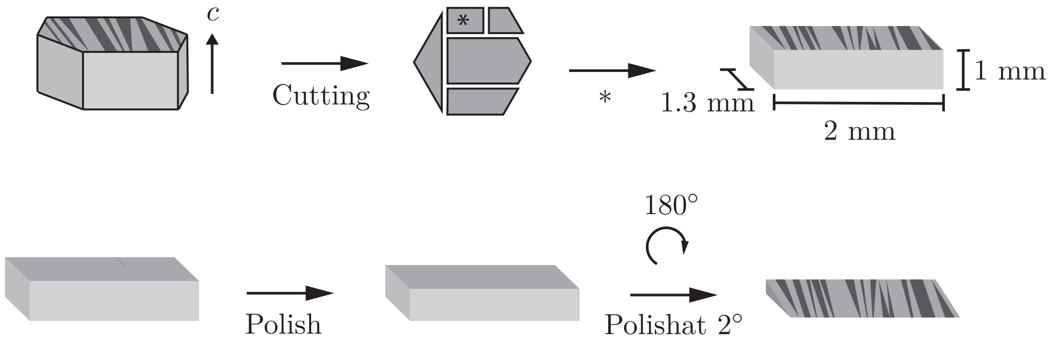

Figure 3.4: Tripod polishing scheme for the c-axis out-of-plane specimen. The sample was first imaged by PLM in the c-direction to identify regions with a large number of domains. The bulk KNBO material was cut along the major symmetry lines of the hexagonal prism. The specimen marked with an asterisk was selected for polishing. The specimen was thereafter polished into a wedge-shaped TEM specimen.

The *c*-axis out-of-plane specimen was prepared from another KNBO single crystal with a height of approximately 1 mm. The crystal was cut into a specimen of approximately 2 mm × 1.3 mm in width and length. To polish the specimen, it was mounted on a sample holder with the *c*-facet on the pyrex stub such that numerous domains would intersect the wedge of the specimen after polishing. This is illustrated in figure 3.4.

An *Allied Multistep* tripod polishing machine with diamond lapping films (DLF) was used to polish the crystals. The specimens were sequentially polished with DLFs of coarseness 15, 6, 3, 1, 0.5, 0.1 µm at 30 rpm. Lastly, a felt cloth stained with *Allied 20* nm *Colloidal Silica* was used to polish the specimens. The KNBO specimens were frequently inspected in a *Zeiss Axio Scope A.1* visual light microscope (VLM) to ensure proper dimensions, and to ensure that flaking had not occurred. To polish the second face, the specimens were detached from the pyrex stub in an acetone bath. Following, they were glued on the pyrex stub again, but with the polished face down. The polishing procedure was repeated, but at an angle 2° for all polishing steps proceeding the 15 µm DLF to make a wedge-shaped specimen.

Before detaching the specimens from the pyrex stub, a TEM grid was glued on each of the specimens using *Araldite* epoxy adhesive to the thick wedge of the KNBO specimens, ensuring that no glue was in direct contact with the pyrex stub. A 3 mm Cu TEM slot-grid was glued to the *c*-axis out-of-plane specimen, and a 3 mm Mo half-grid to the *c*-axis in-plane specimen. After the adhesive had cured, the specimens were detached from the pyrex stubs in another acetone bath overnight.

The specimens were prepared in different directions from two separate bulk KNBO samples, and can henceforth not be directly related to one another.

3.4 TEM

TEM inspections were performed at the TEM Gemini centre at NTNU, using two different microscopes: A *JEOL JEM-2100* with a LaB_6 thermionic electron source and Gatan inc. *ORIUS SC 200D* CCD Camera; and a *JEOL JEM-2100F* microscope with a ZrO/W(100) Schottky emitter electron source, and a *Gatan inc UltraScan* CCD. A *Quantum Detectors MerlinEM* direct electron detector is also installed on the *JEOL JEM-2100F*. This detector is from now referred to as the Merlin detector. Both microscopes were operated at an acceleration voltage of 200 keV.

Because the thin KNBO specimens were extremely brittle, they were permanently mounted on a *JEOL EM-31680* double tilting beryllium specimen holder. Areas of interest were initally mapped and stage positions and tilts were logged. All experiments on the *c*-axis out-of-plane specimen were carried out before performing the experiments on the *c*-axis in-plane specimen.

STEM was performed on the *JEOL JEM-2100F* with a *JEOL* annular detector at 8-80 cm and a spot size 0.2 nm and 1 nm. *Digiscan* was used to acquire STEM data in *Digital Micrograph.* Specifications of the HAADF STEM and HR-HAADF STEM set-up will be given below.

3.5 Structural characterisation with TEM

Structural characterisation was carried out by performing SAED, CBED, LACBED and HRTEM on both specimens. The 10 µm and 40 µm condenser apertures were used for the CBED experiments. The 250 µm aperture was used for LACBED of the *c*-axis in-plane specimen. When inspecting the *c*-axis out-of-plane specimen, the condenser aperture was removed completely during the LACBED experiments.

SAED and CBED thickness series were performed to increase the probability of acquiring a diffraction pattern that matched one of the simulated patterns. The thickness series were acquired with the *JEOL JEM-2100F*. The Merlin detector was used to acquire the SAED thickness series because it has a higher sensitivity for weak reflections, while the CBED thickness series were performed using the CCD camera to observe the HOLZ lines at a high resolution. The CBED thickness series of the *c*-axis in-plane specimen was also acquired with the Merlin detector in an attempt to distinguish intensity variations in $+g$ and $-g$ reflections. It was ensured that these thickness series were performed on a monocrystalline region of the specimens.

Since LACBED require a 100-200 nm large area to be defect-free for optimal symmetry assignment, they were performed in regions of the specimens where there were few-to-no visible line-defects present in a 100-200 nm region.

3.5.1 Additional analysis of the *c*-axis out-of-plane specimen

Structural analysis of the *c*-axis out-of-plane specimen were performed to find a methodology for assigning crystal orientation and polarisation. The experimental structural analysis was performed as described above, and compared to simulations. Furthermore, HR-HAADF STEM was performed under the supervision of Professor Antonius T.J. van Helvoort in an attempt to utilise the direct imaging of the atomic columns together with diffraction data to assign crystal orientation. The specimen was plasma cleaned prior to HRSTEM to remove organic contamination using 25% oxygen and 75% argon for 30 seconds in a *Fischione 1020 plasma cleaner*. HR-HAADF STEM was performed using a nominal spot size of 0.2 nm, the 10 µm condenser aperture, and a camera length of 8-20 cm.

3.5.2 Additional analysis of the *c*-axis in-plane specimen

Zones within the 15° tilt-limit of the specimen holder were mapped in a single domain. ReciPro was utilised for zone determination and indexing using the *SpotID v1* tool for the zones in the tilting series. JEMS was thereafter used to simulate the SAED patterns of the zones suggested by Recipro. These simulations were performed using the same parameters as stated in table 3.1, but for a thickness of 200 nm, and the zones suggested by ReciPro. These zones will be presented in the results in Section 4.1.2.

3.6 Correlated microscopy techniques

The correlated microscopy studies were based on Oskar Ryggetangen's work [45], where a set of complementary techniques accompanied the TEM studies. These correlated TEM studies included the imaging the KNBO crystals using PLM in the *c*-facet before TEM specimen preparation because it simplified the identification of the ferroelastic domain walls which were to be inspected in the TEM. Finally, the correlated studies included PFM to investigate the functional properties of the specimens. The structural analysis part of the correlated domain studies only applies to the *c*-axis in-plane specimen.

3.6.1 PLM

The specimens were inspected in the *c*-facet using an *Olympus BX60* VLM with a home-made set up for conducting PLM, as illustrated in figure 3.5. This is a conventional light microscope with a $\frac{1}{4}\lambda$ plate above the specimen[3]. To produce domain contrast, a separate polarisation filter was inserted below the specimen, and the microscope was set to transmission mode. The $\frac{1}{4}\lambda$ plate and polarisation filter were rotated until maximum domain contrast was observed.

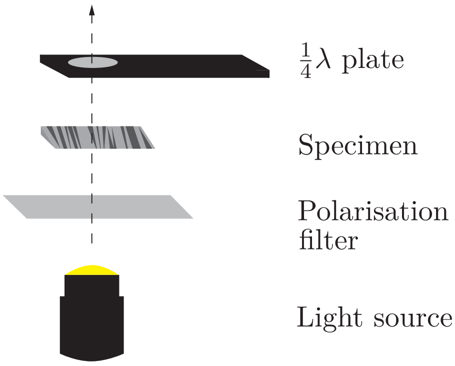

Figure 3.5: Illustration of the home-made PLM setup consisting of a conventional visual light microscope in transmission mode, an $\frac{1}{4}\lambda$ plate above the specimen, and a polarisation filter below the specimen.

3.6.2 Structural characterisation of domains with TEM

During the correlated TEM studies, the *c*-axis in-plane specimen was first imaged by HAADF STEM with a spot size 0.2 nm and camera lengths between 8-80 cm. The specimen was also imaged using BF and DF TEM to compare the effectiveness of HAADF STEM and conventional BF and DF imaging to identify the domains. A 5 µm objective aperture was used for BF and DF. SAED, CBED and LACBED were thereafter conducted on several domains to structurally characterise them and to investigate the suggested polar *a*-axis. This analysis was based on the findings from the structural characterisation described in Section 3.5.

---

[3] A $\frac{1}{4}\lambda$ plate is a simple polariser

3.6.3 PFM

After the TEM inspections were finished, PFM was performed on both specimens. PFM measurements were performed by PhD candidate and co-supervisor Ivan Ushakov at NTNU's Department of Materials Science and Engineering using a *NT-MDT NTEGRA* scanning probe microscope with a *SF005* head and *AU020* insert. The tip was grounded, and an alternating voltage of 10 V and frequency 40.13 kHz was applied to the specimen stage. The PFM tips used on the c-axis in-plane and the c-axis out-of-plane specimens were a *ASYELEC-01-R2 Asylum* electrolever tip with a tip radius of approximately 25 nm and a *HA_HR_DCP ETALON* tip with a tip radius of approximately 100 nm respectively. PFM measurements of the c-axis in-plane specimen were acquired with a scan rate of 0.22 Hz, with 1024 × 601 points and an area of size 30 µm × 17.6 µm, while the PFM measurements of the c-axis out-of-plane specimen were acquired with a scan rate of 0.44 Hz, with 512 × 512 points and an area of size 70 µm × 70 µm. The PFM images were processed and analysed with *Gwyddion* [8].

4 Results

This chapter presents the results from the structural analysis and domain inspections of KNBO. First, the results for the *c*-axis in-plane specimen will be presented, followed by the *c*-axis out-of-plane specimen. The simulated diffraction patterns will be presented alongside the experimental results.

4.1 *c*-axis in-plane specimen

Here, the results from the *c*-axis in-plane specimen are reported, including the quality of the specimen preparation, structural analysis, domain inspections, and PFM. The structural analysis is presented as a tilt series in a mono-crystalline region of the specimen. Further structural analysis is also included while presenting the domain inspections, as the location of structural domains allowed for the analysis of other zones.

4.1.1 Specimen preparation

The starting material and the polished TEM specimen are shown in figure 4.1. Figure 4.1a show a PLM micrograph of the unpolished starting material. Although it had been cut and used prior to this project, the outline of the characteristic hexagonal prism morphology was still recognisable. The specimen shape could therefore easily be used to prepare a specimen in one of the possible $(0\,1\,0)$ facets intersecting several needles domains. The hexagon shown in the lower right corner illustrates the orientation of the sample with respect to the hexagonal prism morphology. The needle domains can be seen as a weak contrast in the upper left corner of the unpolished sample. The TEM specimen shown in figure 4.1b was prepared from the indicated region in figure 4.1a, where the arrow indicates the facet from which the specimen was prepared.

Figure 4.2 presents HAADF STEM and conventional TEM micrographs of the specimen. Note that the STEM images are rotated with respect to the TEM image. The *c*-direction is indicated on the micrographs. From figures 4.2a and 4.2b, the specimen can be observed to preferably fracture along specific planes parallel and perpendicular to the *c*-direction. Additionally, the thinnest regions were more severely fractured than the thicker regions. Figure 4.2b also show signs that KNBO is susceptible to beam damage, as indicated by BD on the micrograph. Further, several defect structures can be observed, such as line defects (LD) and dislocation loops (DL). Dislocation loops can also be observed in the conventional TEM image in figure 4.2c. Some regions of the specimen displayed Moiré fringes as given in figure 4.2c, indicating that fractured rectangular flakes have been repositioned on the surface during polishing.

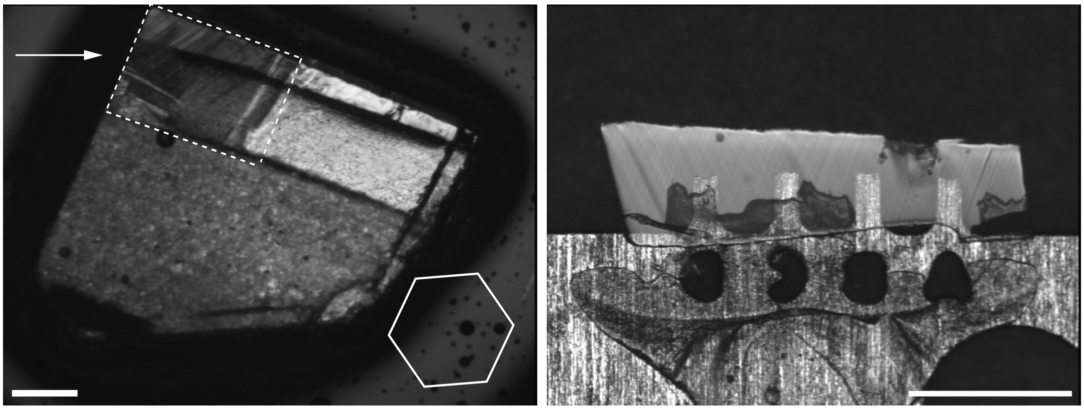

(a) (b)

Figure 4.1: (a) PLM image of a bulk KNBO crystal in the *c*-direction prior to polishing of the *c*-axis in-plane specimen. The arrow indicates the facet that the TEM specimen was prepared from, where several ferroelastic needle domains can be observed as a weak contrast in the upper left corner of the crystal. The hexagon illustrates the orientation of the KNBO hexagonal prism with respect to its original morhology. (b) VLM image of the final TEM specimen on the TEM half-grid. The scale bars are 500 µm.

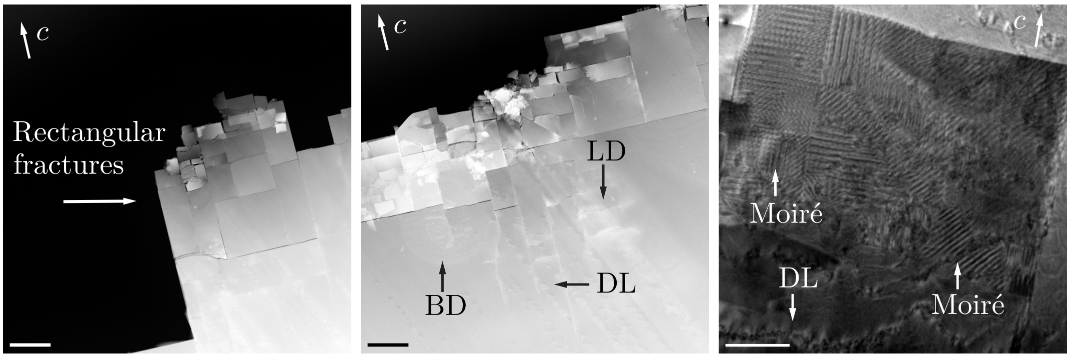

(a) (b) (c)

Figure 4.2: Representative TEM images showing the quality of the specimen preparation. (a-b) HAADF STEM images of the specimen acquired at a camera length of 20 cm. Several fractured rectangular flakes can be observed along specific crystallographic planes. (b) Dislocation loops (DL) and line defect (LD) are indicated on the micrograph. Beam damage (BD) can also be observed. (c) Conventional TEM image of overlapping fractured rectangles creating a Moiré pattern. The scale bars for (a, b) are 1 µm, and (c) is 200 µm. The *c*-direction is indicated on the images.

4.1.2 Tilt series

A tilt series was acquired in a mono-crystalline region of the specimen, where few defects were observed. This region of the specimen is shown in figure 4.3.

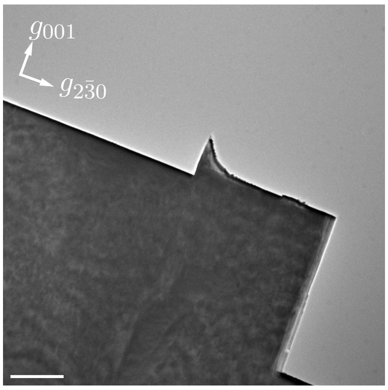

Figure 4.3: TEM image showing the region from which the tilt series was acquired. The scale bar is 200 nm.

The SAED patterns from the experimental tilt series are given in figure 4.4. Nine zones were accessible within the tilt-range of the specimen holder. The holder tilt-values at each of these zones are sketched out in figure 4.4a, including the angle between them. Zone-analysis in ReciPro of the SAED patterns from the tilt series suggested six indexing schemes given in table 4.1. Bloch wave simulations in JEMS revealed a vast similarity between these schemes, but the best fit is given in figure 4.5, where the major zone is $[\bar{3}\,\bar{2}\,0]$. This zone corresponds to the SAED pattern in 4.4 at a holder tilt-value of (2.4°, 1.2°). Hence, the experimental SAED patterns from the tilt series are indexed according to that scheme. The relative distance between two given reflections are given in table 4.2 as a measure of the similarity between the experimental and simulated SAED patterns. The simulated tilt series from the other suggested schemes are given in Appendix E. In addition to the experimental SAED patterns, Kikuchi patterns and CBED patterns were also acquired at the zones in the tilt series. These are also given in Appendix E, including SAED patterns acquired at a lower camera length.

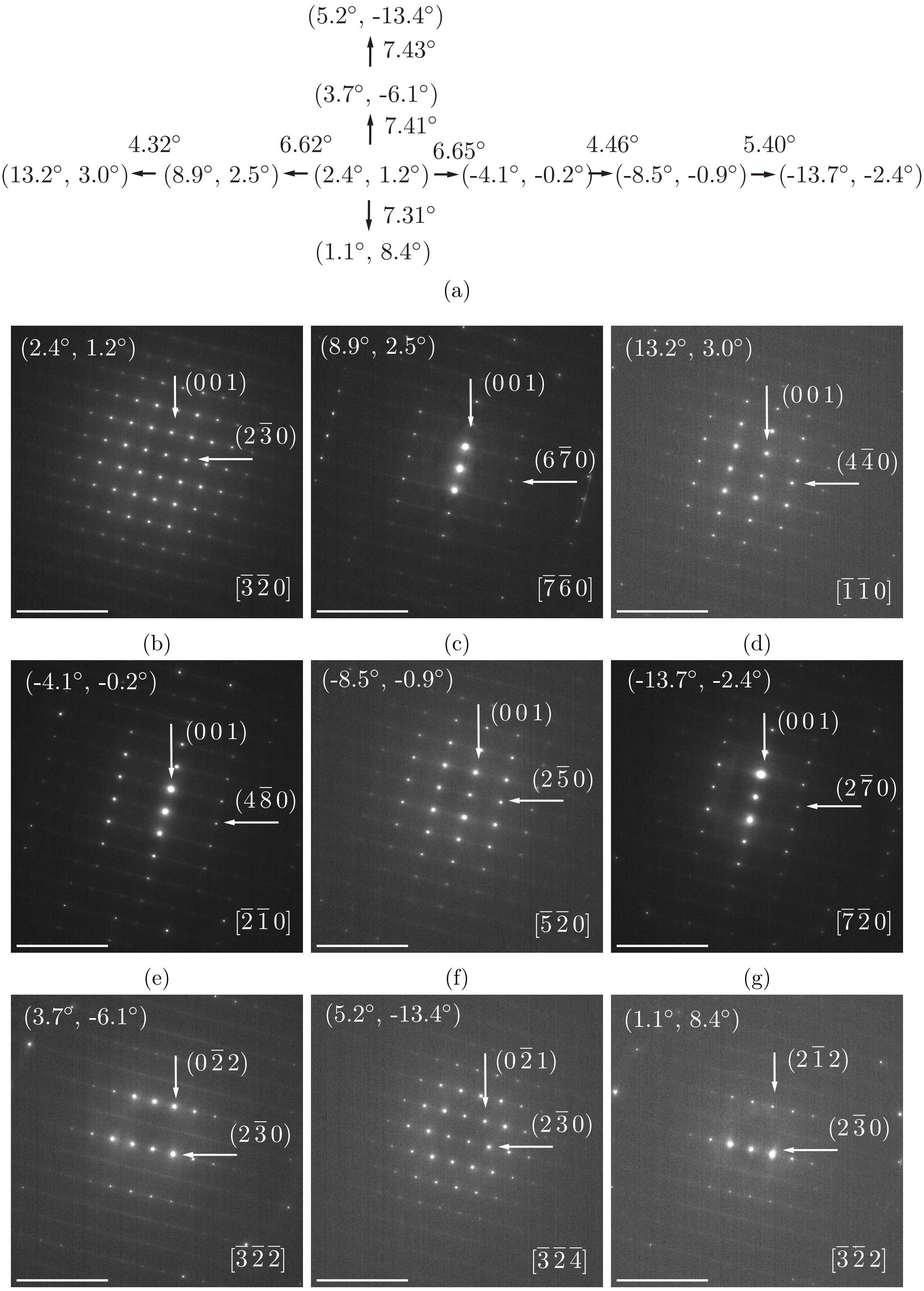

Figure 4.4: (a) Schematic of the holder tilt-values from the experimental tilt series and translated angles between zones, where the tilt values are written on the form (x-tilt, y-tilt). The experimental tilt series was acquired in a single domain of the c-axis in-plane specimen. (b-j) SAED from the tilting series at x- and y-tilts (2.4°, 1.2°), (8.9°, 2.5°), (13.2°, 3.0°), (-4.1°, -0.2°), (-8.5°, -0.9°), (-13.7°, -2.4°), (3.7°, -6.1°), (5.2°, -13.4°), and (1.1°, 8.4°) respectively. The scale bars are 10 nm^{-1}.

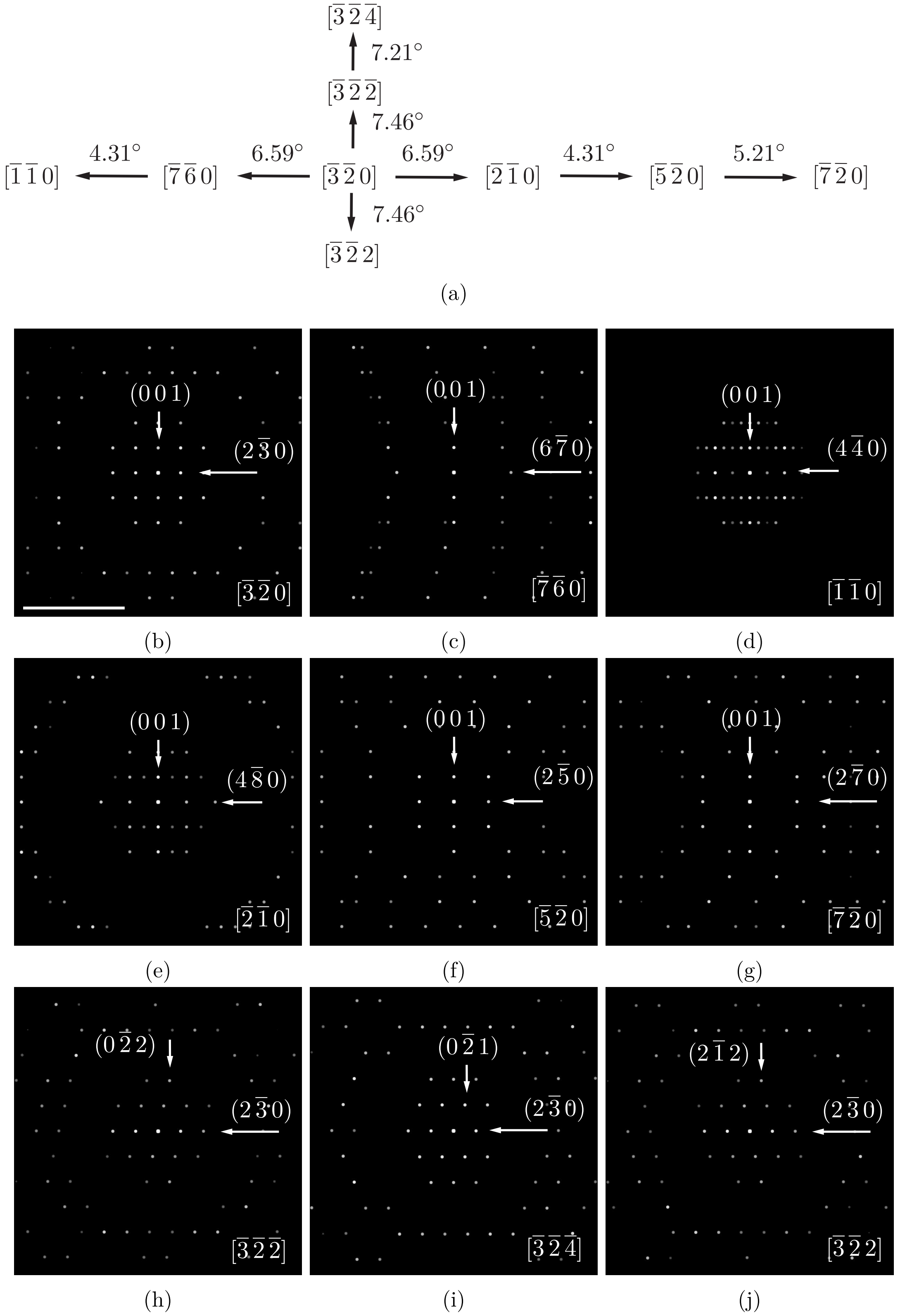

(a)

(b) (c) (d)

(e) (f) (g)

(h) (i) (j)

Figure 4.5: (a) Schematics of the $[\bar{3}\,\bar{2}\,0]$ and surrounding zones, including the angle between them. (b-j) Simulated SAED patterns corresponding to the zones given in (a).

Table 4.1: Suggested zones for the SAED patterns from the tilt series in figure 4.4 analysed in ReciPro. Six indexing schemes were compatible with the geometry of each zone and the angle between them. Suggestion 4 in bold is the scheme used in figures 4.4 and 4.5.

(x-tilt, y-tilt)	Sugg.1	Sugg. 2	Sugg. 3	**Sugg. 4**	Sugg. 5	Sugg. 6
(2.4, 1.2)	$[\bar{3}\,2\,0]$	$[3\,\bar{2}\,0]$	$[3\,2\,0]$	$[\bar{3}\,\bar{2}\,0]$	$[0\,\bar{1}\,0]$	$[0\,1\,0]$
(8.9, 2.5)	$[\bar{7}\,6\,0]$	$[2\,\bar{1}\,0]$	$[7\,6\,0]$	$[\bar{7}\,\bar{6}\,0]$	$[1\,\overline{10}\,0]$	$[\bar{1}\,10\,0]$
(13.2, 3.0)	$[\bar{1}\,1\,0]$	$[5\,\bar{2}\,0]$	$[1\,1\,0]$	$[\bar{1}\,\bar{1}\,0]$	$[1\,\bar{6}\,0]$	$[\bar{1}\,6\,0]$
(-4.1, -0.2)	$[\bar{2}\,1\,0]$	$[7\,\bar{6}\,0]$	$[2\,1\,0]$	$[\bar{2}\,\bar{1}\,0]$	$[\bar{1}\,\overline{10}\,0]$	$[1\,10\,0]$
(-8.5, -0.9)	$[\bar{5}\,2\,0]$	$[1\,\bar{1}\,0]$	$[5\,2\,0]$	$[\bar{5}\,\bar{2}\,0]$	$[\bar{1}\,\bar{6}\,0]$	$[1\,6\,0]$
(-13.7, -2.7)	$[\bar{7}\,2\,0]$	$[5\,\bar{6}\,0]$	$[7\,2\,0]$	$[\bar{7}\,\bar{2}\,0]$	$[\bar{1}\,\bar{4}\,0]$	$[1\,4\,0]$
(3.7, -6.1)	$[\bar{3}\,2\,2]$	$[3\,\bar{2}\,\bar{2}]$	$[3\,2\,\bar{2}]$	$[\bar{3}\,\bar{2}\,\bar{2}]$	$[0\,\bar{2}\,\bar{1}]$	$[0\,2\,\bar{1}]$
(5.2, -13.4)	$[\bar{3}\,2\,4]$	$[3\,\bar{2}\,\bar{4}]$	$[3\,2\,\bar{4}]$	$[\bar{3}\,\bar{2}\,\bar{4}]$	$[0\,\bar{1}\,\bar{1}]$	$[0\,1\,\bar{1}]$
(1.1, 8.4)	$[\bar{3}\,2\,\bar{2}]$	$[3\,\bar{2}\,2]$	$[3\,2\,2]$	$[\bar{3}\,\bar{2}\,2]$	$[0\,\bar{2}\,1]$	$[0\,2\,1]$

Table 4.2: The ratio $d^1_{\mathrm{hkl}}/d^2_{\mathrm{hkl}}$ for the experimental and the simulated patterns presented in figures 4.4 and 4.5. For the $[\bar{3}\,\bar{2}\,2]$, $[\bar{3}\,\bar{2}\,\bar{2}]$ and $[\bar{3}\,\bar{2}\,\bar{4}]$ zones, the angle between the given reflections are given because the respective spots are not perpendicular to each other.

(x-tilt, y-tilt)	Zone	$d^1_{\mathrm{hkl}}/d^2_{\mathrm{hkl}}$	Experimental	Simulations
(2.4, 1.2)	$[\bar{3}\,\bar{2}\,0]$	$(2\,\bar{3}\,0)/(0\,0\,1)$	0.91	0.90
(8.9, 2.5)	$[\bar{7}\,\bar{6}\,0]$	$(6\,\bar{7}\,0)/(0\,0\,1)$	2.32	2.30
(13.2, 3.0)	$[\bar{1}\,\bar{1}\,0]$	$(4\,\bar{4}\,0)/(0\,0\,1)$	1.37	1.41
(-4.1, -0.2)	$[\bar{2}\,\bar{1}\,0]$	$(4\,\bar{8}\,0)/(0\,0\,1)$	2.28	2.30
(-8.5, -0.9)	$[\bar{5}\,\bar{2}\,0]$	$(2\,\bar{5}\,0)/(0\,0\,1)$	1.39	1.38
(-13.7, -2.7)	$[\bar{7}\,\bar{2}\,0]$	$(2\,\bar{7}\,0)/(0\,0\,1)$	1.95	1.88
(3.7, -6.1)	$[\bar{3}\,\bar{2}\,\bar{2}]$	$(2\,\bar{3}\,0)/(0\,\bar{2}\,2)$	0.44, 77.3°	0.44, 77.0°
(5.2, -13.4)	$[\bar{3}\,\bar{2}\,\bar{4}]$	$(2\,\bar{3}\,0)/(0\,\bar{2}\,1)$	0.79, 66.1°	0.79, 66.7°
(1.1, 8.4)	$[\bar{3}\,\bar{2}\,2]$	$(2\,\bar{3}\,0)/(2\,\bar{1}\,2)$	0.44, 78.6°	0.44, 77.1°

4.1.3 Domain inspections

Domain inspections were mainly initialised by locating possible structural domains by HAADF STEM. Several bands of alternating light and dark contrast and a width in the order of 200 nm – 500 nm could easily be observed along the specimen by HAADF STEM. From structural characterisation across two such bands, three distinct structural domains were identified. These inspections are presented in detail below, where the structural characterisation across the two bands are presented separately.

Figure 4.6a display an HAADF STEM image where a dark band, denoted B1, is clearly visible. The two regions on either side of B2, denoted R1 and R2[1], were observed to generate two distinct SAED patterns given in figures 4.6b and 4.6c respectively. [2] The SAED in R1 was acquired in the $[0\,1\,0]$ zone, and the SAED in R2 in the $[\bar{3}\,\bar{2}\,0]$ zone without changing the holder tilt-values. The $[0\,1\,0]$ and $[\bar{3}\,\bar{2}\,0]$ zones are 120° from each other, hence suggesting that R1 and R2 are 120° twin domains.

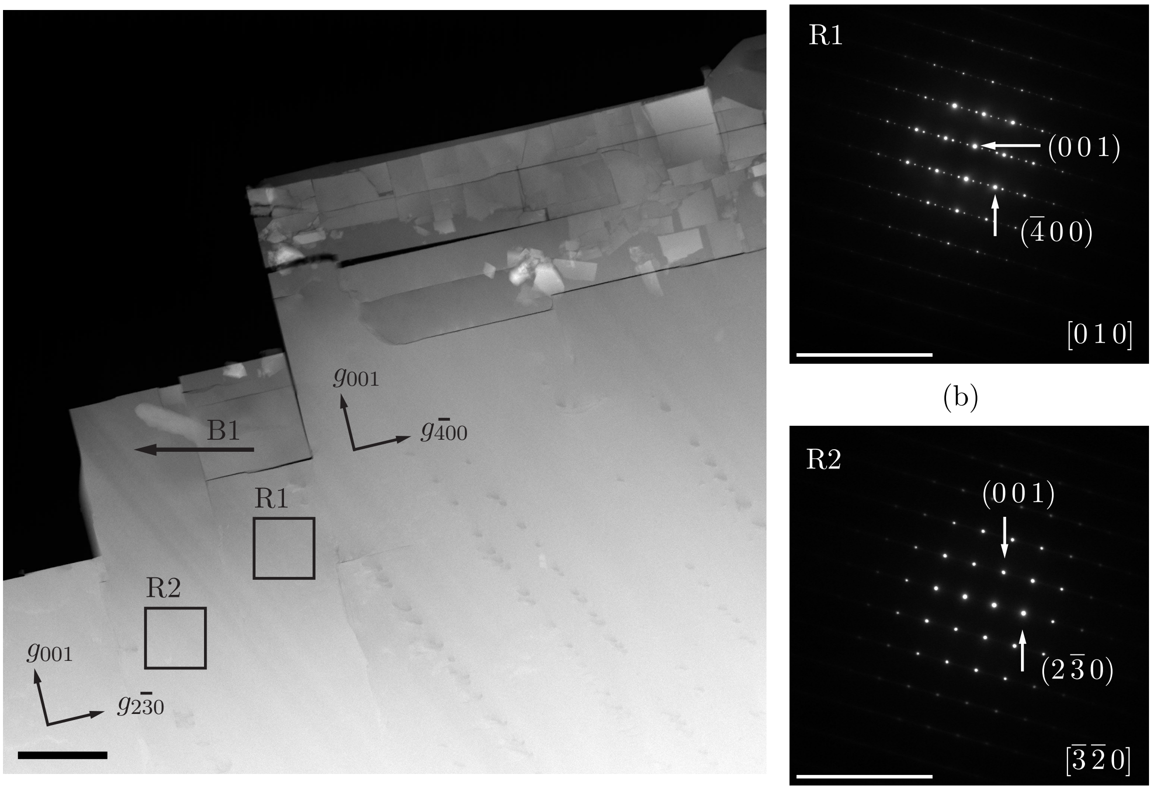

(b)

(a)

(c)

Figure 4.6: (a) HAADF STEM image of R1 and R2 separated by the band B1. (b, c) SAED patterns from R1 and R2 respectively, indicating that R1 and R2 are 120° twins. The scale bars are 1 µm on the HAADF STEM image, and 10 nm^{-1} on the SAED patterns. Note that the SAED patterns are rotated with respect to the STEM images, as indicated by the direction of g_{001} with respect to $(0\,0\,1)$.

---

[1] Although it might seem odd that the region on the left side of the band is denoted R2 and the region on the right side is denoted R1, it will become obvious why this definition has been chosen when the next band and region is introduced in figure 4.10.

[2] Notice that the crystallographic directions in the SAED patterns do not coincide with the directions indicated on the STEM image because the STEM images are rotated with respect to the SAED images.

The Kikuchi patterns and FOLZ SAED patterns from R1 and R2 are given in figure 4.7. Experimentally, some key characteristics of the $[0\,1\,0]$ and $[\bar{3}\,\bar{2}\,0]$ can be observed. The Kikuchi patterns of $[\bar{3}\,\bar{2}\,0]$ and $[0\,1\,0]$ zones display many of the same features. The main distinction between the two Kikuchi patterns is the higher visibility of the HOLZ and the Kikuchi lines in the $[0\,1\,0]$ pattern compared to the $[\bar{3}\,\bar{2}\,0]$. In the SAED patterns, the prime feature distinguishing the $[0\,1\,0]$ from $[\bar{3}\,\bar{2}\,0]$ is the number of reflections included perpendicular to the c-direction. For $[0\,1\,0]$, the $(1\,0\,0)$, $(2\,0\,0)$, $(3\,0\,0)$ and $(4\,0\,0)$ are all visible, while for $[\bar{3}\,\bar{2}\,0]$, the first reflection visible perpendicular to the c-direction is $(2\,\bar{3}\,0)$. Notice also that the reflections in the FOLZ do not directly coincide with the ZOLZ for either of the SAED patterns. The diameter of the FOLZ circle was measured to be 48.10 nm^{-1} in $[\bar{3}\,\bar{2}\,0]$, and 45.10 nm^{-1} in the $[0\,1\,0]$.

Figures 4.8 and 4.9 compare the experimental and simulated SAED, CBED and LACBED patterns at the $[\bar{3}\,\bar{2}\,0]$ and $[0\,1\,0]$ respectively. The CBED and LACBED patterns were acquired in slightly thicker regions than the SAED because the focused beam burned the specimen and caused beam damage at thin regions of the specimen.

The experimental SAED pattern in figure 4.8a matches the simulated pattern in figure 4.8b from R2 well. The main difference between them is the FOLZ diameter which is approximately 20 nm^{-1} in the simulated pattern, while it is approximately 48 nm^{-1} experimentally. The experimental and simulated LACBED patterns in figures 4.8c and 4.8d slightly deviate from each other, as the simulated pattern exhibits a single mirror line, while the experimental pattern displays a $2m$ symmetry . Many of the same features can be observed in the simulated and experimental LACBED micrographs, although the difference between them increases further out in reciprocal space. The experimental CBED pattern in figure 4.8e was acquired slightly off-zone. Still, a single mirror symmetry can be observed. The corresponding CBED pattern from the Bloch wave simulations is given in figure 4.8f. Notice the dissimilarities between the experimental and simulated patterns.

Figure 4.9 presents the SAED, LACBED and CBED patterns from R1 with corresponding simulated diffraction patterns at the $[0\,1\,0]$ zone. The experimental and simulated SAED patterns in figures 4.9a and 4.9b coincide well. The main dissimilarities between them is the absence of the $(1\,0\,0)$ and $(3\,0\,0)$ reflections in the simulated SAED patterns. The experimental and simulated LACBED patterns in figure 4.9c and 4.9d of the $[0\,1\,0]$ both display a $2m$ symmetry. However, it may be observed that the HOLZ lines do not directly coincide. The experimental CBED pattern in figure 4.9e can be observed to display one symmetry line, and the pattern matches well with both the Bloch wave and the multislice simulations in figures 4.9f and 4.9g.

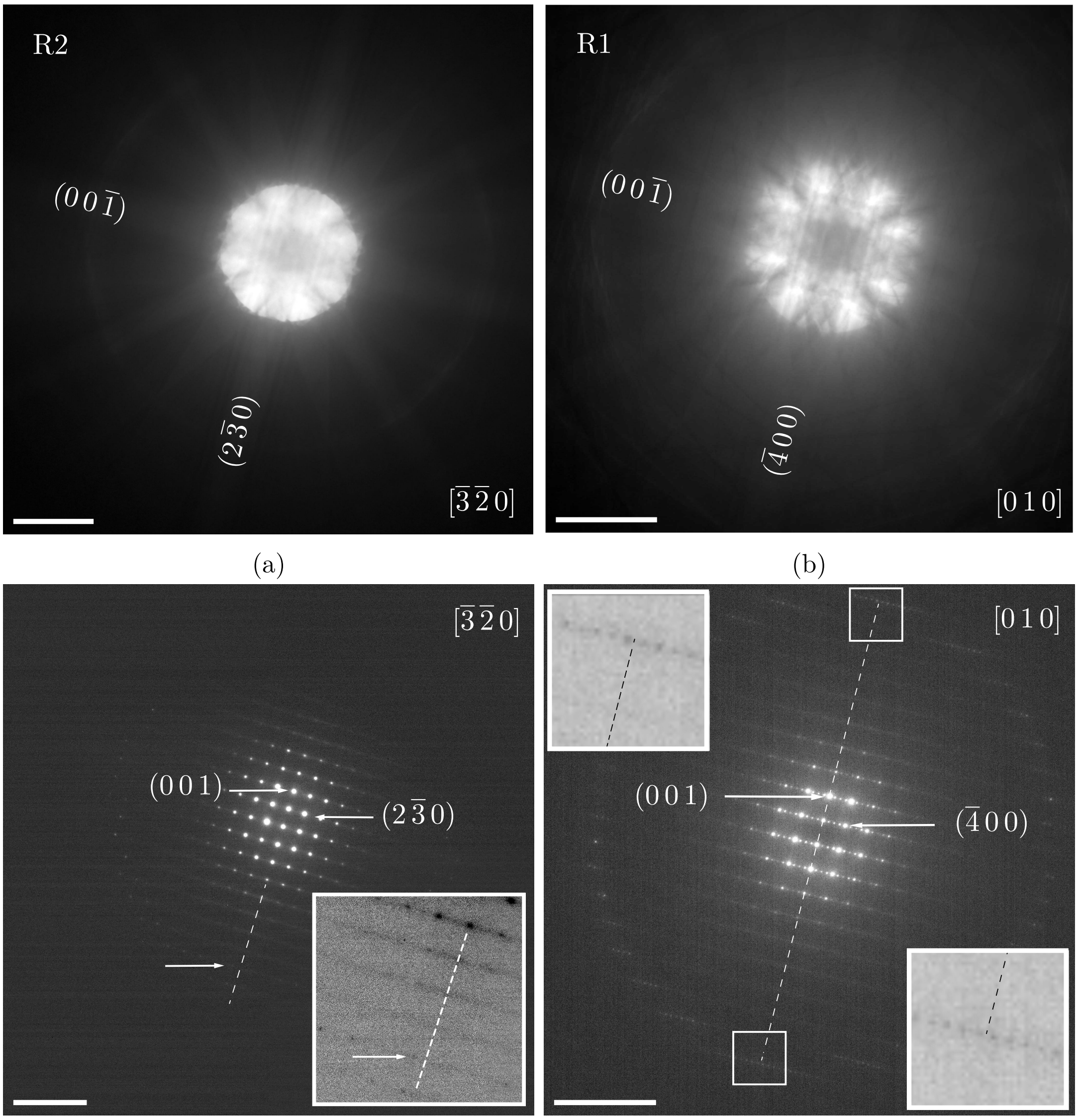

(a) (b)

(c) (d)

Figure 4.7: (a, b) The Kikuchi pattern of $[\bar{3}\,\bar{2}\,0]$ and $[0\,1\,0]$ acquired at R2 and R1 respectively. (c,d) Corresponding SAED patterns including the FOLZ reflections. The dashed lines are drawn between $(0\,0\,1)$ and $(0\,0\,\bar{1})$ and through $(0\,0\,0)$ to better visualise that the HOLZ does not coincide with FOLZ. The contrast of the enlarged images has been inverted to enhance the visibility of the FOLZ reflections. The scale bars are 10 nm^{-1}.

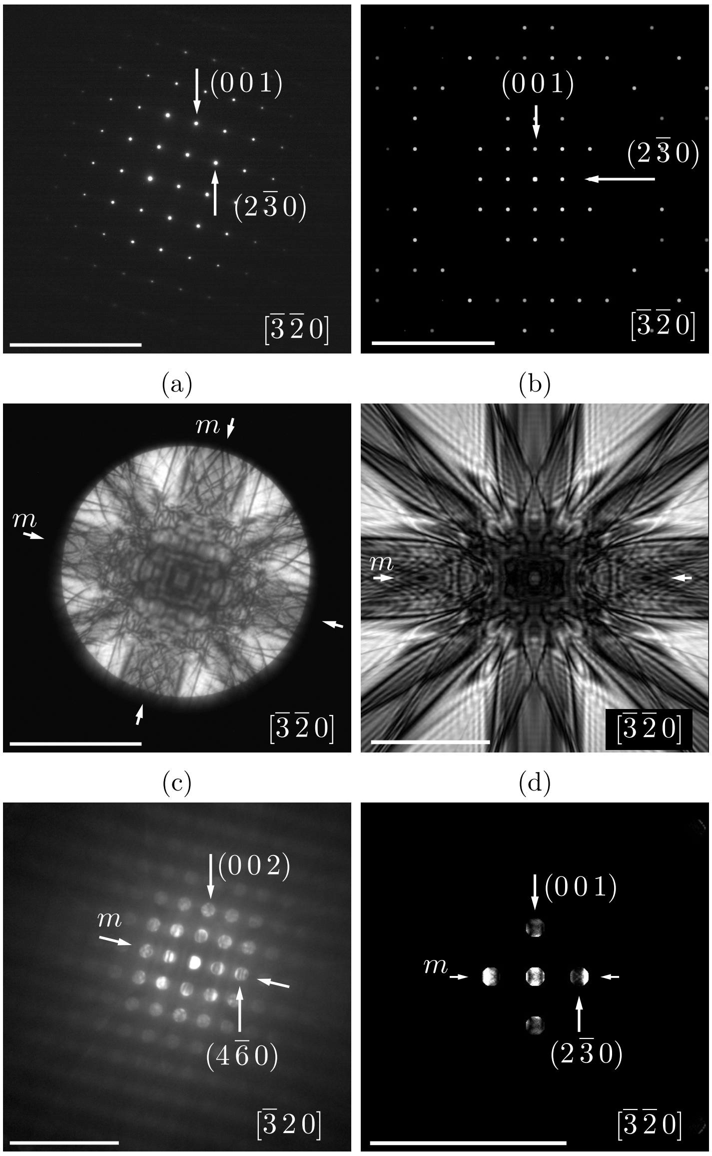

(a) (b)

(c) (d)

(e) (f)

Figure 4.8: (a, c, e) Experimental SAED, LACBED, and CBED patterns from R2 in figure 4.6, where the CBED pattern was acquired slightly off-zone. (b, d, f) Corresponding simulated SAED, LACBED and CBED patterns. The SAED pattern was simulated at a thickness of 200 nm, while the CBED and LACBED simulations correspond to a specimen thickness of 450 nm. The scale bars are 10 nm^{-1}.

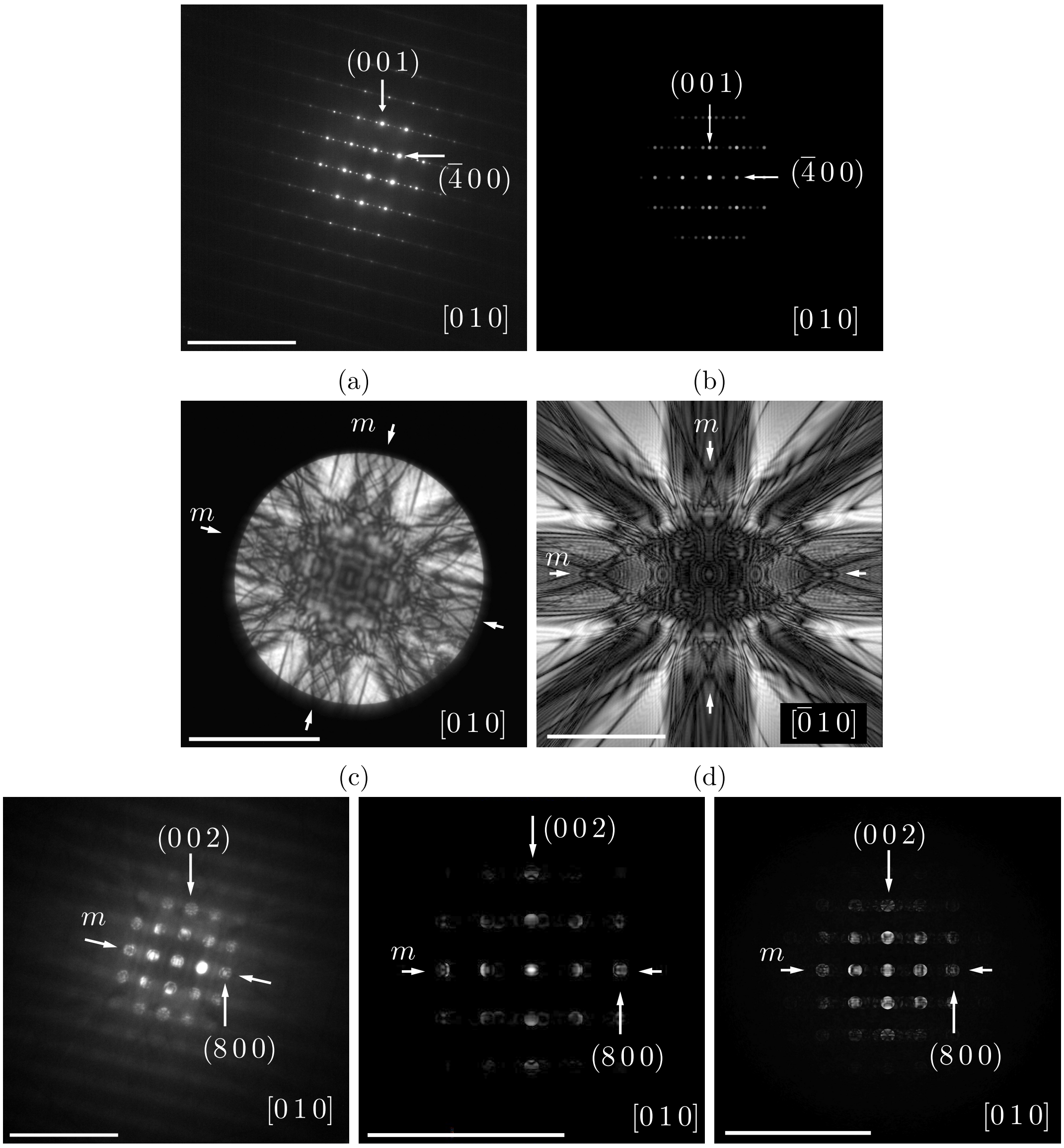

(a) (b)

(c) (d)

(e) (f) (g)

Figure 4.9: (a, c, e) Experimental SAED, LACBED, and CBED patterns from R1 indicated in figure 4.6. (b, d, f) Bloch wave simulations of the SAED, LACBED, and CBED patterns at 450 nm, 450 nm and 500 nm respectively. (g) Multislice [0 1 0] CBED simulation of a specimen thickness 500 nm. The scale bars are 10 nm^{-1}.

In addition to the two twin domains that were observed in figure 4.6, another set of structural domains were observed. These are presented in figure 4.10. The HAADF STEM image display two bands, but the structural analysis here is limited to the regions labelled R2 and R3 on either side of the band labelled B2, where R2 is the same region as previously presented in figure 4.6. [3]

Across the band, B2, a small structural reorientation was observed as a relative movement of the Kikuchi pattern along the weak $(2\,\overline{3}\,2)$ Kikuchi band. This may indicate that the crystal structure rotated about an axis perpendicular to the $(2\,\overline{3}\,2)$ plane. This is illustrated in figures 4.10c, 4.10d and 4.10e. Further, the bands run along $g_{2\bar{3}\bar{2}}$. The relative movement of the Kikuchi patterns can be translated to a 0.6° rotation from R3 to R2, and an intermediate 0.2° from R3 onto the band B2, suggesting that B2 is a low-angle grain boundary. HRTEM images on either side of the band are also given in figure 4.10a and 4.10b, with the $g_{2\bar{3}\bar{2}}$ direction indicated. In R2, the fringes are observed to periodically coincide with the $g_{2\bar{3}\bar{2}}$ direction, while in R3 the fringes almost coincide with the $g_{2\bar{3}\bar{2}}$ direction. The edge at B2 was too thick to acquire high-quality HRTEM images. The distance between lattice fringes in the HRTEM images were measured using Digital Micrograph and basic Fourier analysis. The lattice fringes repeat 0.42 nm in the $g_{2\bar{3}0}$ direction, where the distance between five fringes is similar to the size of the KNBO unit cell in the a-direciion; the 1.73-1.79 nm. The spacing between the lattice fringes in the g_{001} direction was measured to be 0.37-0.42 nm, in other words comparable to the size of the unit cell in the c-direction.

Figure 4.11 give auxiliary images to the relation between the SAED and Kikuchi patterns, and the relation between $g_{2\bar{3}\bar{2}}$ and the band observed in the HAADF STEM image given in figure 4.10. Figure 4.11a is a standard SAED image at the $[\overline{3}\,\overline{2}\,0]$ zone. This SAED has been superimposed on the Kikuchi pattern in R3 given in figure 4.10, but the image has been enlarged to ensure that the scale of the SAED and Kikuchi patterns are the same. The $(2\,\overline{3}\,2)$ Kikuchi band is indicated by the dashed beige arrow because it was too weak to resolve in the image, although clearly visible in the TEM. The Kikuchi band was indexed by determining the reflections that make a line perpendicular to the band, as illustrated in figure 4.11b. Figure 4.11c gives the HAADF STEM image in figure 4.10 with the SAED from 4.11a superimposed. The SAED was rotated to correct for the relative rotation of the HAADF STEM image with respect to the SAED pattern. Thus, it is evident that the bands run along $g_{2\bar{3}2}$. Note also that the twin boundaries were observed to run along the same direction.

---

[3] The regions R1, R2 and R3 refer to the extended regions between bands, and are not limited to the squares.

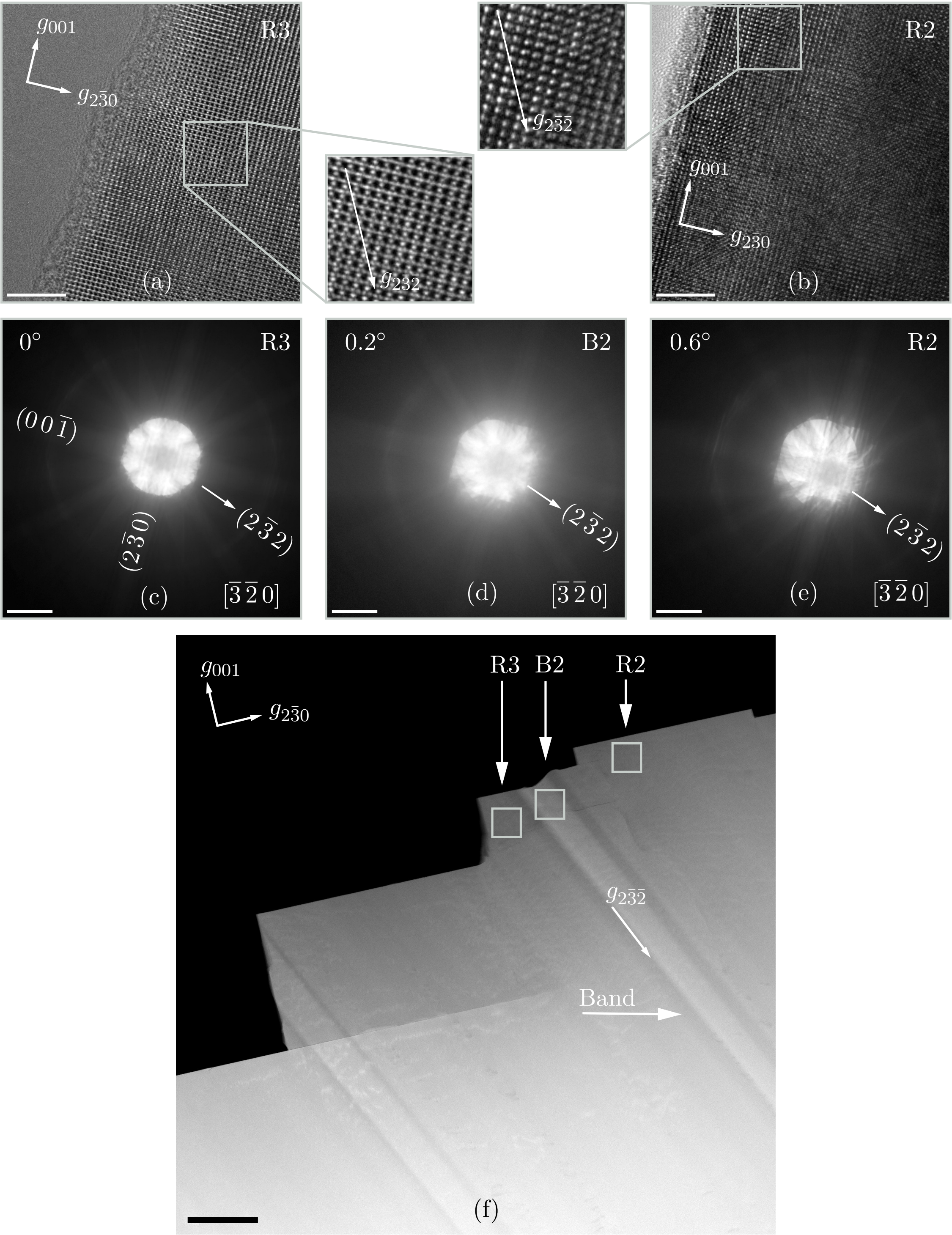

Figure 4.10: Figure showing two regions R2 and R3 of the specimen where the crystal structure slightly reorient across the band B2. (a, b) HRTEM images from R3 and R2, (c, d, e) Kikuchi patterns from R3, B2 and R2, and (f) an HAADF STEM image indicating the respective regions and the band. R2 is the same region as in figure 4.6. The scale bar on the HAADF STEM image is 1 µm, the scale bars on the Kikuchi patterns are 10 nm^{-1}, and the scale bars on the HRTEM images are 5 nm. Note that the HRTEM and Kikuchi patterns are rotated with respect to the STEM images, as indicated by the direction of g_{001} and $g_{2\bar{3}0}$.

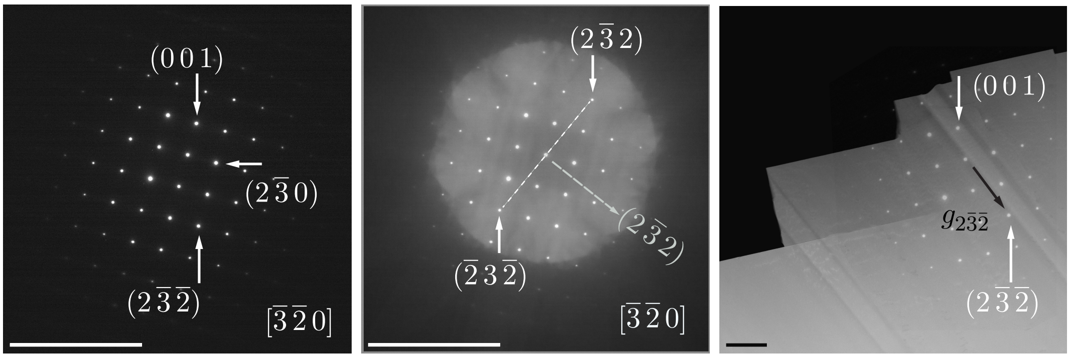

(a) (b) (c)

Figure 4.11: Auxiliary figures to figure 4.10. (a) SAED at $[\bar{3}\,\bar{2}\,0]$ observed in region R2. (b) The SAED from (a) superimposed on the Kikuchi pattern. The weak $(2\,\bar{3}\,2)$ Kikuchi band is perpendicular to the line drawn between the $(2\,\bar{3}\,2)$ and $(\bar{2}\,3\,\bar{2})$ diffraction spots, and has the general direction indicated by the dashed arrow. (c) The SAED from (a) superimposed on the HAADF STEM image, where the SAED pattern was rotated to correct for the relative rotation with respect the HAADF STEM image. The scale bars are (a, b) 10 nm^{-1} and (c) 1 µm.

Apart from this small shift of the Kikuchi pattern, no other changes were observed in the diffraction patterns at the $[\bar{3}\,\bar{2}\,0]$ zone axis. Hence, the SAED, CBED and LACBED patterns at this zone in region R3 were similar to those previously given in figure 4.8 for R2. In other words, the small rotation of the crystal structure could not be observed by the SAED or CBED pattern at the $[\bar{3}\,\bar{2}\,0]$ zone. Any SAED pattern in R2 and R3 displayed the same geometries and hence, the SAED acquired with a large field-limiting aperture including R2, R3, and B2 were also similar. In other words, the SAED pattern given in figure 4.11a is representative of both R2 and R3.

Interesting remarks can be made from the CBED patterns acquired from R2 and R3 at the $[\bar{7}\,\bar{6}\,0]$ zone. The SAED patterns from $[\bar{7}\,\bar{6}\,0]$ in region R3 and R2 are given in figure 4.12a and 4.12b respectively as a reference. The CBED patterns in R3 and R2 can be observed to be directly on-zone because of the recognisable features that are visible in both figures 4.12c and 4.12d. However, details in the central CBED disks revealed a small difference between the two patters. The light line observed in the (0 0 1) disk of the CBED pattern acquired from R3 appears dark in the CBED pattern from R2. This is indicated on the enlarged images of the CBED patterns in figures 4.12e and 4.12f.

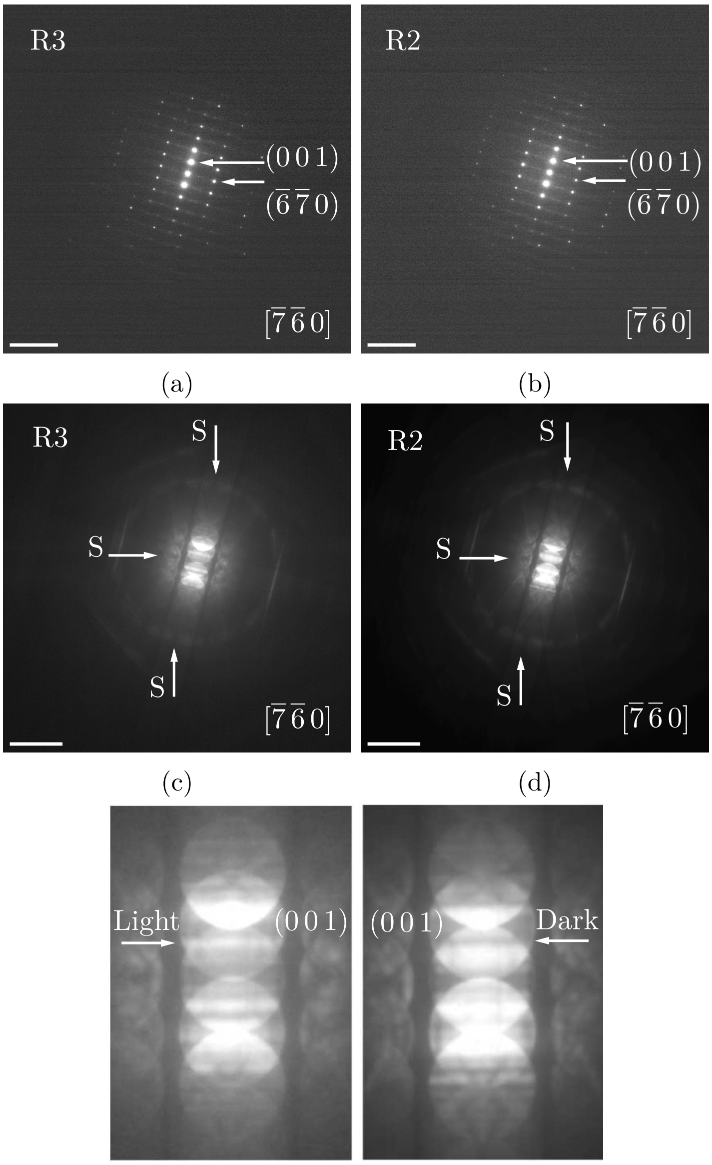

(a) (b)

(c) (d)

(e) (f)

Figure 4.12: (a, b) SAED from R3 and R2 in figure 4.10 acquired at the $[\bar{7}\,\bar{6}\,0]$ zone. (c-f) CBED at $[\bar{7}\,\bar{6}\,0]$ from R3 and R2 respectively, where (e, f) are enlarged images from (c, d). A line appearing light in the CBED pattern from R3 appears dark in the CBED pattern from R2. Features observed in both CBED patterns are marked S, as they can be thought of as "stationary features" indicating that both patterns were acquired on-zone. The scale bars are 10 nm^{-1}.

4.1.3.1 Remark on BF and DF TEM for structural domain imaging

BF and DF imaging were also assessed for possible domain inspections. The bands that were easily observed by HAADF STEM could be noticed by simple BF imaging with a large objective aperture if the specimen was oriented off-zone between $[\overline{3}\,\overline{2}\,0]$ and $[\overline{7}\,\overline{6}\,0]$. However, these bands appeared weaker when imaged by conventional BF TEM than by HAADF STEM. An example of a BF micrograph acquired off-zone is given in figure 4.13 for the band B2 previously presented in figure 4.10. The bands were however not visible when BF and DF images were acquired on-zone, as presented in figure 4.14 of the region where B1 was observed by HAADF STEM in figure 4.6. Hence, domain localisation can be performed by BF TEM, but may be less efficient than HAADF STEM.

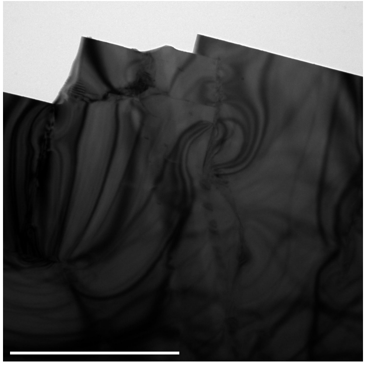

(a)

Figure 4.13: Off-zone BF TEM micrograph acquired with a large objective aperture in the region where R2, B2 and R3 were observed by HAADF STEM in figure 4.10. The scale bar is 1 µm.

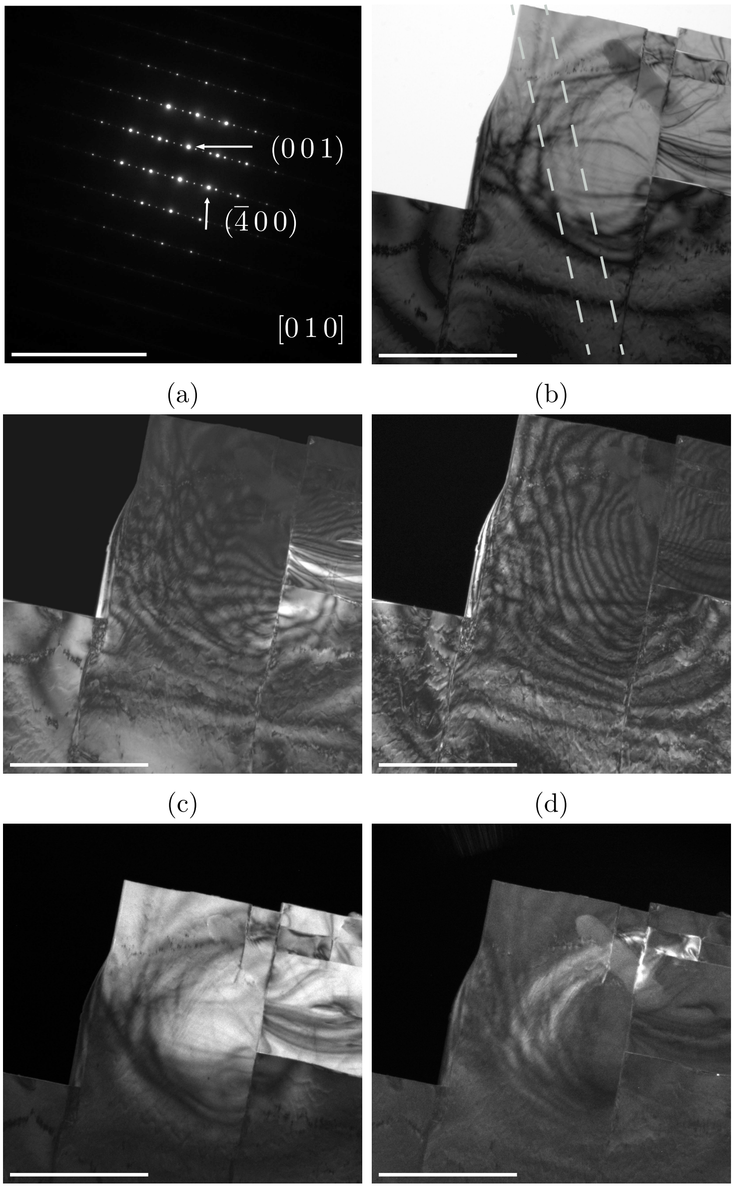

(a) (b)

(c) (d)

(e) (f)

Figure 4.14: (a) SAED pattern acquired from the same region as the BF and DF TEM images in (b-f). The BF and DF images were acquired where R1, B1, and R2 were observed by HAADF STEM in figure 4.6. (b) On-zone BF TEM image where the dashed lines indicate where B2 was expected. (c-f) DF micrographs where the objective aperture was inserted about the $(\bar{4}\,0\,0)$, $(0\,0\,1)$, $(2\,0\,0)$, and $(\bar{2}\,0\,\bar{1})$ reflections respectively. The scale bars are 1 µm.

4.1.3.2 PFM

PFM measurements from the *c*-axis in-plane specimen were acquired in the same area as inspected in the TEM, and are given in figure 4.15. The height profile of the specimen is given in figure 4.15a, where the height is observed to vary approximately 20 nm within a region of approximately 30 × 20 µm. The in-plane and out-of-plane piezo-response are given in figures 4.15b and 4.15c respectively. The only piezo-response that was observed varied with the height profile of the specimen, hence indicating the absence of polar domains.

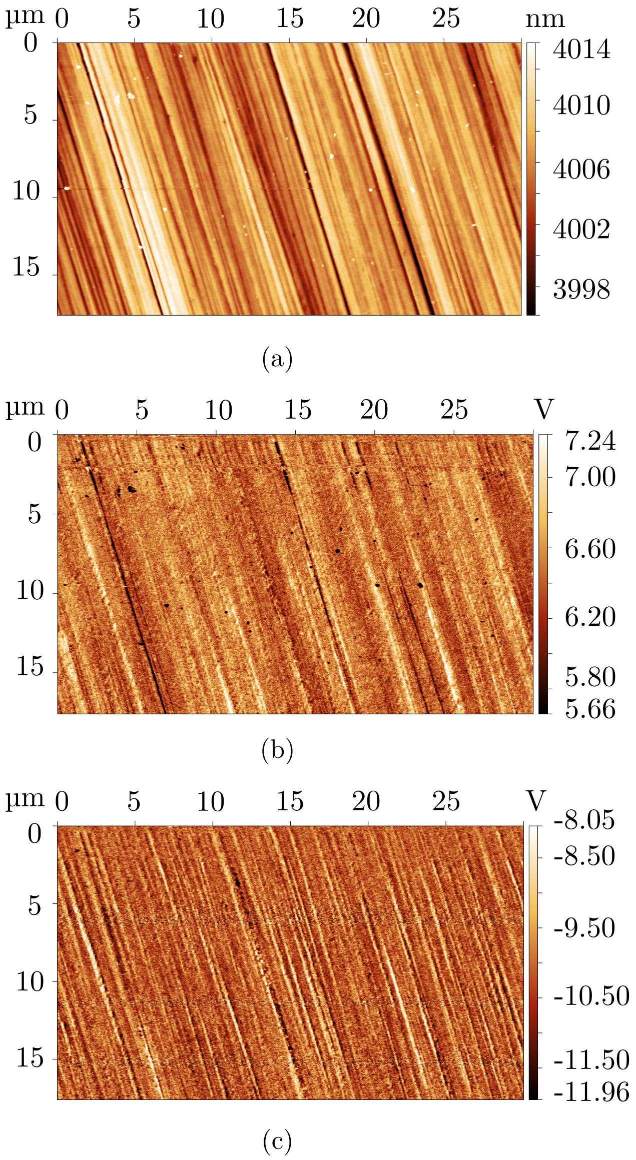

(a)

(b)

(c)

Figure 4.15: Calibrated PFM measurements of the *c*-axis in-plane specimen. (a) Height profile, (b) in-plane piezo-response, and (c) out-of-plane piezo-response.

4.2 *c*-axis out-of-plane specimen

This section presents the structural analysis of the *c*-axis out-of-plane specimen in an effort to correctly assign the crystallographic directions, and PFM measurements to confirm the presence or absence of polar domains.

4.2.1 Structure determination

Overview images from the region where the structural analysis was performed are given in figure 4.16. HRTEM and HR-HAADF STEM images were acquired in the region labelled HR, while SAED and CBED thickness series were performed in the region labelled ED. LACBED patterns were obtained in a region close to ED. Notice also the large number of defects present and fracturing along random crystallographic planes in the specimen that are easily recognized in the TEM image in figure 4.16c.

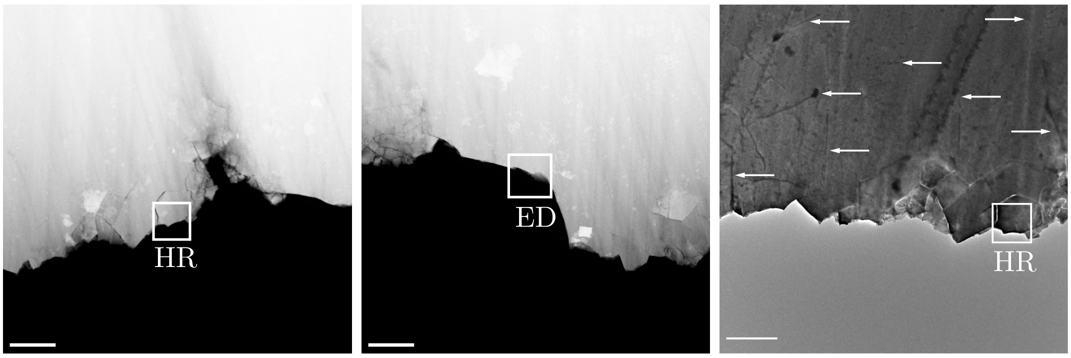

(a) (b) (c)

Figure 4.16: (a, b) HAADF STEM images from regions where the structural analysis of the *c*-axis out-of-plane specimen were performed. The region labelled HR is where HR(S)TEM images were acquired, and the region labelled ED shows where diffraction experiments were conducted in a thickness series. (c) Conventional TEM image where no objective aperture was used. Several fractures and defects are indicated by the arrows. The region labelled HR is shown for reference. The scale bars are 1 µm.

Experimental CBED patterns acquired with the CCD camera and Merlin detector are given in figure 4.17. Figures 4.17a and 4.17b are CBED patterns at the same specimen thickness with the CCD and Merlin detector respectively. The multislice simulation at a specimen thickness of 40 nm match these patterns well, as given in figure 4.17c. Experimental CBED patterns at a slightly thicker region are given in figures 4.17d and 4.17e, and a matching multislice simulation is given in figure 4.17f at a specimen thickness of 200 nm.

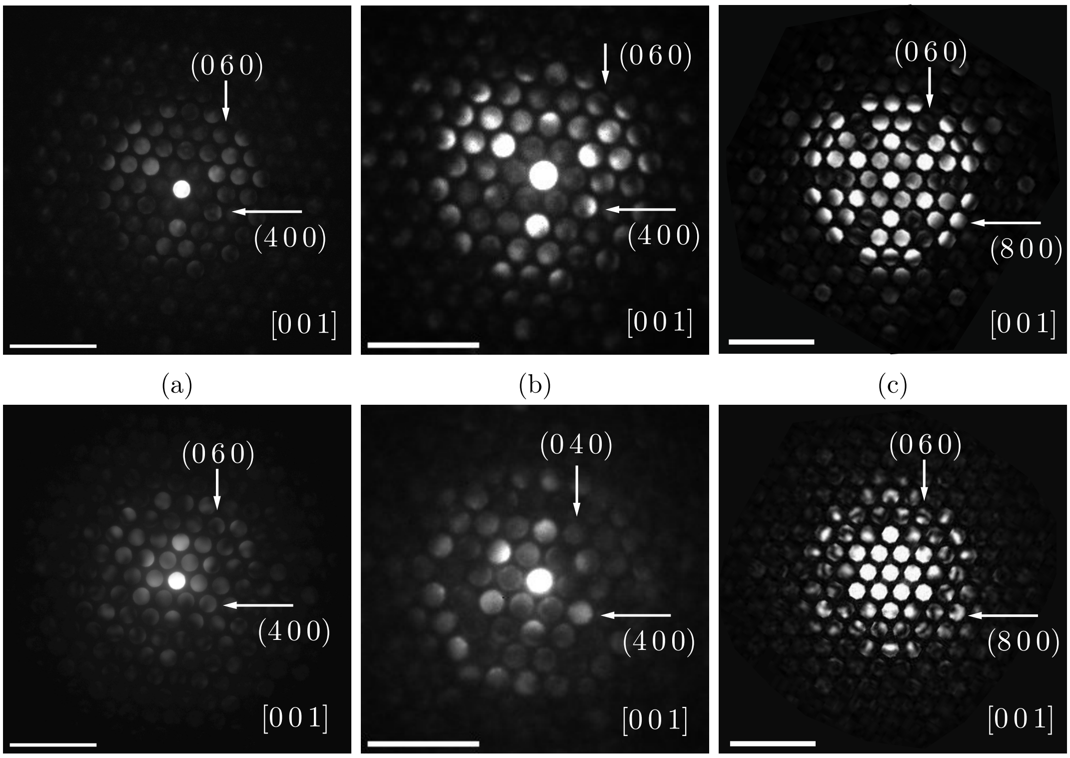

(a) (b) (c)

(d) (e) (f)

Figure 4.17: CBED patterns from the same region as annotated in figure 4.16b, acquired with (a, d) the CCD and (b, e) the Merlin detector. (c, f) Multislice simulations of [0 0 1] at a thickness of 40 nm and 200 nm respectively. (a, b) were acquired at in the same area and match the multislice simulation in (c), and (d, e) in a thicker area and match the multislice simulation in (f). The gamma value was altered to enhance features in the patterns acquired with the CCD. The scale bars are 5 nm^{-1}.

The experimental and multislice CBED patterns display almost the same symmmetry, where the symmetry of the experimental CBED patterns are $3m$, while the multislice simulations are close to $3m$. The $3m$ symmetry in the multislice simulations are only broken by the small difference in the relative distance between the direct beam and the (4 0 0), $(\bar{2}\,\bar{3}\,0)$ and $(2\,\bar{3}\,0)$ reflections, as given in table 4.3. However, this does not match the experimental data, where the distances between these reflections and the direct beam are the same. Hence, there are three possible indexing schemes matching the experimental data. The indexing scheme with the g_{400} direction approximately perpendicular to the wedge of the specimen was chosen, as shown in figure 4.17.

Bloch wave simulations from JEMS are shown in figure 4.18. These simulations predict that the $(\bar{2}\,\bar{3}\,0)$, $(\bar{2}\,3\,0)$ and (4 0 0) reflections are positioned at equal relative distances from the direct beam, as presented in table 4.3, and an angle 120° apart. Hence, the simulations match what was experimentally observed. Most of the simulated CBED patterns in figure 4.18 display a $3m$ symmetry. At specific specimen thicknesses, the $3m$ symmetry is only broken by small intensity variations within the CBED disks. In the range of 50 – 500nm, only the CBED patterns at 250, 300 and 400 nm were observed to display a single mirror line. Although the experimental CBED patterns in figure 4.17 display some intensity variations within the $+g$ and $-g$ CBED disks, none of these intensity variations can be used to define the crystal orientation unambiguously.

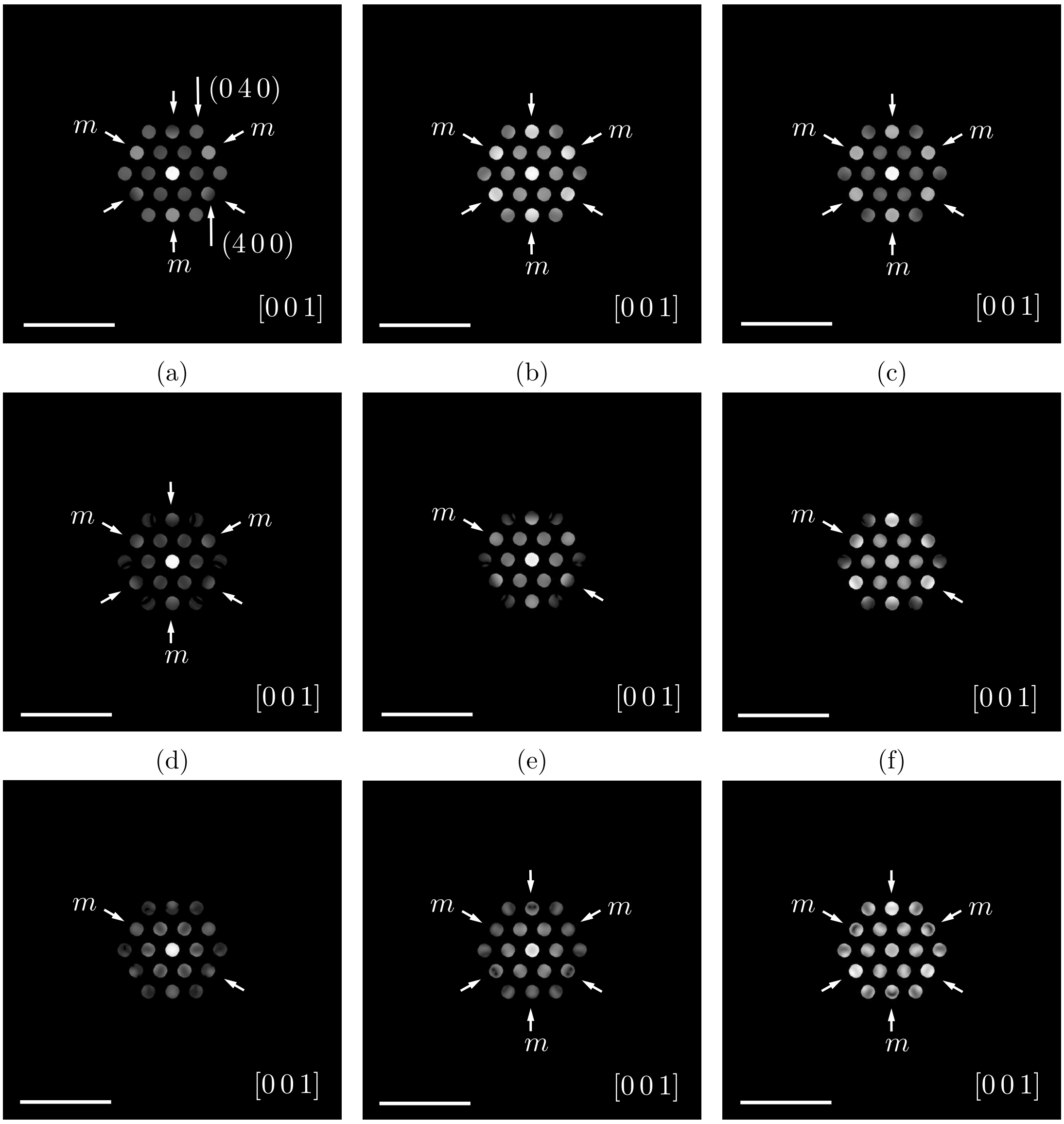

(a) (b) (c)

(d) (e) (f)

(g) (h) (i)

Figure 4.18: Simulated CBED thickness series with the Bloch wave algortihm in JEMS at (a-i) 50 nm, 100 nm, 150 nm, 200 nm, 250 nm, 300 nm, 400 nm, 450 nm, and 500 nm respectively. The indexing in (a) follows for (b-i) as well. The scale bars are 5 nm^{-1}.

Table 4.3: Relative distances between the (4 0 0), ($\bar{2}\,\bar{3}\,0$) and ($\bar{2}\,3\,0$) spots in the experimental CBED pattern, multislice simulations and Bloch wave simulations in JEMS in the [0 0 1] zone.

	Experimental	Bloch wave simulations (JEMS)	Multislice simulations
$d_{400}/d_{\bar{2}30}$	1.00	0.99	1.04
$d_{400}/d_{\bar{2}\bar{3}0}$	1.00	0.99	1.04
$d_{\bar{2}\bar{3}0}/d_{\bar{2}30}$	1.00	1	1.00

Experimental and simulated LACBED patterns from the [0 0 1] zone are given in figure 4.19a and 4.19b respectively. The LACBED simulation that matched the experimental data best was simulated at 400 nm, and display a 6*mm* symmetry. In the experimental LACBED pattern, dark defect lines from line-defects and dislocations can be observed. These lines break the symmetry of the HOLZ lines, hence making it difficult to assess crystallographic symmetry. If the defect lines are disregarded, the symmetry of the experimental LACBED pattern resembles 6*mm*. A simulated SAED pattern at the same thickness is included for reference of the crystal orientation in figure 4.19c.

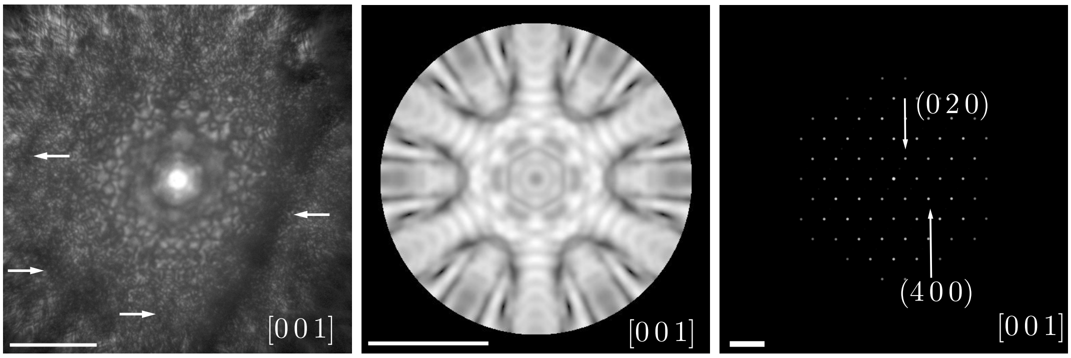

(a) (b) (c)

Figure 4.19: (a) Experimental LACBED patterns of the *c*-axis out-of-plane specimen. The arrows indicate defect lines. (b) Simulated LACBED pattern at 400 nm. (c) Auxiliary simulated SAED pattern at 400 nm as a reference for crystal orientation. The scale bars are 5 nm^{-1}.

Selected diffraction patterns from the experimental and simulated SAED thickness series are given in figure 4.20. The experimetnal patterns were only acquired with the Merlin detector because the specimen suffered from extensive charging and moved when SAED patterns were acquired close to the wedge. Figure 4.20a, 4.20c, and 4.20e give the experimental SAED patterns from increasingly thicker regions. The simulations that matched the experimental patterns best are given in figure 4.20b, 4.20d and 4.20f at a thickness of 100 nm, 400 nm and 500 nm respectively. Notice that the intensity distribution between the diffraction spots change with the thickness.

The SAED simulations predicted that additional weak spots would uniquely appear between the (0 2 0) and (4 0 0) at 400 and 500 nm, as indicated by the arrow heads on the insets in figures 4.20d and 4.20f, but not in between the $(\bar{2}\,\bar{3}\,0)$, $(\bar{2}\,3\,0)$, (2 1 0), and $(2\,\bar{1}\,0)$ spots. Although the experimental SAED experiments were gradually performed at thicker areas of the specimen, no such additional spots were observed as the specimen thickness increased. Instead, a diffuse background began to appear, as shown in figure 4.20e. Hence, (0 1 0) and (2 0 0) spots could not be resolved. The experimental SAED patterns are therefore indexed according to the scheme where the g_{400} direction is approximately parallel to the wedge of the specimen, although the experimental data do not provide enough information to uniquely define the crystal orientation.

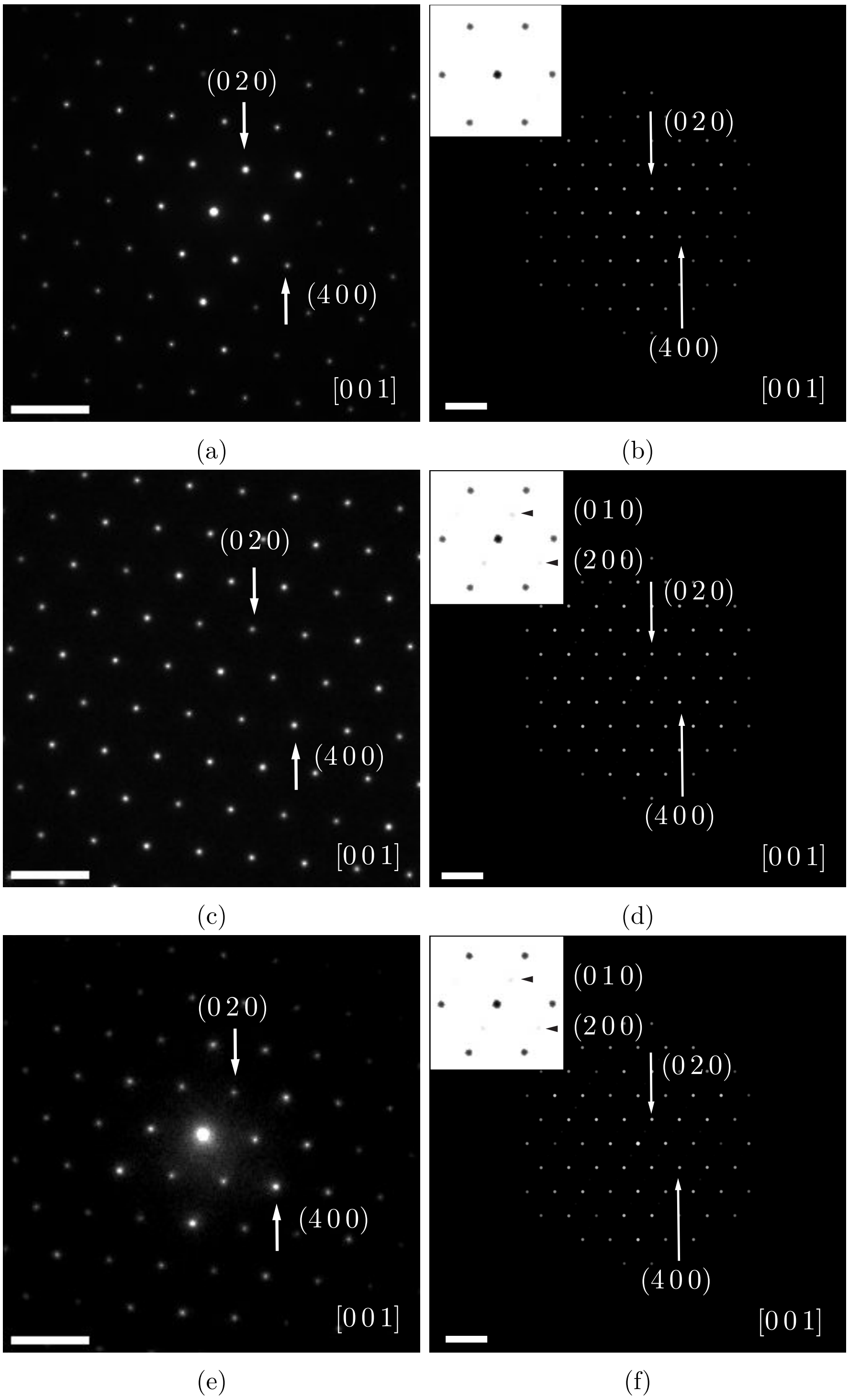

(a) (b) (c) (d) (e) (f)

Figure 4.20: (a, c, e) SAED patterns acquired at increasingly thicker regions of the specimen in the [0 0 1] zone axis in the region annotated in figure 4.16b. (b, d, f) Corresponding dynamical Bloch wave simulations from JEMS that matched the SAED images best at 100, 400 and 500 nm respectively. The insets in (b, d, f) show the surrounding spots to the direct beam. The colour was inverted to enhance the visibility of the weak additional (0 1 0) and (2 0 0) spots in (e) and (f) as indicated by the arrow heads. The scale bars are 2 nm^{-1}.

Figure 4.21 presents the HRTEM and HR-HAADF STEM images acquired from the *c*-axis out-of-plane specimen. A hexagonal fringe pattern can be observed, where each dot in the fringe-pattern is related to a niobate triplet in the KNBO unit cell. In figures 4.21a and 4.21b, one can almost separate the three individual niobate octahedra in the triplets, as observed by the v-shaped dots in the fringe pattern. The two images in figures 4.21a and 4.21b were acquired at two different defocus values, and the v-shaped fringes can be observed to be flipped with respect to each other as a result of the phase contrast. HR-HAADF STEM images were acquired in an attempt to image the individual niobate octahedra directly, as shown in figure 4.21c. However, a high enough resolution could not be achieved, probably due to surface relaxation or surface damage.

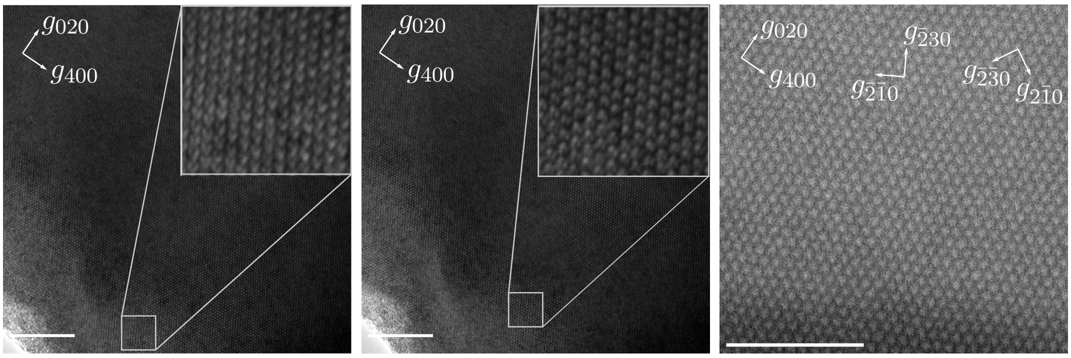

(a) (b) (c)

Figure 4.21: HR-images acquired in the region annotated in figure 4.16a. (a, b) HRTEM images acquired at two different defocus values. The single niobate octohedra in the triplets are almost resolved, and can be observed as v-shaped dots in the fringe-pattern. The v-shaped fringes in (a) and (b) are switched as a result of a slight change in the defocus. (c) HR-HAADF HRSTEM image attempted to resolve the correct orientation of the niobate triplets, but the single niobate octahedra could not be resolved. The scale bars in (a) and (b) are 20 nm, and the scale bar in (c) is 10 nm.

The distance between three lattice fringes in the g_{400}, $g_{\bar{2}\bar{3}0}$ and $g_{\bar{2}30}$ were measured to be 17.47 – 17.62 Å, and the distance between two lattice fringes in the g_{020}, $g_{\bar{2}\bar{1}0}$ and $g_{2\bar{1}0}$ were measured to be 15.06 – 15.55 Å. One pixel on the image is 0.53 Å, and thus this variation in the unit cell dimensions are within the dimensional limit of the image.[4] Hence, the distance between the abovementioned fringes all coincide with the unit cell parameters, and the HRTEM images cannot be used to assess the real *a*- and *b*-directions of the crystal at the [0 0 1] zone axis.

---

[4] Although one pixel was assessed to be 0.53 Å, this does not mean that the resolution is 0.53 Å.

4.2.2 Correlated microscopy

The correlated microscopy included PLM and PFM. The PLM and PFM micrographs are given in figure 4.22, where the PLM micrograph in figure 4.22a was acquired in the project preceeding this thesis [1]. The structural inspection outlined above were performed in an area close to domain 1 indicated on the PLM micrograph. However, the specimen fractured when the PFM tip was scanned across that area. Hence, the height profile and piezo-response micrographs in figures 4.22b and 4.22c were acquired in area 3. Two distinct polar regions can be observed from the PFM image. Additionally, the measured piezo-response does not overlap with the height profile of the specimen, and can therefore be assumed to image the ferroelastic domain labelled 3 on the PLM micrograph. Hence, PFM confirmed the presence of polar domains in the *c*-axis out-of-plane specimen. Please note that any rotation or flipping of the specimen has not been corrected for, which is why the bands on the PLM images and PFM images are not observed in the same direction.

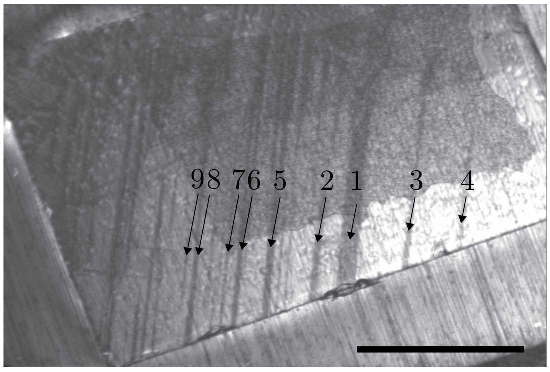

(a)

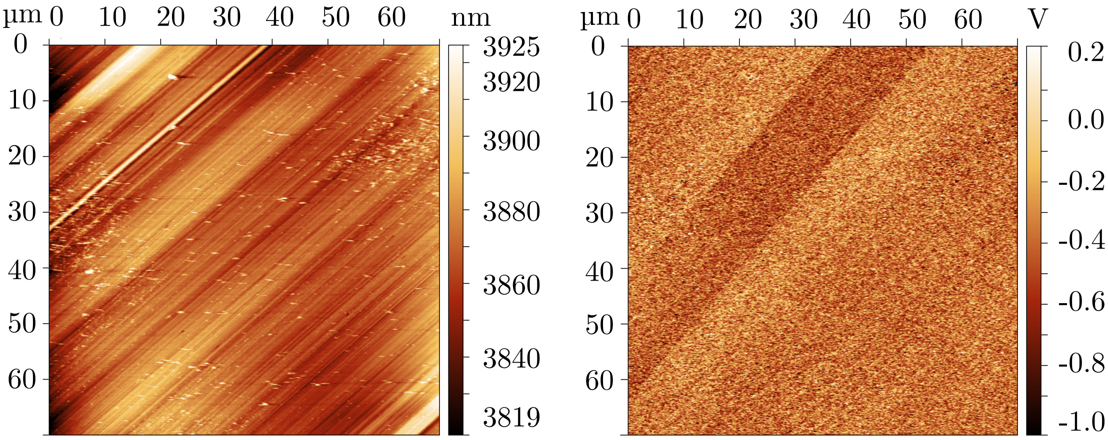

(b)

(c)

Figure 4.22: Correlated microscopy of the *c*-axis out-of-plane specimen. (a) PLM, (b) the height profile from the PFM measurements, and (c) piezo-response from the PFM measurements. The domain wall imaged by PFM corresponds to area 3 in the PLM image. The PLM image is reprinted from the project predeeding this thesis [1], and the scale bar is 500 µm. The piezo-response was not calibrated.

5 Discussion

Several interesting results were obtained from the structural analysis of KNBO thin films and its domain structures. This section will present a discussion on these curious and somewhat confusing results, where the *c*-axis in-plane specimen and *c*-axis out-of-plane specimen are discussed simultaneously as the impacts of specimen preparation, structural analysis and correlated microscopy techniques for ferroic domain inspections are presented.

First, the specimen preparation will be considered, including a discussion on beam damage, charging, and correspondingly induced defects on the TEM inspections of KNBO. Furthermore, several of the results indicate that thin film KNBO prepared by mechanical polishing is described by another crystal structure than that of bulk KNBO. A section is therefore dedicated to a discussion on the crystal structure analysis, the complex diffraction properties of KNBO, possible explanations for crystal restructuring, and important implications for deducing the correct crystal structure of thin film KNBO. Additionally, the simulated CBED patterns from the Bloch wave and multislice simulations were observed to differ, not only from the experimental CBED patterns, but also with respect to each other. A section is therefore dedicated to explaining possible factors causing the discrepancies between the experimental CBED patterns, the Bloch wave simulations, and the multislice simulations. After this, the domain inspections of KNBO are considered, including the PFM measurements of both specimens and the TEM inspections of the *c*-axis in-plane specimen. This will include an analysis of the domain boundaries and the two categories of structural domains observed. Finally, a section is dedicated to exploring the optimal framework for domain inspections of KNBO, and how it may be optimised further.

5.1 Specimen preparation and behaviour in the TEM

The mechanical polishing scheme for preparing TEM specimens from bulk KNBO has been shown to produce large, high-quality TEM specimens. Especially, a procedure for preparing specimens with the *c*-axis in-plane was successfully developed, as it allowed for the inspection of several structural domains. However, as shown in Section 4.1, dislocation loops and line defects could be observed on the *c*-axis in-plane specimen. Such dislocation loops and line defects were previously also reported in the *c*-axis out-of-plane specimen in the related project work by the same author and in the master's thesis of Ryggetangen [1, 45]. The large presence of dislocation loops and defects may therefore indicate that the polishing scheme induces structural defects and strain in the specimen.

In addition to the induced defects, the TEM inspections also indicate that KNBO preferably fracture in a rectangular pattern when prepared in a facet with the *c*-axis in-plane. As shown in figure 4.2, cleaving was observed along the *c*-plane and planes perpendicular to the *c*-plane, such as the $(4\,0\,0)$ and $(2\,\overline{3}\,0)$ planes. Contrarily, the *c*-axis out-of-plane specimen was observed to be fractured along random crystallographic directions, as could be easily observed in figure 4.16. Cleaving and other forms of fracturing are not desirable because it may prevent the specimen from being thinned sufficiently at the edges during mechanical polishing, and it may lead to easier fracturing during scanning probe microscopy techniques such as PFM. Fracturing was most prominent in thin regions of both specimens. Additionally, the *c*-axis out-of-plane specimen appeared to contain more defects than the *c*-axis in-plane specimen, while the *c*-axis in-plane specimen appeared to be more fractured at the edges than the *c*-axis out-of-plane specimen. Thus, the polishing scheme induced cleaving and other defects that may be characteristic for the plane that is polished.

Fracturing and crystal defects are highly undesirable because a thin monocrystalline region is essential for obtaining high-quality diffraction patters, HRTEM and HRSTEM micrographs, and avoiding several aberrations, as described in Section 2.5. Additionally, a tilt series would become exceedingly more tedious if the crystal orientation changes slightly due to fractures. Similarly, the location of possible structural and ferroic domains become harder to trace and identify if the region of interest has fractured. This is because the reorientation of the fractured regions must also be considered when assessing the diffraction patterns. Large defect-free specimen areas are also essential for proper symmetry assessment with CBED and LACBED, as any defects in the specimen may cause symmetry breaking that may confuse crystallographic assessment. Thus, the large occurrence of fractures, dislocation loops and other defects in the specimens complicated symmetry considerations in the CBED and LACBED analysis, as will be further described in Section 5.2. Henceforth, alternative methods for specimen preparation should be considered, as a large single-crystal with few-to-no fractures or defects is highly desirable when inspecting possible structural or ferroic domains. Specific suggestions will be given in Chapter 6 on future work.

The STEM images of the *c*-axis in-plane specimen in figure 4.2 also imply that KNBO is susceptible to beam damage if the electron beam is focused on the specimen over a period of time. This is undesirable, as it may indicate that the crystal structure may be slightly altered by the high-energy electron beam. While carrying out the experiments, it was also experienced that the beam burned the specimens in the thinnest regions of the specimen, making them amorphous in certain areas. This was especially prominent when performing experiments with the *JEOL JEM-2100F*, which is equipped with a field-emission gun. A more prominent example is also given in figure 5.1, where the *c*-axis out-of-plane specimen was observed to be damaged after carrying out the CBED thickness series in the same region.

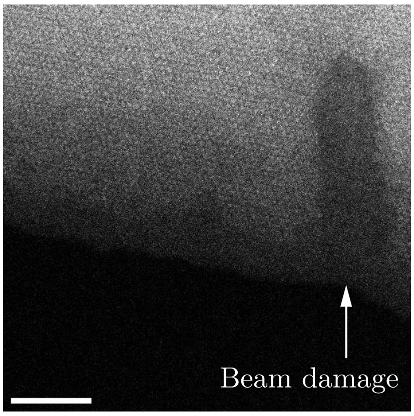

Figure 5.1: HRSTEM image showing the presence of beam damage in the *c*-axis out-of-plane specimen caused by the CBED thickness series. The scale bar is 10 nm.

Additionally, the specimens were susceptible to charging when performing SAED and HRTEM experiments at the thinnest regions of both specimens especially with the *JEOL JEM-2100F* microscope. These issues were partly solved by acquiring the SAED patterns with the Merlin quantum detector and acquiring the HRTEM images in view-mode rather than the acquire-mode. Albeit, it underlines the susceptibility of the poorly conducting KNBO specimen to charging. Hence, solutions to reduce charging should be considered, such as low-dose (S)TEM techniques, to improve the practicalities of the TEM work [76, 77].

In summary, TEM specimens with the *c*-axis in-plane and the *c*-axis out-of-plane were readily prepared by mechanical polishing. Although the structural analysis and domain inspections of KNBO were complicated by the presence of defects and cleaved regions, the characterisation of KNBO was still achievable because the large wedge ensured that at least one region of the specimen had a sufficiently low density of defects and was thin enough for structural analysis. Correlated approaches for domain inspections were readily performed both before specimen preparation with PLM, but also after specimen preparation with PFM. However, this study has shown that special care must be taken while performing correlated microscopy after TEM specimen preparation to avoid further fracturing of the specimen, and that the challenges related to the beam sensitivity of KNBO needs to be tackled.

5.2 Structural analysis of KNBO

As described in Section 2.6, the existing literature on KNBO reports disagreements on the crystal structure and ferroic properties of KNBO. TEM analysis has previously not been widely reported, and a detailed structural characterisation of planar defects such as twins and domain walls have been lacking. That was the starting point prior to this study. The structural analysis given in Section 4.1.2 and 4.2.1 produced a new set of conflicting results that have raised further questions on the true crystal structure of thin film KNBO. These conflicting results will be discussed in this section.

As presented in Section 4.1.2, the zones from the experimental tilt series of the *c*-axis in-plane specimen were observed to match the [$\bar{3}\,\bar{2}\,0$] and surrounding zones best. Still, some of the simulated neighboring zones to [$\bar{3}\,\bar{2}\,0$] in a simulated tilt series were observed to severely deviate from the experimental patterns, as observed in figures 4.4 and 4.5, and in table 4.2. The simulations indicated that there would be a distinct difference between the SAED patterns of the [$\bar{7}\,\bar{6}\,0$] and [$\bar{2}\,\bar{1}\,0$] zones, but experimentally these two zones were mirrors of each other. This is illustrated in figure 5.2 for the two zones closest to [$\bar{3}\,\bar{2}\,0$], where the experimental and simulated patterns are compared. Hence, the experimental tilt series indicate that the geometry of the zones about [$\bar{3}\,\bar{2}\,0$] are less distinguishable than those simulated. Additionally, the angle between the given zones are slightly larger experimentally than what was suggested by the simulations. This may suggest that the thin KNBO TEM specimen had a crystal structure that is less anisotropic than that of bulk KNBO. In other words, the *a* and *b* axes of the thin film KNBO are more similar than in the bulk model structure.

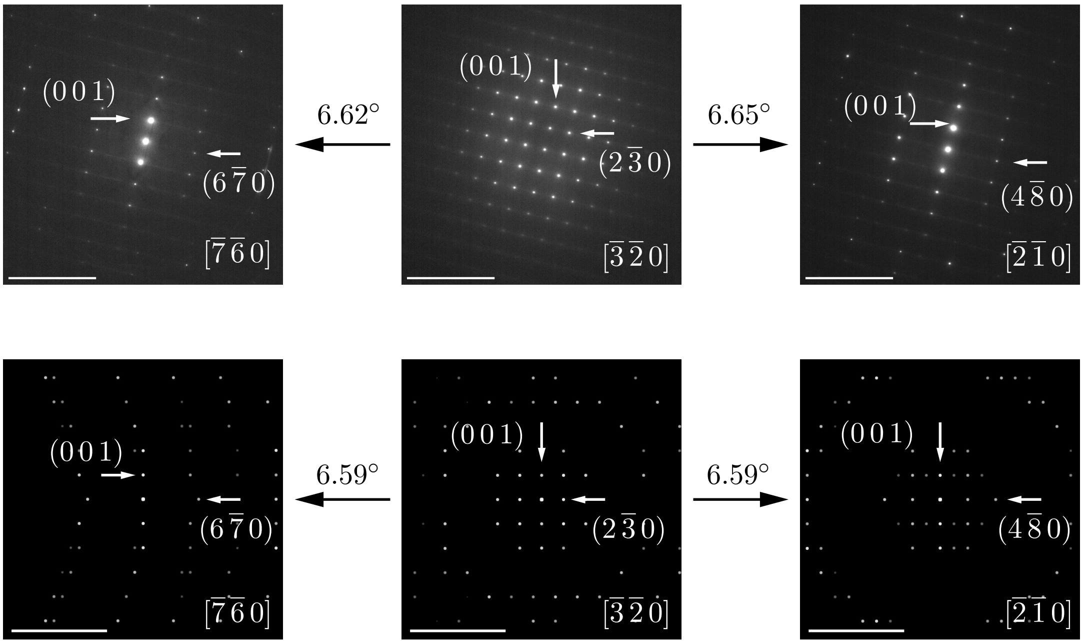

Figure 5.2: Comparison between the experimental (top) and simulated (bottom) [$\bar{7}\,\bar{6}\,0$], [$\bar{3}\,\bar{2}\,0$], and [$\bar{2}\,\bar{1}\,0$] SAED patterns. The Bloch wave simulations are reprinted from figure 4.5 for a crystal thickness of 200 nm. The angle between the zones are also indicated. The scale bars are 10 nm^{-1}.

Moreover, the reflections in the FOLZ did not directly coincide with the ZOLZ in neither $[\bar{3}\,\bar{2}\,0]$ nor $[0\,1\,0]$, as presented in figure 4.7. According to Fultz and Howe, a simple rule of thumb is that the FOLZ should directly coincide with the ZOLZ in the diffraction pattern from a low index zone in an orthorhombic crystal that has a primitive unit cell [28]. However, this was not observed experimentally for KNBO. Contrarily, the experimental FOLZ SAED pattern resembles the FOLZ pattern of a base-centered unit cell as presented by Fultz and Howe [28]. Thus, based on the simple rule of thumb, the FOLZ pattern of the $[0\,1\,0]$ may indicate that the crystal structure of thin film KNBO is base-centered rather than primitive as bulk KNBO has been determined to be. As presented in Section 2.6, other literature has suggested that KNBO may be described by another space group than the currently acknowledged $P2_1ma$, but none has proposed KNBO as a base-centered orthorhombic crystal, as far as the author could verify.

As presented in figure 4.17, the $[0\,0\,1]$ CBED pattern was identified to display a $3m$ symmetry. Because the simulations also displayed a symmetry that resembles $3m$, it is likely that the basis of the unit cell in KNBO adds symmetries to the CBED pattern that makes it close to $3m$ in the $[0\,0\,1]$. Although the multislice simulations in figure 4.17 suggest that the CBED patterns should possess a close-to $3m$ symmetry, they also suggest that it should be possible to uniquely observe that the $3m$ symmetry is broken by a slight difference in the relative distances to the $(4\,0\,0)$, $(\bar{2}\,\bar{3}\,0)$ and $(\bar{2}\,3\,0)$ reflections as given in table 4.3. Hence, the difference in the reciprocal lattice spacings along the $(4\,0\,0)$, $(\bar{2}\,\bar{3}\,0)$ and $(\bar{2}\,3\,0)$ should result in a single m diffraction symmetry instead. However, the distance from the $(0\,0\,0)$ to the $(4\,0\,0)$, $(\bar{2}\,\bar{3}\,0)$ and $(\bar{2}\,3\,0)$ reflections in the experimental diffraction patterns were indistinguishable. This has also been previously reported in the related project by the same author and by Ryggetangen [1, 45]. Furthermore, the Bloch wave simulations suggest that a small intensity variation in the CBED disks of specific thicknesses break the $3m$ symmetry, hence representing the true m symmetry with the a-axis as the mirror line. Similar symmetry breakage was not observed. However, such small intensity variations predicted by the Bloch wave simulations may not be possible to observe experimentally. Even so, a $3m$ symmetry should not be compatible with space group 26, as explained in Section 2.6. Possible explanations for the observed differences between the Bloch wave simulations, multislice simulations and experimental CBED patterns will be given in Section 5.3.

From the discussion above, several of the findings indicate that KNBO as a thin film TEM specimen cannot be described by the $P2_1ma$ space group. Ideally, a complete space group determination, as outlined by Williams and Carter [29, 68], should be performed to refine the space group of the specimens. This was not done here, as the BF and WP symmetry was not attainable for several low-index zones. This will be further discussed in the next paragraphs. It is also not clear whether the altered crystal structure is present in all thin KNBO specimens, or if the KNBO specimens prepared in this thesis restructured because of the mechanical force exerted on the crystal during polishing. For example, Ryggetangen determined a $2mm$ symmetry in the $[0\,0\,1]$ [45], which was not attainable in the c-axis out-of-plane specimen inspected in this work. Therefore, a complete space group analysis should be performed on several TEM specimens prepared by a selection of methods. Specific methods will be suggested in Chapter 6 on the suggestions for future work.

Several observations from this thesis may provide information that could be useful for a complete space group determination of KNBO. The first considers the assessment of symmetries, the second is on the assessment of kinematically forbidden reflections and GM lines, and the third is on the assessment of the bright-field symmetry of [0 0 1]. LACBED was conducted on the specimens prepared in both directions as an "easier approach" towards symmetry assignment with respect to the CBED approach. Because of the large unit cell of KNBO, the smallest condenser aperture was required to secure that no CBED disks overlapped. Smaller CBED disks make it more challenging to assess symmetries in the HOLZ lines. Acquiring the required CBED patterns exactly on-zone is therefore increasingly important, which is an even more tedious task. The same issues were not faced when acquiring and analysing LACBED patterns, as a large condenser aperture is used for LACBED imaging. However, the experimental and simulated BF-LACBED patterns of the [0 1 0] and [0 0 1] zones were observed to appear more symmetric than the CBED patterns. Hence, DF-LACBED may be essential for acquiring the correct symmetry if LACBED is to substitute the CBED approach for symmetry assessment in KNBO.

To identify screw axes and glide planes, it is important to assess kinematicly forbidden reflections and the presence or absence of GM lines in these reflections, as was explained in Section 2.5.8. Although the kinematically forbidden (1 0 0) and (3 0 0) spots were observed experimentally in the [0 1 0] SAED pattern, these reflections were very weak in the CBED patterns. Hence, GM lines could not be assessed in the experimental on-zone CBED patterns. A point for future work is to first acquire the CBED patterns directly on zone, and after this carefully tilt the specimen such that the GM lines can be observed in a disk further out in reciprocal space [68]. GM lines could neither be observed in the BF-LACBED patterns. DF-LACBED could be attempted with the field-limiting aperture about one of the kinematically forbidden reflections to investigate if GM lines are present [29, 68]. An initial attempt was performed, but it was difficult to distinguish the kinematically forbidden spots from the neighbouring spots. Because these spots are very close to each other, the defocus would have had to be very large to separated them, or the SAED aperture would have to be smaller than those that were available. Hence, to observe GM lines, the next approach may be to perform CBED, and systematically tilt the specimen slightly off-zone along the direction of the forbidden reflections.

Additionally, to define the crystallographic axis system from [0 0 1] diffraction patterns, one would need to observe the (2 0 0) spot or the (0 1 0) spot, as predicted by the simulations shown in figure 4.20. Nevertheless, these were predicted to be weak and only visible for relatively thick specimens of size 400 nm − 500 nm. Experimentally, these kinematically forbidden reflections could not be observed, and a diffuse background began to appear at sufficiently thick regions, as also shown in figure 4.20. Furthermore, since GM lines are expected to be observed in kinematically forbidden reflections, GM lines could not be assessed in the [0 0 1] zone axis either. DF-LACBED to investigate the presence of GM lines would neither be possible if such kinematically forbidden reflections are not distinctly visible.

The symmetry of the BF disk is also an important symmetry to consider for structure determination by CBED [28, 68]. As seen in figure 4.17, the direct beam was overexposed in all CBED patterns in the [0 0 1] zone axis. This underlines the difficulty with assessing the BF pattern symmetry. Additionally, the LACBED images in the [0 0 1] zone axis also displayed a very bright direct beam, as can be seen in figure 4.19. Other methods for considering the BF symmetry of the [0 0 1] pattern should be considered if possible.

From the above discussion, it is evident that KNBO possesses complex diffraction properties that may be attributed to the pseudo-hexagonal nature of KNBO, unfortunate ratios of the lattice parameters, and experimental conditions. The structural analysis addressed above may also suggest that the KNBO TEM specimens prepared for this thesis is described by another space group than the bulk crystal. This change in crystal structure may be a thickness effect, or it may be an effect from the mechanical force exerted on the specimen during polishing. Specific suggestions for investigating this will be presented in Chapter 6 on future work. Note that although the crystal structure of the TEM specimens were observed to deviate from the crystal structure of bulk KNBO, and although a complete space group determination was not conducted, this did not affect the identification or assessment of structural twin boundaries and small-angle grain boundaries, as the deviation in the crystal structure of the specimens were not exceptionally larger, but rather close to, that of bulk KNBO.

5.3 Discrepancies in the simulated diffraction patterns

Although most of the experimental and simulated SAED, CBED and LACBED patterns displayed many of the same characteristics, none of them were perfect matches. There may be several reasons why the simulated patterns deviate from the experimental ones. Both the multislice and the Bloch wave simulations were performed under the assumption that the crystal structure of the thin film KNBO specimens were $P2_1ma$. The major difference between the Bloch wave and multislice simulations, apart from the description of the incident and diffracted electrons outlined in Section 2.4.3, is the model for the crystal potential. The Bloch wave simulations were performed with the PRDW model for the crystal potential, while the multislice simulations modelled the crystal potential with the Lobato and Van Dyck model[1]. One of the main reasons why the CBED patterns simulated by these two methods differed, may be the choice of models used for the crystal potential. Another possible explanation for the discrepancies may be that the crystal structure of thin film KNBO is not correctly described by space group 26, which has been a major assumption for the simulations. A final suggestion is that the choice of other simulation parameters – such as the number of HOLZ included, potential thresholds, or sampling frequencies – may not have been sufficient for simulating the CBED patterns realistically. These possible explanations for the discrepancies between the simulated and experimental diffraction patterns are further explored in this section.

---

[1] Note that not all models are available in the softwares used in this thesis. The PRDW was not available in py_multislice, and the Lobato and Van Dyck model was not available in JEMS.

As shown in Section 4.2, the Bloch wave simulated [0 0 1] SAED patterns were observed to match fairly well with the experimental pattern. The geometry of the diffraction spots were simulated with correct distances from the (0 0 0) spot, including the angles between them. For example, the distance between the (0 0 0) to the $(\bar{2}\,3\,0)$ and $(\bar{2}\,\bar{3}\,0)$, and (4 0 0) spots were of the same length and separated by an angle of 120° between each other, as was observed experimentally. However, the SAED patterns of the [0 1 0] and $[\bar{3}\,\bar{2}\,0]$ and surrounding zones were observed to slightly deviate from the experimental patterns. If the PRDW model is correct, the most likely explanation for the discrepancy between the simulated and experimentally observed CBED pattern is that the crystal structure used to simulate the diffraction patterns is slightly different from the true crystal structure of the thin film KNBO TEM specimens. Nevertheless, as the simulated and experimental (LA)CBED patterns displayed many of the same features, it is likely that the true crystal structure of the KNBO thin films is close to the crystal structure as the bulk, as concluded in the discussion above.

The $[\bar{3}\,\bar{2}\,0]$ CBED patterns simulated with the Bloch wave algorithm were observed to severely deviate from the experimental patterns. In figure 4.8e and 4.8f, it can be seen that the simulations only included five reflections, while the experimental pattern included several more. No matter the efforts to change certain simulation thresholds, no changes in the diffraction patterns were observed. From the SAED patterns in figure 4.7, the diameter of the FOLZ circle was measured to be 48.10 nm^{-1} in $[\bar{3}\,\bar{2}\,0]$, which is of similar size as the FOLZ diameter in the [0 1 0]; 45.10 nm^{-1}. This is not compatible with the simulations in figures 4.8 and 4.9, where the diameter of the FOLZ in $[\bar{3}\,\bar{2}\,0]$ should be noticeably smaller than the FOLZ diameter in [0 1 0]. The smaller FOLZ diameter in the simulated patterns may explain why the simulated CBED patterns in the $[\bar{3}\,\bar{2}\,0]$ deviate from the experimental patterns, as the experimentally observed FOLZ were larger. This may provide further evidence that the observed deviations between the simulated and experimental patterns is a result from an altered crystal structure.

The most evident parameter affecting the Bloch wave CBED and LACBED patterns was the number of HOLZ included in the simulations. As observed in figure 4.18, only a few reflections were successfully simulated in the [0 0 1] CBED patterns with the Bloch wave algorithm in JEMS. Furthermore, the simulated LACBED patterns were observed to deviate most from the experimental LACBED patterns far out reciprocal space, which is also attributed to the limited number of HOLZ included. One of the major limitations of the Bloch wave simulations in JEMS[2] was therefore the increased computing time when the number of HOLZ was increased. The LACBED and CBED simulations of the [0 0 1], including the LACBED patterns of the [0 1 0] and $[\bar{3}\,\bar{2}\,0]$, were computed over several hours when five HOLZ were included in the computations. When attempting to include more than five HOLZ for the [0 0 1] CBED simulations, JEMS typically froze and returned an error message. Henceforth, the Bloch wave simulations became too computationally heavy when attempting to simulate details further out in reciprocal space that could be important for the investigation of possible symmetry breaking.

---

[2] Running on a standard desktop PC.

Since the symmetry of the CBED patterns further out in reciprocal space may be essential to distinguish several crystallographic directions, complementary simulations to the Bloch wave simulations were essential for the [0 0 1]. The Python-based multislice code, py_multislice, can run on a standard computer, but can also be GPU accelerated, allowing for vastly faster calculations. Hence, hardware restrictions were not a limitation when running multislice simulations in the [0 0 1], as was the case for the Bloch wave simulations. The multislice simulations provided more information about the CBED patterns further out in reciprocal space, although the geometry of the reflections slightly deviated from the experimental data. The distances and angles between spots were observed to slightly deviate from the experimental CBED patterns. For example in the [0 0 1], the distance between the (0 0 0) to the $(\bar{2}\,3\,0)$ and $(\bar{2}\,\bar{3}\,0)$, and (4 0 0) spots were easily distinguished, as shown described in Section 4.2.1. However, in the experimental data, the distance between these spots were indistinguishable. The pattern geometry was therefore more anisotropic in the multislice simulations than what was experimentally observed.

A possible explanation for this may be that the model used for the crystal potential. py_multislice uses a model for the crystal potential by Lobato and Van Dyck, which has been shown to have a root-mean-square value smaller than both PRDW and EJK, and hence should simulate diffraction patterns more precisely [67]. However, from the preliminary simulations performed prior to this thesis [1], the Bloch wave simulations with the PRDW model was observed to match the experimental diffraction patterns best. Additionally, the results presented in this thesis also propose that the PRDW model provided a better model for the crystal potential than the mulitslice simulations with the Lobato and Van Dyck model. Hence, by implementing the PRDW model to the multislice simulations, more accurate simulations may be obtained. It is important to note that the model by Lobato and Van Dyck was not implemented in JEMS [3], and it is therefore difficult to say whether the observed differences between the Bloch wave simulations in JEMS and the multislice simulations with py_multislice is truly a result from the crystal model, or if other parameters caused these differences. Hence, it is important to further investigate the possible implementation of the PRDW model with the multislice algorithm, and the effect of this model on the simulated diffraction patterns. One could also test other multislice softwares such as MULTEM [78] for direct comparisons of different algorithms. This was not prioritized in the present study as it was considered to be out of the scope of this thesis.

A note should be made on the model for the crystal potential implemented in ReciPro, and why the suggested zones for the tilt series were simulated in JEMS instead of using the simulated patterns from ReciPro directly. When ReciPro is used to index diffraction patterns, it uses a Bloch wave method to simulate several diffraction patterns and compares these to the experimental SAED patterns [5]. In the process of assigning the zones in the tilt series, it was observed that the six suggested indexing schemes that matched the experimental patterns deviated by up to 3%, and it was suggested that this deviation could be a result of the model for the crystal potential implemented in ReciPro[3]. This is the main reasons why it was decided to separately simulate the suggested zones in JEMS after they had been suggested by ReciPro, as it had previously been shown that the PRDW model in JEMS simulated the [0 0 1] zones correctly [1, 45].

---

[3] As described in Section 3.1, ReciPro uses their own model for the crystal potential only including the imaginary part of the crystal potential.

The results in figure 4.9 also showed that the Bloch wave simulations in JEMS fitted the experimental [0 1 0] CBED patterns better than the multislice simulations. One reason may be the choice of sampling frequency and tiling of the crystal.[4] The choice of these parameters may severely influence the beam spread and intensity. The convergence tests included in Appendix C present how the beam spreads, and how the intensity of the diffracted beam is affected by these parameters when the thickness of the crystal increases. The convergence tests revealed that a sampling frequency of [2048, 2048] and a tiling of [32, $\lfloor 32(a/c) \rfloor$] were not sufficient for simulating [0 1 0] CBED patterns up to 500 nm, as the intensity dropped below a certain threshold [5]. However, any higher sampling frequencies nor a larger tiling could be implemented due to memory issues, even with a 32 GB GPU on a supercomputer in the IDUN cluster.

The main contributor to these memory issues is attributed to the large anisotropy of the crystal. py_mulitslice requires the real space crystal to be close to a square in the projection plane in order to ensure that the simulated CBED disks are perfectly round disks. The unit cell of KNBO is $a = 17.506$ Å, $b = 15.162$ Å, and $c = 3.968$ Å. This results in a large anisotropy in the [0 1 0] direction that is not optimal for the multislice simulations, where a tiling of [32, $\lfloor 32(a/c) \rfloor$] $\approx$ [32, 128] requires a large amount of memory. Hence, switching to a GPU with larger memory may not necessarily be sufficient to improve the multislice CBED simulations in the [0 1 0] zone axis. The same memory issues were not faced when simulating the [0 0 1], where the integer division of [32, $\lfloor 32(a/c) \rfloor$] $\approx$ [32, 32], and the convergence tests easily passed. Thus, the projection of the [0 0 1] was close to square when an even tiling was used. However, the projection of [0 1 0] is largely anisotropic, and the tiling had to correct for this anisotropicity such that the real-space crystal was close to square, as schematically illustrated in figure 5.3. The tiling and sampling frequency are important factors determining the memory needed for the CBED computations in py_multislice. A point for future work is therefore to optimise the multislice script for the crystal structure of KNBO by for example implementing an alternative approach where the crystal does not need to be square in the plane perpendicular to the zone axis of which CBED patterns are simulated.

To summarise, it is essential to enhance and optimise the dynamical diffraction simulations for KNBO thin films in order to correctly assess crystal directions and perform polarity assessment from CBED patterns. This includes the choice of algorithms, the crystal potential used for models for the crystal structure, and other important parameters specific to the choice of algorithm. When these parameters have been optised, the orientational and polarity assessments of KNBO may be more easily carried out.

---

[4] Sampling frequency is determined by the so-called grid shape of the simulations, and the crystal repetition is determined by the so-called tiling, as given in Appendix C.

[5] Floor division was used when implemented in Python.

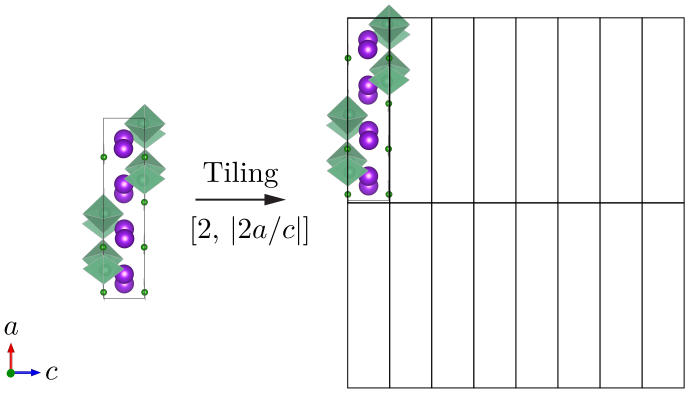

Figure 5.3: Schematic illustrating the anisotropic repetition of KNBO in real space to make it close to a squared crystal for multislice simulations in the [0 1 0]. Here, it has been shown for a tiling of [2, $|2a/c|$] = [2, 8] with floor division for simplicity.

5.4 Domain inspections

This work has aimed to build a framework for domain characterisation of KNBO. From the insight gathered from the structural analysis of KNBO, a goal has been to identify the zones at which the crystal structure and hence also the diffraction pattern sufficiently change to obtain contrast at a domain boundary. Further, another goal has been to determine the diffraction techniques that most efficiently assess the polar axis. A final goal was to combine correlated microscopy techniques such as PLM and PFM to investigate the functional properties of the structural twin domains in order to gain a better understanding of the interplay between the structural and ferroic properties of KNBO. Note that the domain structure has previously been studied in some detail using PLM and PFM [35, 36, 73], but never with TEM. This section presents a discussion on the domain inspections performed in this thesis. Firstly, the observed presence and absence of polar domains as measured by the correlated microscopy techniques will be presented. After this, the structural domains observed in the c-axis in-plane specimen will be considered, including a discussion on its domain boundaries.

5.4.1 Ferroic properties

The correlated microscopy techniques combined with the TEM inspections produced a set of curious results. PFM measurements verified the presence of polar domains in the c-axis out-of-plane specimen where no structural domains were observed by electron diffraction. Contrarily, the PFM measurements indicated an absence of polar domains in the c-axis in-plane specimen, where several structural domains were observed by TEM. These curious observations will be discussed below.

Before specimen preparation, the specimens prepared in both directions, in other words with the *c*-axis in-plane and the *c*-axis out-of-plane, had shown the presence of ferroelastic needle domains in the *c*-facet of the bulk crystal by PLM, as indicated in figures 4.1a and 4.22a. The PFM micrograph presented in figure 4.22c corresponded to the domain indicated by the number 3 in the PLM image in figure 4.22a. The specimen fractured while PFM was performed in an area close to the domain indicated by the number 1 in figure 4.22a, which was the region inspected in TEM. Although the presence of domain 1 could not be confirmed by PFM, it may be assumed that it was not removed by the specimen preparation due to the confirmation of its neighbouring domain; domain 3. Furthermore, this stresses how fragile and brittle the TEM specimens of KNBO are.

A challenge faced when preparing the *c*-axis in-plane specimen, was the inability to assess the ferroelastic twin domains in the polishing facet with PLM. Although it could not be confirmed that ferroelastic twin domains were present in the polishing facet, the pre-polishing PLM micrographs in the *c*-facet, as shown in figure 4.1a, indicated that these should be present. The presence of twins were confirmed by the structural analysis of the specimen, as presented in figure 4.6. Hence, it can therefore be concluded that the preparation scheme successfully prepared a specimen for structural analysis of twin domains. However, the piezo-response of the *c*-axis in-plane specimen overlapped with its topography, as shown in figure 4.15, hence suggesting that none of the twin domains were ferroelastic. Previous research has reported that the topography of ferroelastic and ferroelectric specimens overlap with the polar domain walls, and that materials that have undergone a phase transition to a non-ferroic state may display a trace of the ferroelastic domain walls in the topography of the specimen [79]. Henceforth, the absence of polar domains may suggest that the TEM specimen preparation of a specimen with the *c*-axis in-plane removed the polar properties of KNBO by altering the crystal structure to a more centrosymmetric one.

Possible explanations for the absence of polar domains may be that the TEM specimen preparation altered the crystal structure. Previous research has reported that the crystal structure of a material can change due to mechanical treatment such as polishing [80–83]. Since the properties of a crystal is strongly related to its crystal structure, any structural changes as a result of a mechanical force may also alter the ferroic properties of the material. Furthermore, ferroelectricity has been reported to be weakened or even eliminated in materials that are thinner than a material-specific threshold thickness [84–86]. Hence, the absence of polar domains may either be an artefact from the polishing scheme, or a reduced-thickness effect. For KNBO, such details have not yet been reported. Even so, the measured absence of polar domains further supports the hypothesis that the specimen preparation altered the crystal structure of KNBO, as was discussed in Section 5.2.

Although no structural domains were observed in the *c*-axis out-of-plane specimen in the TEM, the PFM measurements in figure 4.22 indicated that extended polar domains were present in that specimen. The height profile of the *c*-axis out-of-plane specimen did not overlap with its piezo-response, hence confirming the presence of polar domains. Although the PFM measurements confirmed the presence of polar domains in that specimen, the $3m$ symmetry of the diffraction patterns complicated the identification of structural domains in the TEM. The complicated diffraction properties of KNBO in the $[0\,0\,1]$ underlines that this zone may not be the optimal zone for domain inspections, although polar domains were verified in that facet.

In summary, the PFM measurements indicate that the polar domains of thin film KNBO are removed when bulk KNBO is polished with the *c*-axis in-plane, but not when it is polished with the *c*-axis out-of-plane, in other words in the *c*-facet. Whether this is a general reduced-thickness effect or an artefact from the polishing is currently unknown, but specific suggestions to investigate the observed disappearance of the polar domains will be given in Chapter 6.

5.4.2 Domain boundaries

The structural domains in KNBO were observed to be separated by bands of width $\sim 200 - 500$ nm. Several of these bands were identified in KNBO, and they were easily observed by HAADF STEM, especially when the specimen was tilted slightly off zone between $[\bar{3}\,\bar{2}\,0]$ and $[\bar{7}\,\bar{6}\,0]$. This off-zone imaging was a prerequisite for imaging the bands by conventional BF imaging, as given in figures 4.13 and 4.14, but was not essential for locating the boundaries with HAADF STEM, as shown in figures 4.6 and 4.10. Hence, HAADF STEM is the best choice for initial localisation of areas with planar defects in large wedge-shaped specimens prepared by mechanical polishing. The low-angle grain boundaries and twin boundaries were observed to run along the $g_{2\bar{3}\bar{2}}$ direction. The origin of this orientation remains unknown, and should be explored further in future work. Notice also that the bands are characterised by a bending at the edge of the specimen, which elsewise is sharp along the $(0\,0\,1)$ and perpendicular planes.

Whether the bands themselves are structural domains or extended domain walls cannot be concluded. These two possibilities are illustrated in figure 5.4. By defining the bands as extended domain walls, as in figure 5.4a the whole band is a transition from one structural orientation of the specimen to another structural orientation. However, by defining the lines along which there is a change in contrast as the domain walls, the domain walls are defined as sharp boundaries, where the lighter region within the band is an isolated structural sub-grain. Structural analysis on the narrow bands could not be easily performed without including effects from the neighboring domains because of charging that resulted in vibrations. Thus, an absolute conclusion cannot be made. However, it is assumed that the bands are extended domain boundaries, as will be further motivated in the coming paragraph.

If the bands indeed are extended domain boundaries, there may be several suggestions for this. One possible hypothesis is that the boundaries are extended due to surface relaxations, causing a volume change across the boundary. Grillo has demonstrated that surface relaxation may be observed as light bands in an HAADF STEM image [87]. Surface relaxation may occur at strained regions of the specimen, for instance from specimen thinning to obtain an electron transparent specimen. This surface relaxation may further cause the crystal to swell at the strained regions, causing an altered topography that is observed in an HAADF STEM image as light bands. It is proposed that a similar effect has taken place at the strained domain boundaries in KNBO. However, the bands observed by Grillo were several orders of magnitude smaller than those observed in this thesis. The topography measured by PFM varied approximately 20 nm, which is also a much larger volumetric change than that observed by Grillo. Further, Beyer *et al.* has shown that lattice plane bending at strained interfaces influences ADF images [88]. Hence, it is not unlikely that the observed intensity change at the bands are a result from strain and lattice plane bending. The slight bending of the specimen at the edge of the specimen at the bands may further be explained by such lattice distortions due to strain. A previous study by Yu *et al.* has also documented channelling or dechanneling contrast in strained or tilted regions of a specimen [89]. Due to the ferroelastic nature of bulk KNBO, including its twinning, strain is likely to be the cause of the contrast observed in HAADF STEM.

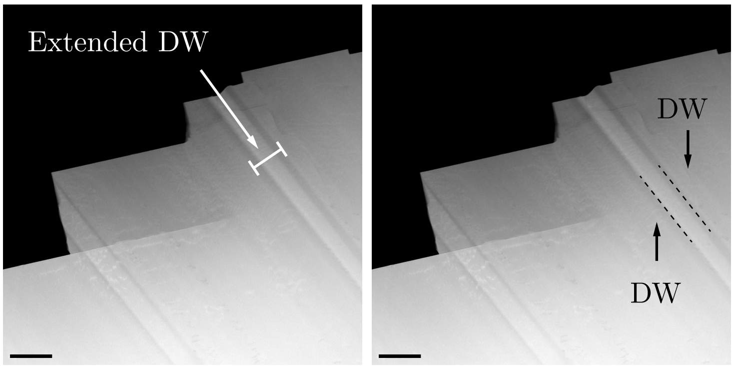

(a) (b)

Figure 5.4: HAADF STEM images illustrating the possible nature of the bands separating two structural domains. The bands may be (a) extended domain walls, or (b) individual domains. This is indicated on the images with the abbreviation DW. The scale bars are 1 µm.

It is also important to consider the possibility that the contrast along the bands are a result from an accumulation of interstitials, vacancies, or impurities. HAADF STEM give atomic-mass contrast, as described in Section 2.5.2.1. Hence, some contribution to the contrast in the bands could be the result of an accumulation of interstitials, vacancies or other defects from crystal growth, as has been reported in the literature [90, 91]. The presence of such point defects would affect the conductive properties of the boundaries, as was outlined in Section 2.3.4, and may therefore have a big influence of its applications for domain wall engineering. There is a need for more work with higher resolution on thinner specimens of KNBO to make any further conclusions on this.

In summary, several planar defects were easily observed in KNBO by HAADF STEM. These bands were considered to either be individual domains separated by sharp domain walls, or extended boundaries resulting from strain, surface relaxation, or lattice plane bending. It is considered that the bands most likely are extended domain walls, and that the contrast observed at the bands are dechanneling contrast due to a strained crystal structure at the band because of the ferroelastic nature of bulk KNBO.

5.4.3 Twin domains

Two structural twin domains were observed in the *c*-axis in-plane specimen by their distinctly unique SAED patterns, as presented in figure 4.6. When one domain, R1, was imaged in the $[0\,1\,0]$ zone axis, the other domain, R2, was imaged in the $[\bar{3}\,\bar{2}\,0]$ zone axis without changing the holder tilt values as identified by SAED. This confirms the presence of 120° twin domains because these two zones are 120° to each other. This is the first observation of twinning of KNBO by electron diffraction techniques that verify the 120° rotation of KNBO at the twin boundary. The twinning axis was confirmed to be the *c*-axis, as will be further discussed below. Although the twinning axis is the *c*-axis, the two twin domains did not meet at the $(0\,0\,1)$. The boundaries ran along the $g_{2\bar{3}\bar{2}}$ direction, as discussed in Section 5.4.2 indicating that the plane at which the two twins meet is $(2\,\bar{3}\,\bar{2})$ in the $[\bar{3}\,\bar{2}\,0]$ domain and $(\bar{4}\,0\,\bar{2})$ in the $[0\,1\,0]$ domain[6]. Several such twins were identified along the wedge of the specimen. Although TEM is not statistical, it is assumed that the observed broad twin boundaries are representative. Several findings from this thesis may demonstrate why KNBO easily twins, and will be discussed in this section.

From the experimental and simulated tilt series of the *c*-axis in-plane specimen, it was observed that KNBO contains several minor zones close to the $[\bar{3}\,\bar{2}\,0]$ zone and corresponding twins, in other words the $[0\,1\,0]$ and $[3\,\bar{2}\,0]$ zones, as presented in Section 4.1. Contrarily, KNBO possesses few minor zones close to the $[0\,0\,1]$ zone. Furthermore, the geometry of the $[0\,0\,1]$ SAED pattern demonstrated that the $(4\,0\,0)$, $(\bar{2}\,3\,0)$ and $(\bar{2}\,\bar{3}\,0)$ spots were not easily distinguished, but rather observed at the same distances from $(0\,0\,0)$ at 120° angles from each other, as seen in figure 4.17. These combined observations may explain why twinning occurs with the *c*-axis as the twin axis.

Moreover, the simulations provided information that the crystallographic zones 120° to the $[0\,1\,0]$ zones – the $[\bar{3}\,\bar{2}\,0]$ and $[3\,\bar{2}\,0]$ zones – have very similar diffraction patterns, hence indicating that their respective planes display many of the same symmetries and geometries. This is evident from the simulated tilt series of all of the zone schemes proposed for the experimental tilt series, as presented in table 4.1. The surrounding zones to the $[0\,1\,0]$, $[\bar{3}\,\bar{2}\,0]$ and $[3\,\bar{2}\,0]$ displayed many of the same features, but with small details allowing for uniquely separating the $[0\,1\,0]$ from $[\bar{3}\,\bar{2}\,0]$ and $[3\,\bar{2}\,0]$. The same arguments can be made for $[0\,\bar{1}\,0]$, $[3\,2\,0]$, and $[3\,\bar{2}\,0]$. Hence, this might explain why KNBO easily twins. The diffraction patterns from the simulated tilt series about the $[\bar{3}\,2\,0]$, $[3\,2\,0]$, $[3\,\bar{2}\,0]$, $[0\,1\,0]$, and $[0\,\bar{1}\,0]$ zones are given in Appendix E.

The above-mentioned proposed explanations for the twinning in KNBO is further supported by the HRTEM data acquired in the $[\bar{3}\,\bar{2}\,0]$ and $[0\,0\,1]$. Figure 5.5 illustrates the relation between the modelled crystal structure of bulk KNBO in the $(0\,1\,0)$, $(\bar{2}\,\bar{1}\,0)$ and $(0\,0\,1)$ planes, and the HRTEM images acquired in the $[\bar{3}\,\bar{2}\,0]$ and $[0\,0\,1]$ zone axes. The relationship between the crystallographic planes and directions are also indicated, where for example the corresponding zone axis to the $(\bar{2}\,\bar{1}\,0)$ plane is $[\bar{3}\,\bar{2}\,0]$. In the $[0\,0\,1]$, the g_{020}, $g_{2\bar{1}0}$, and $g_{\bar{2}\bar{1}0}$ cannot be distinguished by the spacing between the fringes in the respective directions. The same argument can be made for the g_{400}, $g_{\bar{2}30}$, and $g_{\bar{2}\bar{3}0}$. Furthermore, the HRTEM images that were acquired in the $[\bar{3}\,\bar{2}\,0]$ display

---

[6] This can be deduced from the $[0\,1\,0]$ SAED pattern by comparing that pattern to the $[\bar{3}\,\bar{2}\,0]$ SAED pattern and the corresponding $(2\,\bar{3}\,\bar{2})$ spot.

fringes separated by a distance that match the interatomic distances in KNBO viewed from the [0 1 0]. The distance between 5 fringes in the $g_{2\bar{3}0}$ direction was 1.73-1.79 nm, which is comparable to the lattice parameter a, while the spacing between the lattice fringes in the g_{001} direction was 0.37-0.42 nm, comparable to the lattice parameter in the c-direction. The twinning may therefore be associated with the similar interatomic distances of the planes at which two neighbouring 120° twin domains meet. Thus, the twinning in KNBO may be ascribed to its pseudo-hexagonal crystal structure.

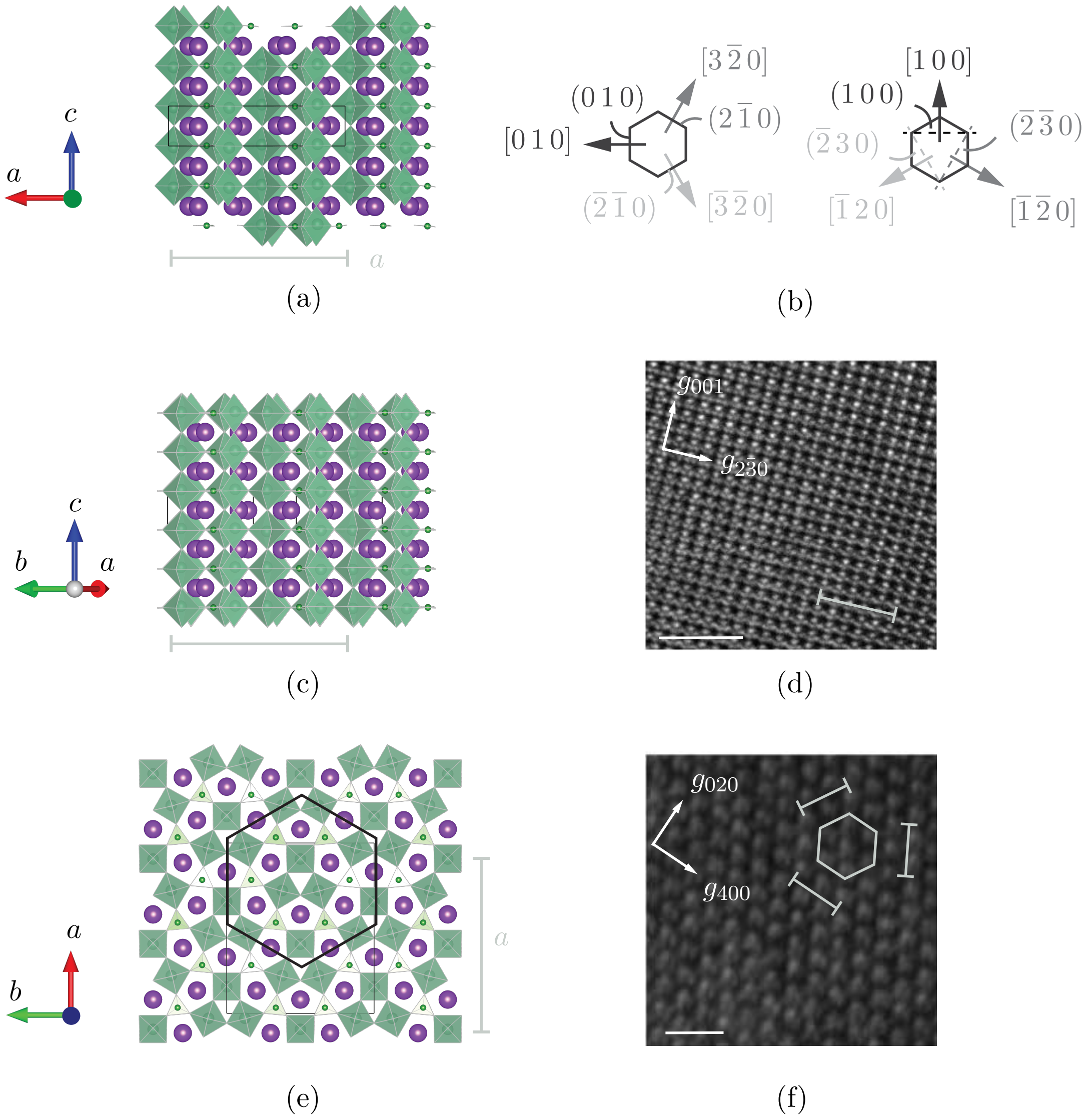

(a) (b) (c) (d) (e) (f)

Figure 5.5: Relationship between the modelled crystal structures in the (a) (0 1 0), (c) $(\bar{2}\bar{1}0)$ and (e) (0 0 1) planes and HRTEM images acquired in the (d) $[\bar{3}\bar{2}0]$ and (f) [0 0 1] zones. (b) Schematic illustrating the relations between the crystallographic directions and planes. The zones [0 1 0], $[\bar{3}\bar{2}0]$ and [0 0 1] are related to the (0 1 0), $(\bar{2}\bar{1}0)$ and (0 0 1) planes respectively. The line-bars indicate distances that are of similar length as the lattice parameter in the a-direction. (d, f) The scale bars are 2 nm.

In summary, the observed twinning may be attributed to the similar symmetry relations between two neighbouring twins, as evidenced by the similar diffraction geometries, diffraction symmetries and interatomic distances. Furthermore, the twinning of KNBO was for the first time imaged by TEM, and experimental evidence for the twinning could be compared to the crystal model for KNBO.

5.4.4 Low-angle grains

In addition to the structural twin domains, structural domains were identified where the crystal reoriented approximately 0.6°, as presented in figure 4.10. The reorientation occurred about an axis perpendicular to the $(2\,\overline{3}\,2)$ plane as observed by the movement of the Kikuchi pattern along the $(2\,\overline{3}\,2)$ Kikuchi band. The origin of this rotational axis is unknown, and should be explored further. Several such bands were observed across the wedge of the specimen, displaying a similar low-angle structural re-orientation. The low-angle boundary discussed here is henceforth representative of several such bands observed in the specimen. The low-angle boundaries were observed to occur at a higher frequency than the twin domains.

Two hypotheses for the nature of the low-angle grains, R2 and R3, and the band, B2, separating them are given in figure 5.6. One of the hypotheses is that these grains are antiferroelectric domains where the antiferroelectric configuration changes from an up - down - up - down - up - down configuration, to an up - down - up - up - down - up configuration at the boundary, as shown in figure 5.6. At the domain wall, it is hypothesised that the crystal needs to relax because the crystal structure does not directly fit at the boundary, hence forcing the crystal structure to slightly reorient, and the band to extend. The second hypothesis is that the band B2 is a low-angle grain boundary separating two ordinary sub-grains, as will be further explained later.

The hypothesis that KNBO orders in ferroelastic and antiferroelectric domains rather than ferroelectric domains supports the observations reported by Ushakov [73]. Ushakov measured three polar domains with PFM rather than six as was expected for a ferroelectric arrangement. Antiferroelectric domains would not be distinguished by PFM, and could hence explain the observations of only three distinct polar domains. Furthermore, the antiferroelectric hypothesis are supported by the measured antiferroelectric hysteresis loops by Shan *et al.* [37]. However, antiferroelectic domains are typically observed as antiphase boundaries [92] that are 1-10 nm wide, in other words 20-200 times narrower than the bands observed here. To the author's knowledge, no such behaviour has been reported on the length scales observed in this thesis.

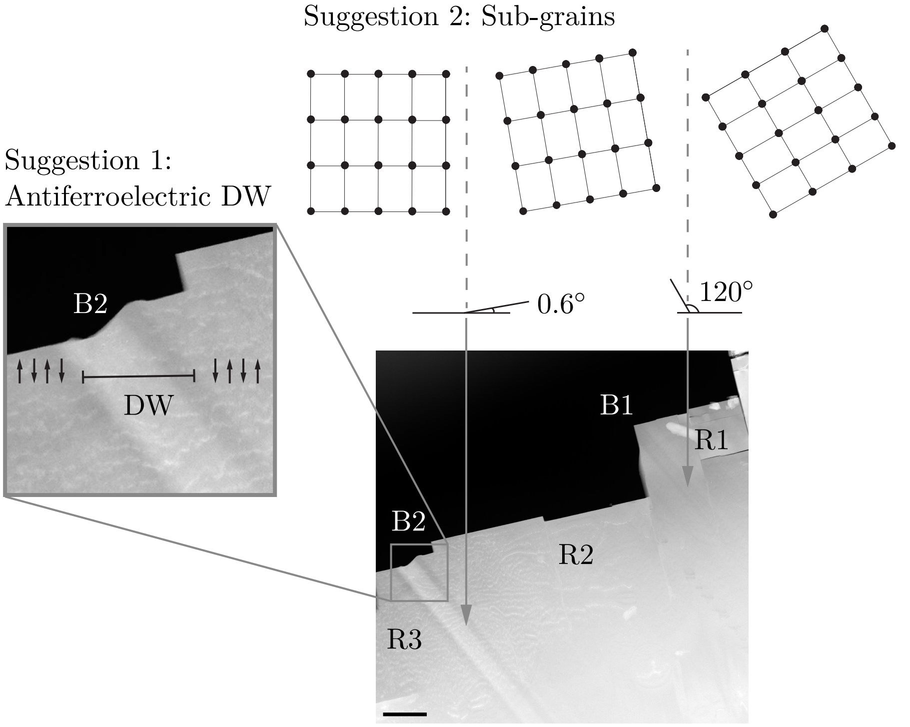

Figure 5.6: Schematic illustrating the possible nature of R2, B2 and R3. Suggestion 1 presents the possible antiferroelectric arrangement on either side of B2, where a relaxed crystal structure is present at the extended domain boundary. Suggestion 2 presents B2 as a sub-grain boundary, where the 0.6° reorientation is a necessary intermediate of the twins. The rotation in suggestion 2 has been exaggerated to make the rotation visible. The scale bar is 1 µm.

Furthermore, the CBED patterns from the possible antiferroelectric domains at the $[\bar{7}\,\bar{6}\,0]$ zone axis showed interesting features that should be considered. The $(0\,0\,1)$ disk in the $[\bar{7}\,\bar{6}\,0]$ CBED pattern from R3 displayed a dark line that was light in the $(0\,0\,1)$ disk in the $[\bar{7}\,\bar{6}\,0]$ CBED pattern from R2. To the author's knowledge no previous research have reported such an inversion of contrast in the CBED pattern at opposite antiferroelectric domains. Most work identifying antiferroelectric domains include SAED at the damain wall where so-called satellite spots or superlattice reflections are observed [52, 93–95]. These superlattice reflections are typically described by a fraction of the $(h\,k\,l)$ reflection, such as 1/2 $(1\,0\,0)$ or $1/4(1\,0\,0)$. However, satellites were not seen at the boundaries observed in this work. In KNBO, such reflections may be challenging to identify due to the already short distance between $(h\,k\,l)$ reflections.

Ferroelectric domains and corresponding polar axes, on the other hand, are typically found by an inversion of symmetry in the CBED pattern, much similar to that observed in the $[\bar{7}\,\bar{6}\,0]$ zones in R2 and R3. Even so, a ferroelectric arrangement is neither compatible with the measured absence of polar domains by PFM, nor the SAED patterns of the $[\bar{7}\,\bar{6}\,0]$ and neighbouring zones. The SAED patterns from each of the domains indicate that both are described by the same orientation. The neighbouring zones to $[\bar{7}\,\bar{6}\,0]$ were observed at the same geometries about the $[\bar{7}\,\bar{6}\,0]$ in both domains, similar to that reported in the tilt series in Section 4.1.2. Hence, it is a low probability that the switched dark and light lines in the CBED patterns describe a flipping of the *c*-axis. To describe it in other words, it is unlikely that the domains are described by a 180° structural rotation such that the g_{001} has been flipped, as would be the case for a ferroelectric material. If the two structural domains were ferroelectric, the SAED patterns on either side of the boundary would be related to the $[\bar{3}\,\bar{2}\,0]$ and $[3\,2\,0]$ respectively. However, the data gathered in this thesis do not provide enough evidence to conclude that these domains are ferroelectric, especially since the PFM measurements indicated an absence of polar domains in the specimen.

To verify that the inverted contrast of the lines within the $(0\,0\,1)$ CBED disks truly is a result of some structural rearrangement, one could do a small tilt series with the dark-tilt deflector in the TEM along the *c*-direction. If the appearance of the lines stay constant, the tilt series would confirm that these observations are not a result of the patterns being acquired slightly off-zone or out-of-focus.

As previously discussed in Chapter 5.4.1, the PFM measurements showed that the height profile of the specimen overlapped with the piezo-response. It has previously been reported that antiferroelastic domain walls may themselves display polar or even ferroelectric properties because the octahedral rotations are suppressed at the domain wall, although the material itself is non-ferroelectric [92, 96]. Hence, it may be that the height profile of the specimen overlaps with the domain boundaries, and that these boundaries display polar properties.

A final proposal of the nature of the two domains, R1 and R2, and the domain boundary between them is that they are sub-grains separated by a sub-grain boundary. This is illustrated in figure 5.6 as *Suggestion 2*. Kogure *et al.* have reported sub-grain boundaries at an array of dislocation loops where the misorientation of the sub-grains range from 0.8° to 21° [97]. Such arrays of dislocation loops were also observed along the bands in the *c*-axis in-plane specimen. It may therefore be possible that the crystal structure orders in a sub-grain between twins to correct for a slight mismatch in the crystal structure of the twins. It would be interesting to investigate the crystal structure at these arrays of dislocation loops by HRTEM and HR-HAADF STEM. However, as previously addressed, the specimen was too thick to obtain high-quality HRTEM images in the areas where these bands and dislocation arrays were observed.

5.4.5 Summary and outlook of the domain inspections

From the above discussions, some key findings can be summarised. 120° twin domains were identified based on diffraction, and the boundaries were for the first time imaged by TEM. The twin domains were readily inspected in a specimen with the *c*-axis in-plane. This is attributed to the shorter lattice parameter in the *c*-direction than in the *a* and *b* directions. Additionally, a low-angle grain boundary with an 0.6° rotation was also easily inspected by the distinct bands visible in HAADF STEM and the sensitivity of Kikuchi patterns to small structural changes. This boundary may be either an antiferroelectric or a sub-grain boundary. Finally, the CBED patterns on either side of the low-angle boundary appeared identical in the $[\bar{3}\,\bar{2}\,0]$ zone axis, but fine details in the $[\bar{7}\,\bar{6}\,0]$ zone distinguish them. Hence, the $[\bar{7}\,\bar{6}\,0]$ is likely a crucial zone for distinguishing the structural rearrangement in domains such as R2 and R3. Note that such boundaries have never been suggested before, but PLM or PFM would likely not achieve contrast from such fine structural reorientations. Note also that several of these boundaries were observed in this specimen. The example in figure 4.10, is therefore a representative case. The low-angle grain boundaries and twin boundaries were observed several micrometres apart, and hence the occurance of these are assumed to be independent of each other.

In addition, several questions have been raised based on the reported observations and the discussion above. It is for example curious that the polar domains were observed by PFM in the *c*-axis out-of-plane specimen, since no structural domains could be identified in the TEM. This is especially curious because the polar domains were expected to be ferroelastic twin domains. Further, although structural domains were observed in the *c*-axis in-plane specimen, the measured piezo-response may indicate that no polar domains were present. Finally, the crystal structure of the thin film KNBO TEM specimens were observed to be altered. It remains unknown whether the observed structural change of the KNBO thin film with respect to its bulk form is a reduced thickness effect or a result of the polishing scheme.

Hence, to understand how these issues may affect the ferroic properties and domain inspections in KNBO, some of the abovementioned questions should be systematically investigated further. Specifically how to further investigate and solve these questions will be proposed in Chapter 6 on future work.

5.5 Framework for domain inspections in KNBO

This work has demonstrated that the structural domains in KNBO are readily inspected if the specimen is prepared in a facet with the *c*-axis in-plane. However, it has also been shown that the complex electron diffraction, large unit cell, and possible restructuring of the KNBO TEM specimens may complicate the structural analysis and the domain inspections in KNBO. Thus, the findings discussed above underline that several unresolved questions need answering before an absolute framework for domain inspections of KNBO is established.

The most pressing queries to solve are the correct crystal structure of thin film KNBO, whether the polishing scheme altered the crystal structure, or if the altered crystal structure of a thin film KNBO is a reduced-thickness effect. After these matters have been solved, the framework for domain inspections in KNBO is proposed as follows:

1. Perform PLM in the *c*-facet to localise a facet perpendicular to the *c*-facet intersecting several needle domains, such that there is an increased probability of finding structural domains in the final TEM specimen.
2. Perform PFM on the selected facet with the *c*-axis in-plane to confirm the presence of polar domains.
3. Prepare a TEM specimen with the *c*-axis in-plane. Either by polishing or another non-mechanical method depending on whether it is found that mechanical polishing alters the crystal structure.
4. Localise domains by HAADF STEM at medium magnification.
5. Further thinning of the specimen may be performed at the regions of interest identified by HAADF STEM, for example by FIB, ion etching or ion milling.
6. Perform SAED, CBED and LACBED on either side of and on the domain boundary.
7. Compare experimental data to simulations for structural and polar assessment.

An additional note is given on domain inspections of specimens with the *c*-axis out-of-plane. If one wishes to investigate the $[0\,0\,1]$ direction further, PFM seems to be essential for localising the polar domains, and should be performed prior to TEM inspections, as conventional BF and DF TEM and HAADF STEM has been shown to be inefficient in localizing domains in this direction [1]. However, as discussed above, a thin TEM specimen is likely to break while performing PFM, and most of the results from this thesis indicate that observing any structural change at the domain wall is challenging.

6 Future work

This first extensive study into the structure of KNBO using specimens with the *c*-axis in- and out-of-plane answers some of the open questions that existed prior to this work. For example, the TEM study of a 120° twin shows, for the first time, that the twin boundary is extended to a width of hundreds of nanometres, and that there were a presence of intermediate low-angle boundaries between twin domains. The goal was to acquire a more detailed structural analysis of KNBO in several domains by TEM, and with this provide insight into the structure-property relationship in KNBO. From the discussion above, it is discernible that the PLM, PFM and structural analysis by TEM produced a set of conflicting results. It is not clear whether the absence of extended polar domains in the *c*-axis in-plane specimen was a result from a structural change due to the reduced thickness of the specimen, or if it was induced from the mechanical thinning to obtain an electron transparent specimen. The observed height profile may be an artefact from the polishing, an induced swelling due to strain at the domain boundaries, or a by-product from the previously polar domains of the bulk crystal. Further, it remains unclear why polar domains were observed in the *c*-axis out-of-plane specimen when no structural domains could be observed. The origin of the observed physical properties of KNBO gathered in this thesis remains unclear and should be further investigated. Some suggestions for future work to gain better insight into the structure-property relation of KNBO based on correlated microscopy are proposed in this section.

The first pronounced point for future work is to determine the correct space group for thin KNBO TEM specimens. As discussed in Section 5.2, the crystal structure was observed to deviate from the proposed crystal structure of bulk KNBO, which was supported by the electron diffraction patterns from different diffraction techniques and corresponding simulations. This was not only supported by the discrepancies between experimental and simulated patterns, but also from the non-coinciding ZOLZ and FOLZ in the [0 1 0]. Hence, a complete space group determination as outlined in Section 2.5.8 should be conducted on a thin film KNBO specimen. Such a study would be challenging due to characteristics of the zone patterns as outlined in Section 5.2, where the diffuse background, visibility of GM lines, and dense patterns complicate these inspections at low-index zones. This could mean that the structure analysis has to be performed at multiple higher-index zones. Nevertheless, a complete space group determination of thin film KNBO is important for correctly performing dynamical diffraction simulations that can be used for correct orientation deductions and possible polarity deductions. Other possible methods for absolute structural assessment of small single crystals are 3D electron diffraction, where the crystal structure is reconstructed from diffraction data at several directions [98], or digital-LACBED, where a large set of DF-LACBED patterns are acquired by computer-control and can be used to assess important symmetries and GM lines [99].

For polarity assessment of ferroic domains in KNBO, one must be able to correctly simulate electron diffraction from thin film KNBO. Apart from introducing the correct crystal structure of thin film KNBO as the input crystal in the simulations, the model for the crystal potential needs to be adapted to the experimentally observed diffraction patterns of KNBO. Refined models may be required for some materials. This was the starting point for developing the PWDR model for materials with large Debye-Waller factors [64]. As discussed in Sections 5.2 and 5.3, the PWDR model did fit the experimental low-index diffraction patterns of KNBO rather well. Although it gave reasonable results for the ZOLZ, it is still a too crude description for the crystal potential in KNBO. A refined description of the crystal potential in KNBO may therefore be needed. However, it is deemed unnecessary to optimise a model for the crystal potential before the correct space group of a thin film KNBO specimen has been thoroughly assessed. For research applications, open-source simulation programmes should be used, as it allows for tweaking important parameters essential for correct simulations of dynamical diffraction experiments for complex crystal structures. The combined refinement of the crystal structure of thin film KNBO and the optimised model for simulations are important as it may provide an explanation for the observed presence and absence of polar domains in the *c*-axis in-plane and out-of-plane specimens respectively.

As discussed in Sections 5.1 and 5.2, the polishing scheme may have altered the crystal structure of KNBO such that it is less anisotropic with more equal *a* and *b* lattice parameters, hence removing the polar properties of the crystal domains. To investigate if this is true, it is proposed to first perform PFM on a bulk KNBO specimen in a facet where one domain is expected to be the *b*-direction. After this, one may prepare two specimens of the same crystal by 1) focused ion beam (FIB), and 2) mechanical tripod polishing. Other specimen preparation methods could also be assessed, such as ion milling or ion etching [29]. After TEM specimen preparation and space group determination, PFM should be performed on these specimens again. If the crystal structure of the specimens prepared by different methods are found to be the same, and the PFM identifies no polar domains in all specimens, it may be concluded that the change in the crystal structure and hence also the disappearance of polar domains were not a result from the polishing scheme, but a reduced-thickness effect. Hence, it could be helpful to perform PFM both before and after specimen preparation of several specimens prepared by different preparation schemes in order to understand the impact of TEM specimen preparation on changes in the physical properties of KNBO.

Performing PFM before making the TEM specimen may also be an easier approach to confirm the presence of polar domains in the specimen when it is prepared with the *c*-axis in-plane. PLM could only confirm the presence of ferroelastic domains in the *c*-facet, and that several such needle domains intersected the facet from which the TEM specimen was prepared, as presented in Section 4.1.1. However, PLM could not confirm how these domains oriented along that facet. For a complete correlated microscopy study, PFM should therefore be performed both before polishing the bulk crystal, but also after TEM inspections of the polished TEM specimen. This is because the specimen was observed to fracture when PFM was performed, as previously discussed. Another possibility could be to prepare two specimens in parallel from the same bulk crystal, and use one of them for PFM, and the other for TEM investigations.

In the *c*-axis in-plane specimen, several bands of contrast were observed with HAADF STEM, indicating the presence of several domain boundaries. As discussed in Section 5.4, the intensity variations adjacent to the boundaries could be due to defects or strain, both of which would affect the local conductivity, which is in turn relevant for using these types of materials in devices [17]. However, the wedge was often in a cluster of fractured pieces in which SAED, (LA)CBED and HRTEM would include confusing information from overlapping sheets. In the domains presented in this thesis, the only regions thin enough for HRTEM inspections were observed on either side of the bands, but not on or across them. For acquiring high-quality HR(S)TEM images across the domains, further thinning of the region identified by HAADF STEM should be performed. This could be done by either cutting out the identified region with FIB, thinning that specific region with ion milling, or etching the specimen. This will also be advantageous because it is expected that thinning will remove defects and fractured regions. The atomic structure at the domain walls will henceforth be more readily investigated by HR-HAADF STEM, and the symmetry of the (LA)CBED patterns will be more readily assessed.

Additionally, a thinner specimen would be advantageous for easier polarisation deductions by CBED. It has been shown that it is easier to isolate intensity variations that are results from polarity by evaluating the intensity variations of the CBED disks at a specimen thickness lower than the extinction length [100, 101]. This is because dynamical effects are not significant when the thickness of the specimen is lower than the extinction length. In such cases, one can directly identify the polar direction by comparing the intensity of Bijvoet pairs.[1] If a zone axis is chosen such that Bijvoet pairs occur symmetrically about a *m*-*m*' symmetry line, one would directly observe that all diffraction disks on one side of the symmetry line are brighter than the Bijvoet pairs on the other side of it. For orthorhombic point groups $2mm$, Tanaka *et al.* reported that the appropriate zone axes where Bijvoet pairs are separated by a mirror line are $\langle 0\,v\,w \rangle$.[2] Hence, the $[0\,1\,0]$ and $[0\,0\,1]$ zone axes should be such appropriate zones.

In the structural analysis of a material, simulation packages are crucial tools, already in the initial step of a study. From softwares such as JEMS and Recipro, the extinction length can be calculated from the given cif-file. Quick inspections in JEMS showed that the extinction length of most reflections close to the direct beam were larger than 100 nm. Hence, by ensuring that large regions of the specimen are thinner than this, CBED inspections should be more easily carried out. A shown in Section 4.2.1, the $[0\,0\,1]$ was observed in regions thinner than 100 nm, thus a distinct difference between the intensity on either side of the mirror line of Bivjoet pairs drawn between the $(4\,0\,0)$ and $(\bar{4}\,0\,0)$ reflections should have been visible if the specimen was polar in the *a*-direction. However, no such distinct intensity could be observed, even in the simulated patterns. The intensity of each CBED disk in both simulated an experimental diffraction patterns were quickly inspected with ImageJ in

---

[1] Bijvoet pairs are similar to Friedel pairs ($(h\,k\,l)$ and $(\bar{h}\,\bar{k}\,\bar{l})$), but may also include any reflection equivalent to the $(h\,k\,l)$ planes. For example, in a an orthorhombic crystal written in the **cab** setting, any set of equivalent indices $(h\,k\,l) = (h\,\bar{k}\,l) = (h\,k\,\bar{l}) = (h\,\bar{k}\,\bar{l})$ can form a Bijvoet pair with any of the second set of equivalent indices $(\bar{h}\,\bar{k}\,\bar{l}) = (\bar{h}\,k\,\bar{l}) = (\bar{h}\,\bar{k}\,l) = (\bar{h}\,k\,l)$. See Tanaka *et al.* and Mader *et al.* for further details [100, 101].

[2] This zone has been translated from the **abc** setting given in the paper by Tanaka *et al.* to the **cab** setting.

an attempt to assess polarisation of the specimen. However, no obvious difference could be observed in the intensity of Bijvoet pairs on either side of the Bijvoet mirror line. Hence, similar inspections should be carried out at other appropriate zones. To summarize, initial simulations showed that the analysis of the simulated intensities should be extended to other appropriate zones for the direct assessment of Bijvoet pairs.

The symmetry of the CBED and LACBED patterns presented in this thesis were assigned based on subjective judgement and the ability of the eye to recognise symmetry. This is tedious, and important details may be overlooked or discarded. It would therefore be an advantage to perform objective symmetry recognition by implementing a code that assigns symmetries to the CBED and LACBED patterns based on for example cross-correlation. Krajnak and Etheridge developed a code that recognise symmetry elements in scanning CBED patterns [102]. In that script, the symmetry of the CBED patterns are assigned by comparing the CBED pattern with itself after applying a symmetry operation to the pattern and calculating their cross-correlation. Hence, it should be possible to implement a similar code that purely assigns symmetries to a CBED and LACBED pattern. This is a suggestion for future work.

Another point for future work is to acquire scanning CBED patterns and use those patterns to reconstruct an image with symmetry contrast. By assigning local symmetries from the scattered intensity distribution, Krajnak and Etheridge's has also written a script to assign symmetry contrast by acquiring CBED patterns in a single point by 4D STEM data acquisition, reconstructing a STEM image from the CBED data. Such advanced imaging may be advantageous for KNBO, as it would provide symmetry contrast for identifying different domains. Note that scanning precession electron diffraction (SPED), which is often suggested for reconstructing STEM images, will average out the directional intensity variations. Initial SPED runs were done as a part of the project work and by Ryggetangen [1, 45], where it was discussed that SPED is inconclusive for structure and polar direction analysis in KNBO. This is why scanning CBED is rather suggested. Scanning CBED has the advantage that it would also acquire a large set of CBED patterns for each domain, thus acquiring the data required for assigning crystal orientations and assigning the polar directions in one session. Furthermore, Shao and Zuo have acquired similar 4D symmetry contrast images of extended regions using microscopes similar to those which were available for the current thesis, such as the *JEOL JEM-2100* with a LaB_6 thermionic electron source [46, 47]. Hence, it should be possible to perform such experiments with the same facilities as those available for this thesis. Further, scanning CBED could also help with characterizing whether the extended bands observed by HAADF STEM were individual domains or extended domain walls. The main disadvantage of scanning CBED to gain symmetry contrast is that it is susceptible to other factors that break the symmetry of the patterns, such as surface defects, bending and fractured regions. Hence, the specimen preparation of KNBO need to be optimised before symmetry contrast imaging by scanning CBED can be useful.

As discussed in Section 5.2, the intensity variations of specific reflections of interest, especially in the [0 0 1] CBED patterns, were subtle, and the orientation analysis was hampered by a diffuse background. To tackle the deteriorating background, energy filtering may be advantageous. Shao and Zuo have also shown that energy-filtered CBED may be helpful for assessing symmetries when the true symmetry of the crystal is expected to be observed by small intensity differences in the CBED disks [47]. This could be helpful for assigning symmetries in the [0 0 1], as the true crystal symmetry was expected to be observed as a small intensity variation in the CBED pattern. Additionally, the small intensity variations in the [0 0 1] were only expected at specific specimen thicknesses. For the structural analysis, acquiring CBED patterns at different specimen thicknesses might therefore be required. A wedge-shaped specimen, as was prepared for this work, offers the possibility of acquiring CBED patterns at several thicknesses, and future work should therefore ensure that a wedge-shaped specimen is prepared for structural analysis.

A final suggestion for future work is to perform in-situ or in-operando studies for characterising the ferroic nature of the bands. In these studies, the effect of temperature, pressure and an external electric field may be assessed while changes in the crystal structure are tracked by for example CBED, giving information on the evolution of the strain and polarisation of the crystal. It could also provide insight into the movement of domain walls by external fields, and hysteresis. Such experiments have previously been performed on similar ceramic materials, where the crystal structure has been characterised by CBED and BF TEM [94, 103, 104]. By performing in-situ and in-operando studies, it would be possible to gain direct and controlled insight into the structure-property relationship in KNBO, which is the main motivation in the scientific and technological interest of these multiferroic crystals.

7 Conclusion

This work has outlined a suggested framework for high-spatial-resolution ferroic domain inspections of KNBO using TEM. Electron diffraction patterns were successfully mapped for several zones in a single domain of the specimen through a tilt series. The most efficient technique for initially finding domain boundaries was HAADF STEM, and it was found that the optimal orientation of the specimen for domain localisation was slightly off a major zone with the *c*-axis in-plane. Correlated microscopy combining the structural characterisation of KNBO by TEM with the direct imaging of polar domains with PLM and PFM were also successfully performed. The four sub-goals that were set prior to this work have therefore been accomplished; 1) To map the electron diffraction patterns of KNBO at several zones, 2) to identify the diffraction and imaging techniques that are most optimal for assessing ferroic domains, 3) to identify the zones which display a sufficient change in the diffraction pattern to obtain domain contrast, and 4) to conduct correlated microscopy studies of KNBO as a proof-of-concept.

High-quality, millimetre-sized TEM specimens were prepared by mechanical tripod polishing with the *c*-axis in-plane and the *c*-axis out-of-plane to investigate the proposed polar axes of KNBO. Although KNBO was readily assessed with TEM, it was observed to be susceptible to charging and beam damage which may hamper detailed characterisation of KNBO below a threshold thickness. Low-dose (S)TEM was therefore proposed as an alternative to conventional TEM to avoid beam damage and charging. Thinner specimens are required for lattice imaging and practical polarity studies with CBED. The observed square fracturing in the *c*-axis in-plane specimen was proven to be a complication in achieving this.

Structural analysis of the specimens were performed by comparing experimental and simulated dynamical SAED, CBED and LACBED patterns, also in combination with HRTEM and HR-HAADF STEM images. The structural characterisation revealed that thin film KNBO specimens were not correctly described by the same space group as its bulk form. It was proposed that the altered crystal structure was an effect from the mechanical polishing, or the thin film geometry. Future work should therefore investigate the origin of the altered crystal structure of the TEM specimens with respect to the bulk crystal. Regarding the dynamic simulations, the PRDW model for the crystal potential simulated the diffraction patterns most realistically for ZOLZ patterns. However, refinements are required, as there were deviations between the experimental patterns and the simulated patterns, both when the PRDW model and other models were used.

120° twin domains in KNBO were for the first time investigated down to the lattice scale. The 120° twinning was attributed to the pseudo-hexagonal crystal structure of KNBO, where the symmetry of crystal planes 120° to each other were observed to almost coincide from electron diffraction and high-resolution imaging experiments. The twinning axis was also confirmed to be the *c*-axis, but the twins were observed to meet at $(2\,\bar{3}\,\bar{2})$, as the boundaries ran along the $g_{2\bar{3}\bar{2}}$. Another set of structural low-angle grain boundaries were for the first time observed, where the respective domains were related by an 0.6° rotation about an axis perpendicular to the $(2\,\bar{3}\,2)$ plane. These domains were suggested to be either antiferroelectric or sub-grain domains. Future work should investigate the origin of the 0.6° rotation by for example high-resolution lattice imaging in thinner specimens and by scanning CBED to achieve a higher-spatial resolution for structural analysis.

Both types of structural domains were observed to be separated by bands of width 200 nm –500 nm. The physical extent of the bands was up to two orders of magnitude larger than typical twin and ferroic domain boundaries. The bands were proposed to either be individual intermediate domains with adjacent altered domain structures, or extended domain walls. The latter was concluded to be most likely. Several suggestions for the origin of the bands were discussed, including surface relaxation and the accumulation of point defects.

The correlated microscopy study revealed an absence of extended polar domains in the specimen prepared with the c-axis in-plane, although structural twin domains were observed by electron diffraction in TEM. It was suggested that the absence of polar domains in the specimen prepared with the c-axis in-plane was an effect of the altered ferroic crystal structure. Contrarily, a presence of polar domains was identified in the specimen prepared with the c-axis out-of-plane, although no structural twin domains were observed by TEM in this specimen. The inability to assess structural domains in the c-axis out-of-plane specimen was attributed to the near $3m$ symmetry of the crystal in the $(0\,0\,1)$ plane. The inability to easily identify structural domains also underlined that specimens prepared with the c-axis out-of-plane may not be optimal for domain inspections of KNBO at the atomic scale with TEM.

From the combined structural analysis and correlated microscopy study of KNBO thin films, a framework for domain inspections at the atomic scale has been suggested. First, the origin of the altered crystal structure must be found, and the correct space group and lattice parameters of thin film KNBO must be determined. The framework should include PFM measurements to localise and determine the size of the ferroic domains before specimen preparation of a specimen with the c-axis in-plane. After this, HAADF STEM should be used to localise the domains in the TEM. If applicable, the specimen should be further thinned at a region of interest with FIB or ion milling. Structural analysis should be performed by SAED, CBED, LACBED, HRTEM and HR-HAADF STEM in separate domains and across the pre-located boundaries. The experimental diffraction patterns should be compared to simulated patterns for polarity assessment after the crystal structure of thin film KNBO has been determined. Finally, it would be interesting to investigate the polar and ferroic properties of KNBO by in-situ and in-operando studies.

To conclude, this work is so far the most elaborated TEM study of KNBO. It proposes a framework for domain characterisation of KNBO that may also be applicable to other multiferroic materials with similar challenging crystal structures that are candidates for novel devices based on ferroic domain wall engineering.

This page is intentionally left blank.

Bibliography

[1] M. Linnerud. Correlated transmission electron microscopy studies for high spatial resolution and lattice defect structure analysis in single crystal $K_3Nb_3B_2O_{12}$ and its domain wall structures. Project thesis, Norwegian University of Science and Technology, Høgskoleringen 1, 7491 Trondheim, Norway, 12 2021.

[2] K. Momma and F. Izumi. *VESTA3* for three-dimensional visualization of crystal, volumetric and morphology data. *Journal of Applied Crystallography*, 44(6): 1272–1276, Dec 2011. doi: 10.1107/S0021889811038970. URL `https://doi.org/10.1107/S0021889811038970`.

[3] P. Stadelmann. Simulation of diffraction patterns and high resolution images using jems, June 2008. URL `https://www.jems-swiss.ch/`.

[4] H. G. Brown and T. Aarholt. HamishGBrown/py_multislice: For publication with MeasureIce, December 2021. URL `https://doi.org/10.5281/zenodo.5762736`.

[5] Y. Seto and M. Ohtsuka. *ReciPro*: free and open-source multipurpose crystallographic software integrating a crystal model database and viewer, diffraction and microscopy simulators, and diffraction data analysis tools. *Journal of Applied Crystallography*, 55(2):397–410, Apr 2022. doi: 10.1107/S1600576722000139. URL `https://doi.org/10.1107/S1600576722000139`.

[6] J. Schindelin, I. Arganda-Carreras, E. Frise, V. Kaynig, M. Longair, T. Pietzsch, S. Preibisch, C. Rueden, S. Saalfeld, B. Schmid, J.-Y. Tinevez, D. J. White, V. Hartenstein, K. Eliceiri, P. Tomancak, and A. Cardona. Fiji: an open-source platform for biological-image analysis. *Nature Methods*, 9(7):676–682, June 2012. doi: 10.1038/nmeth.2019. URL `https://doi.org/10.1038/nmeth.2019`.

[7] Gatan Inc. Digitalmicrograph, 2020. URL `https://www.gatan.com/products/tem-analysis/gatan-microscopy-suite-software`.

[8] D. Nečas and P. Klapetek. Gwyddion: an open-source software for SPM data analysis. *Central European Journal of Physics*, 10:181–188, 2012. ISSN 1895-1082. doi: 10.2478/s11534-011-0096-2.

[9] Adobe Inc. Adobe illustrator, 2019. URL `https://adobe.com/products/illustrator`.

[10] Inkscape Project. Inkscape, 2020. URL `https://inkscape.org`.

[11] G. E. Moore. Cramming more components onto integrated circuits, reprinted from electronics, volume 38, number 8, april 19, 1965, pp.114 ff. *IEEE Solid-State Circuits Society Newsletter*, 11(3):33–35, 2006. doi: 10.1109/N-SSC.2006.4785860.

[12] J. M. Shalf and R. Leland. Computing beyond moore's law. *Computer*, 48(12): 14–23, December 2015. doi: 10.1109/mc.2015.374. URL `https://doi.org/10.1109/mc.2015.374`.

[13] Z. Guan, H. Hu, X. Shen, P. Xiang, N. Zhong, J. Chu, and C. Duan. Recent progress in two-dimensional ferroelectric materials. *Advanced Electronic Materials*, 6(1):1900818, 2020. doi: https://doi.org/10.1002/aelm.201900818. URL `https://onlinelibrary.wiley.com/doi/abs/10.1002/aelm.201900818`.

[14] J. Seidel. Domain walls as nanoscale functional elements. *The Journal of Physical Chemistry Letters*, 3(19):2905–2909, September 2012. doi: 10.1021/jz3011223. URL `https://doi.org/10.1021/jz3011223`.

[15] E. K. H. Salje. Functional twin boundaries: Steps towards domain boundary engineering. In *Mesoscopic Phenomena in Multifunctional Materials*, pages 201–223. Springer Berlin Heidelberg, 2014. doi: 10.1007/978-3-642-55375-2_8. URL `https://doi.org/10.1007/978-3-642-55375-2_8`.

[16] E. K. H. Salje and X. Ding. Ferroelastic domain boundary-based multiferroicity. *Crystals*, 6(12):163, December 2016. doi: 10.3390/cryst6120163. URL `https://doi.org/10.3390/cryst6120163`.

[17] D. Meier and S. M. Selbach. Ferroelectric domain walls for nanotechnology. *Nature Reviews Materials*, October 2021. doi: 10.1038/s41578-021-00375-z. URL `https://doi.org/10.1038/s41578-021-00375-z`.

[18] S. S. P. Parkin, M. Hayashi, and L. Thomas. Magnetic domain-wall racetrack memory. *Science*, 320(5873):190–194, 2008. doi: 10.1126/science.1145799. URL `https://www.science.org/doi/abs/10.1126/science.1145799`.

[19] E. K. H. Salje. Domain boundary engineering – recent progress and many open questions. *Phase Transitions*, 86(1):2–14, January 2013. doi: 10.1080/01411594.2012.694434. URL `https://doi.org/10.1080/01411594.2012.694434`.

[20] S. Li, X. Ding, J. Ren, X. Moya, J. Li, J. Sun, and E. K. H. Salje. Strain-controlled thermal conductivity in ferroic twinned films. *Scientific Reports*, 4(1), September 2014. doi: 10.1038/srep06375. URL `https://doi.org/10.1038/srep06375`.

[21] D. D. Viehland and E. K. H. Salje. Domain boundary-dominated systems: adaptive structures and functional twin boundaries. *Advances in Physics*, 63 (4):267–326, July 2014. doi: 10.1080/00018732.2014.974304. URL `https://doi.org/10.1080/00018732.2014.974304`.

[22] G. Catalan, J. Seidel, R. Ramesh, and J. F. Scott. Domain wall nanoelectronics. *Reviews of Modern Physics*, 84(1):119–156, February 2012. doi: 10.1103/revmodphys.84.119. URL `https://doi.org/10.1103/revmodphys.84.119`.

[23] E. K. H. Salje. Ferroelastic domain walls as templates for multiferroic devices. *Journal of Applied Physics*, 128(16):164104, October 2020. doi: 10.1063/5.0029160. URL `https://doi.org/10.1063/5.0029160`.

[24] R. Sbiaa. Multistate magnetic domain wall devices for neuromorphic computing. *physica status solidi (RRL) - Rapid Research Letters*, 15(7):2100125, 2021. doi: https://doi.org/10.1002/pssr.202100125. URL `https://onlinelibrary.wiley.com/doi/abs/10.1002/pssr.202100125`.

[25] P. Sharma, T. S. Moise, L. Colombo, and J. Seidel. Roadmap for ferroelectric domain wall nanoelectronics. *Advanced Functional Materials*, 32 (10):2110263, 2022. doi: https://doi.org/10.1002/adfm.202110263. URL `https://onlinelibrary.wiley.com/doi/abs/10.1002/adfm.202110263`.

[26] E. K. H. Salje and H. Zhang. Domain boundary engineering. *Phase Transitions*, 82(6):452–469, 2009. doi: 10.1080/01411590902936138. URL `https://doi.org/10.1080/01411590902936138`.

[27] S. Van Aert, S. Turner, R. Delville, D. Schryvers, G. Van Tendeloo, and E. K. H. Salje. Direct observation of ferrielectricity at ferroelastic domain boundaries in $CaTiO_3$ by electron microscopy. *Advanced Materials*, 24(4):523–527, December 2011. doi: 10.1002/adma.201103717. URL `https://doi.org/10.1002/adma.201103717`.

[28] B. Fultz and J. Howe. *Transmission Electron Microscopy and Diffractometry of Materials.* Graduate Texts in Physics. Springer Berlin Heidelberg, Berlin, Heidelberg, 4th ed. 2013 edition, 2013. ISBN 3642297609.

[29] D. B Williams and C. B. Carter. *Transmission Electron Microscopy.* Springer US, 2009. doi: 10.1007/978-0-387-76501-3. URL `https://doi.org/10.1007/978-0-387-76501-3`.

[30] E. K. H. Salje. Multiferroic domain boundaries as active memory devices: Trajectories towards domain boundary engineering. *ChemPhysChem*, 11(5):940–950, March 2010. doi: 10.1002/cphc.200900943. URL `https://doi.org/10.1002/cphc.200900943`.

[31] G. Catalan, J. Seidel, R. Ramesh, and J. F. Scott. Domain wall nanoelectronics. *Rev. Mod. Phys.*, 84:119–156, Feb 2012. doi: 10.1103/RevModPhys.84.119. URL `https://link.aps.org/doi/10.1103/RevModPhys.84.119`.

[32] E. K. H. Salje. Robust templates for domain boundary engineering in $ErMnO_3$. *New Journal of Physics*, 18(5):051001, may 2016. doi: 10.1088/1367-2630/18/5/051001. URL `https://doi.org/10.1088/1367-2630/18/5/051001`.

[33] E. K. H. Salje, O. Aktas, and X. Ding. Functional topologies in (multi-) ferroics: The ferroelastic template. In *Topological Structures in Ferroic Materials*, pages 83–101. Springer International Publishing, 2016. doi: 10.1007/978-3-319-25301-5_4. URL `https://doi.org/10.1007/978-3-319-25301-5_4`.

[34] D. Meier. Functional domain walls in multiferroics. *Journal of Physics: Condensed Matter*, 27(46):463003, November 2015. doi: 10.1088/0953-8984/27/46/463003. URL `https://doi.org/10.1088/0953-8984/27/46/463003`.

[35] A. A. Kaminskii, P. Becker, L. Bohatý, H. J. Eichler, A. N. Penin, K. Ueda, J. Hanuza, K. Takaichi, and H. Rhee. Room-temperature high-order stokes and anti-stokes generation in orthorhombic ferroelectric-ferroelastic $K_3Nb_3O_6(BO_3)_2$ crystal. *physica status solidi (a)*, 201(9):2154–2169, 2004. doi: https://doi.org/10.1002/pssa.200406834. URL `https://onlinelibrary.wiley.com/doi/abs/10.1002/pssa.200406834`.

[36] P. Becker, P. Held, and L. Bohaty. Crystal growth of ferroelectric and ferroelastic $K_3[Nb_3O_6|(BO_3)_2]$ and crystal structure of the room temperature modification. *Zeitschrift Fur Kristallographie - Z KRISTALLOGR*, 211:449–452, 07 1996. doi: 10.1524/zkri.1996.211.7.449.

[37] P. Shan, J. Xiong, Z. Wang, C. He, X. Yang, R. Su, and X. Long. Lead-free polar borate crystal $K_3Nb_3B_2O_{12}$: a novel antiferroelectric structure type. *J. Mater. Chem. C*, 8:6654–6658, 2020. doi: https://doi.org/10.1039/D0TC01383H. URL `http://dx.doi.org/10.1039/D0TC01383H`.

[38] J. Choisnet, D. Groult, B. Raveau, and M. Gasperin. Nouvelles structures à tunnels de section pentagonale $K_3Nb_3B_2O_{12}$ et $K_3Ta_3B_2O_{12}$. *Acta Crystallographica Section B: Structural Crystallography and Crystal Chemistry*, 33(6):1841–1845, 1977.

[39] V. I. Voronkova, E. P. Kharitonova, V. K. Yanovskii, S. Yu Stefanovich, A. V. Mosunov, and N. I. Sorokina. Growth, structure, and properties of ferroelectric—ferroelastic—superionic $K_3Nb_3B_2O_{12}$ and $K_3{-}xNaxNb_3B_2O_{12}$ crystals. *Crystallography Reports*, 45(5):816–820, 2000. doi: https://doi.org/10.1134/1.1312928.

[40] E. P. Kharitonova, V. I. Voronkova, V. K. Yanovskii, and S. Y. Stefanovich. Polymorphism of ferroelectric, ferroelastic, superionic crystals $K_3Nb_3B_2O_{12}$ and $K_3{-}xNaxNb_3B_2O_{12}$. *Inorganic materials*, 38(8):819–824, 2002. doi: https://doi.org/10.1023/A:1019782912439.

[41] E. P. Kharitonova, V. I. Voronkova, and V. K. Yanovskii. Phase transitions and ferroelectric and superionic properties of $K_3Nb_3B_2O_{12}$–$K_3Nb_3Si_2O_{13}$ single crystals. *Inorganic materials*, 39(2):127–132, 2003. doi: https://doi.org/10.1023/A:1022190411905.

[42] P. Shan, B. Li, L. Huang, J. Shang, C. He, Z. Wang, X. Yang, R. Su, G. Zhang, and X. Long. Electro-optic modulation in a non-centrosymmetric antiferroelectric crystal. *J. Mater. Chem. C*, 9:9431–9435, 2021. doi: 10.1039/D1TC02309H. URL `http://dx.doi.org/10.1039/D1TC02309H`.

[43] M. Maczka, W. Paraguassu, P. T. C. Freire, A. G.S Souza Filho, J. Mendes Filho, and J. Hanuza. High-pressure raman scattering study of ferroelectric $K_3Nb_3O_6(BO_3)_2$. *Phys. Rev. B*, 82:014106, Jul 2010. doi: 10.1103/PhysRevB.82.014106. URL `https://link.aps.org/doi/10.1103/PhysRevB.82.014106`.

[44] M. Mączka, J. Hanuza, and S. Kojima. High-resolution temperature-dependent brillouin scattering studies of ferroelectric $K_3Nb_3O_6(BO_3)_2$. *Phys. Rev. B*, 77:104116, Mar 2008. doi: 10.1103/PhysRevB.77.104116. URL `https://link.aps.org/doi/10.1103/PhysRevB.77.104116`.

[45] O. Ryggetangen. Domain imaging of multiferroic $K_3Nb_3B_2O_{12}$ by transmission electron microscopy. Master's thesis, Norwegian University of Science and Technology, Høgskoleringen 1, 7491 Trondheim, Norway, 06 2021.

[46] Y.-T. Shao and J.-M. Zuo. Symmetry-breaking nanoregions in single-phase high entropy alloys determined using scanning convergent beam electron diffraction. *Microscopy and Microanalysis*, 23(S1):348–349, 2017. doi: 10.1017/S1431927617002422.

[47] Y.-T. Shao and J.-M. Zuo. Nanoscale symmetry fluctuations in ferroelectric barium titanate, $BaTiO_3$. *Acta Crystallographica Section B*, 73(4):708–714, Aug 2017. doi: 10.1107/S2052520617008496. URL `https://doi.org/10.1107/S2052520617008496`.

[48] Z. Dauter and M. Jaskolski. How to read (and understand) volume a of international tables for crystallography: An introduction for nonspecialists. *J. Appl. Cryst. J. Appl. Cryst*, 43:1150–1171, 10 2010. doi: 10.1107/S0021889810026956.

[49] C. Hammond. *The Basics of Crystallography and Diffraction.* Oxford University Press, 4th edition, 2015.

[50] IUCr and T. Hahn. *International Tables for Crystallography, Volume A: Space Group Symmetry.* Kluwer Academic Publishers, Dordrecht, Boston, London, 5th revised edition, 2002.

[51] C. Kittel. *Introduction to Solid State Physics.* Wiley, 8th edition, 2004. ISBN 9780471415268. URL `http://www.amazon.com/Introduction-Solid-Physics-Charles-Kittel/dp/047141526X/ref=dp_ob_title_bk`.

[52] A. R. West. *Solid state chemistry and its applications*, page 470. Wiley, Chichester, England, 2nd edition, student edition, 2014. ISBN 9781118676240.

[53] R. J. D. Tilley. *Understanding solids : the science of materials.* Wiley, John Wiley & Sons Inc., Chichester, West Sussex, United Kingdom, 2nd edition, 2013. ISBN 9781118423288.

[54] E. K. H. Salje. Ferroelastic materials. *Annual Review of Materials Research*, 42(1):265–283, 2012. doi: 10.1146/annurev-matsci-070511-155022. URL `https://doi.org/10.1146/annurev-matsci-070511-155022`.

[55] H. Schmid. Polarized light microscopy (PLM) of ferroelectric and ferroelastic domains in transmitted and reflected light. In N. Setter and E. L. Colla, editors, *Ferroelectric Ceramics*, pages 107–126, Basel, 1993. Birkhäuser Basel. ISBN 978-3-0348-7551-6.

[56] B. E. A. Saleh and M. C. Teich. *Fundamentals of photonics*, pages 238–239. John Wiley & Sons, 3rd edition, 2019.

[57] G. F Nataf and M. Guennou. Optical studies of ferroelectric and ferroelastic domain walls. 32(18):183001, feb 2020. doi: 10.1088/1361-648x/ab68f3. URL `https://doi.org/10.1088/1361-648x/ab68f3`.

[58] A. Gruverman, M. Alexe, and D. Meier. Piezoresponse force microscopy and nanoferroic phenomena. *Nature Communications*, 10(1), April 2019. doi: 10.1038/s41467-019-09650-8. URL `https://doi.org/10.1038/s41467-019-09650-8`.

[59] M. De Graef. *Introduction to Conventional Transmission Electron Microscopy.* Cambridge University Press, 2003. doi: 10.1017/CBO9780511615092.

[60] E. J. Kirkland. *Theory of Calculation of Images of Thick Specimens*, pages 143–195. Springer International Publishing, Cham, 2020. ISBN 978-3-030-33260-0. doi: 10.1007/978-3-030-33260-0_6. URL `https://doi.org/10.1007/978-3-030-33260-0_6`.

[61] P. A. Doyle and P. S. Turner. Relativistic Hartree–Fock X-ray and electron scattering factors. *Acta Crystallographica Section A*, 24(3):390–397, May 1968. doi: 10.1107/S0567739468000756. URL `https://doi.org/10.1107/S0567739468000756`.

[62] E. J. Kirkland. *Advanced Computing in Electron Microscopy.* Springer International Publishing, Cham, 3rd edition, 2020. ISBN 3030332594. doi: 10.1007/978-3-030-33260-0.

[63] D. M. Bird and Q. A. King. Absorptive form factors for high-energy electron diffraction. *Acta Crystallographica Section A*, 46(3):202–208, Mar 1990. doi: 10.1107/S0108767389011906. URL `https://doi.org/10.1107/S0108767389011906`.

[64] L.-M. Peng, G. Ren, S. L. Dudarev, and M. J. Whelan. Robust Parameterization of Elastic and Absorptive Electron Atomic Scattering Factors. *Acta Crystallographica Section A*, 52(2):257–276, Mar 1996. doi: 10.1107/S0108767395014371. URL `https://doi.org/10.1107/S0108767395014371`.

[65] L.-M. Peng. Electron Scattering Factors of Ions and their Parameterization. *Acta Crystallographica Section A*, 54(4):481–485, Jul 1998. doi: 10.1107/S0108767398001901. URL `https://doi.org/10.1107/S0108767398001901`.

[66] A. Weickenmeier and H. Kohl. Computation of absorptive form factors for high-energy electron diffraction. *Acta Crystallographica Section A*, 47(5):590–597, Sep 1991. doi: 10.1107/S0108767391004804. URL `https://doi.org/10.1107/S0108767391004804`.

[67] I. Lobato and D. Van Dyck. An accurate parameterization for scattering factors, electron densities and electrostatic potentials for neutral atoms that obey all physical constraints. *Acta Crystallographica Section A*, 70(6):636–649, Nov 2014. doi: 10.1107/S205327331401643X. URL `https://doi.org/10.1107/S205327331401643X`.

[68] C. B. Carter and D. B Williams, editors. *Transmission Electron Microscopy.* Springer International Publishing, 2016. doi: 10.1007/978-3-319-26651-0. URL `https://doi.org/10.1007/978-3-319-26651-0`.

[69] B. F. Buxton, J. A. Eades, J. W. Steeds, and G. M. Rackham. The symmetry of electron diffraction zone axis patterns. *Philosophical Transactions of the Royal Society of London. Series A, Mathematical and Physical Sciences*, 281(1301): 171–194, March 1976. doi: 10.1098/rsta.1976.0024. URL `https://doi.org/10.1098/rsta.1976.0024`.

[70] F. A. Ponce, D. P. Bour, W.T. Young, M. Saunders, and J. W. Steeds. Determination of lattice polarity for growth of gan bulk single crystals and epitaxial layers. *Applied Physics Letters*, 69(3):337–339, 1996. doi: 10.1063/1.118052. URL `https://doi.org/10.1063/1.118052`.

[71] B. Daudin, J. L. Rouvière, and M. Arlery. Polarity determination of gan films by ion channeling and convergent beam electron diffraction. *Applied Physics Letters*, 69(17):2480–2482, 1996. doi: 10.1063/1.117504. URL `https://doi.org/10.1063/1.117504`.

[72] J. Taftø and J. C. H. Spence. A simple method for the determination of structure-factor phase relationships and crystal polarity using electron diffraction. *Journal of Applied Crystallography*, 15(1):60–64, Feb 1982. doi: 10.1107/S0021889882011352. URL `https://doi.org/10.1107/S0021889882011352`.

[73] I. Ushakov and D. Meier. On the piezo-response in $K_3Nb_3B_2O_{12}$. Unpublished, Norwegian University of Science and Technology, Department of Materials Science and Technology, Retrieved June 2022.

[74] M. Själander, M. Jahre, G. Tufte, and N. Reissmann. EPIC: An energy-efficient, high-performance GPGPU computing research infrastructure, 2019.

[75] H. W. Ånes. Tripod cross-section polishing scheme. Unpublished, TEM Gemini Centre, Department of Physics, NO-7491 Trondheim, Norway, 01 2017.

[76] J. G. Lozano, G. T. Martinez, L. Jin, P. D. Nellist, and P. G. Bruce. Low-dose aberration-free imaging of li-rich cathode materials at various states of charge using electron ptychography. *Nano Letters*, 18(11):6850–6855, 2018. doi: 10.1021/acs.nanolett.8b02718. URL `https://doi.org/10.1021/acs.nanolett.8b02718`. PMID: 30257093.

[77] M. Ilett, M. S'ari, H. Freeman, Z. Aslam, N. Koniuch, M. Afzali, J. Cattle, R. Hooley, T. Roncal-Herrero, S. M. Collins, N. Hondow, A. Brown, and R. Brydson. Analysis of complex, beam-sensitive materials by transmission electron microscopy and associated techniques. *Philosophical Transactions of the Royal Society A: Mathematical, Physical and Engineering Sciences*, 378(2186):20190601, 2020. doi: 10.1098/rsta.2019.0601. URL `https://royalsocietypublishing.org/doi/abs/10.1098/rsta.2019.0601`.

[78] I. Lobato, S. Van Aert, and J. Verbeeck. Progress and new advances in simulating electron microscopy datasets using multem. *Ultramicroscopy*, 168:17–27, 2016.

[79] Á. Butykai, S. Bordács, I. Kézsmárki, V. Tsurkan, A. Loidl, J. Döring, E. Neuber, P. Milde, S.C. Kehr, and L. M. Eng. Characteristics of ferroelectric-ferroelastic domains in néel-type skyrmion host GaV4s8. *Scientific Reports*, 7(1), March 2017. doi: 10.1038/srep44663. URL `https://doi.org/10.1038/srep44663`.

[80] W. Park and J.-B. Lee. Mechanically tunable photonic crystal structure. *Applied Physics Letters*, 85(21):4845–4847, 2004. doi: 10.1063/1.1823019. URL `https://doi.org/10.1063/1.1823019`.

[81] V. Šepelák, K. Tkácová, V. V. Boldyrev, and U. Steinike. Crystal structure refinement of the mechanically activated spinel-ferrite. *Materials Science Forum*, 228-231:783–788, July 1996. doi: 10.4028/www.scientific.net/msf.228-231.783. URL `https://doi.org/10.4028/www.scientific.net/msf.228-231.783`.

[82] V. Šepelák, S. Bégin-Colin, and G. Le Caër. Transformations in oxides induced by high-energy ball-milling. *Dalton Transactions*, 41(39):11927, 2012. doi: 10.1039/c2dt30349c. URL `https://doi.org/10.1039/c2dt30349c`.

[83] K. Regulska, B. Januszewicz, L. Klimek, and A. Palatyńska-Ulatowska. Analysis of the surface condition and changes in crystallographic structure of zirconium oxide affected by mechanical processing. *Materials*, 14(14), 2021. ISSN 1996-1944. doi: 10.3390/ma14144042. URL `https://www.mdpi.com/1996-1944/14/14/4042`.

[84] G. Cao. *Nanostructures and nanomaterials : synthesis, properties, and applications*, volume vol. 2 of *World Scientific series in nanoscience and nanotechnology*. World Scientific, New Jersey, 2nd edition, 2011. ISBN 9789814324557.

[85] N. Setter, D. Damjanovic, L. Eng, G. Fox, S. Gevorgian, S. Hong, A. Kingon, H. Kohlstedt, N. Y. Park, G. B. Stephenson, I. Stolitchnov, A. K. Taganstev, D. V. Taylor, T. Yamada, and S. Streiffer. Ferroelectric thin films: Review of materials, properties, and applications. *Journal of Applied Physics*, 100(5): 051606, September 2006. doi: 10.1063/1.2336999. URL `https://doi.org/10.1063/1.2336999`.

[86] H. Qiao, C. Wang, W. S. Choi, M. H. Park, and Y. Kim. Ultra-thin ferroelectrics. *Materials Science and Engineering: R: Reports*, 145:100622, 2021. ISSN 0927-796X. doi: https://doi.org/10.1016/j.mser.2021.100622. URL `https://www.sciencedirect.com/science/article/pii/S0927796X21000176`.

[87] V. Grillo. The effect of surface strain relaxation on HAADF imaging. *Ultramicroscopy*, 109(12):1453–1464, 2009. ISSN 0304-3991. doi: https://doi.org/10.1016/j.ultramic.2009.07.010. URL `https://www.sciencedirect.com/science/article/pii/S0304399109001831`.

[88] A. Beyer, L. Duschek, J. Belz, J. O. Oelerich, K. Jandieri, and K. Volz. Influence of surface relaxation of strained layers on atomic resolution ADF imaging. *Ultramicroscopy*, 181:8–16, 2017. ISSN 0304-3991. doi: https://doi.org/10.1016/j.ultramic.2017.04.019. URL `https://www.sciencedirect.com/science/article/pii/S0304399116303606`.

[89] Z. Yu, D.A. Muller, and J. Silcox. Effects of specimen tilt in ADF-STEM imaging of a-Si/c-Si interfaces. *Ultramicroscopy*, 108(5):494–501, 2008. ISSN 0304-3991. doi: https://doi.org/10.1016/j.ultramic.2007.08.007. URL `https://www.sciencedirect.com/science/article/pii/S0304399107001982`.

[90] Courtney-Davies, Ciobanu, Verdugo-Ihl, Slattery, Cook, Dmitrijeva, Keyser, Wade, Domnick, Ehrig, Xu, and Kontonikas-Charos. Zircon at the nanoscale records metasomatic processes leading to large magmatic–hydrothermal ore systems. *Minerals*, 9(6):364, June 2019. doi: 10.3390/min9060364. URL `https://doi.org/10.3390/min9060364`.

[91] H. Vahidi, K. Syed, H. Guo, X. Wang, J. L. Wardini, J. Martinez, and W. J. Bowman. A review of grain boundary and heterointerface characterization in polycrystalline oxides by (scanning) transmission electron microscopy. *Crystals*, 11(8):878, July 2021. doi: 10.3390/cryst11080878. URL `https://doi.org/10.3390/cryst11080878`.

[92] X.-K. Wei, A. K. Tagantsev, A. Kvasov, K. Roleder, C.-L. Jia, and N. Setter. Ferroelectric translational antiphase boundaries in nonpolar materials. *Nature Communications*, 5(1), January 2014. doi: 10.1038/ncomms4031. URL `https://doi.org/10.1038/ncomms4031`.

[93] M. Gao, X. Tang, S. Dai, J. Li, and D. Viehland. Depth dependent ferroelectric to incommensurate/commensurate antiferroelectric phase transition in epitaxial lanthanum modified lead zirconate titanate thin films. *Applied Physics Letters*, 115(7):072901, 2019. doi: 10.1063/1.5113720. URL `https://doi.org/10.1063/1.5113720`.

[94] M. Otonicar, J. Park, M. Logar, G. Esteves, J. L. Jones, and B. Jancar. External-field-induced crystal structure and domain texture in (1-x)$\mathrm{Na_0 \cdot 5\,Bi_0 \cdot 5\,TiO_3{-}xK_0 \cdot 5\,Bi_0 \cdot 5\,TiO_3}$ piezoceramics. *Acta Materialia*, 127:319–331, 2017. ISSN 1359-6454. doi: https://doi.org/10.1016/j.actamat.2017.01.052. URL `https://www.sciencedirect.com/science/article/pii/S1359645417300642`.

[95] M.-H. Zhang, L. Fulanović, S. Egert, H. Ding, P. B. Groszewicz, H.-J. Kleebe, L. Molina-Luna, and J. Koruza. Electric-field-induced antiferroelectric to ferroelectric phase transition in polycrystalline nanbo3. *Acta Materialia*, 200:127–135, 2020. ISSN 1359-6454. doi: https://doi.org/10.1016/j.actamat.2020.09.002. URL `https://www.sciencedirect.com/science/article/pii/S1359645420306960`.

[96] G. Catalan. Physics of ferroic and multiferroic domain walls. In *Mesoscopic Phenomena in Multifunctional Materials*, pages 225–247. Springer Berlin Heidelberg, 2014. doi: 10.1007/978-3-642-55375-2_9. URL `https://doi.org/10.1007/978-3-642-55375-2_9`.

[97] T. Kogure, H. Raimbourg, A. Kumamoto, E. Fujii, and Y. Ikuhara. Subgrain boundary analyses in deformed orthopyroxene by TEM/STEM with EBSD-FIB sample preparation technique. *Earth, Planets and Space*, 66(1), August 2014. doi: 10.1186/1880-5981-66-84. URL `https://doi.org/10.1186/1880-5981-66-84`.

[98] M. Gemmi, E. Mugnaioli, T. E. Gorelik, U. Kolb, L. Palatinus, P. Boullay, S. Hovmöller, and J. P. Abrahams. 3D Electron Diffraction: The Nanocrystallography Revolution. *ACS Central Science*, 5(8):1315–1329, 2019. doi: 10.1021/acscentsci.9b00394. URL `https://doi.org/10.1021/acscentsci.9b00394`. PMID: 31482114.

[99] R. Beanland, P. J. Thomas, D. I. Woodward, P. A. Thomas, and R. A. Roemer. Digital electron diffraction – seeing the whole picture. *Acta Crystallographica Section A*, 69(4):427–434, Jul 2013. doi: 10.1107/S0108767313010143. URL https://doi.org/10.1107/S0108767313010143.

[100] W. Mader and A. Rečnik. Determination of crystal polarity by electron diffraction from thin crystals. *physica status solidi (a)*, 166(1):381–395, 1998. doi: https://doi.org/10.1002/(SICI)1521-396X(199803)166:1<381::AID-PSSA381>3.0.CO;2-R. URL https://onlinelibrary.wiley.com/doi/abs/10.1002/%28SICI%291521-396X%28199803%29166%3A1%3C381%3A%3AAID-PSSA381%3E3.0.CO%3B2-R.

[101] K. Tanaka, N. L. Okamoto, S. Fujio, H. Sakamoto, and H. Inui. Appropriate zone-axis orientations for the determination of crystal polarity by convergent-beam electron diffraction. *Journal of Applied Crystallography*, 48(3):736–746, Jun 2015. doi: 10.1107/S1600576715004884. URL https://doi.org/10.1107/S1600576715004884.

[102] M. Krajnak and J. Etheridge. A symmetry-derived mechanism for atomic resolution imaging. *Proceedings of the National Academy of Sciences*, 117(45): 27805–27810, 2020. doi: 10.1073/pnas.2006975117. URL https://www.pnas.org/doi/abs/10.1073/pnas.2006975117.

[103] J. Gao, Y. Hao, R. Shuai, T. Kimoto, M. Fang, H. Li, Y. Wang, L. Zhong, S. Li, and X. Ren. Large piezoelectricity in Pb-free $0.96\,(\mathrm{K}_0\cdot 5\,\mathrm{Na}_0\cdot 5)0.95\,\mathrm{Li}_0\cdot 05\,\mathrm{Nb}_0\cdot 93\,\mathrm{Sb}_0\cdot 07\,\mathrm{O}_3-0.04\,\mathrm{BaZrO}_3$ ceramic: A perspective from microstructure. *Journal of Applied Physics*, 117:084106, 02 2015. doi: 10.1063/1.4913454.

[104] P. Gao, J. Britson, C. T. Nelson, J. R. Jokisaari, C. Duan, M. Trassin, S.-H. Baek, H. Guo, L. Li, Y. Wang, Y.-H. Chu, A. M. Minor, C.-B. Eom, R. Ramesh, L.-Q. Chen, and X. Pan. Ferroelastic domain switching dynamics under electrical and mechanical excitations. *Nature Communications*, 5(1), May 2014. doi: 10.1038/ncomms4801. URL https://doi.org/10.1038/ncomms4801.

Appendices

A Transformation of space group settings

This appendix is based on the corresponding appendix outlined for the project thesis that was written prior to this work [1]. The transformation of a space group setting involves the transformation of the crystallographic coordinate system. Further details can be found in Chapter 5.2 in *The International Tables of Crystallography, Volume A* [50].

The transformation of the **abc**-setting to the **cab**-setting in real space is described by equation A.1.

$$(c, a, b) = (a, b, c) \begin{pmatrix} 0 & 1 & 0 \\ 0 & 0 & 1 \\ 1 & 0 & 0 \end{pmatrix} \tag{A.1}$$

To transform the **abc**-setting to the **cab**-setting in reciprocal space, equation A.2 must be used.

$$\begin{pmatrix} c^* \\ a^* \\ b^* \end{pmatrix} = \begin{pmatrix} 0 & 0 & 1 \\ 1 & 0 & 0 \\ 0 & 1 & 0 \end{pmatrix} \begin{pmatrix} a^* \\ b^* \\ c^* \end{pmatrix} \tag{A.2}$$

B KNBO cif-file

Created by the author, based on the crystal data from Becker *et al.* [36].

```
#=====================================================
# CRYSTAL DATA
#-----------------------------------------------------
data_VESTA_phase_1

_chemical_name_common                  'potassium niobate borate'
_cell_length_a                         17.506(2)
_cell_length_b                         15.162(3)
_cell_length_c                         3.9680(4)
_cell_angle_alpha                      90.000000
_cell_angle_beta                       90.000000
_cell_angle_gamma                      90.000000
_cell_volume                           1053.210250
_space_group_name_H-M_alt              'P 21 m a'
_space_group_IT_number                 26

loop_
_space_group_symop_operation_xyz
   'x, y, z'
   'x+1/2, -y, -z'
   'x+1/2, y, -z'
   'x, -y, z'

loop_
   _atom_site_label
   _atom_site_occupancy
   _atom_site_fract_x
   _atom_site_fract_y
   _atom_site_fract_z
   _atom_site_adp_type
   _atom_site_U_iso_or_equiv
   _atom_site_type_symbol
   K1         1.0     0.83089(10)  0.000000     0.4866(2)    Uani
    0.013367  K
   K2         1.0     0.88392(8)   0.70192(7)   0.49308(16)  Uani
    0.013900  K
   K3         1.0     0.58096(10)  0.500000     0.4933(4)    Uani
    0.013800  K
   K4         1.0     0.63371(8)   0.20207(7)   0.4975(2)    Uani
    0.013933  K
   Nb1        1.0     0.65582(8)   0.000000     0.95441(11)  Uani
    0.003900  Nb
   Nb2        1.0     0.97116(4)   0.87691(2)   0.9643(2)    Uani
    0.005000  Nb
   Nb3        1.0     0.90594(9)   0.500000     0.9784(4)    Uani
    0.005167  Nb
   Nb4        1.0     0.72117(4)   0.37686(2)   0.9724(2)    Uani
    0.004000  Nb
   O1         1.0     0.6635(7)    0.000000     0.5007(13)   Uani
    0.010433  O
   O2         1.0     0.9135(7)    0.500000     0.520(2)     Uani
    0.012333  O
   O3         1.0     0.9413(4)    0.000000     0.9997(7)    Uani
    0.009567  O
```

```
   O4         1.0     0.6921(4)    0.500000     0.0114(8)   Uani   0.009600 O
   O5         1.0     0.0004(4)    0.7485(4)    0.0074(7)   Uani   0.013600 O
   O6         1.0     0.7503(4)    0.2485(2)    0.0206(7)   Uani   0.013833 O
   O7         1.0     0.9683(5)    0.8696(2)    0.5054(13)  Uani   0.013000 O
   O8         1.0     0.7181(5)    0.3698(2)    0.5189(14)  Uani   0.012467 O
   O9         1.0     0.8601(4)    0.1580(4)    0.0087(7)   Uani   0.014367 O
   O10        1.0     0.6103(4)    0.3421(4)    0.0209(7)   Uani   0.013200 O
   O11        1.0     0.5775(2)    0.9096(2)    0.9960(7)   Uani   0.008233 O
   O12        1.0     0.8278(2)    0.5900(2)    0.0139(5)   Uani   0.008800 O
   O13        1.0     0.7377(4)    0.9065(4)    1.0002(7)   Uani   0.014333 O
   O14        1.0     0.9878(4)    0.5937(4)    0.0240(7)   Uani   0.012800 O
   B1         1.0     0.7834(4)    0.1667(4)    0.0083(7)   Uani   0.008467 B
   B2         1.0     0.0332(4)    0.6667(4)    0.0029(8)   Uani   0.007500 B

loop_
   _atom_site_aniso_label
   _atom_site_aniso_U_11
   _atom_site_aniso_U_22
   _atom_site_aniso_U_33
   _atom_site_aniso_U_12
   _atom_site_aniso_U_13
   _atom_site_aniso_U_23
   K1  0.00860  0.01910  0.01240  0.00000  0.00030  0.00000
   K2  0.01490  0.01470  0.01210 -0.00290 -0.00010 -0.00010
   K3  0.00940  0.02040  0.01160  0.00000  0.00070  0.00000
   K4  0.01540  0.01430  0.01210 -0.00320 -0.00020  0.00070
   Nb1   0.00270  0.00530  0.00370  0.00000  0.00030  0.00000
   Nb2   0.00310  0.00520  0.00670 -0.00028  0.00000  0.00006
   Nb3   0.00300  0.00590  0.00660  0.00000  0.00000  0.00000
   Nb4   0.00360  0.00560  0.00280 -0.00037  0.00010  0.00008
   O1  0.00500  0.02200  0.00430  0.00000  0.00050  0.00000
   O2  0.00800  0.02400  0.00500  0.00000  0.00000  0.00000
   O3  0.00700  0.00800  0.01370  0.00000  0.00080  0.00000
   O4  0.00600  0.00900  0.01380  0.00000  0.00250  0.00000
   O5  0.01000  0.00600  0.02480  0.00300  0.00090  0.00030
   O6  0.01300  0.00540  0.02310  0.00500  0.00040 -0.00030
   O7  0.01400  0.01800  0.00700 -0.00200  0.00060  0.00020
   O8  0.01600  0.01700  0.00440 -0.00100  0.00020  0.00040
   O9  0.00600  0.01500  0.02210  0.00000 -0.00010 -0.00090
   O10   0.00100  0.01400  0.02460 -0.00020 -0.00050  0.00060
   O11   0.00500  0.00590  0.01380  0.00210 -0.00010 -0.00030
   O12   0.00500  0.00720  0.01420 -0.00160 -0.00030 -0.00060
   O13   0.00800  0.01000  0.02500  0.00400 -0.00070 -0.00030
   O14   0.00700  0.00900  0.02240 -0.00360 -0.00010  0.00040
   B1  0.00800  0.00900  0.00840 -0.00100  0.00010 -0.00010
   B2  0.00700  0.00700  0.00850  0.00100  0.00020  0.00030
```

C Multislice simulations

This appendix presents the scripts used to simulate the [0 1 0] and [0 0 1] CBED patterns with the multislice algorithm provided by the open source Python package py_multislice [4]. The simulations were ran on the IDUN cluster [74]. The job-script is therefore also presented. The convergence tests and CBED simulations were ran with several values for the grid shape, tiling and condenser aperture convergence angle, including grid shapes of [2048, 2048] and [3072, 3072], a convergence angle of 1 mrad and 1.25 mrad, and tilings of [8,$|8a/b|$] and [32, $|32a/b|$] for [0 0 1], and [8,$|8a/c|$] and [32,$|32a/c|$] for [0 1 0]. Figures presnting the beam spread and intensity from the convergence tests are also included. Only selected representative convergence tests will be shown. The simulations can also run on a CPU by specifying the device to *'cpu'*.

C.1 IDUN cluster jobscript

Line 30 was changed to the name of the python file which was to be run, and the virtual environment for the simulations provided by Postdoctoral Fellow Jonas Frafjord was specified in line 27.

```
1  #!/bin/bash
2
3  #SBATCH --partition=GPUQ
4  #SBATCH --time=00-03:21:00
5  #SBATCH --nodes=1
6  #SBATCH --ntasks-per-node=1
7  #SBATCH --gres=gpu:V10032:1
8  #SBATCH --constraint="V100"
9  #SBATCH --job-name="JOBNAME"
10 #SBATCH --mem=32000
11 ##SBATCH --mail-user= ""
12 #SBATCH --account=share-nv-fys-tem
13
14 echo "we are running from this directory: $SLURM_SUBMIT_DIR"
15 echo "The name of the job is: $SLURM_JOB_NAME"
16 echo "The job ID is $SLURM_JOB_ID"
17 echo "The job was run on these nodes: $SLURM_JOB_NODELIST"
18 echo "Number of nodes: $SLURM_JOB_NUM_NODES"
19 echo "We are using $SLURM_CPUS_ON_NODE cores"
20 echo "We are using $SLURM_CPUS_ON_NODE cores per node"
21 echo "Total of $SLURM_NTASKS cores"
22
23 module load Python/3.8.6-GCCcore-10.2.0
24 module list
25 source /path/to/source
26
27 python3 CBED_python_script.py
28
29 scontrol show job ${SLURM_JOB_ID} -d
```

C.2 Python script in the [001]

C.2.1 Convergence tests

```python
import pyms
import numpy as np
import torch
import os
import matplotlib.pyplot as plt

relative_path =   os.path.dirname(__file__)

crystal_file_path = os.path.join(relative_path, "KNBO_unit_cell.p1")
structure = pyms.structure.fromfile(crystal_file_path,
    atomic_coordinates = 'fractional', temperature_factor_units = 'ums')

gridshape = [2048, 2048]
tiling = [8, int(8*(17.506/15.162))]
slices = np.asarray([0.2, 0.4, 0.6,  0.8, 1.0])
eV = 2e5
app = 1.25
df = 0
nfph = 25
thickness = 5000
device = torch.device('cuda:0')

# Slicing figure
slicing_fig = structure.generate_slicing_figure(slices,show=False)
filename = "slicing_001.png"
slicing_fig.savefig(filename, transparent= False)

# Probe spread plot
fig= pyms.generate_probe_spread_plot(
    gridshape,
    structure,
    eV,
    app,
    thickness,
    subslices=slices,
    tiling=tiling,
    showcrossection=True,
    df = df,
    show = False,
    device=device
)

filename = "gs_2048_2048_tiling_8_8a_b__thickness_5000_app_1p25_001.png"
fig.savefig(filename, transparent= False)
```

C.2.1.1 Figures on beam spread and intensity

The convergence tests passed for all of the tilings and grid shapes tested for simulating CBED patterns in the [0 0 1] zone axis. Hence, only two example of the convergence tests of [0 0 1] is shown at [0 0 1] with a grid shape [2048, 2048], tiling [8, |8a/b|], and convergence angles of 1 mrad and 1.25 mrad.

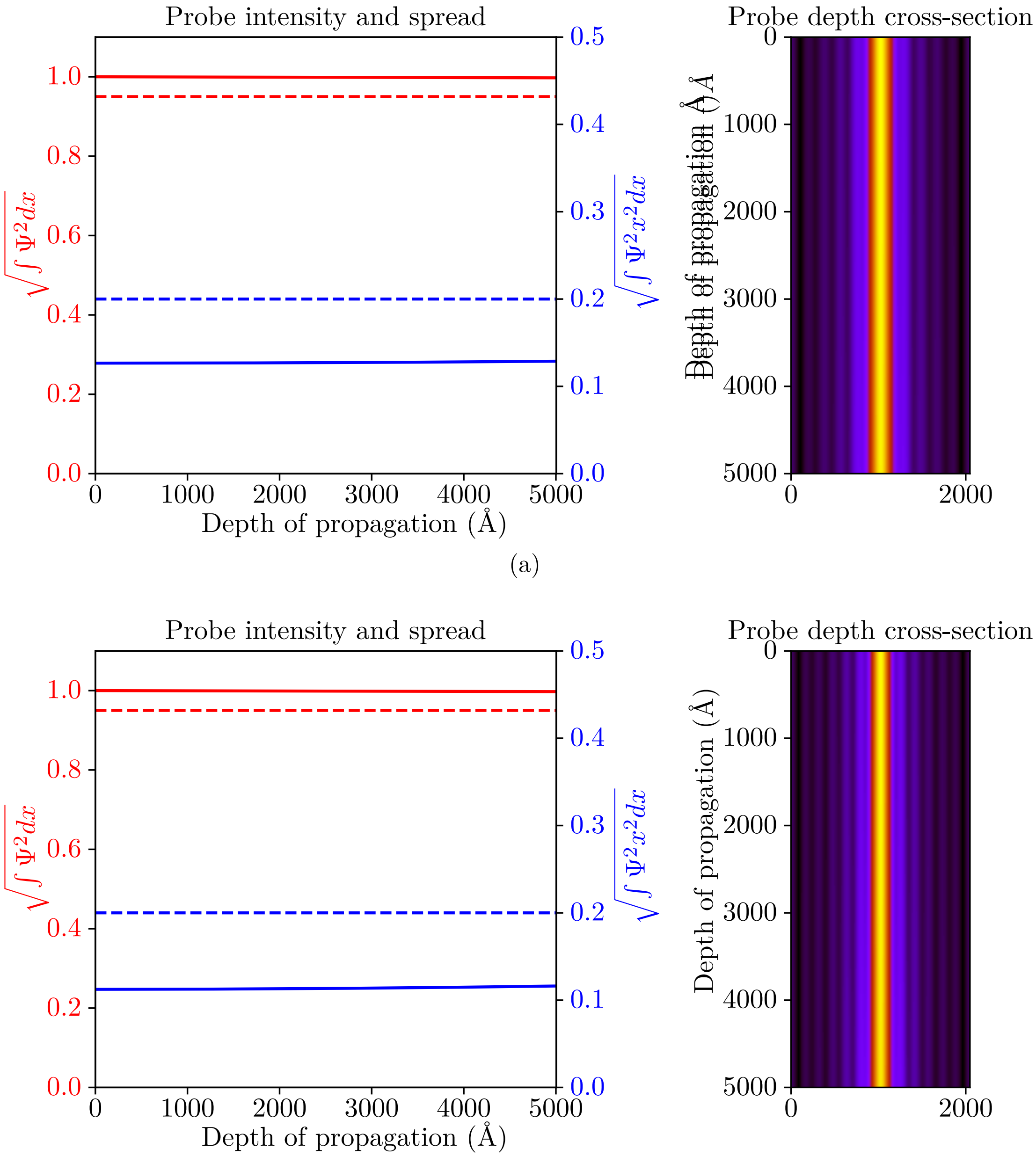

(a)

(b)

Figure C.1: Convergence tests for CBED simulations at [0 0 1] with a grid shape [2048, 2048], tiling [8, |a/b|], and (a) with convergence angle 1 mrad and (b) 1.25 mrad respectively. All other conditions were as stated in the script given above. The convergence test is passed when the probe intensity (red) is above the red dashed line, and the probe spread (blue) is below the blue dashed line.

C.2.2 CBED simulations

```python
import pyms
import numpy as np
import torch
import os
from PIL import Image

relative_path =   os.path.dirname(__file__)
crystal_file_path = os.path.join(relative_path, "KNBO_unit_cell.p1")
structure = pyms.structure.fromfile(crystal_file_path,
    atomic_coordinates = 'fractional', temperature_factor_units = 'ums')

gridshape = [3072, 3072]
tiling = [8, int(8*(17.506/15.162))]
eV = 2e5
app = 1.25
df = 0
nfph = 25
probe_posn = [0.5, 0.5]
device = torch.device('cuda:0') # or use 'cpu'
slices = np.asarray([0.2, 0.4, 0.6,  0.8, 1.0])
thicknesses = np.array([100, 150, 200, 250, 300, 400, 500, 600, 700,
    800, 900, 1000, 1500, 2000, 2500, 3000, 3500, 4000, 4500, 5000])

output = pyms.CBED(
    structure,
    gridshape,
    eV,
    app,
    thicknesses,
    subslices=slices,
    tiling=tiling,
    nfph=nfph,
    showProgress=True,
    device_type=device,
    probe_posn = probe_posn,
    dtype=torch.float64)

for i,out in enumerate(output):
    filename_png = "CBED_001_gs_3072_tiling_8a_b_nfpn_25_pp_0p5_ca_1p25_
    "+ str(thicknesses[i]) + ".png"
    filename_txt = "CBED_001_gs_3072_tiling_8a_b_nfpn_25_pp_0p5_ca_1p25_
    " + str(thicknesses[i]) + ".txt"
    filename_tif = "CBED_001_gs_3072_tiling_8a_b_nfpn_25_pp_0p5_ca_1p25_
    " + str(thicknesses[i]) + ".tif"
    save_dir_png = os.path.join(relative_path, filename_png)
    save_dir_txt = os.path.join(relative_path, filename_txt)
    save_dir_tif = os.path.join(relative_path, filename_tif)
    pyms.utils.output.save_array_as_png(out, save_dir_png)
    np.savetxt(save_dir_txt , out)
    Image.fromarray(out).save(save_dir_tif)
```

C.3 Python script in the [010]

C.3.1 Convergence tests

```
import pyms
import numpy as np
import torch
import os
import matplotlib.pyplot as plt

relative_path =   os.path.dirname(__file__)

crystal_file_path = os.path.join(relative_path, "KNBO_unit_cell.p1")
structure = pyms.structure.fromfile(crystal_file_path,
    atomic_coordinates = 'fractional', temperature_factor_units = 'ums')
structure = structure.rotate(np.pi/2, [1,0,0]) # To simulated the [010]

gridshape = [2048, 2048]
tiling = [8, int(8*(17.506/3.968))]
slices  = np.asarray([0.06, 0.115, 0.15, 0.185, 0.23, 0.28, 0.32, 0.36,
    0.39, 0.47, 0.55, 0.615, 0.645 ,0.685, 0.735, 0.78, 0.82, 0.855,
    0.89, 0.95, 1.0])
eV = 2e5
app = 1.25
df = 0
nfph = 25
thickness = 5000
device = torch.device('cuda:0')

# Slicing figure
slicing_fig = structure.generate_slicing_figure(slices,show=False)
filename = "slicing_010.png"
slicing_fig.savefig(filename, transparent= False)

# Probe spread plot
fig= pyms.generate_probe_spread_plot(
    gridshape,
    structure,
    eV,
    app,
    thickness,
    subslices=slices,
    tiling=tiling,
    showcrossection=True,
    df = df,
    show = False,
    device=device)

filename = "gs_2048_2048_tiling_8_8a_c__thickness_5000_app_1p25_010.png"
fig.savefig(filename, transparent= False)
```

C.3.1.1 Figures on beam spread and intensity

With the same parameters as tested for the [0 0 1] zone, the [0 1 0] convergence test resulted in a larger variation of probe intensity and probe spread. The results from the convergence tests in the [0 1 0] zone axis varied with respect to how many times the crystal was repeated in real space (tiling), the number of sampling points (grid shape) and convergence angles tested. A larger crystal in real space generally reduced the probe spread, while a larger number of sampling points increased the intensity. They were dependent on each other, such that if the grid shape was increased to enhance the intensity, the tiling had to be increased to make sure the probe spread was low. The convergence test did not pass even for grid shapes of [3072, 3072] and tiling [32,$\lfloor 32a/c \rceil$]. No larger values could be used, due to memory issues. Four examples are given below.

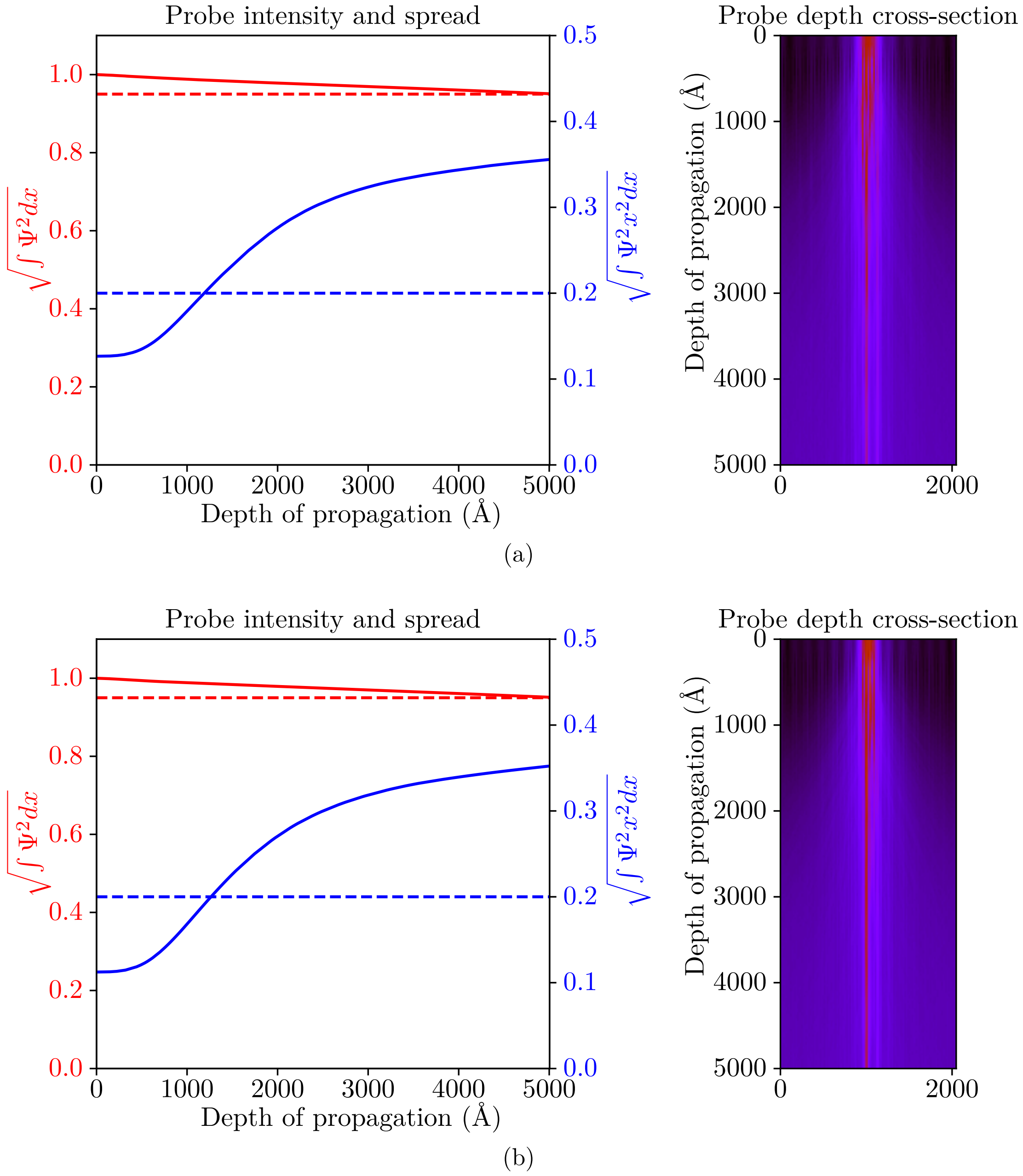

Figure C.2: Convergence tests for CBED simulations at [0 1 0] with a grid shape [2048, 2048], tiling [8, |8a/c|], and (a) with convergence angle 1 mrad and (b) 1.25 mrad respectively. All other conditions were as stated in the script given above. The convergence test is passed when the probe intensity (red) is above the red dashed line, and the probe spread (blue) is below the blue dashed line.

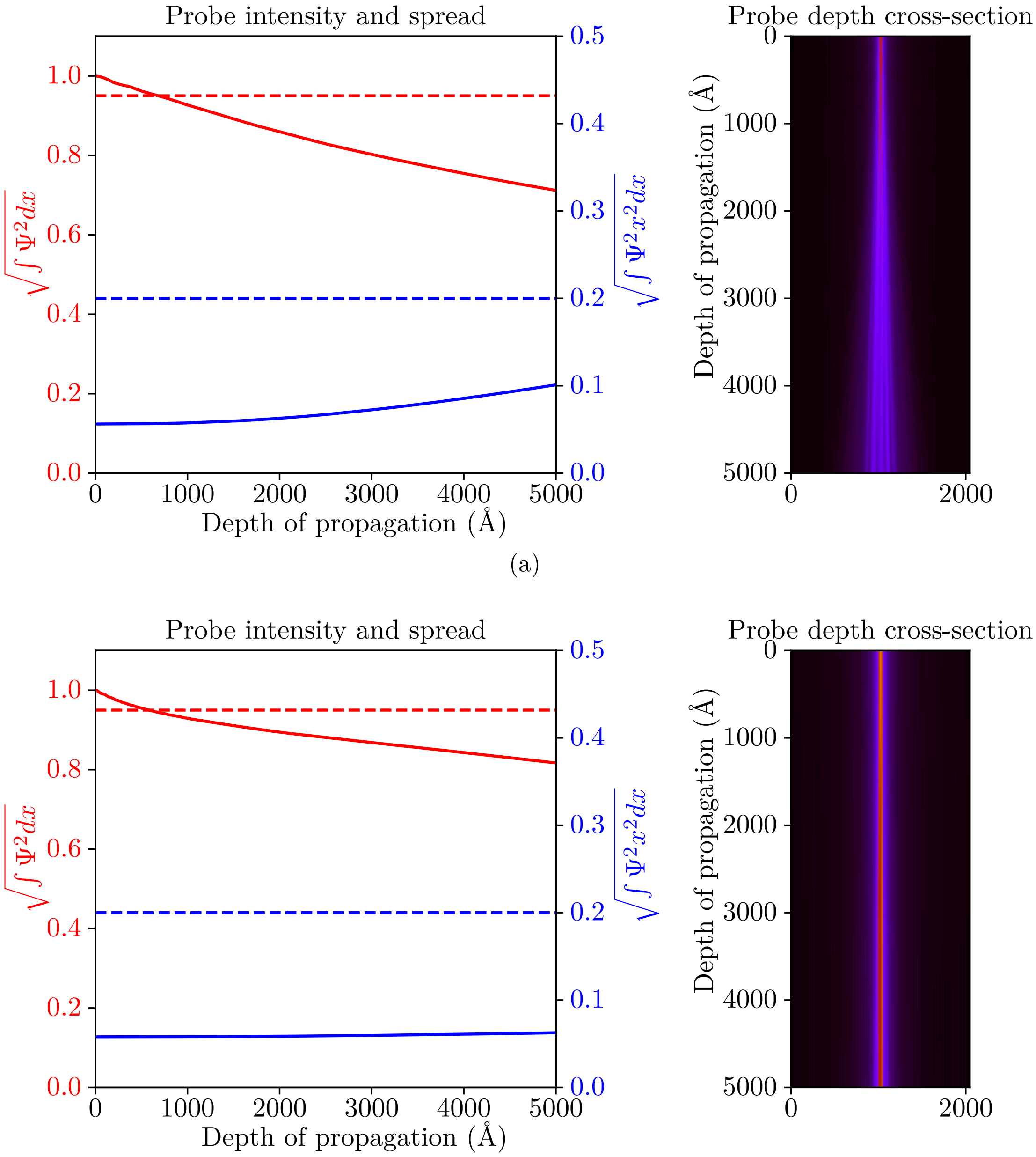

(a)

(b)

Figure C.3: Convergence tests for CBED simulations at [0 1 0] with a grid shape (a) [2048, 2048], tiling [32, |32a/c|], and with convergence angle 1.25 mrad, and (b) grid shape [2048, 2048], tiling [32, |32a/c|] with floor division, and 1.25 mrad. All other conditions were as stated in the script given above. The convergence test is passed when the probe intensity (red) is above the red dashed line, and the probe spread (blue) is below the blue dashed line.

C.3.2 CBED simulations

```
import pyms
import numpy as np
import torch
import os
from PIL import Image

relative_path =   os.path.dirname(__file__)
crystal_file_path = os.path.join(relative_path, "KNBO_unit_cell.p1")
structure = pyms.structure.fromfile(crystal_file_path,
    atomic_coordinates = 'fractional', temperature_factor_units = 'ums')
structure = structure.rotate(np.pi/2, [1,0,0])

gridshape = [2048, 2048]
tiling = [8, int(8*(17.506/3.968))]
eV = 2e5
app = 1.25
df = 0
nfph = 25
probe_posn = [0.5, 0.5]
device = torch.device('cuda')
slices  = np.asarray([0.06, 0.115, 0.15, 0.185, 0.23, 0.28, 0.32, 0.36,
    0.39, 0.47, 0.55, 0.615, 0.645 ,0.685, 0.735, 0.78, 0.82, 0.855,
    0.89, 0.95, 1.0])
thicknesses = np.array([100, 150, 200, 250, 300, 350, 400, 450, 500,
    550, 600, 650, 700, 750, 800, 850, 900, 950, 1000, 1050, 1100, 1150,
     1200, 1250, 1300, 1350, 1400, 1450, 1500, 2000, 2500, 3000, 3500,
    4000, 4500, 5000])

output = pyms.CBED(
    structure,
    gridshape,
    eV,
    app,
    thicknesses,
    subslices=slices,
    tiling=tiling,
    nfph=nfph,
    showProgress=True,
    device_type=device,
    probe_posn = probe_posn,
    dtype=torch.float32)

for i,out in enumerate(output):
    filename_png = "CBED_010_gs_2048_tiling_8_8_a_c_nfpn_25_pp_0p5_app_1
    .25_"+ str(thicknesses[i]) + ".png"
    filename_txt = "CBED_010_gs_2048_tiling_8_8_a_c_nfpn_25_pp_0p5_app_1
    .25_" + str(thicknesses[i]) + ".txt"
    filename_tif = "CBED_010_gs_2048_tiling_8_8_a_c_nfpn_25_pp_0p5_app_1
    .25_" + str(thicknesses[i]) + ".tif"
    save_dir_tif = os.path.join(relative_path, filename_tif)
    save_dir_png = os.path.join(relative_path, filename_png)
    save_dir_txt = os.path.join(relative_path, filename_txt)
    pyms.utils.output.save_array_as_png(out, save_dir_png)
    np.savetxt(save_dir_txt , out)
    Image.fromarray(out).save(save_dir_tif)
```

D Tripod polishing

This appendix describes in detail the specimen preparation of the *c*-axis in-plane specimen, and the *c*-axis out-of-plane specimen. It is a step-by-step procedure for the tripod polishing scheme. The procedure is adapted from Oskar Ryggetangen's work [45], which was based on Håkon Wiik Ånes [75].

The tripod polishing scheme consists of cutting the material in a region where there is large number of domains, followed by polishing the specimen to create a wedge-shaped specimen. Please note that it is based on the text written in the project that was carried out prior this thesis [1], with a few modifications to include the preparation of the *c*-axis in-plane specimen.

D.1 Cutting

The starting material should not be larger than 3×3 mm and a have thickness of ~ 2 mm. This is to avoid fracture in later steps. To cut the specimen, it should be mounted on a glass plate with hot wax. Let the wax harden before cutting. The specimen is cut using a *Testbourne Model 650 Low Speed Diamond WeelSaw* with a 60-20085 diamond metal bonded, low concentration, 150µm wafering blade, a speed of 3-4 rpm, and a load of approximately 100 g.

To prepare the *c*-axis out-of-plane specimen, the following steps should be followed:

1. Inspect the KNBO starting material by PLM to locate ferroelastic domains.
2. Make sure the specimen size is $\sim 3 \times 3$ mm and has a thickness > 800 µm.
3. Mount the specimen on a glass plate with hot wax. Let it harden
4. Cut a specimen which is approximately 2×1.5 mm along the *a*- and *b*-directions.
5. Inspect using PLM, and confirm that there is a high density of ferroic domains present.
6. Remove the specimen from the glass plate by heating it on a hot plate to liquefy the wax.
7. Clean the specimen in an acetone bath for a few minutes to remove the wax, followed by a 96% ethanol bath for a few seconds. Let the specimen dry. It is now ready for polishing.
8. Mount the specimen (as outlined in the next section), such that the *c*-direction is approximately normal to the pyrex surface.

To prepare the *c*-axis in-plane specimen, the following procedure should be followed:

1. Cut the KNBO starting material such that it is between 1-2 mm along the *c*-direction, if appropriate.
2. Inspect the *c*-facet of the specimen by PLM. Identify a facet which intersects several needle domains.
3. Cut the specimen such that the specimen is 1-2 mm in width and length in the plane of the chosen facet, and > 2 mm in the direction perpendicular to that facet.
4. Inspect the specimen's *c*-facet using PLM, and confirm that there is a high density of ferroic domains present.
5. Remove the specimen from the glass plate by heating it on a hot plate to liquefy the wax.
6. Clean the specimen in an acetone bath for a few minutes to remove the wax, followed by a 96% ethanol bath for a few seconds. Let the specimen dry. It is now ready for polishing.
7. Mount the specimen (as outlined in the next section), such that the *c*-direction is perpendicular to the wedge, and has a large number of twin needle domains intersecting the wedge. This will ensure that there is a high probability that at least one of the twin domains is oriented such that the [0 1 0]-direction is perpendicular to the pyrex surface.

D.2 Polishing facet 1

An *Allied Multistep* tripod polishing machine is used to polish the specimen. Different diamond lapping films (DLF) are used to determine the coarseness and speed of the polishing.

D.2.1 Specimen preparation

1. Make sure the DLF is clean and not damaged.
2. The specimen will be loaded on a pyrex stub. It is important that it is flat but still has some surface roughness to allow the glue to properly adhere to the surface. Therefore, polish the pyrex stub with a 6µm DLF to make it flat.
3. Rinse the pyrex stub with acetone, followed by ethanol with a q-tip.
4. Apply *Loctite* acetone soluble glue to the pyrex stub. Make sure it covers the whole stub, especially the corners and edges
5. Mount the specimen on the stub using a toothpick.
6. Let the glue cure overnight.

D.2.2 Polishing

The goal of polishing the first facet is to make a flat, polished surface. Between each polishing step, the specimen must be inspected in a light microscope to verify the polishing quality. The polishing is done when the rougher polishing lines from the previous polishing is no longer present. It is important to be cautious when polishing. The micrometre-scale can be used as a guide for the amount of material removed. Note, however, that the micrometre-scale is not accurate. Take caution, and only polish for a few seconds in the final steos of this procedure. Use a VLM to measure the height of the specimen.

1. Align the instrument.
2. Write down the 0° position by noting the position of the left micrometre screw on the polishing instrument.
3. Set the rotation speed of the plate to 30 rpm. For the following steps, this speed can be reduced if the thickness of the specimen is below the target.
4. Polish using a 15 µm DLF and 200 g load with lateral oscillation until the surface is completely flat. Rinse DLF with water continuously. Inspect in a VLM to ensure proper removal of any surface roughness on the material. Take note of any crack formation.
5. Polish using a 6 µm DLF under 200 g load with lateral oscillation until approximately 50 µm of material is removed. Rinse DLF with water continuously. Inspect in VLM.
6. Polish using a 3 µm DLF under 200 g load with lateral oscillation until approximately 20 µm of material is removed. Rinse DLF with water continuously. Inspect in VLM.
7. Polish using a 1 µm DLF under 50 g load without lateral oscillation until approximately 10 µm of material is removed. This is done by polishing for a few seconds at a time and measuring the specimen height in a VLM. Do not rinse with water, but apply *Allied GreenLube* to the DLF prior to polishing.
8. Polish with a 0.5 µm DLF under 50 g load without lateral oscillation for a few seconds at a time until 0.1 µm is removed. Do not rinse with water, but apply *Allied GreenLube* to the DLF prior to polishing. Inspect in VLM to measure the specimen height between each polish. Continue to the next step when 0.1 µm is removed.
9. Polish using a 0.1 µm DLF under 50 g load without lateral oscillation for 5-10 s. Do not rinse with water, but apply *Allied GreenLube* to the DLF prior to polishing. Inspect in VLM.
10. Apply *Allied 20* nm *Colloidal Silica* to a felt cloth. Polish the specimen for approximately 30 s under 0 g load without water.

D.2.3 Post-polishing considerations

To polish the opposite facet, the specimen must be clean and detached from the pyrex surface.

1. Dilute *Allied Micro Organic soap* to a 2% solution.
2. Clean the specimen with the solution using an *Allied* cotton tip. Rinse with deionized water. Repeat several times to ensure proper removal of silica particles.
3. Inspect the specimen in VLM.
4. Place the specimen in an acetone bath for 1-24 h. This will detach the specimen from the pyrex surface.
5. Rinse the specimen with ethanol.

D.3 Polishing facet 2

After polishing the first facet, the opposite facet should be polished at a 2° angle.

D.3.1 Pre-polishing considerations

Mount the specimen on the pyrex with the polished facet down as previously described. Ensure that the domain walls are parallel to the polishing direction. Also, make sure the specimen is mounted near the edge of the stub with appropriate orientation, as the specimen will be thinnest closest to the edge of the stub after polishing.

D.3.2 Polishing

It is important to be very careful when polishing this facet, as the KNBO specimen is thin and brittle at this point. Most of these steps should be performed at 3-10 second intervals before inspections in VLM to determine the specimen height and to ensure that no cracks have been introduced.

1. Set the rotation speed of the plate to 30 rpm.
2. Check if the thickness of the specimen is > 500 µm using a VLM.
3. If the thickness is > 500 µm, Polish using a 15 µm DLF and 200 g load with lateral oscillation until the thickness of the specimen is approximately 500 µm. If the thickness is < 500 µm, polish for a few seconds without lateral oscillation to make the surface flat. Rinse DLF with water continuously. Inspect in VLM.
4. Set the angle to 2° relative to the platen. This corresponds to two full rotations of the left micrometre screw.
5. Polish using a 15 µm DLF and 200 g load with lateral oscillation until the thickness of the specimen is approximately 250 µm. Rinse DLF with water continuously. Inspect in VLM. If the specimen is < 250µm, only polish for a few seconds.
6. Polish using a 6 µm DLF under 150 g load without lateral oscillation until the thickness of the specimen is approximately 150 µm. Rinse the DLF with water continuously. Inspect in VLM.
7. Polish using a 3 µm DLF under 150 g load without lateral oscillation until the thickness of the specimen is approximately 60 µm. Rinse the DLF with water continuously. Inspect in VLM or PLM. For the *c*-axis out-of-plane specimen, capture images using polarized light microscopy for easier identification of ferroic domain walls later.
8. Apply *Allied GreenLube* to the DLF. Polish using a 1 µm DLF under 0 g load without lateral oscillation at 10 s intervals. Inspect in VLM before the next interval. There should be clear thickness fringes after this step performed.
9. This step should be skipped for the *c*-axis in-plane specimen, as it tends to fracture. Apply *Allied GreenLube* to the DLF. Polish using a 0.5 µm DLF under 0 g load without lateral oscillation for 5-10 s. Inspect in VLM. The thickness fringes should be visible at lower magnifications and/or more pronounced.
10. This step should be skipped for the *c*-axis in-plane specimen, as it tends to fracture. Apply *Allied GreenLube* to the DLF. Polish using a 0.1 µm DLF under 0 g load without lateral oscillation for a maximum 5 s. Inspect in VLM.
11. Apply *Allied 20* nm *Colloidal Silica* to a felt cloth. Polish the specimen for a few seconds under 0 g load.

Follow the same cleaning procedure as previously described. Do not remove the specimen from the pyrex stub.

D.4 Mounting the specimen

The final step is to mount the specimen on a TEM grid. It may be desirable to further thin the specimen at a later stage by ion milling. Therefore, the specimen should be mounted on a 3 mm half-grid. If this is not available, use a Cu slot-grid.

1. Apply a few drops of an *Araldite* epoxy adhesive to the thick side of the KNBO specimen using a sharp toothpick. Make sure that it is not applied to the pyrex stub.
2. Place the grid on top. Ensure no adhesive spills on the pyrex stub. Also, ensure that the thin part of the specimen is not covered by the grid.
3. Push the grid gently on the specimen.
4. Let the adhesive cure for approximately 24 h.
5. Remove the TEM specimen from the pyrex stub by placing the specimen in an acetone bath for approximately 1-24 h.
6. Put the specimen in a clean acetone bath for approximately 15 min.
7. Rinse the specimen in an ethanol bath for 5 min.

The specimen should be handled carefully to avoid chipping. Store the specimen in a membrane box.

E Additional data from the tilt series

This appendix presents additional Kikuchi, CBED and SAED diffraction patterns acquired in experimental the tilt series, and simulated SAED patterns from a simulated tilt series. These are given to document the diffraction properties of several planes in KNBO. Additionally, they may be useful for orientational purposes in the lab.

E.1 Experimental tilt series

The set of diffraction patterns from several zones of the tilt series are included to document these patterns of KNBO experimentally. This includes Kikuchi and CBED patterns, and SAED patterns at a lower camera length than those given in section 4.1.2.

$$\begin{tikzcd}
 & & (5.2^\circ, -13.4^\circ) & & & \\
 & & (3.7^\circ, -6.1^\circ) \arrow[u, "7.43^\circ"'] & & & \\
(13.2^\circ, 3.0^\circ) & (8.9^\circ, 2.5^\circ) \arrow[l, "4.32^\circ"'] & (2.4^\circ, 1.2^\circ) \arrow[l, "6.62^\circ"'] \arrow[u, "7.41^\circ"'] \arrow[r, "6.65^\circ"] \arrow[d, "7.31^\circ"] & (-4.1^\circ, -0.2^\circ) \arrow[r, "4.46^\circ"] & (-8.5^\circ, -0.9^\circ) \arrow[r, "5.40^\circ"] & (-13.7^\circ, -2.4^\circ) \\
 & & (1.1^\circ, 8.4^\circ) & & &
\end{tikzcd}$$

Figure E.1: Schematic of the holder-tilt values from the experimental tilt series. The corresponding SAED, CBED and Kikuchi patterns are given in figures E.2, E.3, and E.4.

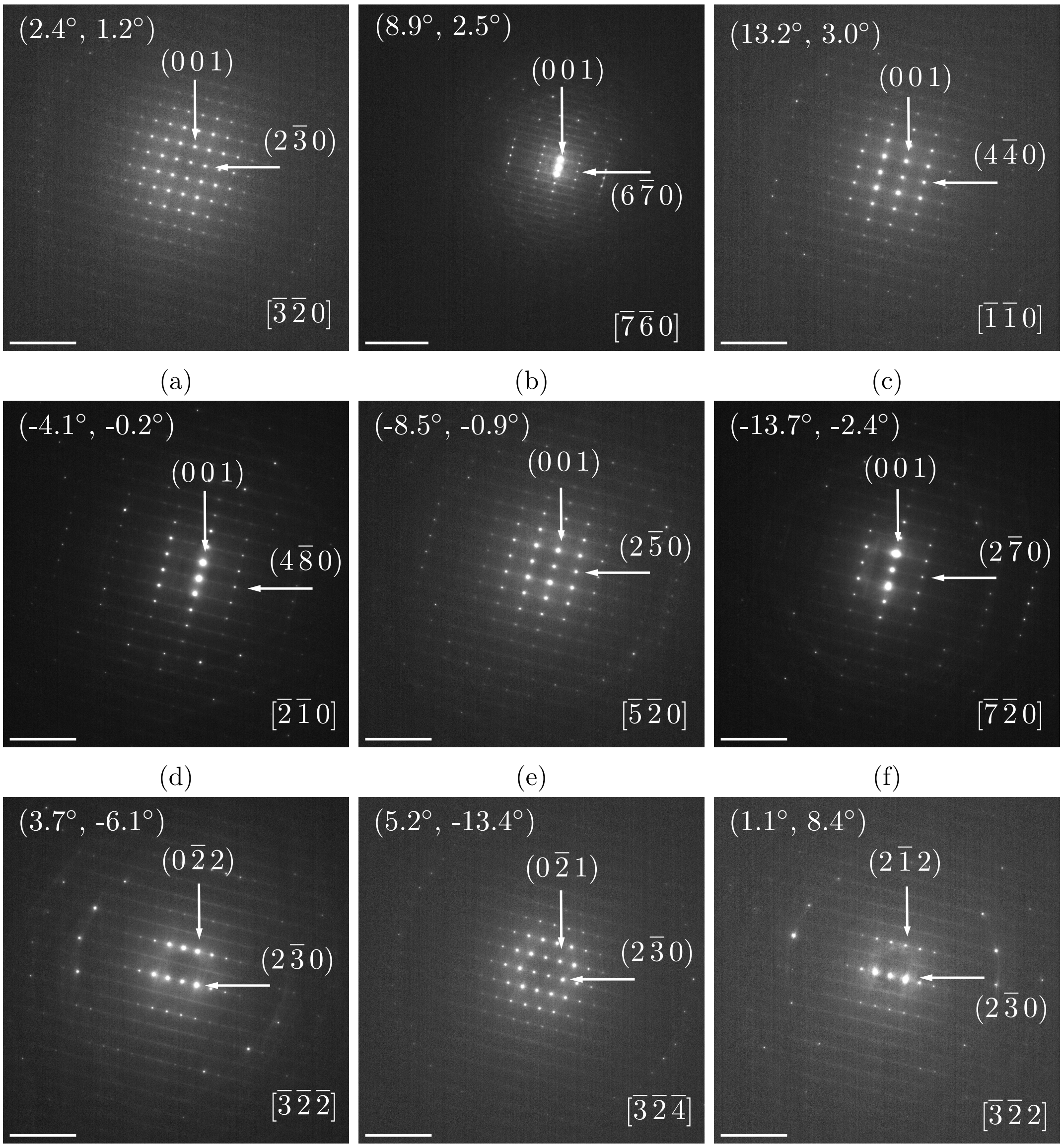

(a) (b) (c)

(d) (e) (f)

(g) (h) (i)

Figure E.2: (a-i) SAED patterns from the tilt series at holder-tilt values (2.4°, 1.2°), (8.9°, 2.5°), (13.2°, 3.0°), (-4.1°, -0.2°), (-8.5°, -0.9°), (-13.7°, -2.4°), (3.7°, -6.1°), (5.2°, -13.4°), and (1.1°, 8.4°) respectively. The scale bar in (b) is 20 nm^{-1}, and the scale bars in (a, c-i) are 10 nm^{-1}.

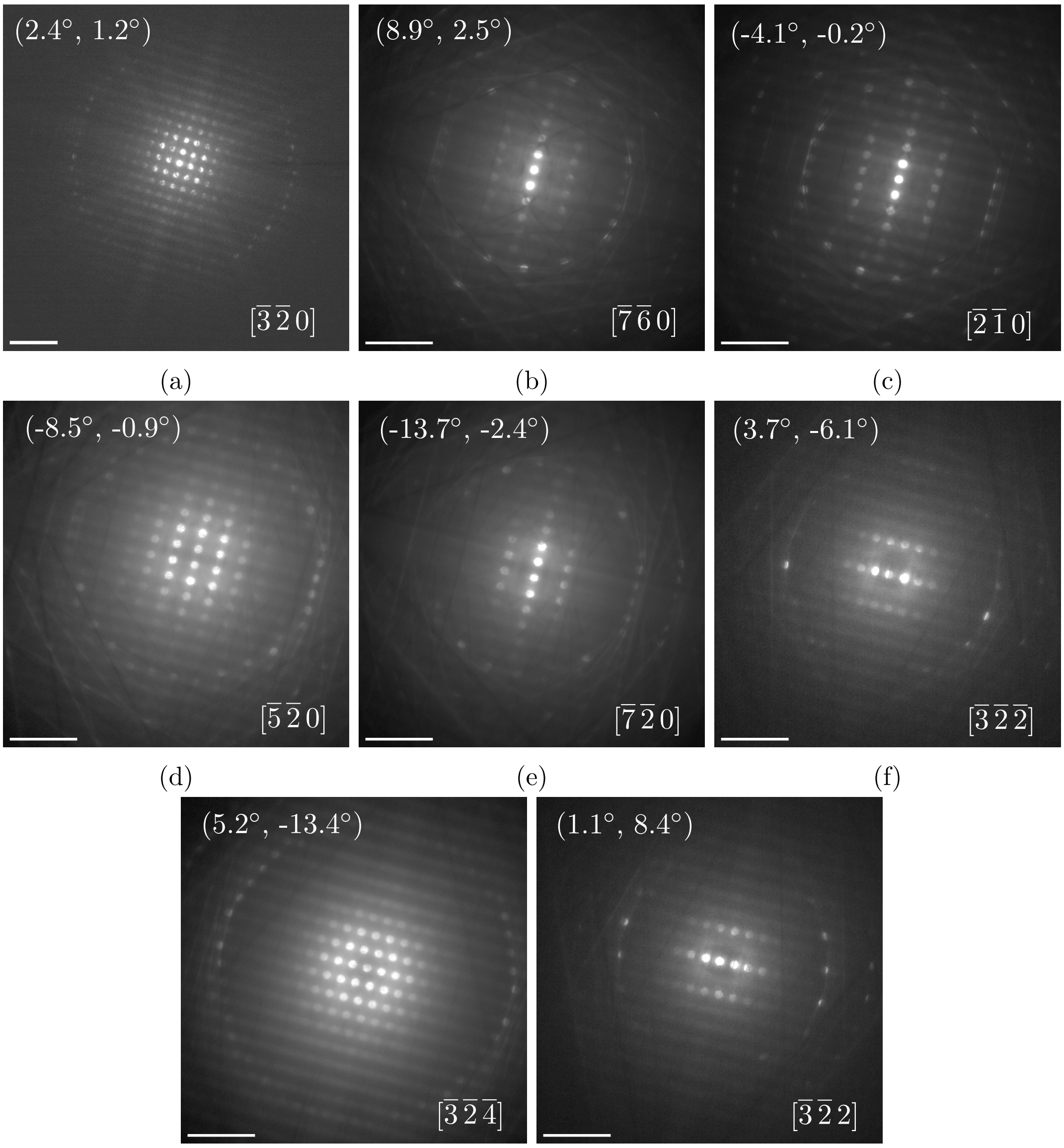

(a) (b) (c)

(d) (e) (f)

(g) (h)

Figure E.3: (a-i) CBED patterns from the tilt series at holder-tilt values (2.4°, 1.2°), (8.9°, 2.5°), (-4.1°, -0.2°), (-8.5°, -0.9°), (-13.7°, -2.4°), (3.7°, -6.1°), (5.2°, -13.4°), and (1.1°, 8.4°) respectively. (a-b) The scale bars are 10 nm^{-1}. Unfortunately, no CBED pattern was acquired at (13.2°, 3.0°). The CBED patterns are indexed as given in figure E.2.

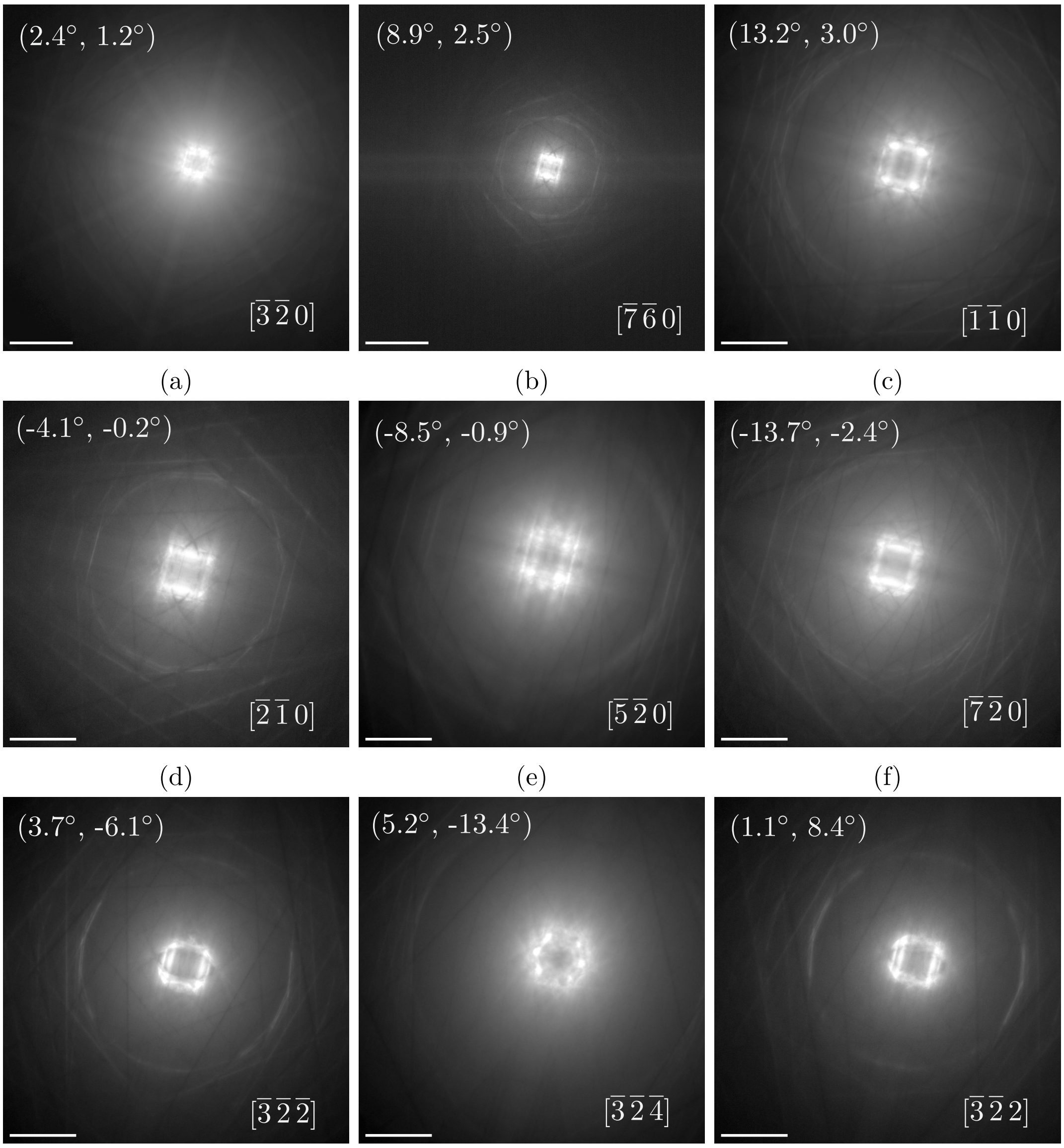

(a) (b) (c) (d) (e) (f) (g) (h) (i)

Figure E.4: (a-i) Kikuchi patterns from the tilt series at holder-tilt values (2.4°, 1.2°), (8.9°, 2.5°), (13.2°, 3.0°), (-4.1°, -0.2°), (-8.5°, -0.9°), (-13.7°, -2.4°), (3.7°, -6.1°), (5.2°, -13.4°), and (1.1°, 8.4°) respectively. (a-b) The scale bar is 20 nm^{-1} (c-i) The scale bars are 10 nm^{-1}. The kikuchi lines are not indexed to perserve the symmetry observations. See figure E.2 for reference with respect to indexing.

E.2 Simulated SAED patterns of suggested zone schemes for the tilt series

Simulated tilt series from suggested indexing scheme where the tilt series is centered about the $[\bar{3}\,2\,0]$, $[3\,\bar{2}\,0]$, $[3\,2\,0]$, $[0\,1\,0]$, and $[0\,\bar{1}\,0]$, in other words the other suggestions by ReciPro given in table 4.1. The similarity between these zones and their respective neighbouring zones are striking. The SAED patterns were simulated with JEMS.

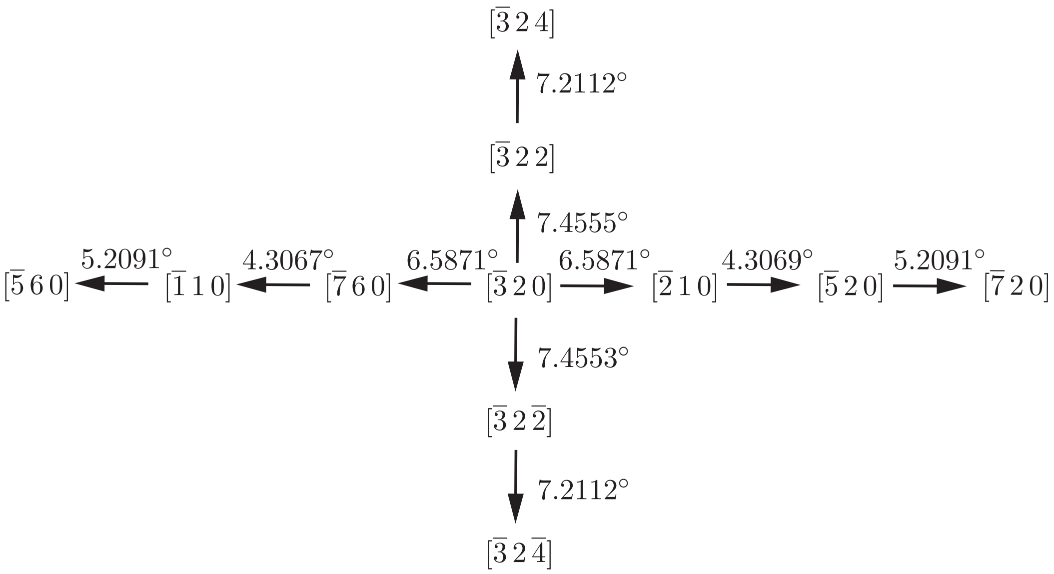

Figure E.5: Simulated $[\bar{3}\,2\,0]$ tilt series. The corresponding SAED patterns are given in figure E.6.

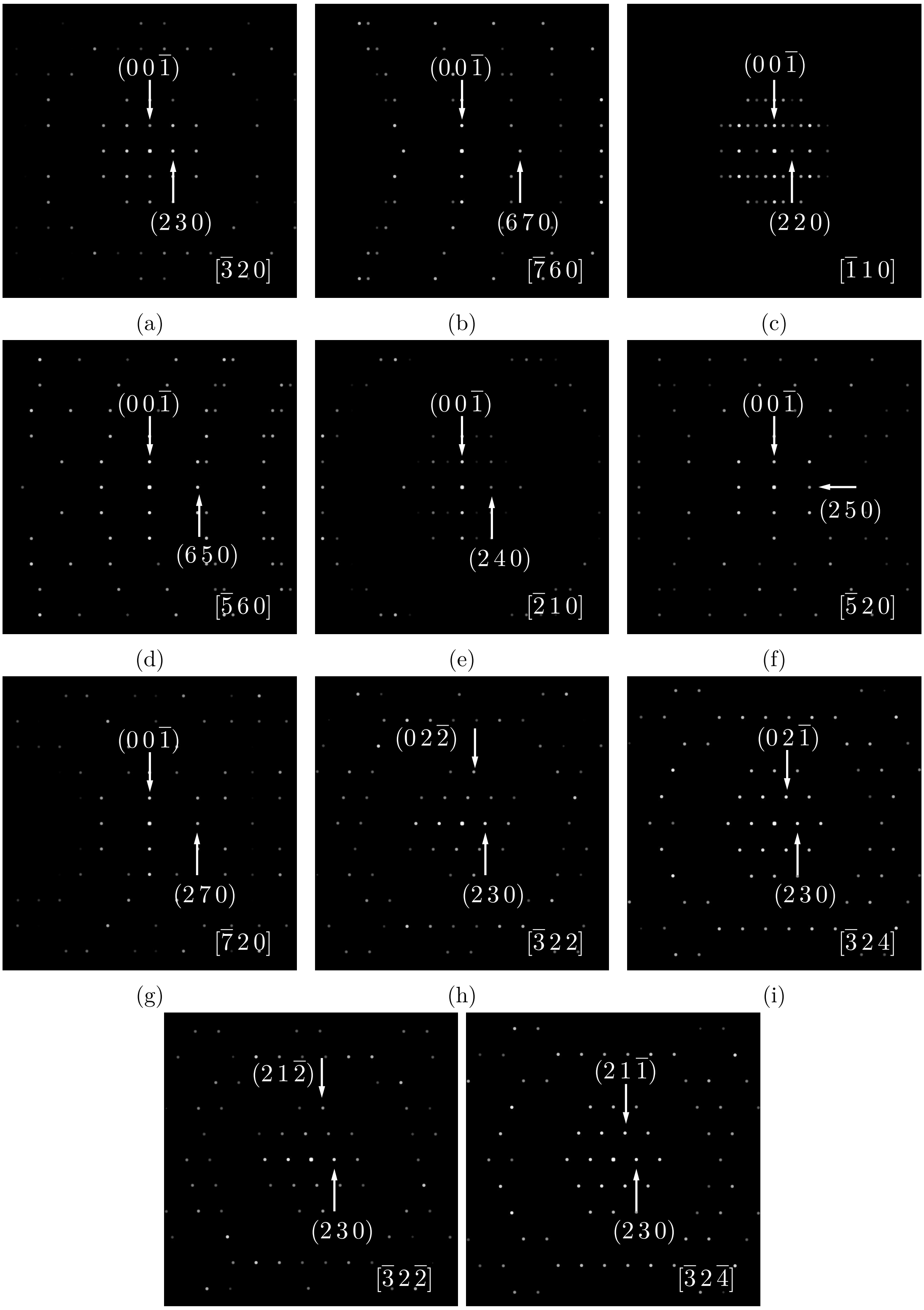

(a) (b) (c)

(d) (e) (f)

(g) (h) (i)

(j) (k)

Figure E.6: Simulated SAED patterns for the neighboring zones to $[\bar{3}\,2\,0]$, as illustrated in figure E.5.

$$\begin{tikzcd}
 & & & {[3\,\bar{2}\,\bar{4}]} & & & \\
 & & & {[3\,\bar{2}\,\bar{2}]} \arrow[u, "7.2112^\circ"'] & & & \\
{[7\,\bar{2}\,0]} & {[5\,\bar{2}\,0]} \arrow[l, "5.2091^\circ"'] & {[2\,\bar{1}\,0]} \arrow[l, "4.3067^\circ"'] & {[3\,\bar{2}\,0]} \arrow[l, "6.5871^\circ"'] \arrow[r, "6.5871^\circ"] \arrow[u, "7.4555^\circ"'] \arrow[d, "7.4553^\circ"] & {[7\,\bar{6}\,0]} \arrow[r, "4.3069^\circ"] & {[1\,\bar{1}\,0]} \arrow[r, "5.2091^\circ"] & {[5\,\bar{6}\,0]} \\
 & & & {[3\,\bar{2}\,2]} \arrow[d, "7.2112^\circ"] & & & \\
 & & & {[3\,\bar{2}\,4]} & & &
\end{tikzcd}$$

Figure E.7: $[3\,\bar{2}\,0]$ tilt series. The corresponding SAED patterns are given in figure E.8.

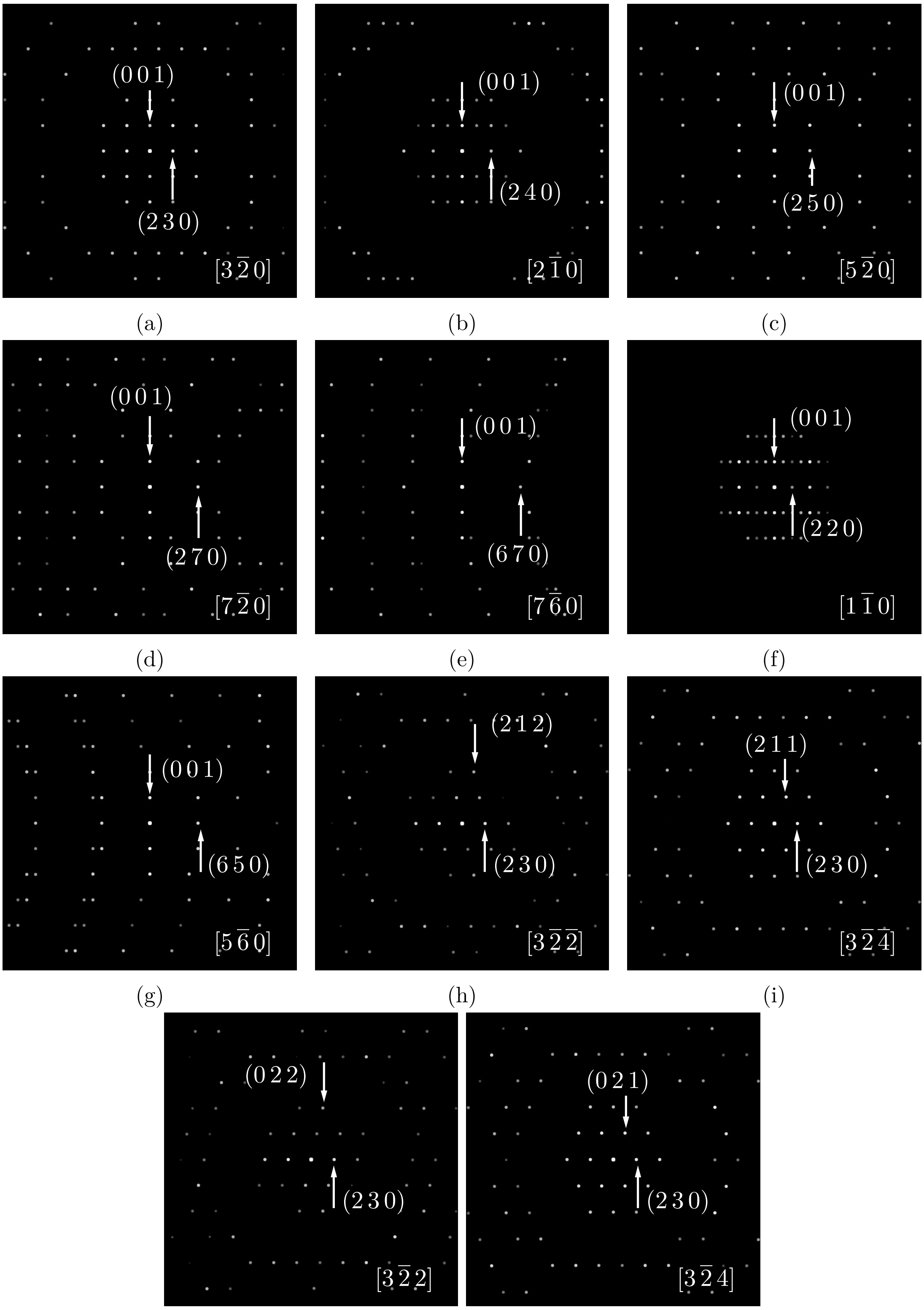

(a) (b) (c)

(d) (e) (f)

(g) (h) (i)

(j) (k)

Figure E.8: Simulated SAED patterns for the neighboring zones to [3 $\bar{2}$ 0], as illustrated in figure E.7.

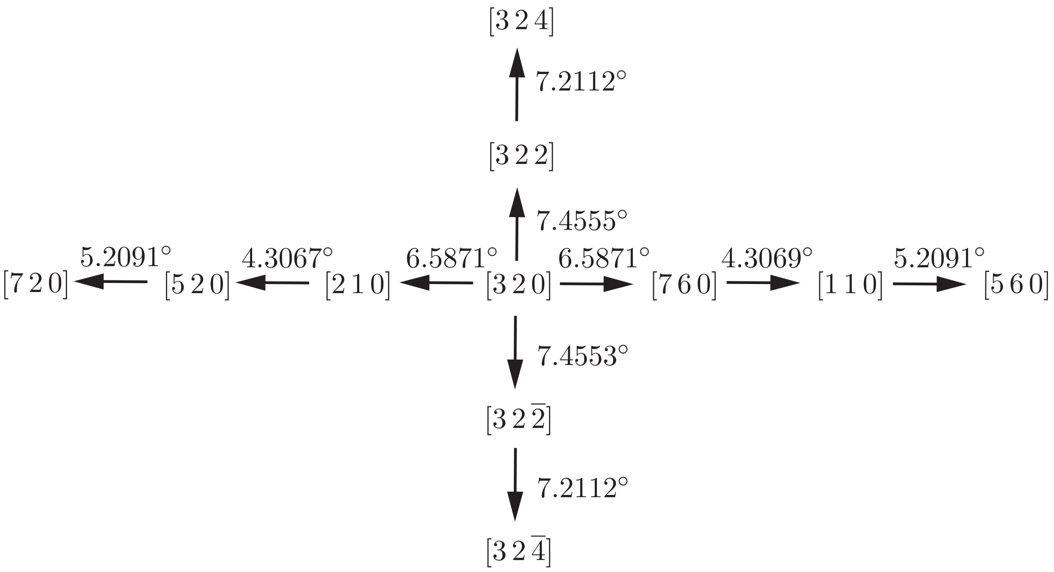

Figure E.9: Simulated [3 2 0] tilt series. The corresponding SAED patterns are given in figure E.10.

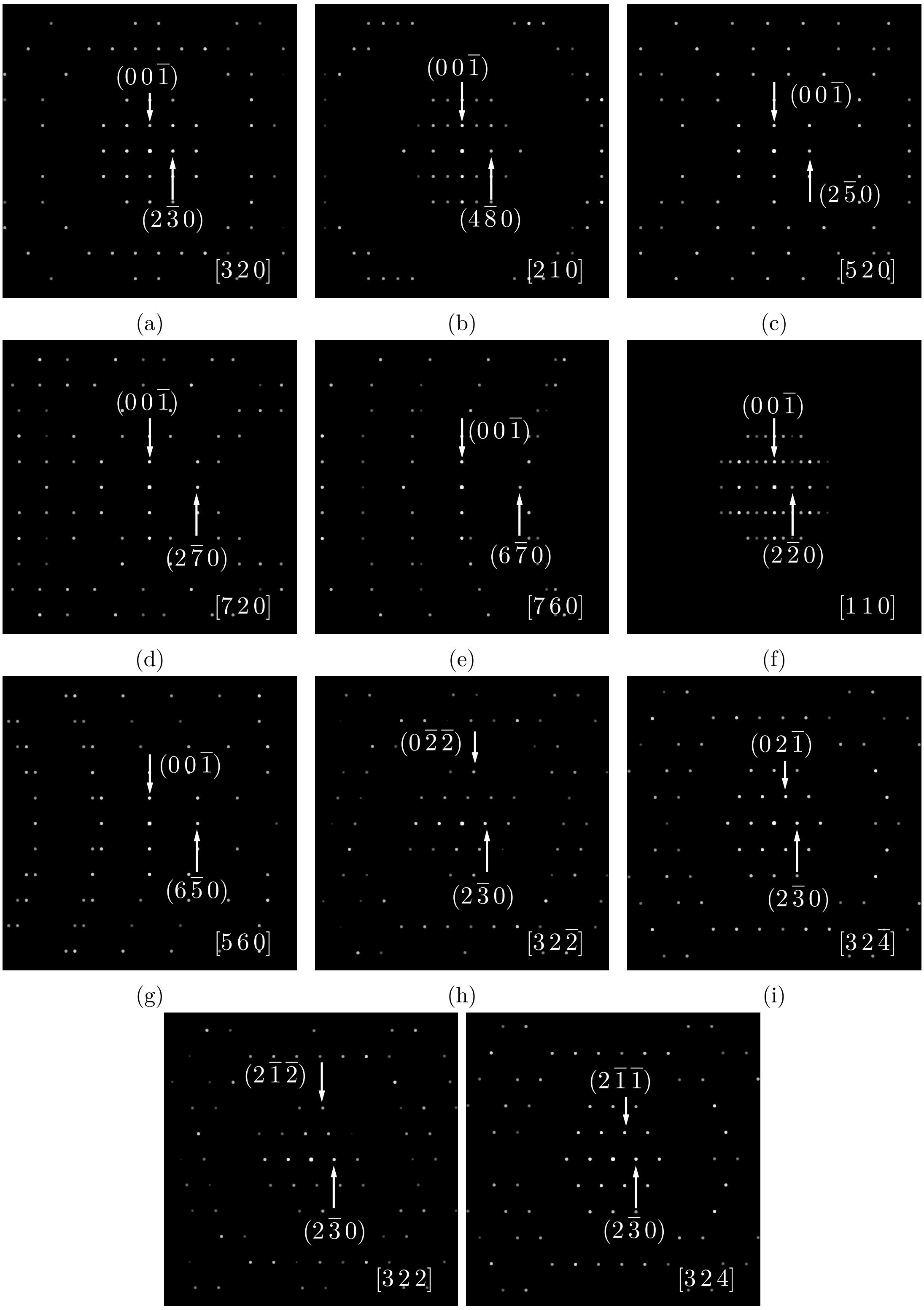

(a) (b) (c) (d) (e) (f) (g) (h) (i) (j) (k)

Figure E.10: Simulated SAED patterns for the neighboring zones to [3 2 0], as illustrated in figure E.9.

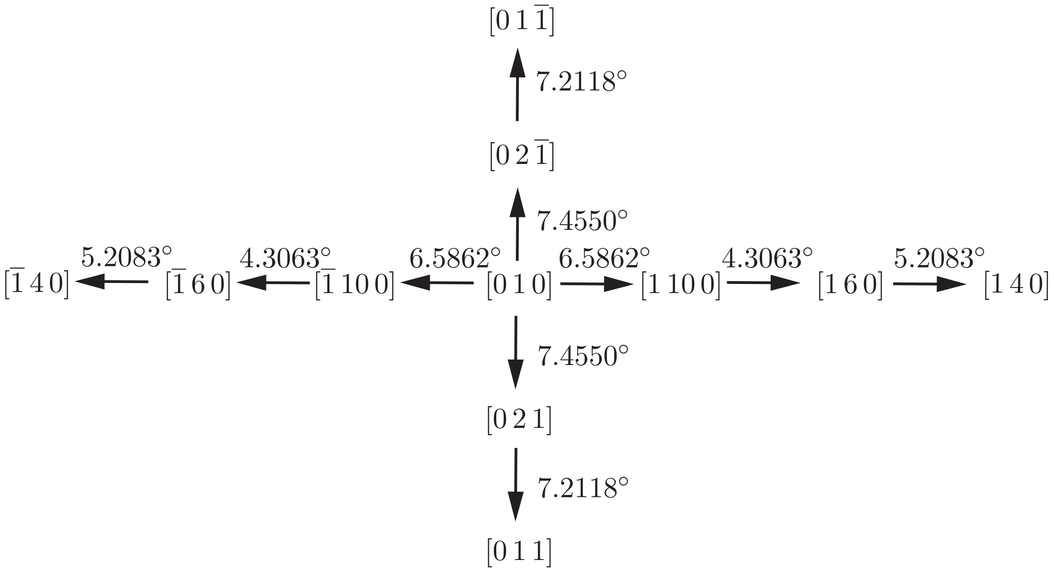

Figure E.11: Simulated [0 1 0] tilt series. The corresponding SAED patterns are given in figure E.12.

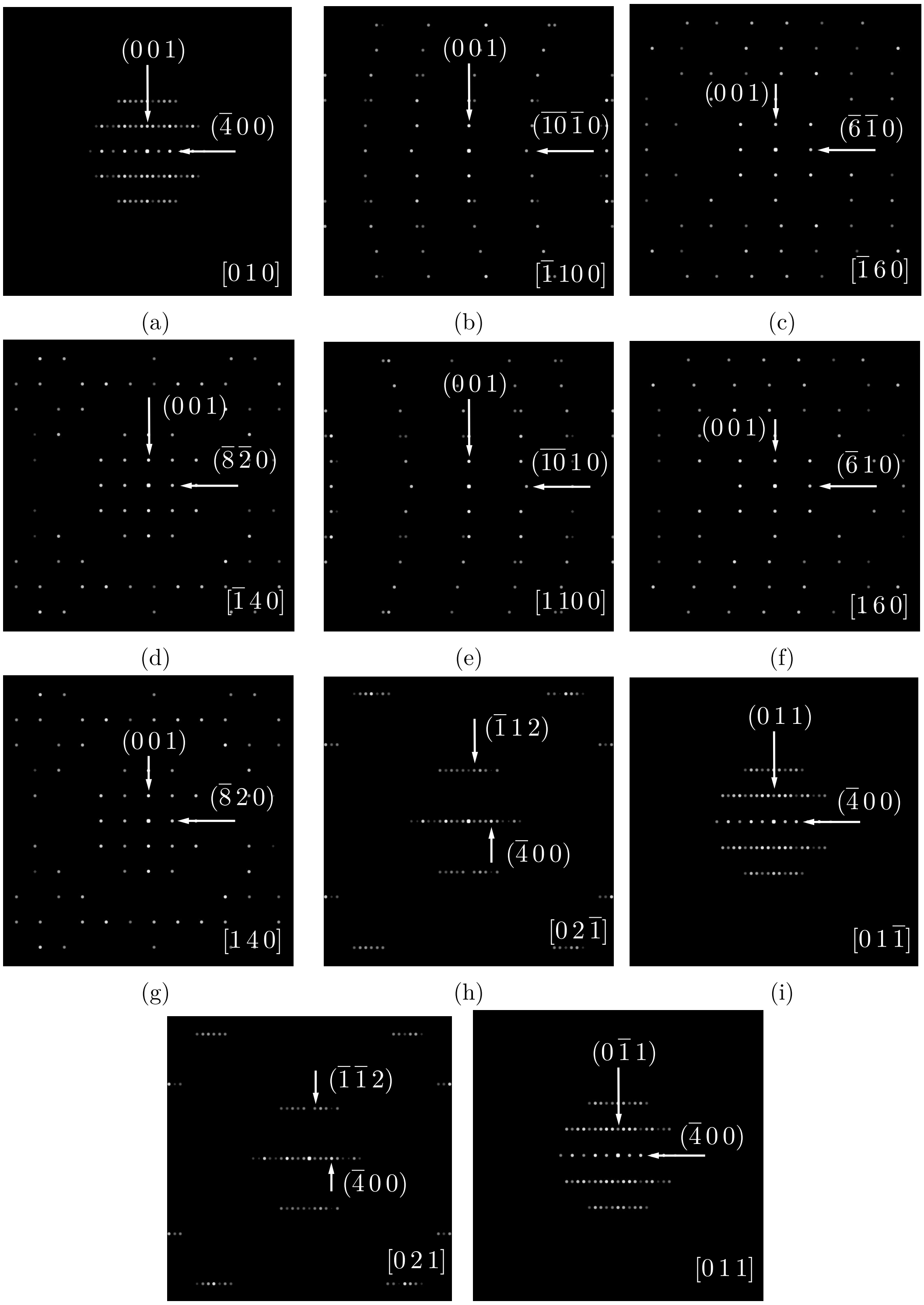

(a) (b) (c)

(d) (e) (f)

(g) (h) (i)

(j) (k)

Figure E.12: Simulated SAED patterns for the neighboring zones to $[0\,1\,0]$, as illustrated in figure E.11.

$$\begin{tikzcd}
 & & & {[0\,\bar{1}\,\bar{1}]} & & & \\
 & & & {[0\,\bar{2}\,\bar{1}]} \arrow[u, "7.2118^\circ"'] & & & \\
{[1\,\bar{4}\,0]} & {[1\,\bar{6}\,0]} \arrow[l, "5.2083^\circ"'] & {[1\,\overline{10}\,0]} \arrow[l, "4.3063^\circ"'] & {[0\,\bar{1}\,0]} \arrow[l, "6.5862^\circ"'] \arrow[r, "6.5862^\circ"] \arrow[u, "7.4550^\circ"'] \arrow[d, "7.4550^\circ"] & {[\bar{1}\,\overline{10}\,0]} \arrow[r, "4.3063^\circ"] & {[\bar{1}\,\bar{6}\,0]} \arrow[r, "5.2083^\circ"] & {[\bar{1}\,\bar{4}\,0]} \\
 & & & {[0\,\bar{2}\,1]} \arrow[d, "7.2118^\circ"] & & & \\
 & & & {[0\,\bar{1}\,1]} & & &
\end{tikzcd}$$

Figure E.13: Simulated $[0\,\bar{1}\,0]$ tilt series. The corresponding SAED are given in figure E.14.

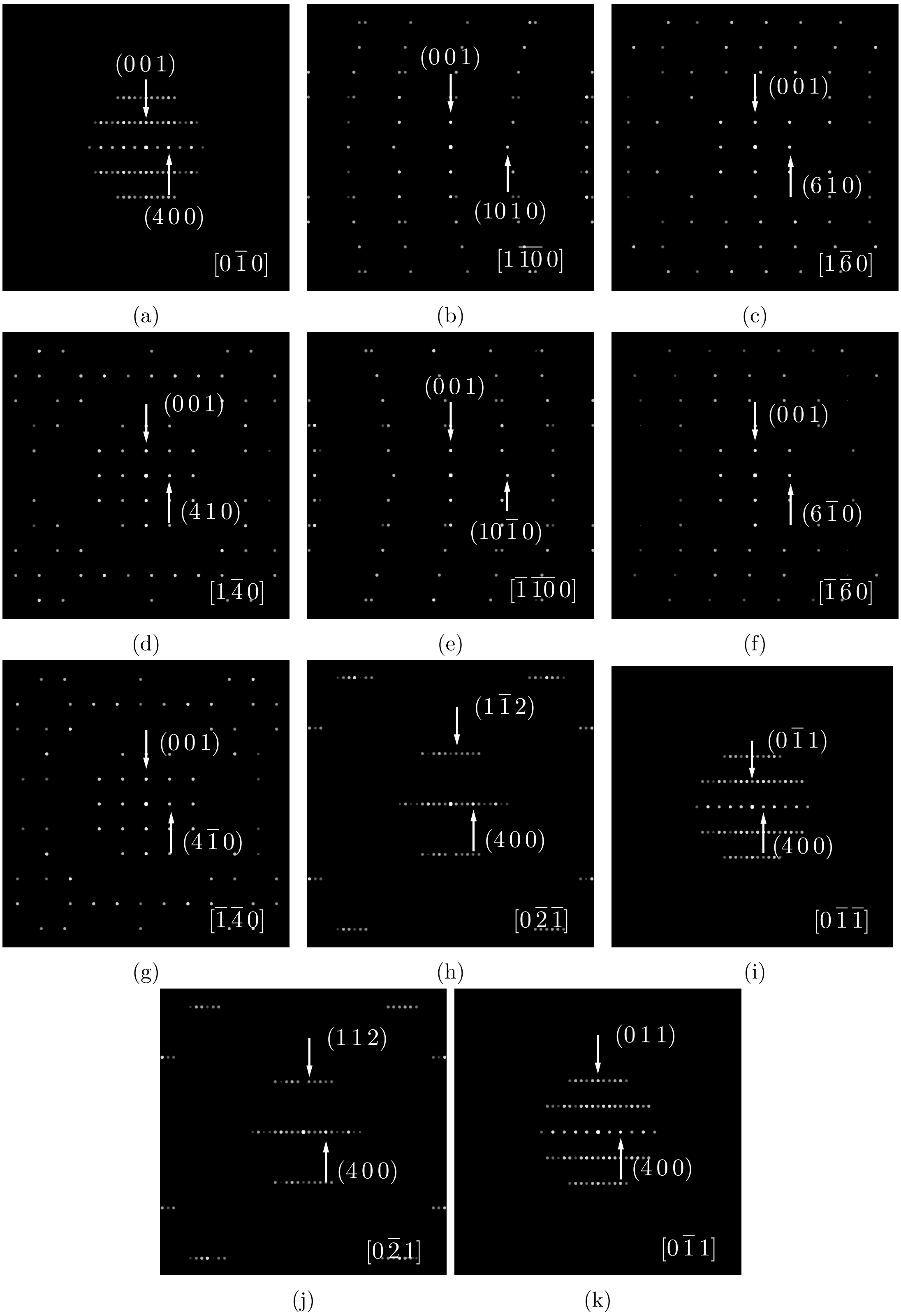

Figure E.14: Simulated SAED patterns for the neighboring zones to [0 $\bar{1}$ 0], as illustrated in figure E.13.

Marthe Linnerud

Building a framework for domain characterisation of KNBO by TEM

NTNU
Norwegian University of
Science and Technology